

IVW - Schriftenreihe Band 158

Leibniz-Institut für Verbundwerkstoffe GmbH
Kaiserslautern

Max Kaiser

**Transient electro-thermomechanical modeling of shape
adaptive Shape Memory Alloy Hybrid Composites
under influence of ambient temperature and static
external load**

Bibliografische Information Der Deutschen Bibliothek

Die Deutsche Bibliothek verzeichnet diese Publikation in der Deutschen Nationalbibliografie; detaillierte bibliografische Daten sind im Internet über <<http://dnb.dnb.de>> abrufbar.

Bibliographic information published by Die Deutsche Bibliothek

Die Deutsche Bibliothek lists this publication in the Deutsche Nationalbibliografie; detailed bibliographic data is available in the Internet at <<http://dnb.dnb.de>>.

Herausgeber: Leibniz-Institut für Verbundwerkstoffe GmbH
Prof. Dr.-Ing. Ulf Breuer
Erwin-Schrödinger-Straße 58
Technische Universität Kaiserslautern
67663 Kaiserslautern
<http://www.ivw.uni-kl.de>

Verlag: Leibniz-Institut für Verbundwerkstoffe GmbH

Druck: pri-me Printservice & Medienservice
Barbarossastraße 1
67655 Kaiserslautern
D-386

© Leibniz-Institut für Verbundwerkstoffe GmbH, Kaiserslautern 2023

Alle Rechte vorbehalten, auch das des auszugsweisen Nachdrucks, der auszugsweisen oder vollständigen Wiedergabe (Photographie, Mikroskopie), der Speicherung in Datenverarbeitungsanlagen und das der Übersetzung.

Als Manuskript gedruckt. Printed in Germany.

ISSN 1615-021X

ISBN: 978-3-944440-55-2

Transient electro-thermomechanical modeling of shape adaptive Shape Memory Alloy Hybrid Composites under influence of ambient temperature and static external load

Vom Fachbereich Maschinenbau und Verfahrenstechnik
der Rheinland-Pfälzischen Technischen Universität Kaiserslautern Landau
zur Verleihung des akademischen Grades

Doktor-Ingenieur (Dr.-Ing.)

genehmigte

Dissertation

von

Dipl.-Ing. Max Kaiser

aus Neustadt an der Weinstraße

2023

| | |
|-----------------------------|--------------------------------------|
| Tag der mündlichen Prüfung: | 05. Oktober 2023 |
| Prüfungsvorsitzender: | Prof. Dr.-Ing. Joachim Hausmann |
| 1. Berichterstatter: | Prof. Dr.-Ing. Ulf Paul Breuer |
| 2. Berichterstatter: | Prof. Dr.-Ing. Stefan Seelecke |
| 3. Berichterstatter: | PD Dr. rer. nat. habil. Martin Gurka |
| Dekan: | Prof. Dr. rer. nat. Roland Ulber |

Vorwort

Diese Arbeit entstand während meiner Zeit als wissenschaftlicher Mitarbeiter in der Abteilung "Tailored and Smart Composites" am Institut für Verbundwerkstoffe GmbH von 2018 bis 2023. In dieser Zeit hatte ich das große Glück, in einem Umfeld arbeiten zu dürfen, in dem Fehler nicht nur toleriert wurden, sondern in dem man ständig dazu ermutigt wurde, aus ihnen zu lernen.

An dieser Stelle möchte ich Martin Gurka, meinem Doktorvater und Abteilungsleiter, danken. Er schenkte mir sein Vertrauen in meine Fähigkeiten und gewährte mir die Freiheit bei meiner Forschung. Darüber hinaus schuf er ein innovatives Arbeitsumfeld. Nicht zuletzt führten unzählige wissenschaftliche Diskussionen mit meinen Kollegen in der Abteilung zum Erfolg meiner Arbeit. Hier möchte ich besonders Julia Vogtmann, Sonja Adler, Harut Yagdijan, Vitalij Popov, Benjamin Kelkel, Maurice Gilberg, Christoph Queck, Sebastian Nissle, Manuel Kunzler, Benedikt Boos und Bai Cheng Jim namentlich erwähnen. Ebenso danke ich Herrn Prof. Dr.-Ing. Ulf Breuer, der mich stets dazu anspornte, mein Bestes zu geben, und durch seinen vorbildlichen Führungsstil maßgeblich zu meiner Entwicklung während der Doktorzeit beitrug. Herr Prof. Dr.-Ing. Stefan Seelecke und Herr Prof. Dr.-Ing. Joachim Hausmann danke ich für die Begutachtung meiner Arbeit bzw. die Übernahme des Vorsitzes.

Mein Interesse an formadaptiven Hybridverbunden wurde erst durch Moritz Hübler geweckt. Er war stets ein Vorbild für mich aufgrund seiner direkten Art, seiner Fokussierung auf das Wesentliche und seiner Kompetenz, auch in schwierigen Situationen einen kühlen Kopf zu bewahren.

Für die körperliche Auslastung zwischen den anspruchsvollen Phasen geistiger Arbeit sorgten meine Kollegen Matthias Bandler, Benedikt Boos, Stefano Cassola, Miro Duhovic, David May und Julian Weber vom C.O.P. In teilweise anstrengenden Trainingssessions kam neben der Fitness auch der Humor nie zu kurz. Dafür gebührt euch mein Dank.

Meinem ehemaligen Studenten, späteren Kollegen und schließlich guten Freund Manuel Kunzler danke ich ebenfalls für das Training, aber auch für viele fruchtbare Diskussionen und erfolgreiche Konferenzen.

Erst durch meinen Bürokollegen Mohamadreza Nasirzade Tabrizi lernte ich, was wahrer Kaffeegenuss bedeutet. An langen Bürotagen halfst du mir stets, meine Aufmerksamkeit auf einem Topniveau zu halten.

Simon Fischer und Rami Al-Khamissi danke ich insbesondere für ihre wichtigen Beiträge zu meiner Arbeit. Durch die tatkräftige Unterstützung bei Versuchen und Simulationen von Studenten wie euch werden solche Arbeiten erst möglich.

Ohne die vielen Verantwortlichen für Technik und Infrastruktur, die die Basis für erfolgreiche Forschung bilden, wäre diese Arbeit nicht möglich gewesen. Ich möchte hier explizit Petra Volk, Pia Eichert, Markus Hentzel, Harald Weber, Christian Ackel, Thorsten Becker und Ralf Schimmele sowie Silke Fischer nennen.

Der größte Dank gebührt jedoch meiner Familie. Meine Eltern ließen mich frei von allen Zwängen entfalten, unterstützten mich stets und wussten in jeder Situation den richtigen Rat. Meine Schwester war mir mit ihrer unbeschwertten und positiven Art immer ein Vorbild und die beste Gesprächspartnerin, die man sich wünschen kann. Meiner Freundin Jacky danke ich für das wunderbarste Geschenk, das man machen kann, sowie für den privaten Rückhalt und die Unterstützung in so einer turbulenten Zeit. Meiner Tochter Charlie danke ich für die außergewöhnlich ruhigen Nächte vor meiner Prüfung.

Kaiserslautern, Oktober 2023

Max Kaiser

Abstract

This thesis aims to establish a transient electro-thermomechanical model capable of characterizing the shape-morphing capabilities of shape memory alloy hybrid composites (SMAHCs). The particular SMAHC type examined in this study comprises a rigid substrate, a soft interlayer, and SMA wires sewed on top. The model was synthesized from the bottom up using well-established equations, methodologies, and solution procedures, taking into account appropriate simplifications and assumptions. The implementation was done with open-source solutions to ensure free availability. The model extends existing models to include aspects of external influences so that, for example, the efficiency and dynamics of the SMAHC can be predicted as a function of external mechanical loads and different ambient temperatures. Inputs to the model include geometric and material design factors and Joule's heat and ambient conditions, while outputs include the SMAHC's deflection, load-carrying capacities, bandwidth, and energy consumption. Individual components of the SMAHC were characterized to create simulation input parameters, and methodologies for characterization were devised. The thermomechanical and electro-thermomechanical model was validated by comparing experimental and simulated data. Regardless of the various assumptions and simplifications, the findings demonstrate that the transient deformation behavior during the electrically induced thermal activation of a SMAHC at room temperature and external loads of less than 19.2 N can be predicted with variations of less than 20 percent. With increasing mechanical stresses in the shape memory alloy attributable to external loads or rigid substrates and temperatures above the austenite start temperature or below -10°C , the model's applicability may become unreasonable.

Kurzfassung

Ziel dieser Arbeit ist es, ein instationäres elektro-thermomechanisches Modell zu erstellen, das in der Lage ist, die Formveränderungsfähigkeiten von hybriden Verbundwerkstoffen mit Formgedächtnislegierung (SMAHC) zu charakterisieren. Der spezielle SMAHC Typ, welcher in dieser Arbeit untersucht wurde, besteht aus einem steifen Substrat, einer weichen Zwischenschicht und darauf vernähten SMA Drähten. Das Modell wurde mithilfe etablierter Gleichungen, Methoden und Lösungsverfahren entwickelt und die Komplexität durch sinnvoll getroffene Annahmen reduziert. Die Implementierung erfolgte mit Python um die freie Verfügbarkeit zu gewährleisten. Das Modell erweitert bestehende Modelle um Aspekte äußerer Einflüsse, so dass z.B. der Wirkungsgrad und die Dynamik des SMAHC in Abhängigkeit von äußeren mechanischen Belastungen und unterschiedlichen Umgebungstemperaturen vorhergesagt werden können. Zu den relevanten Eingangsgrößen in das Modell gehören geometrische und materielle Designfaktoren sowie die Joule'sche Wärmebedingungen und Umgebungsbedingungen. Ausgangsgrößen des Modells stellen die Auslenkung bzw. Biegelinie, das Vermögen, externe Lasten zu ertragen, die Bandbreite und der Energieverbrauch der SMAHC dar. Die Einzelkomponenten der SMAHC wurden zur Generierung von Input Parametern charakterisiert und die Methoden zur Charakterisierung wurden festgelegt. Das thermomechanische und elektro-thermomechanische Modell wurde durch den Vergleich von experimentellen und simulierten Daten validiert. Die Ergebnisse zeigen, dass das transiente Formänderungsverhalten während der elektrisch induzierten thermischen Aktivierung einer SMAHC bei Raumtemperatur und externen Lasten von weniger als 19.2 N mit Abweichungen von weniger als 20% vorhergesagt werden kann. Bei größeren mechanischen Spannungen in der Formgedächtnislegierung, die auf äußere Belastungen oder starre Substrate zurückzuführen sind, und bei Temperaturen oberhalb der Austenit-Starttemperatur oder unter -10 °C können die simulierten Ergebnisse in der Form divergieren, dass das Modell unbrauchbar wird.

Deutsche Zusammenfassung

In dieser Arbeit wurde ein instationäres elektro-thermomechanisches Modell zur Beschreibung der transienten Formänderung dieser hybriden Verbundwerkstoffe mit Formgedächtnislegierung (SMAHC) entwickelt und validiert. Der spezielle SMAHC-Typ, welcher in dieser Arbeit untersucht wurde, besteht im Wesentlichen aus einem steifen Substrat, einer weichen Zwischenschicht und darauf vernähten Drähten aus Formgedächtnislegierung (SMA). Die Formänderung erfolgt aufgrund der durch Joule'schen Wärmeeintrag thermisch induzierten Phasentransformation in dem SMA.

Aktoren bieten die Möglichkeit, verschiedene Energieformen ineinander umzuwandeln. Das Material, das den Hybridverbundwerkstoff zu einem Aktor macht, ist die Formgedächtnislegierung, die thermische Energie in mechanische Energie umwandelt. In einem technisch nutzbaren Temperaturbereich erfährt die Gitterstruktur eine thermoelastische Phasenumwandlung, die mit einer makroskopischen Kontraktion einhergeht. Da das Substrat seine Länge beibehält, entsteht eine Biegebewegung. Dieses Aktorkonzept bietet ein großes Potenzial für die Erschließung von Anwendungen in einer Vielzahl von Sektoren, wie z. B. Konsumgüter, Luftfahrt und Automobil. In der Vergangenheit wurden bereits in zahlreichen Projekten Anwendungen wie eine morphende Hinterkante, aktive Vortexgeneratoren, intelligente Luftklappen oder Ver- und Entriegelungsmechanismen entwickelt. Gegenüber konventionellen Aktoren und Mechanismen bietet diese Klasse von Aktoren Vorteile, vor allem wenn Leichtbaukonzepte, kompakter Bauraum oder verteilte Aktuierung im Vordergrund stehen oder eine geräuschlose Ansteuerung gefordert ist.

Ausgangspunkt für diese Arbeit bildeten die Fragen nach der zuzuführenden elektrischen Leistung, dem Energieverbrauch und dem Wirkungsgrad der formveränderlichen SMAHC in der Anwendung. Zur Auslegung von SMAHC-Systemen, welche auch die Peripherie beinhalten, ist das Wissen über diese Größen unabdingbar. Aus dem Stand der Technik werden vorhandene Modelle zur Vorhersage des Formänderungsverhaltens von SMAHC kategorisiert. Die Modelle wurden auf ihre Eignung untersucht, das elektro-thermomechanische Verhalten von SMAHC in der Anwendung vorherzusagen. Thermomechanische Modelle stellen den Großteil der vorhandenen Modelle dar. Diese ermöglichen präzise Vorhersagen mechanischer Eigenschaften und der Formänderung für bekannte Temperaturverteilungen der SMA. Sie lassen es jedoch nicht zu, Aussagen über den Energieverbrauch und damit korrelierende Größen zu treffen. Die Ergebnisse der Auswertungen der elektro-thermomechanischen Modelle nach dem Stand der Forschung zeigten bei der Berücksichtigung von wesentlichen äußeren Einflussfaktoren wie der Umgebungstemperatur und statischen mechanischen Belastungen eine Wissenslücke. Das in dieser Arbeit entwickelte Modell erweitert bestehende Modelle um Aspekte äußerer Einflüsse, so dass z.B. der

Wirkungsgrad und die Dynamik des SMAHC in Abhängigkeit von äußeren mechanischen Belastungen und unterschiedlichen Umgebungstemperaturen vorhergesagt werden können.

Zunächst wurde das Formänderungsverhalten der genannte Klasse von SMAHC in vier unterschiedlichen Konfigurationen charakterisiert. Zur Erzeugung der Konfigurationen wurden die beiden wesentlichen Parameter, die Dicke der elastischen Zwischenschicht und des steifen Substrats, variiert. Die SMAHC wurden elektrisch, unter Zufuhr verschiedener Ströme thermisch aktiviert und anschließend unter Einwirkung der freien Konvektion wieder auf das Temperaturniveau der Umgebung abkühlt. Dieser Aktivierungszyklus wurde für verschiedene Umgebungstemperaturen im Bereich von -10 bis 45 °C und statischen mechanischen Lasten im Bereich von -200 bis 800 N/mm^2 durchgeführt. Je nach Experiment wurde die Biegelinie mittels digitaler Bildkorrelation, die Temperatur der SMA mithilfe von Infrarotmessungen, sowie der elektrische Widerstand des SMA-Gitters und die Auslenkung an spezifischen Positionen aufgezeichnet. Zur statistischen Absicherung wurden für jedes Experiment mindestens drei unabhängige Messungen durchgeführt. Die Ergebnisse lieferten qualitative und quantitative Informationen über wesentliche zu modellierende Wirkmechanismen und Randeffekte.

Das Modell wurde entsprechend der beobachteten Wirkmechanismen, aufbauend auf etablierten Gleichungen, Methoden und Lösungsverfahren entwickelt. Den Grundbaustein stellt das Materialmodell der SMA dar, welches um die mechanische und thermische Domäne des Verbundes ergänzt wurde. Das Gleichungssystem des vereinfachten SMA Modells setzt sich aus einem konstitutiven Modell nach Tanaka, einem Hysterese Modell nach Liang und Rogers, einem kapazitiven Modell, welches die Energieerhaltung implementiert und einem elektrischen Modell zusammen. Die thermische Domäne der SMAHC ist als Kombination aus einem „lumped“ Modellansatz zur Darstellung der Konvektion und einem zweidimensionalen Wärmetransferproblem zur Darstellung der Wärmeleitung in der Zwischenschicht implementiert. Zur Lösung des Wärmetransferproblems wird eine explizite Finite-Differenzen-Methode mit Vorwärtsdifferenz in der Zeit und zentraler Differenz in der Raumausbreitung verwendet. Die mechanische Domäne implementiert Gleichungen zur Lösung der Differentialgleichung am nichtlinearen Biegebalken für große Deformationen. Die Möglichkeit zur Reduzierung der Komplexität jeder Modellkomponente durch sinnvoll getroffene Annahmen wurde geprüft. Die Implementierung des Differentialgleichungssystems erfolgte mit Open-Source-Lösungen. Dies gewährleistet die freie Nutzung, wie auch Modifikation und Erweiterung des resultierenden Modells. Zu den relevanten Eingangsgrößen des Modells gehören geometrische und materielle Eigenschaften der Komponenten der SMAHC sowie die Umgebungstemperatur, die externe mechanische Belastung und die Dauer und Ausprägung der Joule'schen Wärmezufuhr. Ausgangsgrößen des Modells stellen die Auslenkung bzw. Biegelinie, das Vermögen externe Lasten zu ertragen, die Bandbreite und der Energieverbrauch der SMAHC dar.

Die Einzelkomponenten der SMAHC wurden charakterisiert und die Methoden zur Charakterisierung festgelegt. Zur Charakterisierung der Zwischenschicht und des Substrates konnte auf etablierte Methoden zurückgegriffen werden. Für die SMA konnten die Umwandlungstemperaturen, Transformationsenthalpien und Transformationsdehnungen im lastfreien Zustand, der elektrische Widerstand, das Elastizitätsmodul sowie die spezifische Wärmekapazität ebenfalls mit etablierten Methoden bestimmt werden. Zur messtechnischen Erfassung der lastabhängigen Transformationsdehnungen wurden Messungen an einem eigens dafür entwickelten Prüfaufbau durchgeführt. Dieser ermöglicht die anwendungsnahe zeitaufgelöste Dehnungs- und Temperaturmessung an statisch belasteten SMA Drähten, welche eine durch Joule'schen Wärmeeintrag induzierte Phasentransformation durchlaufen. Dieser Prüfaufbau eignete sich ebenfalls zur Ermittlung der Clausius-Clapeyron Koeffizienten.

Zur Validierung wurden die Resultate aus der Charakterisierung der Einzelkomponenten als Eingabeparameter für das entwickelte SMAHC-Modell genutzt. Die Randbedingungen, welche die Umgebungstemperatur, die externe mechanische Belastung und die Dauer und Ausprägung der elektrischen Stromzufuhr umfassen, wurden entsprechend der Charakterisierungsexperimente an den SMAHC gewählt. Diskretisierungsparameter wurden anhand von Konvergenzstudien festgelegt. Die Ergebnisse der Simulationen wurden mit den entsprechenden experimentellen Ergebnissen der SMAHC-Charakterisierung verglichen. Die Validierung ist in zwei Teile unterteilt. Zunächst ist die Validierung für den unbelasteten Aktor und anschließend für belasteten Aktor erfolgt. Der elektro-thermomechanischen ist stets eine thermomechanische Validierung vorgelagert.

Die Ergebnisse zeigen, dass das transiente Formänderungsverhalten während der elektrisch induzierten thermischen Aktivierung einer SMAHC bei Raumtemperatur und externen Lasten von weniger als 19.2 N pro 50 mm Aktorbreite trotz der zahlreichen Annahmen und Vereinfachungen mit Abweichungen von weniger als 20 % vorhergesagt werden kann. Bei zunehmenden mechanischen Spannungen in der Formgedächtnislegierung, die auf äußere Belastungen oder starre Substrate zurückzuführen sind und bei Temperaturen oberhalb der Austenit-Starttemperatur oder unter -10 °C können simulierte und experimentelle Ergebnisse stark divergieren.

Schlussendlich konnte ein Modell entwickelt werden, welches die Kopplung der elektrischen-, thermischen- und mechanischen Domäne der SMA wie auch des SMAHC zulässt und damit die Dynamik des Aktors beschreibbar macht. Die umfassende Validierung dieses Modellansatzes macht es darüber hinaus möglich, die Grenzen des Modells sowie dessen Genauigkeit abzuschätzen.

Contents

| | |
|--|------------|
| Abstract | i |
| Zusammenfassung | iii |
| Table of contents | vii |
| Nomenclature | xi |
| 1. Introduction | 1 |
| 2. Fundamentals | 3 |
| 2.1. Shape memory alloy hybrid composites (SMAHCs) | 3 |
| 2.1.1. Shape memory alloys and effects | 3 |
| 2.1.2. Hybrid composites | 8 |
| 2.1.3. SMA integration level | 9 |
| 2.1.4. Function | 10 |
| 2.1.5. Applications | 10 |
| 2.2. Modeling of physical systems | 11 |
| 2.2.1. Numerical integration methods | 12 |
| 2.2.2. 1D SMA wire modeling | 12 |
| 2.2.3. Thermal domain modeling | 17 |
| 2.2.4. Electrical domain modeling | 21 |
| 2.2.5. Mechanical domain modeling | 22 |
| 3. State of the art | 25 |
| 4. Objectives of work | 31 |
| 5. SMAHC characterization | 33 |
| 5.1. SMAHC specimens | 33 |
| 5.2. Test method | 38 |
| 5.2.1. Testbench | 38 |
| 5.2.2. Design of experiment | 41 |
| 5.2.3. Test process | 42 |
| 5.3. Evaluation methodology | 44 |
| 5.4. Results and discussion | 47 |
| 5.4.1. Pre cycling | 48 |

| | | |
|-----------|--|------------|
| 5.4.2. | Activation at room temperature (RT) | 49 |
| 5.4.3. | Activation under influence of external loads | 54 |
| 5.4.4. | Activation under influence of ambient temperatures | 61 |
| 5.4.5. | Conclusion | 64 |
| 6. | SMAHC model development | 65 |
| 6.1. | Lumped SMA wire model | 66 |
| 6.1.1. | Constitutive model and hardening law | 66 |
| 6.1.2. | Martensite fraction and hysteresis model | 67 |
| 6.1.3. | Lumped capacitance model | 68 |
| 6.1.4. | Electrical domain | 69 |
| 6.1.5. | Heat losses | 70 |
| 6.1.6. | Mechanical domain | 71 |
| 6.1.7. | Model algorithm | 72 |
| 6.2. | SMAHC model without influence of external load | 74 |
| 6.2.1. | Mechanical domain | 74 |
| 6.2.2. | Thermal domain | 78 |
| 6.3. | SMAHC model with influence of external load | 81 |
| 6.4. | Model algorithm | 83 |
| 6.4.1. | Implementation | 84 |
| 7. | Identification of material parameters | 87 |
| 7.1. | Methods | 87 |
| 7.2. | Results | 94 |
| 8. | Model validation | 97 |
| 8.1. | SMA wire model validation | 97 |
| 8.2. | SMAHC model | 99 |
| 8.2.1. | Without external load applied | 102 |
| 8.2.2. | With influence of external load | 106 |
| 9. | Summary & Conclusion | 109 |
| | Bibliography | 111 |
| A. | Appendix | 129 |
| A.1. | Fundamentals | 129 |
| A.2. | State of the art | 130 |
| A.3. | Active deflection approximation | 130 |
| A.4. | SMAHC characterization | 132 |
| A.5. | Test setups | 136 |

| | |
|--|-----|
| A.6. Python scripts | 137 |
| A.6.1. Main | 139 |
| A.6.2. Lumped SMA model | 141 |
| A.6.3. Heat transfer model | 143 |
| A.6.4. Mechanical domain | 145 |
| A.7. Identification of material parameters | 148 |
| A.8. Convergence studies | 150 |
| A.9. Betreute Arbeiten | 152 |
| A.10. Curriculum vitae | 153 |

Nomenclature

Abbreviations

| | |
|-------|--|
| 1D | O ne D imensional |
| 2D | T wo D imensional |
| CFRP | C arbon F iber R einforced P olymer |
| CL | C onstant L oad |
| CLT | C onstant L oad T estbench |
| CTE | C oefficient of T hermal E xpansion |
| DAQ | D ata A c Q uisition System |
| DIC | D igital I mage C orrelation |
| DOF | D egree O f F reedom |
| DSC | D ifferential S canning C alorimetry |
| ECTEM | E ffective C oefficient of T hermal E xpansion M odel |
| FEM | F inite E lement M ethod |
| FRP | F iber R einforced P olymer |
| ODE | O rdinary D ifferential E quation |
| OWE | O ne- W ay E ffect |
| PDE | P artial D ifferential E quation |
| PE | P seudoelastic E ffect |
| RT | R oom T emperature |

| | |
|-------|-------------------------------------|
| SMA | Shape Memory Alloy |
| SMAHC | Shape Memory Alloy Hybrid Composite |
| SME | Shape Memory Effect |
| TWE | Two-Way Effect |

| Greek formula symbols | | Dimensions |
|-----------------------|----------------------------------|----------------------------|
| α | Heat transfer coefficient | $MT^{-3}\Theta^{-1}$ |
| α_a | Coefficient of thermal expansion | Θ^{-1} |
| ϵ | Strain | — |
| ϵ_e | Emmissivity | — |
| η | Efficiency | — |
| λ | Thermal conductivity | $MLT^{-3}\Theta^{-1}$ |
| Ω | Transformation tensor | $ML^{-1}T^{-2}$ |
| ϕ | Angle of curvature | — |
| ρ | Density | ML^{-3} |
| ρ_{el} | Resistivity | $M^{-1}L^{-3}T^3I^2$ |
| σ | Stress | $L^{-1}MT^{-2}$ |
| σ_B | Stefan Boltzmann constant | $ML^{-1}T^{-2}\Theta^{-4}$ |
| Θ | Thermoelastic tensor | $ML^{-1}T^{-2}\Theta^{-1}$ |
| ξ | Martensite fraction | — |

Indices

| | |
|---|---------|
| 0 | Initial |
|---|---------|

| | |
|-------------|--------------------------------|
| ∞ | Ambient condition |
| σ | Related to stress |
| <i>A</i> | Austenite |
| <i>cell</i> | Cell |
| <i>cond</i> | Conductive |
| <i>conv</i> | Convective |
| <i>curr</i> | Current |
| <i>el</i> | Electrical |
| <i>ext</i> | External |
| <i>f</i> | Finish |
| <i>hsl</i> | Homogeneous SMA-layer |
| <i>in</i> | Inflow |
| <i>int</i> | Interlayer |
| <i>k</i> | Element label along the t axis |
| <i>kin</i> | Kinetic |
| <i>M</i> | Martensite |
| <i>max</i> | Maximum |
| <i>min</i> | Minimum |
| <i>n</i> | Element label along the y axis |
| <i>out</i> | Outflow |
| <i>pl</i> | Plastic |
| <i>pot</i> | Potential |
| <i>pre</i> | Pre |

| | |
|-------------|------------------|
| <i>rad</i> | Radiative |
| <i>RT</i> | Room temperature |
| <i>S</i> | Spring |
| <i>s</i> | Start |
| <i>SMA</i> | SMA-layer |
| <i>sub</i> | Substrate |
| <i>th</i> | Thermal |
| <i>tr</i> | Transformation |
| <i>wire</i> | Wire |

Coordinate systems

| | |
|----------------|--|
| <i>s, y, t</i> | Cartesian coordinate system related to the neutral axis of the substrate |
| <i>x, y, z</i> | Cartesian coordinate system related to the initial position of the substrates neutral axis |

| Latin formula symbols | | Dimensions |
|-----------------------|---------------------------------------|-----------------------|
| \dot{Q} | Heat flow | ML^2T^{-3} |
| <i>A</i> | Surface | L^2 |
| a_l | Active length | L |
| A_s or A_f | Austenitic transformation temperature | Θ |
| <i>B</i> | Flexural rigidity | ML^3T^{-2} |
| <i>Bi</i> | Biot number | – |
| <i>BR</i> | Bending Radius | L |
| <i>C</i> | Clausius-Clapeyron coefficient | $L^{-1}MT^{-2}K^{-1}$ |

| | | |
|----------------|--|------------------------|
| c | Specific heat capacity | $L^2T^{-2}\Theta^{-1}$ |
| D | Deflection | L |
| d | Diameter | L |
| D_a | Active length deflection | L |
| E | Young's modulus | $L^{-1}MT^{-2}$ |
| F | Force | MLT^{-2} |
| H | Transformation enthalpy | ML^2T^{-2} |
| I | Current | I |
| k | Stress dependent transformation strain material constant | — |
| L | Length | L |
| M | Moment | ML^2T^{-2} |
| m | Mass | M |
| M_s or M_f | Martensitic transformation temperature | Θ |
| Nu | Nusselt number | — |
| P | Plastic modulus | $L^{-1}MT^{-2}$ |
| P | Power | ML^2T^{-3} |
| Pr | Prandtl number | — |
| R | Resistance | $ML^2I^{-2}T^{-3}$ |
| r | Radius | L |
| Ra | Rayleigh number | — |
| spx | Sensor position in x-direction | L |
| T | Temperature | Θ |
| t | Thickness | L |

| | | |
|-----|-----------------|--------------------|
| t | Time | T |
| U | Internal Energy | ML^2T^{-2} |
| U | Voltage | $ML^2T^{-3}I^{-1}$ |
| V | Volume | L^3 |
| W | Work | ML^2T^{-2} |
| w | width | L |

1. Introduction

Several timelines in the Periods of human history are named after the materials whose discovery and use have led to technical revolutions. Starting from the stone, iron, and bronze age, we live in an age that, although attributed to silicium, has produced an extreme range of materials. [1]

A particular class of these materials is the so-called smart materials. These materials can transform different types of energy into another or change their key material properties in dependence on external stimuli. New possibilities in terms of functional ability and design freedom are opened. These materials include Shape Memory Alloys (SMA), that when thermally stimulated by an external heat source or Joule heating, respond with a macroscopic change in shape and significantly change their stiffness. In combination with stiff substrates or embedded as fiber in a material matrix, these alloys can be utilized to construct actuator elements that have the capability of active shape control, known as Shape Memory Alloy Hybrid Composites (SMAHC). [2]

For many tasks, these actuator systems are superior to other smart- or conventional actuators due to their extreme load-carrying capabilities compared to their dead weight, large macroscopic deformation potential and low demand on installation space and peripherals. Due to the aforementioned properties, these actuators, for example, outperformed the piezoceramic adaptive structure for static control. Compared to conventional hydraulic or electrical actuators, these types of actuators, when applicable, offer great convenience, especially heaving the peripherals in mind. [3]

Due to the large forces that occur during the actuation of the SMAs, these hybrid materials are most promising, compared to other smart materials, for active shape control. [4]

Various demonstrators have been developed, showing the potential for new applications with this kind of technology. For example, distributed systems were tested in aviation as active vortex generators [5] or as adaptive jet engine chevrons for noise reduction [6], in automotive as smart air inlets to reduce drag [7] or installation space-reduced air vents [8].

Nowadays, thousands of technologies based on the effects provided by shape memory alloys are patented every year. About 1 percent of these patents are commercially successful. In [9] it was concluded that a critical reason for this massive gap between ideas and real-world applications is a lack of formal guidelines, predictive models, and design tools for the effective design of SMA actuators. In [10] and [11], the same was concluded about the design of SMAHC technology and by [12], it was also noted that designing SMAHC

using a trial-and-error approach is too inefficient since production of SMA composites is time and labor intensive. It is evident that an easily accessible and validated, easy-to-use electro-thermomechanical model for the design of Shape Memory Alloy Hybrid Composites for shape adaption would be a significant enhancement. Although some models have already been developed for this purpose, they need more validation and accessibility. The models, some highly complex, were not validated at all or only for very few cases, mostly without considering boundary conditions that are important for application development. Since most models were implemented using proprietary software, accessibility is limited. In many cases, the lack of access means that the use of SMAHC is not even considered by engineers.

Thus, this work aims to develop and implement a tool that allows for the simulation of the transient deformation of SMAHC under the influence of supplied electrical currents and exposed to different ambient temperatures or external loads. In addition, the model was extensively validated by comparing experimental and numerical data. Furthermore accessibility of the model is guaranteed by dispensing with proprietary code in the model implementation. The development process can roughly be divided into four steps. First, the mechanisms of action had to be understood. A series of experiments were used for this purpose. The deformation behavior of different modified SMAHCs was investigated under the abovementioned influences. The knowledge gained from the experiments flowed into the second step, the model development. Well-established equations, methods and solution procedures were used to synthesize a model capable of describing the transient deformation behavior. The model was complex enough to represent the relationships between input and output variables to a sufficient extent. Using appropriate assumptions, the computational effort was limited to a low level, which made the model suitable for design purposes. The input parameters, e.g., geometries and material parameters, emerged from the modeling approach. The third step specified how these parameters are to be measured. Finally, the model was validated. For this purpose, experimentally determined material parameters were used as input for the developed model, and regarding simulation output was compared with the experimental data from the deformation experiments.

The numerical simulation was implemented using Python. The experiments and simulation scope was limited to activation by Joule heating, free convection and static point loads. Limiting the number of cycles focused on obtaining high-quality data for a smaller subset of conditions allows for a more in-depth analysis of the actuator's behavior.

2. Fundamentals

In this chapter, an overview of Shape Memory Alloys (SMA) and the simulation of their material properties is given. In addition, the use of SMA for hybrid material combinations is discussed.

2.1. Shape memory alloy hybrid composites (SMAHCs)

This section introduces the fundamental components and composition of SMAHCs and their functional behavior and applications. SMAHCs consist of a minimum of two components: the substrate and the connected shape memory alloy (SMA). As SMAs give the composite its unique actuator and sensor properties, the first topic discusses SMAs and their diverse shape memory effects (SMEs). The general composition of hybrid composites, the construction and function of SMAHCs, and some of their numerous applications are discussed.

2.1.1. Shape memory alloys and effects

Shape memory alloys (SMAs) are a subclass of smart materials. More precisely, these are among the active materials due to their sensing and actuation capabilities. The sensing and actuation of active materials refer to their intrinsic conversion capability of non-mechanical into mechanical energy and vice versa. The response to external stimuli takes place on a technically usable scale that exceeds that of conventional materials by magnitudes. For example, temperature or magnetic field strength changes can trigger macroscopic transformations in shape. [13]

Due to the shape memory potential, this work focuses on metallic shape memory materials, which undergo a temperature-induced phase transformation between the low-temperature phase (martensite) and the high-temperature phase (austenite). Since the atomic lattice is distorted and atoms do not diffuse during the transformation, the process is reversible. A macroscopic piece of SMA consists of multiple crystals with different orientation directions, so-called variants. In the cold or martensitic phase, the orientation of the crystals can be of a dominant direction, this kind of assembly is referred to as detwinned martensite, or they can be of an undulating pattern with alternating variants, so-called twinned martensite. There is no technically useful change in shape between austenitic and twinned

martensitic structures. Macroscopic shape changes occur during the martensite's mechanical, stress-induced de-twinning or during the temperature-induced transformation from the detwinned martensitic to the austenitic crystal structure. Figure 2.1 illustrates the transition between the phases and the associated shape change together with the characteristic values describing this process, which is referred to as the one-way effect (OWE).[14]

The tangents depicted in figure 2.1 show an idealized curve. For a mono-crystalline SMA also, the plateau would not show any slope. As a macroscopic alloy is composed of many crystals of different sizes and orientations, the conversion is a statistical process. Thus, there are no clear conversion limits in macroscopic alloys. The alloy is loaded at

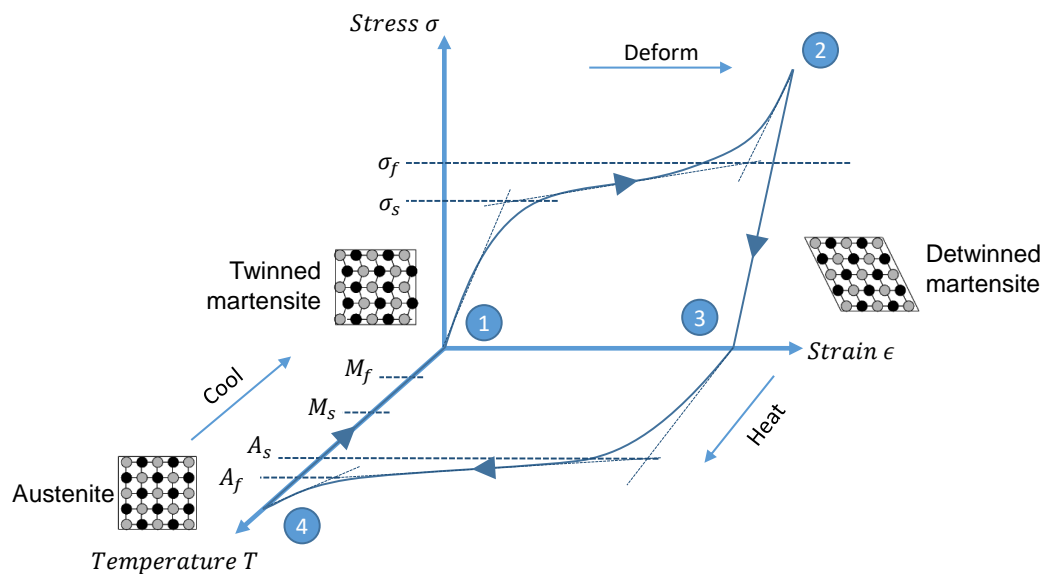


Figure 2.1: One-way-effect (OWE)

low temperature in twinned martensite state (1). Until the detwinning start stress σ_s is attained, the deformation is only of elastic type. Afterward, the material is pseudoplasticly deformed until the load is high enough to reach the detwinning finish stress σ_f . Detwinned martensite is then elastically deformed until the maximum load is applied (2). Removing the load subsequently results in elastic recovery(3). Thus the alloy is elongated between load-free states (1) and (3). In the next step temperature of the alloy is raised until the martensite to austenite transformation is initialized. This transformation region is limited by the austenite start temperature A_s and the austenite finish temperature A_f . After exceeding A_f , the alloy's structure is austenitic. Since the austenite has no variants, the degree of determination of the high-temperature phase is greater than that of the low-temperature phase. Due to this high degree of determination, the austenitic phase is particularly suitable as a reference phase. Elongation is related, for example, to the length of the SMA material in the austenitic phase. Cooling back down the alloy initializes the martensite transformation when the temperature is below the martensite start temperature M_s . Martensite transformation is completed when temperatures below M_f are reached.

In the case of load-free martensite transformation, the resulting structure is of twinned martensite type again, resulting in a closed OWE loop.

Applying a load greater than σ_s during cooling results in partly direct detwinning of martensite and thus in a shape change. This type of direct transformation between the two phases is called two-way-effect (TWE). The detwinning can occur due to external loads (extrinsic TWE) or residual internal stress (intrinsic TWE). In order to obtain the latter effect, the alloys have to undergo a repeated thermomechanical cycling process, referred to as training. [14]

With certain alloys and cooling conditions, the transformation from austenite to martensite can form an intermediate phase, the so-called R phase. Similar to martensite, this phase has a twinned structure. [15]

The R-phase plays a subordinate role in the shape change capabilities investigated in this work and is thus not discussed further.

The TWE is of major importance for this work and is consequently discussed more detailed. Qualitative correlation between stress, strain, and temperature for intrinsic TWE A) and extrinsic TWE due to the influence of constant external load B) and bias spring C) are depicted in figure 2.2.

The transformation temperatures depend on the load. In the case of tensile stresses, they increase proportionally with stress level. For convenience, this effect is neglected in the illustration 2.2 and related discussion. The initial condition for each case is a wire pre-stressed by a load greater than σ_s . In the initial state (1), the unloaded but pre-stressed wire shows a pre-strain ϵ_{pre} .

Heating the unloaded wire to a temperature beyond A_f leads to the corresponding state, marked with a (2). In this state, the transformation to austenite is completed, and the wire exhibits its smallest expansion. This load-free austenitic condition defines the original length L_0 of the SMA wire. In the next step, the unloaded wire is cooled down below martensite finish temperature M_f . Depending on the residual stress σ_{res} , there is a partial direct transformation from austenite into detwinned martensite. For subsequent heating and cooling, the transformation strain ϵ_{tr} is equal to the residual strain ϵ_{res} remains constant, neglecting fatigue and run-in effects. The magnitude of residual strain depends on the trained residual stress of the SMA wire.

Figure B) sketches the case where the wire is under a constant load condition. The cycle's starting point is the loaded wire, marked with a (1). The wire is elongated by the external load acting on it. The magnitude of elongation depends on the elastic modulus of the detwinned martensite. The stretched wire is heated until the austenitic transformation is completed and state (2) is reached. The constant load causes elastic elongation $\epsilon_{e,A}$ of the austenitic phase, and the wire does not retain its original length L_0 . As the load is greater than the detwinning-finish-stress σ_f , while cooling, the wire stretches until it is

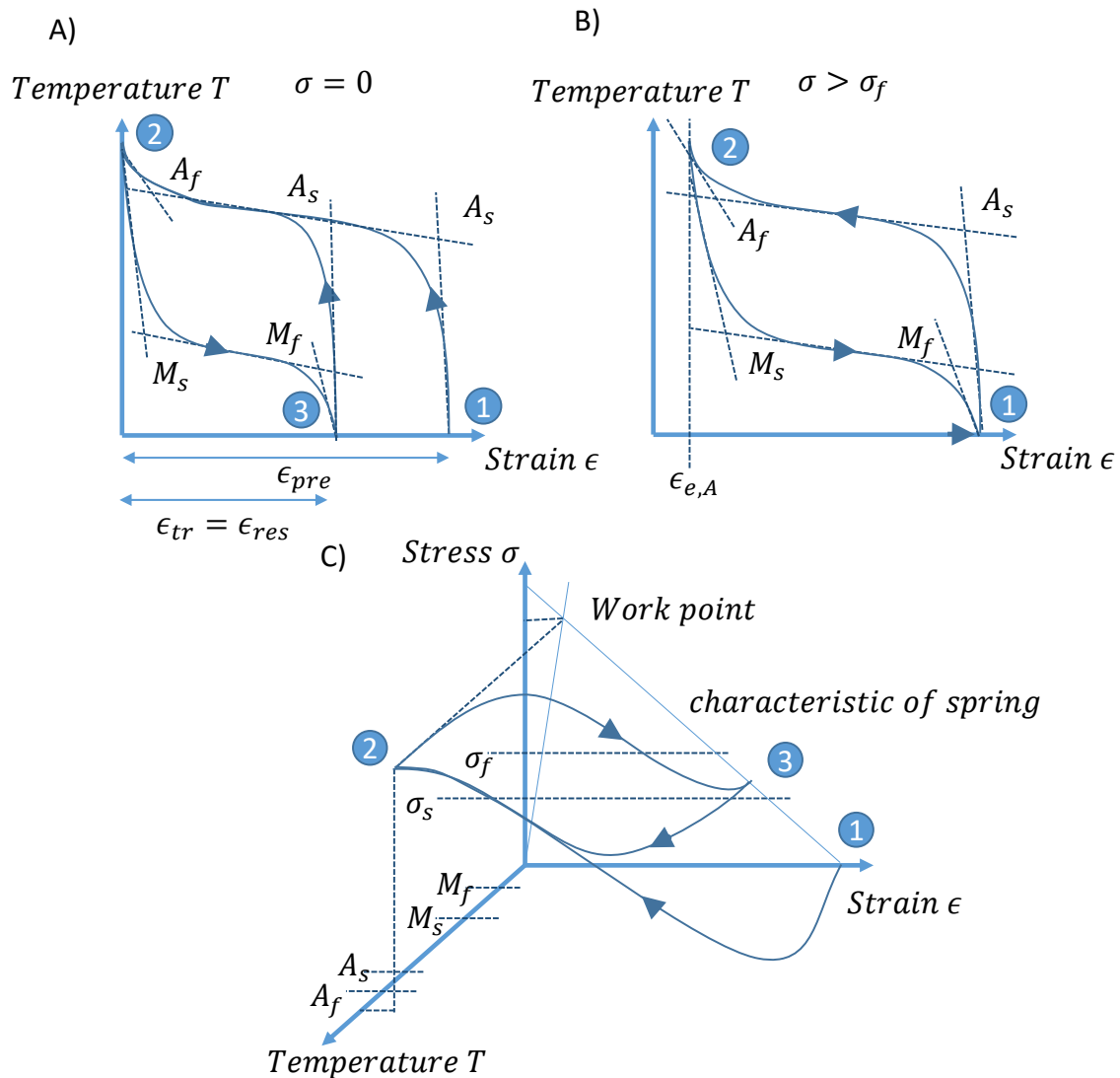


Figure 2.2: Qualitative correlation between stress, strain, and temperature for intrinsic TWE A) and extrinsic TWE due to constant load B) and bias spring C)

in the initial state (1) again. For loads smaller than detwinning-finish-stress σ_f , the wire would not return to the cycle's initial state as during cooling, the detwinning would take place only partially. Thus, depending on the load, the transformation strain can be set. In case of external load below detwinning-start-stress σ_s and use of an untrained wire, the transformation strain would be zero.[14]

The last case to discuss is the wire that operates against a spring. Bias forces play an essential role in developing SMA actuators as they lead to defined stresses and consistent conditions of use. Due to ease of handling, those bias forces are often realized using bias springs. [16]

Spring characteristics can be of any type, but for convenience, we consider a linear one. The linear characteristic is depicted in the stress-strain plain. At the beginning of the cycle

(1), no biasing force is present. During the transformation from detwinned martensite into austenite, the stress increases depending on the strain induced in the spring. The wire's strain in the austenitic state (2) depends on the spring rate and its elastic modulus in the austenitic state. The wire elongates, beginning its transformation to detwinned martensite while cooling, and the springs strain decreases. The reduced loading of the SMA causes a diminishing potential for martensite detwinning. Finally, the detwinning stops in the region of stresses between σ_s and σ_f (3). For the following cycles, the resulting strain defines the wire's elongation in the low-temperature phase. [14]

For completeness, the pseudoelastic effect (PE) is mentioned here, even if this plays only a subordinate role in this work. SMAs show the PE in case of alloy temperatures constantly above the austenite finish temperature A_f . Loading the alloy with a sufficiently large load leads to the direct formation of detwinned martensite. During subsequent unloading, the material transforms to austenite again.[14]

Depending on the performance characteristics, active materials can be used for various fields of applications. Essential assessment characteristics are the actuation stress and strain, bandwidth, efficiency, and the ratio between actuator performance and mass. Actuation stress gives information about the force that can be applied to an actuator per unit cross-sectional area for a single stroke or in cyclic operation, respectively. Strain refers to the shape change during actuation. The bandwidth describes the frequency with which state changes can be performed. The amount of usable energy output achieved by a targeted energy input is referred to as efficiency. By the ratio of actuator performance and mass or volume, it can be classified if the actuator is usable as a lightweight or compact actuator systems. Regarding actuation stress, SMAs are superior to other active materials, like piezoelectrics, dielectric elastomers, or magnetostrictors and they can also compete with conventional actuators such as hydraulics, pneumatics, solenoids, and moving coil transducers. Outstanding is the ratio of actuation performance to actuator mass that exceeds all other active materials. These characteristics of SMA-driven actuator systems make them the obvious choice when designing lightweight and distributed systems. Active controlled SMA actuators are commonly actuated using a constant direct current. The necessary power supply can be implemented with little effort, and the electrical current distribution is simple and cheap compared to handling fluids needed for pneumatics and hydraulics. Thus, the requirements of SMA actuators on peripherals are low compared to other actuator systems. On the other hand, due to the thermal-induced phase transformation, actuator systems based on SMA materials have a relatively low efficiency and, in particular, a low bandwidth due to the time consuming cooling process. [17]

Of all known SMAs, those composed of nearly equiatomic Nickel and Titanium (NiTi or Nitinol) show the best thermomechanical related performance. Their transformation temperatures can be tailored to temperatures relevant to automotive and aeronautic applications. [18, 9] For these reasons, the binary Nitinol, with its ternary and quaternary

derivates, is used for about 99% of all shape memory alloy actuators. While the material can be shaped to form torsion springs, cantilever strips, or torsion tubes, helical springs and wires are more common. Most straight-wire actuators are electrically controlled and thus heating via Joule heating effects, in contrast to helical spring actuators, which are primarily heated indirectly.[16]

Due to the ease of handling and production, SMA wires are used for many applications. Additionally, the SMA actuators subjected to tension show a much higher efficiency compared to SMA actuators subjected to torsion. [19]

2.1.2. Hybrid composites

Composites and **combination of materials** are composed of at least two materials or material variants that can be of significantly different properties. While the individual materials used in composites can only be distinguished at the microscopic level, their phase boundaries in combined materials can be seen at the macroscopic scale. Another distinguishing feature is the mixing of the individual phases. While in composites, there typically is a continuous phase referred to as the matrix in which the discontinuous disperse phase is embedded, the phases in combined materials are not mixed but joined.[20]

The components resulting from these synergetic material combinations have properties different from those of the individual materials. Regarding economics, one of the most important subclasses of composites is fiber-reinforced polymers (FRP). The enormous lightweight construction potential of continuous fiber-reinforced polymers and the associated fuel-saving opportunities makes them indispensable material for commercial aviation. These composites are composed of fibers and a polymer matrix. The most common continuous fiber materials (filaments) are carbon and glass. Matrix materials, in most cases, are thermosets or thermoplastics. In most applications, the mechanical properties, such as strength and tensile modulus of the fibers, are orders of magnitude higher than those of the matrix material. The matrix material has a lower density and, in the case of combination with carbon or glass fibers, a higher elastic ductility. The properties of the final composite also depend on the three-dimensional interphase linking the two components. Determination of the properties and measurement of the interphase is still very complex. Reinforcing the matrix with fibers of different types leads to hybrid reinforcement. [21] Strictly speaking, hybrid composites are those that embed two or more different fiber materials in a matrix[22].

For proper classification, the sandwich structures are to be introduced here. To realize this method of construction, layers with different properties are stacked. The most common layer stack is the one with two face layers and a layer in between, which in addition to its mechanical function and advanced damage tolerance [23], can perform different tasks such as sound insulation or heat conduction. In particular, sandwich structures are suit-

able for building rigid structures with minimal weight. In this case, the face layers are of stiff materials, while the core is material with low density and sufficient shear properties. [21]

2.1.3. SMA integration level

Early scientific studies on SMAHCs, to control the stiffness and, thus, the elastic properties of a conventional laminate were carried out during the late 1980s.[24] As mentioned, SMAHCs consist of at least the active SMA material and the laminate or substrate.

First, a distinction must be made between SMAHC reinforced with continuous and discontinuous SMAs. While continuous reinforcement produces directional properties of the composite, randomly distributed and oriented SMAs provide isotropic properties. Since the work focuses on the shape change capabilities of SMAHC, discontinuous fiber reinforcement that influences stiffness or modal properties is not of interest and is not discussed further. Continuous reinforced SMAHCs, are used for active shape control [25] and therefore are of great interest to the work.

Continuous SMAs can be embedded into the laminate as integral component [26, 27, 28, 29, 30, 12], applied to the surface of a laminate or a substrate [31] or can be joined in some distance to it via an interlayer or lever arms [3, 32, 33, 34]. Depending on the application, the type of integration can have various advantages and disadvantages. The actuators investigated in this work are used for shape control of planar or slightly curved components.

The bending moment implied by an SMA layer interacting with a substrate or laminate is a linear function of the distance between the SMA layer and the neutral axis of that substrate. By maximizing the distance, the bending moment and the overall structure's flexural stiffness are maximized. As a logical consequence, it is necessary to apply the SMA layer outside the substrate or laminate when it comes to shape control (compare figure 2.3). [3]

Due to the macroscopic separation of the individual layers and their stacked structure, as discussed in 2.1.2, the term SMA-Sandwich for the actuators investigated in this work is more appropriate.

When a sandwich structure consisting of a shape memory alloy (SMA) layer and a substrate undergoes bending motion, it can result in high shear loads being especially applied to the edge areas of the structure. To prevent the pullout of SMA wires or ribbons in these areas, it is often necessary to fix them using an elaborate anchorage system. This anchorage system is designed to absorb the generated shear forces and transmit them to the substrate below. [23]

2.1.4. Function

For shape-adaptive SMAHCs, the actuator abilities of SMAs are used. Investigated type of SMAHC in the initial and activated state is shown in figure 2.3. In the initial state, the SMA wire is partly detwinned. Heating the SMA wire to temperatures above A_s causes them to contract. While in the initial state, without the influence of an external load, the length of wire L_{wire} and of substrate L_{sub} is identical, in the activated state, the length of the SMA-wire is smaller compared to the length of the substrate. Without external force acting on the actuator, this results in a constant curvature along the substrate axis in the range of the length of the wire. The shape of the SMAHC can then be described by a bending radius with respect to the substrate BR_{sub} . Subsequent cooling of the SMA wire leads to their expansion and shape resetting of the SMAHC.

During activation and shape reset, the substrate exerts a force on the wire, proportional to deflection. Close to the initial state, this force almost vanishes. Due to the missing force, a complete reset is impossible using OWE SMA wire and the extrinsic TWE, as described in 2.1.1. Accordingly, normalized TWE SMA wire are used, which are applied without bias force in the initial state.[35]

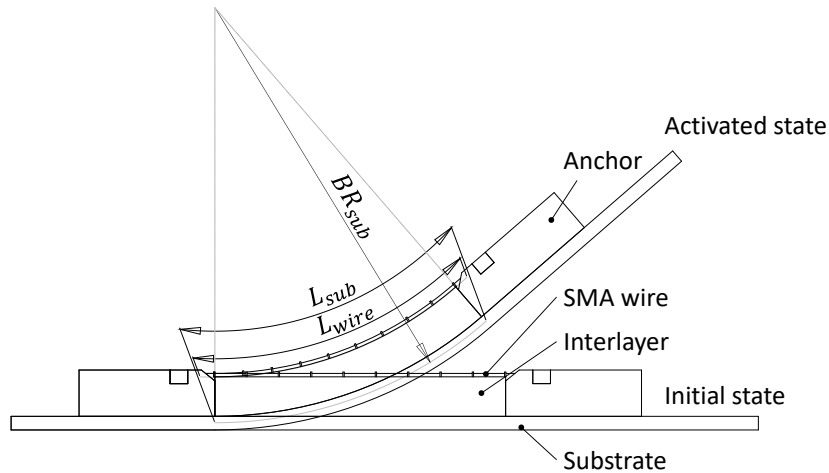


Figure 2.3: Side view of an example of investigated SMAHC in initial and activated state.

2.1.5. Applications

The first ideas to link SMAs, which were already established as an actuator in other applications like the Hitachi robot hand [36], with structures such as beams or laminates appeared in the late 1980s. Without focusing on a specific application, theoretical and experimental investigations were started to modify the composite's properties or behavior actively. The modifications were aimed at stress and strain distribution within a structure,

its modal behavior, buckling control, active displacement, and stiffness.[37, 38]

Today, areas of application that are being researched span shape control [39, 40, 41, 3], stiffness and modulus modification, active and passive vibration control [42, 43, 38, 28], damage suppression [44], self healing [45] and health monitoring [46]. Due to its outstanding lightweight properties, various possible applications in aviation are being investigated. Examples are adaptive winglets, vortex generators, chevrons, trailing edges, and slat-cove fillers. [23]

2.2. Modeling of physical systems

Modeling represents processes in the real physical world using appropriate mathematical equations. A model is validated if the deviation between real-world experiment data and model simulation is inside the limits defined by a previously specified error criterion. An over-developed model is hard to study, challenging to work with, causes mathematical problems, and is expensive in computation time. If a particular state of sufficient quality of the model is reached, an increase in accuracy usually comes with an over-proportional increase in cost. In many cases, models with a higher degree of simplification are not only sufficient but the better choice.[47]

In dynamic systems, state variables change over time. For a given time-dependent input function $u(t)$, the state vector of the system $x(t_1)$ is determined if the initial state of the system $x(t_0)$ is known. A block diagram can illustrate the relationship between the input and output of a dynamic system, where u_i represents input-, y_i output variables, and X is the state matrix (compare figure 2.4).[47] The modeling techniques used in this work

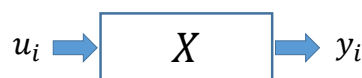


Figure 2.4: Block diagram that illustrates the relationship between input variables u_i , state matrix X , and output variables y_i . [47]

are based on two strategies which are often used in the modeling of SMA and SMAHC, namely the **lumped model** approach and the **finite element method** (FEM).[48, 2, 49] If the elements shown in figure 2.4 are used to transform a spatially distributed system into a system of discrete entities, this is called a lumped model. The physical properties of individual components are idealized and concentrated. The element itself is not spatially discretized. [47]

In contrast, the FEM is used to describe elements whose physical properties cannot be

assumed to be concentrated, which is the case, for example, when complex geometries play an essential role in the system behavior.[50]

2.2.1. Numerical integration methods

Solving complex systems of differential equations today is computer-aided. For this purpose, the continuous problem is transformed into a discrete one, which enables the use of numerical integration methods. The methods presented here are used to solve initial value problems of ordinary differential equations.

The simplest of the methods is the **Euler-Cauchy method**. For discretization, the interval to be examined is divided into an integer number of interpolation points with resulting step size, in this case, time step size Δt . The integral y can be determined according to the rectangle rule by multiplication of the time step size and the corresponding function value f of the actual interpolation point indexed with i . Between two points, the integral is interpolated linearly. The function value of the next point $i + 1$ is calculated using the integral of the previous point y_i . This process is applied iteratively for the entire interval of interest, starting from the given initial point. The mathematical description of the process is given by equation 2.1.

$$y_{i+1} = y_i + \Delta t \cdot f(t_i, y_i) \quad (2.1)$$

As the function value depends on the previous iteration step, errors propagate. This approximation error increases with the step size. In practice, suitable step size is determined by carrying out convergence studies. For this purpose, the step size is reduced iteratively, and the corresponding simulation is carried out. A suitable step size is found if the output variation between subsequent simulations is smaller than the predefined or required numeric accuracy. A further reduction is associated with a disproportionate computational effort compared to increased accuracy. The process generally converges if the approximate solution converges to the exact solution for a step size that tends to be zero. Due to the ease of implementation and low computing time, the Euler-Cauchy method is often used despite the inaccuracies.[50]

The Euler-Cauchy method is used for the implementation of the lumped SMA-wire model and the thermal domain model of the SMAHC.

2.2.2. 1D SMA wire modeling

SMA's are among the so-called inelastic materials. The deformation history must be considered for modeling such a type of material. To describe their behavior, constitutive equations and physical-based balance laws are needed. The constitutive equations allow for the determination of the materials state and the description of its response to external

influences, using a finite set of internal state variables.[51]

This macroscopic phenomenological modeling approach is associated with a high experimental effort to determine the required material state variables. Due to the potential for accurate predictions and the ease of implementation, it is still the preferred option for modeling in engineering. The approach using fundamental physical concepts and balance laws, referred to as microscopic, can explain experimental phenomena. These microscopic modeling approaches are hard to implement, and their predictions often show significant deviations from experiments.[52]

Following, different constitutive models are explained. For all models there is the assumption that $M_s < A_s$ what is the case for most commercial available SMA-materials [52].

The first phenomenological SMA model to describe macroscopic behavior, such as solid-solid thermoplastic phase transformation under the influence of uniaxial loading, was developed in 1982 by Tanaka. Basic modeling ideas are minimization of the free energy and the use of material internal state variables that describe the extent of the phase transformation [53].

Using the approach for a 1D SMA of a certain length and introducing an exponential form for the relation between temperature and martensite fraction, referred to as hardening or evolution law (compare equation 2.2), the model was extended. The resulting rate form of the mechanical constitutive equation (compare equation 2.4) allows for the description of the SMA-materials state by using three of the four state variables stress σ , strain ϵ , temperature T and martensite fraction ξ as well as three material parameters, Young's modulus E , the thermoelastic tensor Θ and the transformation tensor Ω . [54]

$$\xi_{M \rightarrow A} = \exp [A_a(T - A_s) + B_a\sigma] \quad (2.2)$$

$$\xi_{A \rightarrow M} = 1 - \exp [A_m(T - M_s) + B_m\sigma] \quad (2.3)$$

The material constants A_a , B_a , A_m , and B_m can be derived from the transformation temperatures and the Clausius-Clapeyron-coefficient. This coefficient originated from the kinetic theory of gases and was adapted for solid-state physics.

$$\dot{\sigma} = \frac{\delta\sigma}{\delta\epsilon}\dot{\epsilon} + \frac{\delta\sigma}{\delta T}\dot{T} + \frac{\delta\sigma}{\delta\xi}\dot{\xi} = E\dot{\epsilon} + \Theta\dot{T} + \Omega\dot{\xi} \quad (2.4)$$

These equations were the basis for various extensions explained in the following. Instead of using the exponential approach to describe the martensite fraction in accordance to the temperature, by Liang and Rogers, a cosine function was propagated (compare figure 2.5) that also takes the stress dependence of the transformation temperatures into account (equation 2.5). For this purpose, the Clausius-Clapeyron-coefficient C in the following, referred to as the stress-influenced coefficient, is used (compare figure 2.6). [52]

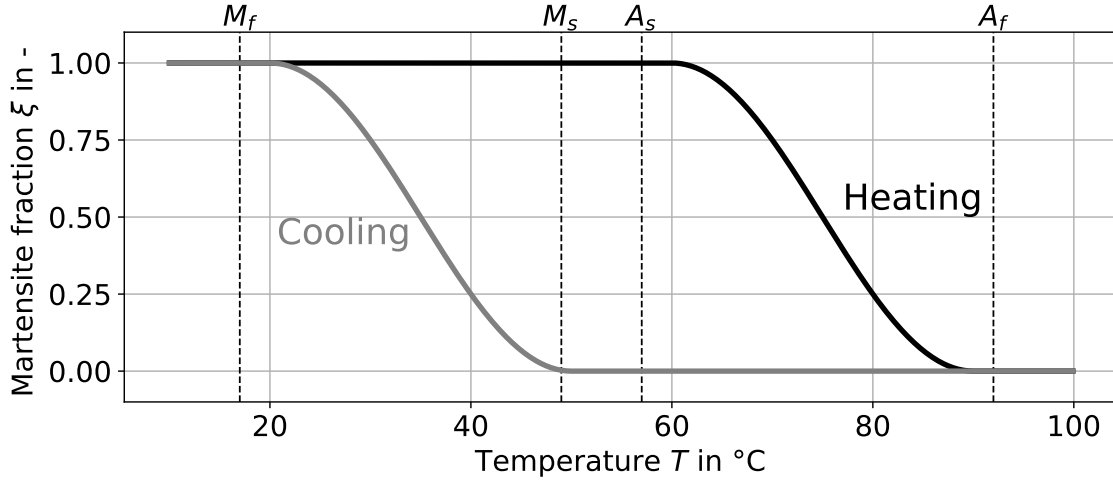


Figure 2.5: Theoretical correlation between martensite fraction ξ and temperature T according to the cosine model established by Liang and Rogers [52].

$$\xi_{M \rightarrow A} = \frac{1}{2} \left\{ \cos \left[\frac{\pi}{(A_f - A_s)} \left(T - A_s - \frac{\sigma}{C_A} \right) \right] + 1 \right\} \quad (2.5)$$

$$\xi_{A \rightarrow M} = \frac{1}{2} \left\{ \cos \left[\frac{\pi}{(M_s - M_f)} \left(T - M_f - \frac{\sigma}{C_M} \right) \right] + 1 \right\} \quad (2.6)$$

Another polynomial approach introduced by Lagoudas for the martensite fraction evolution during phase transformation was compared with the exponential and cosine hardening laws and with experimental data by checking uniaxial stress-strain and heat output-temperature correlations. It was found that the specific enthalpy due to phase transformation differed significantly for all three cases to the experimental data. At the same time, the load paths are similar for the cosine and polynomial functions. [55]

Since the cosine model agrees well with experimental data, and all the material parameters needed for implementation are engineer-based, this approach is the first choice in many cases. [56]

Further, it was demonstrated that the presented constitutive equation 2.4 is only valid for temperatures beyond M_s . A stress-induced transformation cannot be featured for smaller temperatures, starting from a fully martensitic state. Brinson added a new level of complexity to the model to address this issue by distinguishing between temperature-induced martensite ξ_T and stress-induced ξ_σ . Linear changing material parameters during transformation according to the rule of mixture established by Voigt [57] were introduced. The transformation tensor $\Omega(\xi)$ can be expressed using equation 2.7 as the product of Young's modulus $E(\xi)$ and the transformation strain ϵ_{tr} . [56]

$$\Omega(\xi) = E(\xi) \cdot \epsilon_{tr} \quad (2.7)$$

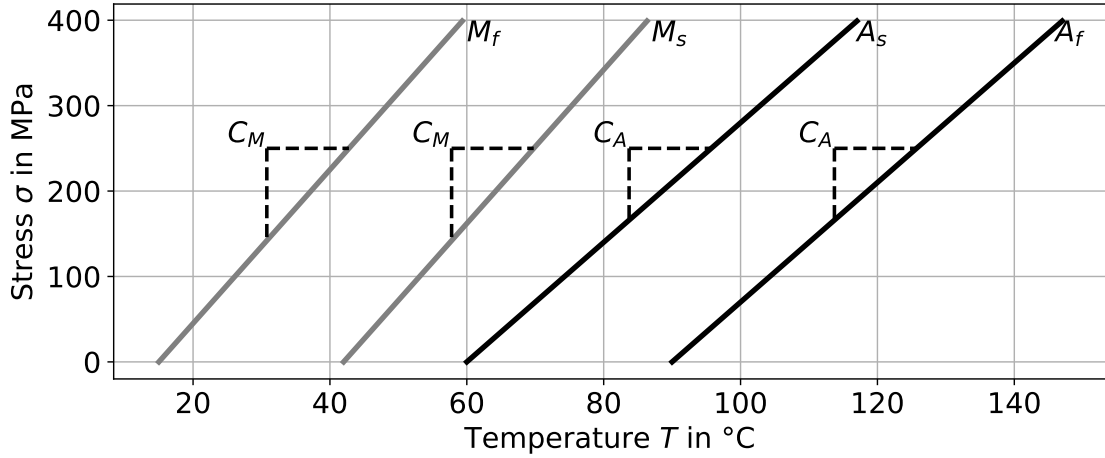


Figure 2.6: Theoretical linear correlation between transformation temperatures M_f, M_s, A_s, A_f and mechanical stress σ described by the stress-influenced coefficients C_M and C_A [52].

Aurichio and Lubliner also distinguished between two martensite variants. However, instead of using an experimentally obtained function for the evolution of these state variables, the generalized plasticity theory was used to develop the 1-Dimensional constitutive model. [58]

A subsequent work by Aurichio and Lubliner investigated how to properly model the changing material parameters during transformation using different homogenization schemes. It was concluded that the Reuss scheme shows for wires and rods experimentally more accurate solutions than the Voigt and Tanaka-Mori scheme. The wire is described as a composite of periodic serial cells of austenite and martensite. Therefore, the elastic modulus E can be considered using equation 2.8. [59]

$$E = \frac{E_A}{1 + \left(\frac{E_A}{E_M} - 1\right) \xi} \quad (2.8)$$

The current maximum uniaxial transformation strain ϵ_{tr} depends on the applied stress and, thus, on the amount of detwinned martensite. Experimental investigations showed that $\epsilon_{tr}(\sigma)$ can be approximated by an exponential fit according to equation 2.9, where $\epsilon_{ps_{max}}$ is the maximum possible transformation strain, and $k_{\epsilon, tr}$ a fit coefficient (compare figure 2.7). The basic assumption for this correlation is that the specimen is temperature-cycled before testing without the influence of external load. For a wire that shows an intrinsic TWE behavior, the transformation strain for zero load level $\epsilon_{tr}(\sigma = 0)$ is greater than zero. The maximum transformation strain possible is reached when the specimens state is 100% detwinned martensite. [60, 61]

$$\epsilon_{tr}(\sigma) = \epsilon_{tr}(0) + (\epsilon_{max} - \epsilon_{tr}(0)) [1 - \exp(-k_{\epsilon, tr} \sigma / E_A)] \quad (2.9)$$

Further models added higher levels of complexity to decrease discrepancies between exper-

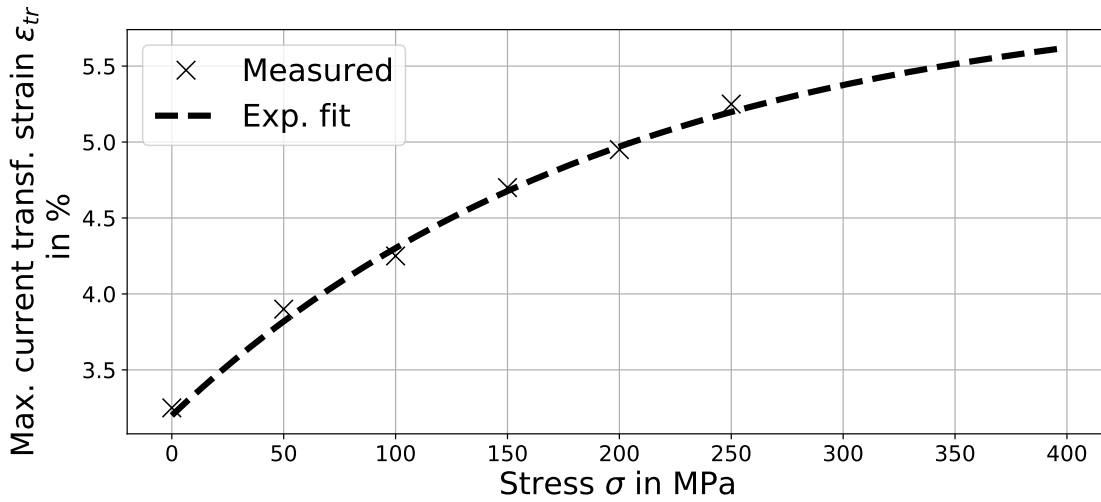


Figure 2.7: Theoretical exponential correlation between the maximum current transformation strain ϵ_{tr} and the mechanical stress σ . [61]

iments and theoretically obtained data or use entirely different approaches to describe the material. For example, De la Flor distinguished between elastic moduli of the two different martensitic variants and introduced a temperature-dependent transformation tensor. [62]

A finite element formulation for SMAHCs under thermal and mechanical loading conditions was developed for constrained, restrained, and free recovery behavior. The extension of the uniaxial thermoelastic constitutive relation of the SMA to two spatial directions resulted in the effective coefficient of thermal expansion model (ECTEM). The uniaxial equation 2.10 underlying the model describes the stress σ_a that is exerted by the SMA as a function of the nonlinear coefficient of thermal expansion (CTE) $\alpha_a(T)$, the temperature-dependent young's modulus E_a and the strain ϵ . The equations were set up for a representative volume element of SMAHC lamina.

$$\sigma_a = E_a \left[\epsilon + \int_{T_0}^T \alpha_a(\tau) d\tau \right] \quad (2.10)$$

where the term $\int_{T_0}^T \alpha_a(\tau) d\tau$ can be equated with the recovery stress σ_r . This stress corresponds to the phase change potential of the alloy under the influence of an external load. The temperature and pre-stress-dependent recovery stress are determined experimentally. For this purpose, the pre-stressed wire is fixed and heated. The resulting mechanical stress is plotted against temperature and reflects the nonlinear behavior of the alloy. The model can be applied to describe the deformation behavior, the thermal buckling, and thermal post-buckling, as well as the dynamic response of SMAHC beams and plates. [2]

An approach for modeling the intrinsic TWE of SMA was done by Zhang based on the conclusion that the training of the alloy results in a residual stress σ_{res} linked with a residual strain ϵ_{re} . Because of this residual stress, the SMA retains its original shape after heating to temperatures beyond A_s and cooling back down to temperatures below M_f without any external load applied. The magnitude of residual stress can be measured by X-ray diffraction, which is of relatively high complexity. Instead, the residual stress is approximated by the plastic modulus P and the true plastic strain ϵ_{pl} , which can be measured directly according to equation 2.12, where L_0 is the length of the specimen before training and L is the length after training at temperatures above A_f (compare equation 2.11). The constitutive equation established by Tanaka was extended to form equation 2.13.[63]

$$\sigma_{res} = P\epsilon_{pl} \quad (2.11)$$

$$\epsilon_{pl} = \ln\left(\frac{L}{L_0}\right) \quad (2.12)$$

$$\sigma - \sigma_0 = E\left(\epsilon - \frac{P}{E}\epsilon_{pl} - \epsilon_0\right) + \Theta(T - T_0) + \Omega(\xi - \xi_0) \quad (2.13)$$

2.2.3. Thermal domain modeling

Conservation of energy

The conservation of energy, also known as the first law of thermodynamics, states that the rate of change of the total energy of a system is equal to the sum of all energy flows through its surface, all thermal energy added by internal sources and mechanical work. Simplified forms of the energy conservation equation in the context of SMAs are introduced, for example, by [64, 65, 66, 67]. For Joule heating of SMA material, the energy input equals the applied electrical energy and is converted into heat and mechanical energy as well as energy losses [65]. Equation 2.14 describes this correlation for an SMA continuum body. The rate of change of the stored thermal energy \dot{U} equals the electrical power input P_{el} that is not transformed into kinetic \dot{W}_{kin} or potential work \dot{W}_{pot} , consumed for phase transformation in terms of the enthalpy \dot{H}_{tr} or losses into the surroundings by conduction \dot{Q}_{cond} , convection \dot{Q}_{conv} or radiation \dot{Q}_{rad} [66].

$$\dot{U} = P_{el} - \dot{H}_{tr} - \dot{W}_{kin} - \dot{W}_{pot} - \dot{Q}_{cond} - \dot{Q}_{conv} - \dot{Q}_{rad} \quad (2.14)$$

Internal energy

The rate of change of the stored thermal energy \dot{U} of a finite SMA element, according to [65, 68, 67], is defined by equation 2.15.

$$\dot{U} = m \cdot c \cdot \dot{T} \quad (2.15)$$

where m is the elements mass and c the specific heat capacity. The specific heat capacity is a temperature-dependent material parameter. However, in the context of temperature-driven phase transformation in SMA, this value is usually assumed to be constant. It is formed from the average value of the heat capacity of the alloy in the austenitic and martensitic states. In the temperature range of application, changes in the specific heat capacity of the individual phases are also negligible compared to the change in the effective heat capacity due to the transformation enthalpy during the phase transformation [65]. The transformation enthalpy can be described as a function of the integral latent heat ΔH , and the rate of change of the martensite fraction $\dot{\xi}$ (compare equation 2.16) [65, 68, 67].

$$\dot{H}_{tr} = m \cdot \Delta H_{tr} \cdot \dot{\xi} \quad (2.16)$$

It is a common assumption for SMA actuators to neglect the influences of mechanical energy as they are up to two magnitudes smaller than other influences taken into account [69]. This assumption still applies to highly dynamic so-called ballistic activation of SMA wires [70].

Heat loss

The heat loss quantity strongly depends on driving temperature differences between SMA and ambient. The amount of energy losses can be quantified using equation 2.17. If the SMA is in contact with solid bodies of different temperatures, a heat flux emerges, proportional to the thermal conductivity λ and the contact surface A . The heat transport via fluids surrounding the SMA can be expressed using the heat transfer coefficient α , the surface A_{sf} , and the ambient temperature T_{∞} . The third component is thermal radiation stated as proportional to the emissivity ϵ_e , the Stefan-Boltzmann constant σ_B and the wires surface A_{sf} . For temperature differences between the wire and surrounding less than 100K, it can be assumed that the losses due to radiation \dot{Q}_{rad} are negligible. [65]

$$E_{loss} = \underbrace{\lambda \cdot A \cdot \frac{T - T_{\infty}}{dx} \cdot dt}_{\text{Conduction energy}} + \underbrace{\alpha \cdot A_{sf} \cdot (T - T_{\infty}) \cdot dt}_{\text{Convection energy}} + \underbrace{\epsilon_e \cdot \sigma_B \cdot A_{sf} \cdot (T^4 - T_{\infty}^4) \cdot dt}_{\text{Radiation energy}} \quad (2.17)$$

The coefficient needed to determine the losses due to convection can be calculated using the Nusselt number Nu , the heat conductivity λ , and the characteristic length L according to equation 2.18. [71]

$$\alpha = \frac{Nu \cdot \lambda}{L} \quad (2.18)$$

The Nusselt number for natural convection for a long horizontal cylinder is defined by Churchill and Chu for Rayleigh numbers smaller 10^{12} (compare equation 2.19) [72]. The

| l | Diameter | T_{SMA} | T_{∞} | Source | h | Conv. heat transfer coefficient |
|------|----------|-------------|--------------|--------|---|---------------------------------|
| mm | mm | $^{\circ}C$ | $^{\circ}C$ | - | - | $W/(m^2K)$ |
| 283 | 0.254 | up to 190 | -30 | [76] | | 131 |
| 1100 | 0.152 | up to 160 | 23 | [77] | | 1.5 |
| 100 | 0.51 | up to 200 | 23 | [75] | | 45 |

Table 2.1: Convective heat transfer coefficients for SMA wire under the influence of free convection from the literature.

characteristic length is $L = 0.5 \cdot \pi \cdot d$.

$$Nu = \left\{ 0.752 + 0.387 \cdot \left[Ra \cdot \left[1 + \left(\frac{0.559}{Pr} \right)^{9/16} \right]^{-16/9} \right]^{1/6} \right\}^2 \quad (2.19)$$

The accuracy for this correlation in the given validity range was verified again by [73]. In this work, various equations from literature to distinguish the Nusselt number were compared against each other and experiments. The Rayleigh number can be calculated using the isobaric thermal expansion coefficient β , gravitational acceleration g , kinematic viscosity ν and Thermal diffusivity κ as shown in equation 2.20. The Prandtl number Pr can be expressed according to equation 2.21. [71].

$$Ra = \frac{\beta g (T - T_{\infty}) L^3}{\nu \kappa} \quad (2.20)$$

$$Pr = \frac{\nu}{\kappa} \quad (2.21)$$

Eisakhani et al. investigated the convective heat transfer for SMA wires with a diameter of 0.5 mm under various inclination angles from horizontal to vertical positions, taking mechanical stress into account. An empirical correlation for the cylinder in the power form and polynomial form was concluded for the stress-free state according to equation 2.22 where ϕ is the inclination angle in radians from 0 to 1.57. Equation is valid for $2.6 \cdot 10^{-8} \leq Ra \leq 6 \cdot 10^{-1}$. Additionally, it was demonstrated that heat transfer has no significant impact due to the applied external load. [74]

$$Nu = (-0.04\phi + 0.19) + (-0.09\phi^2 + 0.003\phi + 0.82)Ra^{(-0.03\phi+0.16)} \quad (2.22)$$

Very different heat transfer coefficients for SMA under the influence of natural or free convection can be found in literature, as depicted in table 2.1. In [75], the convective heat transfer coefficient of Joule heated SMA wire of 0.51 mm diameter was approximated using equation 2.19 and 2.22. The results were compared with experiments, and a good correlation was found. Equations for calculating Nusselt numbers of relevant geometries

can be found in the appendix A.1. The Nusselt number for a vertical cylinder can be calculated according to equation 2.23 where h is the height of the cylinder and d its diameter [71].

$$Nu = \left\{ 0.825 + 0.387 \cdot \left[Ra \cdot \left[1 + \left(\frac{0.492}{Pr} \right)^{9/16} \right]^{-16/9} \right]^{1/6} \right\}^2 + 0.435 \cdot h/d \quad (2.23)$$

Lumped capacitance or spatial discretized models can be used to evaluate the transient conductive heat loss. This model approaches allow for the approximation of system behavior by discrete elements with negligible temperature difference inside each element. To decide if the assumption of homogeneous temperature within an element is valid, the biot number Bi has to be smaller than 0.1. This number indicates the relationship between the thermal resistance of a body R_{cond} and the heat transfer resistance R_{trans} between it and the surrounding medium (Compare eq. 2.24). It can be expressed using the characteristic length L , the heat transfer coefficient α between the solid body and the surrounding, and the thermal conductivity of the solid body λ . For a cylinder, the characteristic length L is given as half radius $r/2$. [78]

$$Bi = \frac{R_{cond}}{R_{trans}} = \frac{L \cdot \alpha}{\lambda} \quad (2.24)$$

For thin embedded wires, the homogeneous temperature assumption is often valid. This statement contrasts the surrounding solid medium, which usually has a significant temperature gradient and therefore can not be represented by a single element with homogeneous temperature.[49] Lumped thermal networks can be composed of heat sources, sinks, and capacitive and resistive elements. These networks are referred to as lumped-capacitance models. The heat flux through a resistive element is given by its thermal resistance R_{th} and the temperature difference across the element $(T_2 - T_1)$ (compare eq. 2.25). The heat transfer mode can be conductive, convective, or radiative. For the conductive mode, the resistance is given as the ratio between thickness d and thermal conductivity λ multiplied by the cross-sectional area A . In the case of convection, it is given as the reciprocal value of the heat transfer coefficient α multiplied by the area flowed through A . The change of the internal energy of a capacitive element \dot{U} is given by the element mass m , its heat capacity c and the temperature change over time \dot{T} (compare eq. 2.26). The analogy to electrical networks allows the application of Kirchhoff's node and mesh rule.

$$\dot{Q}_{resistor} = \frac{(T_2 - T_1)}{R_{th}} \quad (2.25)$$

$$\dot{U}_{capacitor} = m \cdot c \cdot \dot{T} \quad (2.26)$$

For Biot numbers greater than 0.1, approximation of thermal systems by lumped models is no longer applicable. Temperature gradients within individual elements are large, so they have to be spatially discretized. The complexity depends on the temperature gradient in the different spatial directions. In many cases, assumptions allow for the reduction of the problem, and discretization in two or one spatial directions is sufficient. Discretization is the process of dividing into smaller spatial elements. Using different shapes and sizes of elements is a tradeoff between accuracy and implementation effort. The most straightforward implementation is done using identical elements in a structured mesh. Evaluation of each element is performed in its center. For each element, the sum of the incoming and outgoing heat fluxes equals the change in internal energy and enthalpy. The temperature of an element in a structured mesh can be iteratively computed using equation 2.27.

$$T_i^{t+1} = T_i^t + \frac{\lambda}{\rho \cdot c} \cdot \frac{dt}{dx^2} \cdot \left(\sum_{n=0}^N T_N^t - N \cdot T_i^t \right) \quad (2.27)$$

The element to be evaluated is indexed with i . The number of neighbor elements with direct flux into this element is given by N . The equation thus allows for an explicit approximation of the temperature in the next time step $t + 1$. This method is referred to as the forward in time centered in space method (FTCS). The thermal diffusivity a is given by the properties of the elements as $\frac{\lambda}{\rho \cdot c}$. The spatial increment dx is the distance between the centers of two elements, and dt is the time increment. For up to 25% volume fraction of SMA wires embedded in a carbon fiber reinforced composite (CFRP), the heating and cooling behavior, in the case of Joule heat, depends essentially on the thermal conduction and capacitive properties. At the same time, the influence of transformation enthalpy can be neglected.[49]

2.2.4. Electrical domain modeling

The essential parameter to model the SMAs behavior in the scope of an electrical network is its resistance R . The power dissipating in SMA P_{el} for a given electrical network can thus be determined using the Kirchhoff rules [79] and the well-established correlation between voltage U or current I as stated in equation 2.28.

The total resistance of a wire with length L and crosssection area A can be described using its materials-specific resistivity ρ_{el} according to equation 2.29.

$$P_{el} = R \cdot I^2 = \frac{U^2}{R} \quad (2.28)$$

$$R = \rho_{el} \cdot \frac{L}{A} \quad (2.29)$$

In [80], the resistivity of the wire is given as the sum of the resistivities of single phase composition. The authors distinguish between austenitic, martensitic, and R-phase (compare section 2.1.1). Three terms were taken into account to evaluate a single phase resistivity, the resistivity at a specific temperature, and two constitutive terms describing the change of resistivity for change of temperature and stress level.

The correlations mentioned above were taken up again by [76] but ignoring the R-phase and simplifying the system resulting in equation 2.30.

$$R = R_M \cdot \xi + R_A(1 - \xi) \quad (2.30)$$

The resistance in single phase is defined as resistance measured R_{0M} (R_{0A}) at specific temperature T_{0M} (T_{0A}) and the relations between resistance and temperature T and resistance and stress σ , stated as equation 2.31 and 2.32.

$$R_M = R_{0M} + (T - T_{0M}) \frac{\delta R_M}{\delta T} + \sigma \frac{\delta R_M}{\delta \sigma} \quad (2.31)$$

$$R_A = R_{0A} + (T - T_{0A}) \frac{\delta R_A}{\delta T} + \sigma \frac{\delta R_A}{\delta \sigma} \quad (2.32)$$

It is a common assumption in electro-thermomechanical modeling to neglect the resistance dependency of single phases on temperature and stress [65]. The resistivity can then be described using the mixture rule by Voigt (compare equation 2.33).

$$\rho = \rho_M \cdot \xi + \rho_A(1 - \xi) \quad (2.33)$$

For electrical current-carrying conductors, it is often not the current flux I that is specified. However, the heat generation per volume P_{el}/V is given as a function of the specific resistance ρ_{el} and the conductor's cross-sectional area A (compare eq. 2.34)[49].

$$P_{el}/V = \rho_{el} \cdot I^2/A^2 \quad (2.34)$$

2.2.5. Mechanical domain modeling

As depicted in figure 2.3, the deflection's magnitude is in the range of the active beam length. Due to this relatively large deflection during the application, the basic assumptions of elementary beam theory are no longer valid. Deflection thus is therefore modeled using the differential equation of the bending line according to equation 2.35. The flexural rigidity for wide beams (the magnitude of width and length are equal) is given as $B = EI/(1 - \nu^2)$, where E is the elastic modulus, I is the area moment of inertia and ν the Poisson ratio. The bending moment M then is the product of the multiplication of flexural

rigidity B by curvature $\frac{d\phi}{ds}$ which is given by arc length s and slope angle ϕ . The radius of curvature $R = \frac{ds}{d\phi}$ is the reciprocal value of curvature.

$$B \cdot \frac{d\phi}{ds} = M \quad (2.35)$$

For constant flexural rigidity, the slope angle ϕ is given by equation 2.36. Furthermore, the deflection can be derived from ϕ by equation 2.37 with deflection of an infinitesimal beam element given as $dz = \sin(\phi) \cdot ds$.

$$\phi(s) = \frac{1}{B} \int_0^s M ds \quad (2.36)$$

$$z(s) = \int_0^s \sin(\phi) ds \quad (2.37)$$

Bending moments caused by external loads correlate with the deflection due to the change in the lever arm. The elliptic integral resulting from this change is recommended to be solved numerically.[81]

3. State of the art

This chapter reviews the current level of knowledge about the modeling and design of SMAHC. The search was conducted using the keywords and respective synonyms in table 3.1. The columns represent keywords, while the rows represent synonyms. The search was enhanced by truncation and phrase search. The exact search syntax is detailed in the appendix A.2. Scopus searches were conducted and last updated on October 27, 2022.

| | | | |
|----------------------|-----------|---------|----------|
| "Shape memory alloy" | SMAHC | Model* | Deflect* |
| NiTi* | Composite | Design* | Bend* |
| SMA | Beam | | Morph* |
| | | | Adapt* |

Table 3.1: Keyword-synonyms-table: The columns indicate keywords, and the rows indicate synonyms. Asterisk Symbol is used for truncation.

The search returned a total of 1040 documents. A study of the results revealed that the topic had its significant beginnings around 1989 and has developed a steadily increasing level of interest since then, with an average of sixty papers produced annually today. The data was evaluated methodically using the open-source framework ASReview [82].

Regarding the modeling or design of SMAHC, the findings can be loosely classified into eight categories: shape adaptation, thermal buckling, vibration, impact, interface, application, manufacture, and miscellaneous. Table 3.2 summarizes the relevant literature about the modeling and development of SMAHC for shape adaptation. The entries are organized according to their publication year. The columns provide information regarding the model type, the level of integration of SMA components, if and how the model is implemented, the type of study, the external influences considered, the SMA model approach, and any further comments. In the SMA integration level column, there are five distinct possibilities identified. The first possibility, referred to as 'Standalone SMA', considers the SMA a single beam or cantilever without being modeled within a composite. The integration level for integrated SMA components is divided into External, Surface bonded, and Integrated. External concepts involve using SMA components to deform a substrate while being placed outside of it. Surface bonded concepts, conversely, involve directly attaching SMA components to the substrate's surface. Integrated SMA components are further divided into two abstraction levels. In many instances, models are simplified by assuming the SMA components, regardless of their geometry, as a homogeneous layer within the composite. This abstraction is referred to as a 'homogenized layer'. Alternatively, if the SMA component's actual geometry is considered, the designation is 'Integrated'.

| Modeling | SMA integration level | Implementation | Type of Research | External influences | SMA model | Comment | Source |
|--------------------------|-----------------------|----------------|---------------------------|----------------------|-----------------------------|---|--------------------|
| Thermoelectrical | Integrated | - | Theoretical | - | Lumped capacitance | Influence of Biot number and SMA fiber density | [49] |
| Mechanical | External | - | Theoretical; Experimental | - | Substitute as load | - | [4] |
| Electro-thermomechanical | Homogenized layer | FEAP | Theoretical | Convection parameter | Auricchio | Split coupled problem in sequence of uncoupled problems | [83, 84] |
| Electro-thermomechanical | External | NUDOCCS | Theoretical | Load | Müller, Achenbach, Seelecke | SMA Control | [85] |
| Thermomechanical | Integrated | ABAQUS | Theoretical; Experimental | Load | Brinson; ECTEM | Experimentally validated; Application approved | [2, 86, 6, 87, 88] |
| Thermomechanical | Homogenized layer | - | Theoretical; Experimental | - | Brinson | Analytical formulation | [89] |
| Electro-thermomechanical | Integrated | ANSYS | Theoretical | External influences | Brinson | SMAHC subjected to lateral pressure | [90] |
| Thermomechanical | Integrated | RCloop | Experimental; Theoretical | - | ECTEM | ADAPT Project | [91, 12] |
| Thermomechanical | Standalone SMA | ANSYS | Theoretical | Load | Müller, Achenbach, Seelecke | - | [92] |

| Modeling | SMA integration level | Implementation | Type of Research | External influences | SMA model | Comment | Source |
|--------------------------|-----------------------|----------------|---------------------------|---------------------------------|------------------------------|--|----------|
| Electro-thermomechanical | Homogenized layer | FORTRAN 90 | Theoretical | - | - | - | [93] |
| Thermomechanical | Homogenized layer | ABAQUS | Theoretical; Experimental | - | Brinson; ECTEM | - | [94] |
| Electro-thermomechanical | Homogenized layer | Matlab | Theoretical | Load | Tanaka | - | [95] |
| Thermomechanical | Standalone SMA | COMSOL | Theoretical | Load | Müller Achenbach Seelecke | - | [96] |
| Thermomechanical | External | - | Theoretical; Experimental | Load | Brinson | Cyclic investigation | [97] |
| Electro-thermomechanical | External | - | Theoretical; Experimental | Convection, Ambient temperature | Lagoudas; Lumped capacitance | - | [77] |
| Electro-thermomechanical | External | Matlab | Theoretical; Experimental | Ambient temperature | Brinson | - | [98] |
| Thermomechanical | Homogenized layer | - | Theoretical; Experimental | - | Lagoudas | Custom implementation | [99] |
| Thermomechanical | Homogenized layer | ABAQUS | Theoretical; Experimental | Load | Modified ECTEM | Application approved | [100, 5] |
| Electro-thermomechanical | Homogenized layer | - | Theoretical | - | Brinson | Decoupled mechanical and thermal domains | [101] |
| Thermoelectrical | Homogenized layer | - | Theoretical | Convection parameter | Lumped capacitance | - | [102] |

| Modeling | SMA integration level | Implementation | Type of Research | External influences | SMA model | Comment | Source |
|--------------------------|-----------------------|-----------------|---------------------------|---------------------|----------------------------|-----------------------------|------------|
| Electro-thermomechanical | Integrated | - | Theoretical; Experimental | - | Rubberlike material | - | [103, 104] |
| Thermomechanical | Integrated | ANSYS | Theoretical | Load | Brinson; ECTEM | Fluid-structure interaction | [105, 106] |
| Electro-thermomechanical | Homogenized layer | Matlab/Simulink | Theoretical; Experimental | Ambient temperature | Liang and Rogers | - | [107] |
| Electro-thermomechanical | Surface bonded | Matlab/Simulink | Theoretical; Experimental | - | Tanaka; Lumped capacitance | Instant activation | [108] |
| Thermomechanical | Integrated | ABAQUS | Theoretical; Experimental | - | Brinson; ECTEM | High accuracy | [109] |
| Mechanical | Integrated | ABAQUS | Theoretical | Load | Beam theory | - | [110] |
| Electro-thermomechanical | External | ABAQUS | Theoretical; Experimental | Load | ECTEM; Lumped capacitance | Decoupled model domains | [111] |
| Thermomechanical | Integrated | ABAQUS | Theoretical; Experimental | - | Brinson; ECTEM | Multiscale modeling | [112] |
| Thermomechanical | Integrated | ANSYS | Theoretical; Experimental | - | Auricchio | - | [113] |

Table 3.2: Publications and classifications dealing with modeling SMAHC for form adaptation.

Due to its ease of implementation, high accuracy, and well-defined and measurable input parameters, the model developed by Turner [2] is still the gold standard for the thermomechanical development of applications involving SMAHC for shape adaptation [6, 88, 94, 105, 106, 109, 112, 114]. Consequently, this method is a prime example of a model that may be used beyond academia.

When energy consumption or power peaks play a crucial role in electrically actuated SMAHC, thermomechanical models are insufficient for their design. Thermomechanical models can forecast the mechanical output at specified temperatures. These models must be expanded to enable electro-thermomechanical modeling for anticipating the system's dynamics and energy consumption. Although advanced models for this purpose have existed for decades, they are hardly valuable for engineers. This is due to the need for more consideration of essential boundary conditions, undefined methods for measuring model parameters, model restriction to externally attached SMAs, missing model validation, and restricted model access due to proprietary software.

In particular, the need for experimental data to validate electro-thermomechanical models under various circumstances and quantify their uncertainty is an issue that only a few focus on [115, 116].

In addition, it should be highlighted that there are no specific guidelines or standards for SMAHC, although the work for linear SMA actuators can be utilized as a guide due to many parallels. The work of the Consortium for the Advancement of Shape Memory Alloy Research and Technology (CASMAART) deserves special notice. It is stated that there is no conventional procedure to follow, as each product development presents its unique challenges. Numerous case studies illustrate the logical approach to product development with SMA, including SMAHC components.[117]

In German-speaking nations, the VDI Guideline 2248 "Produktentwicklungen with Formgedächtnislegierungen" outlines the development process with shape memory materials [118].

4. Objectives of work

This work aimed to develop and validate an open-source model for the transient electro-thermomechanical behavior of SMAHCs for shape control. The modeling approach addressed its practical use outside the academic world. In order to enable the transition from science, it is essential to:

- consider important boundary conditions,
- adequately define the model parameters and their respective measurement method,
- validate models with experimental data,
- highlight model constraints.

Analysis of the current state of the art revealed that none of the existing models met all the requirements. Existing electro-thermomechanical models either do not consider external loads or ambient temperatures or need to be more validated with experimental data.

The objective was to develop a model capable of describing the shape's transient adaptation behavior under the impact of external load and ambient temperature. Relevant model parameters must be quantifiable using well-defined methods. Also, the model should be open-source and hence accessible.

To reach the indicated objective, answers to the following four questions were required:

- How do external loads, ambient temperature, and applied electrical current affect the actuator's deflection, bandwidth, and power consumption?
- What observed effects and influences are relevant and significant, and how can they be modeled?
- What input parameters are needed, and how can they be measured?
- How accurately can the model describe the adaptive shape behavior under relevant external loads and ambient temperatures?

Experiments were conducted to provide an answer to the first question. Second, based on the results, it was determined which effects must be represented, and a model was formulated and executed using proven equations and techniques. The model-based method

supplied the simulation's input parameters. In the third step, the corresponding measuring methods were specified, and measurements were conducted. The model was validated as the final stage using experimental data. The corresponding steps, inputs, and outputs are depicted in figure 4.1.

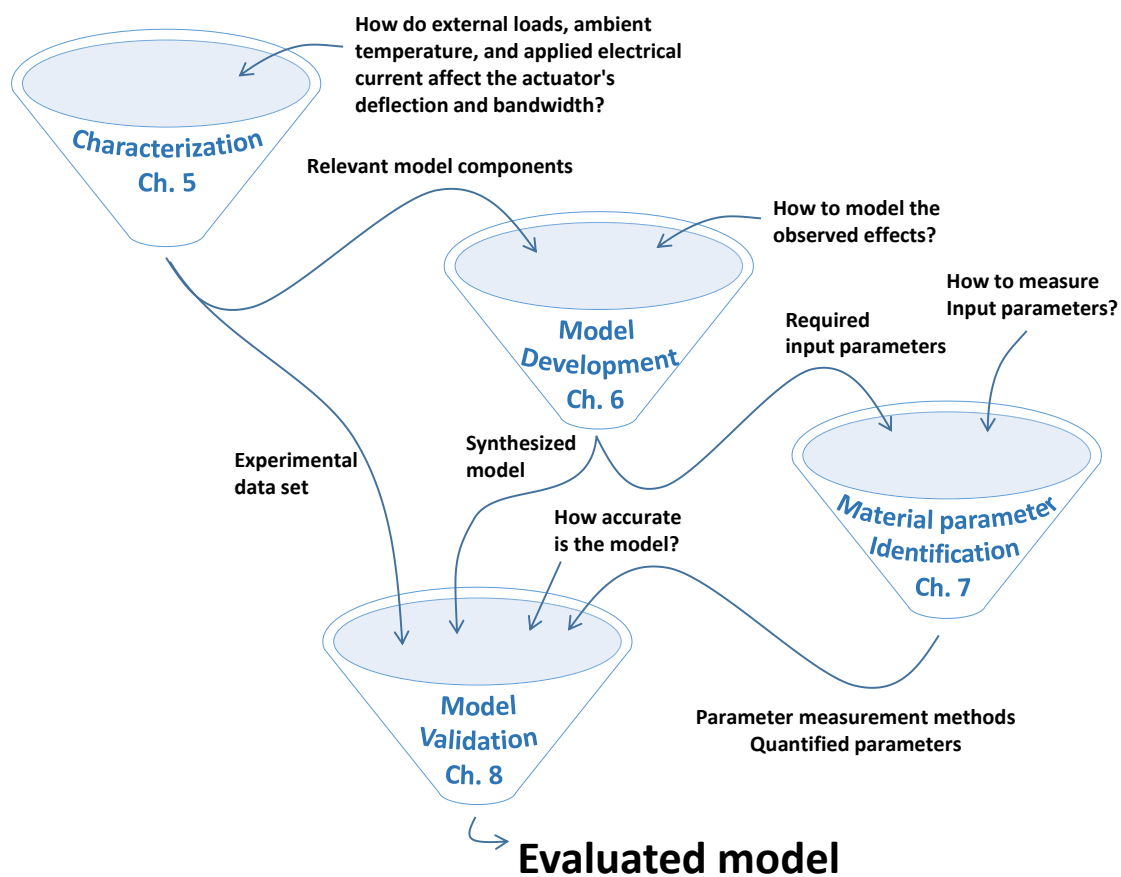


Figure 4.1: Illustration of the main body chapters interlocking, including their logical order and the respective underlying questions.

5. SMAHC characterization

This chapter presents the SMAHC characterization, starting with the materials and methods used and discussing the results.

5.1. SMAHC specimens

In the characterization of Shape Memory Alloy Hybrid Composites (SMAHCs), commercially available actuator modules provided by CompActive GmbH, a spin-off of IVW GmbH, were utilized. The modules of the Curve® series with high, medium, and low deflection served as the foundation [119], [120], [121]. The schematic representation of the SMAHC, its components and states is illustrated in figure 5.1. The general structure was achieved by utilizing a substrate, an interlayer and an SMA grid. The interlayer adjusted the distance between the substrate and the SMA grid.

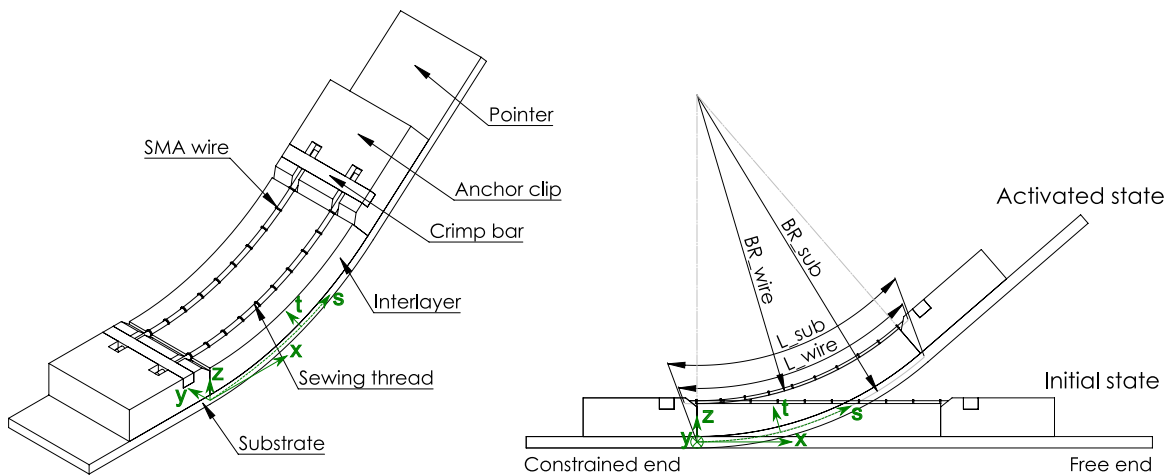


Figure 5.1: Investigated type of SMAHC actuator; Left: Components in isometric view; Right: Actuator in initial and activated state in side view.

As previously discussed in Subsection 2.1.4, deformation occurs due to the relative contraction of the SMA wires with respect to the substrate during thermally induced activation. Each SMAHC investigated was configured as a cantilever with one end constrained without degrees of freedom, referred to as the **constrained end**, and the opposite side as freely movable referred to as the **free end**. The SMA wires are aligned in the direction of these two ends. At temperatures below M_f , the actuator is in its **initial state**, and the substrate exhibits almost no curvature. In case of curvature due to the contraction

of the SMA, the state is referred to as **activated**. The maximum level of activation is reached for temperatures above A_f^* . High shear forces occur at the SMA wire ends during the activation or loading of the actuator. These shear forces need to be transmitted to the substrate to utilize the actuator potential of the SMA wires fully [122]. The forces are absorbed mechanically using additional components. These components are a **crimp bar** that fixes the SMA wires with frictional and form-fitting locking and an **anchor clip** that, in turn, fixes the crimp bar by form-fitting locking. The assembly of SMA wire and crimp bar together forms the **SMA grid**. The distance between the two anchor clips is the **active length** since the deformation is limited to this area. Due to the mechanical properties of the clip, the actuator is rigid in this area. The normal forces between the SMA wire and the interlayer during activation must be transferred sufficiently. Infiltrated **sewing threads** achieve the absorption of these forces and transmission to the substrate. An artifact of the infiltration performed during actuator fabrication is a resin layer covering the interlayer and the grid. The resin layer coating of the SMA wire can be seen in figure 5.3. The grid, clips and interlayer assembly are called the **actuator module**. The module is connected to the substrate by a material bond. Depending on the forces occurring during the application, additional form-fit or force-fit connections can be used for enhancement. Due to the high flexibility of the adhesive system, the excellent adhesion, and the simple and fast processing, double-sided adhesive tapes have established themselves for the material bond between substrate and interlayer.

The performance of the actuator system is primarily dependent on the interaction between the substrate, interlayer, and SMA grid within the active length region. The SMA grid was constructed using established materials, with a centerline spacing s_w of 5 mm between the mechanically parallel SMA wires (compare figure 5.2). Ten SMA wires were utilized per actuator. The crimp bar was fabricated from brass, an electrically conductive material, thus creating an electrical circuit. The SMA wires, with a nominal diameter of 0.5 mm, were composed of a trained binary NiTi alloy provided by SAES Getters under the tradename Smartflex®. In direct contact with the thermally activated SMA wires, the interlayer must withstand temperatures above A_f . It should exhibit the lowest possible resistance to the forces initiated by the contraction of the SMA wires and, at the same time, maintain a consistent distance between the substrate and the SMA wires. For the construction of the interlayer, the established elastomer Kraibon®AA6CFZ provided by Kraiburg was used. A stiff substrate results in a well-defined curvature of the actuator. The stiffness of the substrate is defined by its thickness and modulus of elasticity. An excessive stiffness results in large loads on the SMA wires during activation, thus reducing deflection and cyclic stability. A low stiffness leads to an incomplete macroscopic reset to the initial position of the actuator over several cycles due to the absence of a resetting force [35]. Under certain circumstances, activation takes place under increased ambient temperatures. In such cases, critical transition temperatures, such as the glass-transition

temperature of polymers, must not be exceeded to avoid plastic deformation. The substrate itself must be able to undergo cyclic deformation without plastic deformation. To minimize strains in the substrate, thin substrates with a high modulus of elasticity are preferable. Here, material 1.4310 (Material number according to EN 10027-2) was used. In order to keep boundary effects at a low level, the actuators with the largest dimensions were used. Figure 5.2 shows an exemplary actuator. Connecting leads of copper with a length of about 150 mm and 0.75 mm cross-sections were soldered to the crimp bars for easy electrical contact during experimentation. The exact position of the solder joints can be referred to in figure 5.2. All SMA wires were connected in series by cutting the crimp bar at specific points for galvanic isolation to ensure a uniform current flux.

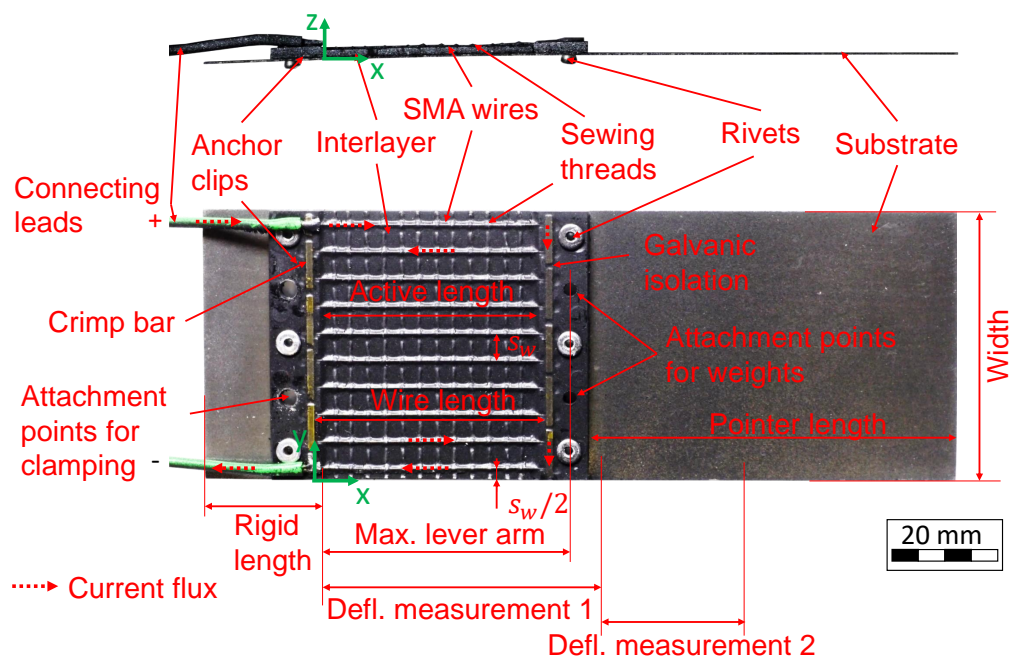


Figure 5.2: Example of a specimen used for experimental characterization, showing components and dimensions. Top: Side view; Bottom: Top view

In order to investigate the influence of essential parameters on the actuator performance, four variants, denoted A, B, C, and D, were manufactured. The two parameters, interlayer thickness and substrate stiffness, were identified as essential as it is well known that these parameters have a significant influence [12, 100, 30, 3]. SMA wire diameter and spacing were not part of the study. These parameters are identical for each configuration. It is generally known that a higher SMA wire diameter and lower surface-to-volume ratio lead to more efficient heating. However, it reduces the dynamics due to slower cooling [70, 123, 124]. Figure 5.3 shows microscopically magnified sections of the four variants in cross-section. The parameters that define the variants are, the thickness of the substrate t_{sub} and the distance between the substrate and center of SMA wire p_{SMA} . Wire diameter d is the same for all variants.

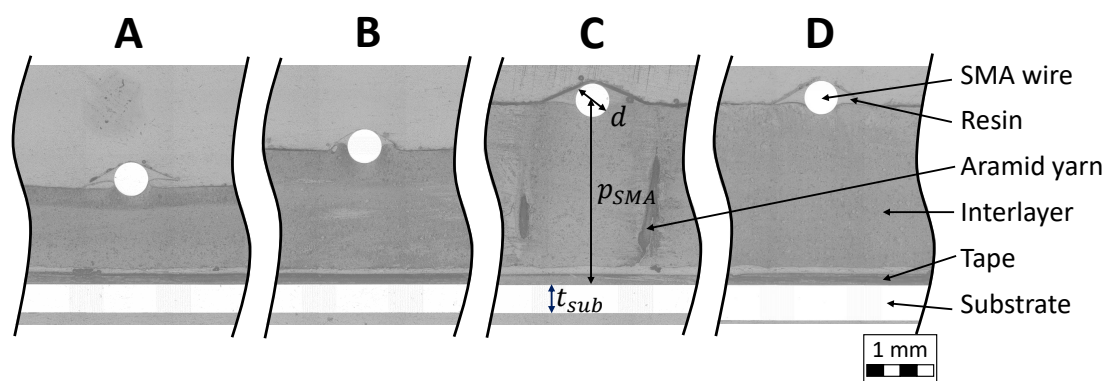


Figure 5.3: Crosssections of the four Actuator variants.

Table 5.1 lists the measured dimensions identical for all the actuator types and table 5.2 lists the measured dimensions that differed between actuator types. The respective measurement method is described in detail in section 7.1.

| | Mean in mm | Conf. interval | n |
|---------------------|------------|----------------|----|
| Active length | 38.65 | 0.09 | 13 |
| SMA wire length | 42.61 | 0.12 | 13 |
| Width | 50.32 | 0.045 | 13 |
| Rigid length | 22.66 | 0.07 | 9 |
| Pointer length | 68.70 | 0.151 | 9 |
| Defl. measurement 1 | 53.47 | 0.17 | 9 |
| Defl. measurement 2 | 34.83 | 0.05 | 4 |
| SMA wire distance | 5 | - | - |
| Max. lever arm | 45.59 | 0.11 | 9 |
| SMA wire diameter | 0.480 | 0.003 | 16 |

Table 5.1: Geometric parameters which are identical for all types of specimens. Labels refer to figure 5.2

In order to conduct various experiments, additional preparation steps were performed on the SMAHC actuators. The surface of the actuator was painted with black ink to facilitate temperature measurement using thermal imaging. The emission coefficient in the investigated temperature range was known and constant. Additionally, a stochastic pattern was applied to the surface of the actuator using white paint. The so-generated gray-scale map enabled digital image correlation (DIC). The painting process was carried out

| | | A | B | C | D |
|--|----------------|-------|-------|-------|-------|
| Substrate to SMA wire distance p_{SMA} | Mean in mm | 1.517 | 2.050 | 2.677 | 2.625 |
| | Conf. interval | 0.031 | 0.103 | 0.048 | 0.201 |
| | n | 4 | 4 | 4 | 4 |
| Substrate thickness t_{sub} | Mean in mm | 0.400 | 0.394 | 0.393 | 0.495 |
| | Conf. interval | 0.013 | 0.015 | 0.017 | 0.011 |
| | n | 4 | 4 | 4 | 4 |

Table 5.2: Geometric parameters that vary with specimen type. Labels refer to figure 5.3

according to the method described in [125]. The depth of field of the camera configuration allowed high-resolution imaging only in the plane of the outermost wire. To enable DIC measurement on this wire directly on its surface and not on the surface of the resin layer surrounding it, the resin layer was removed before the paint layers were applied. Close-up images of the outermost SMA wire with a stochastic speckle pattern on the wire's surface (the resin layer was removed) and an example of another SMA wire in the grid with a speckle pattern on the surface of the resin layer can be viewed in figure 5.4. The DIC measurement directly on the wire surface provides more accurate results concerning the deformation of the wire. Certain actuators were also equipped with two thermocouples placed between the substrate and the spacer layer, as shown in figure 5.4. The location of the thermocouples in the xy-plane is indicated. The thermocouple designated as T1 was located under the middle SMA wires, and T2 was under an outer SMA wire.

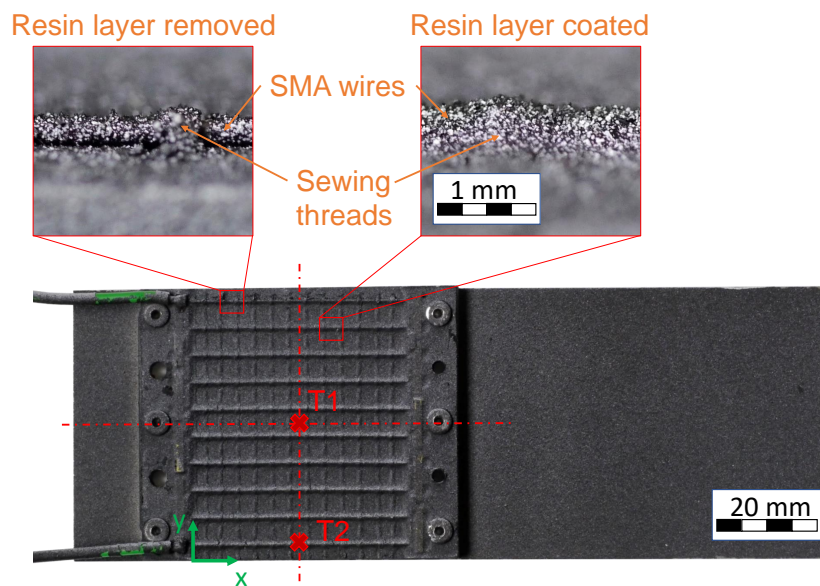


Figure 5.4: Thermocouple positions in xy-plane and close-up of outermost wire with resin layer removed for DIC measurement of wire displacement and strain.

Coordinate system

The origin of the Cartesian coordinate system (refer to figure 5.1) is located at the neutral fiber of the substrate's outer edge at the junction between the anchor clip and the interlayer, which denotes the beginning of the active region. The x-axis runs parallel to the substrate when the actuator is in the initial state. The orthogonal y-axis points in the width direction, and the orthogonal z-axis in the thickness direction of the actuator. Additionally, a coordinate s is introduced, which runs along the neutral fiber of the substrate with the same origin as the Cartesian coordinate system. The t -axis is orthogonal to the s -axis and points in the direction of the SMA wire layer. This coordinate system is valid throughout the study unless otherwise specified.

5.2. Test method

A test bench was developed to characterize the SMAHC actuators, allowing for control of the actuator and simultaneous recording of various measured quantities.

5.2.1. Testbench

The experimental setup is given as scheme in figure 5.5 A. Additionally a close up picture of a specimen with a connected weight is shown in figure 5.5 B. A picture of the whole test bench setup is given in the appendix A.4. For each experiment the respective actuator was positioned on a sample holder and fixed using screw connections. The screws were inserted directly through two holes in the clip at the constrained end. The constrained end is depicted in figure 5.1. An additional weight could be mounted on the free side of the clip using holes in the respective clip and screw connections. The position of the holes can be seen in figure 5.2. A lifting table enabled the weight's continuous upward and downward movement, thereby loading and unloading the SMAHC. A linear motor with a small step width of type *X-NMS17C* from *Zaber* was used to move the lifting table. Two laser triangulation sensors from *Panasonic* of type *HG-C1200-P* with a repeatability of $200\ \mu\text{m}$, arranged in a row along the x-axis, were used to measure the deflection at two locations on the specimen pointer. The positions of the deflection measurement points on the specimen in the initial state with respect to the x-axis are marked in figure 5.2. Deflection measurement position 1 is close to the anchor clip at the free end of the specimen. Deflection measurement position 2, in relation to the x-axis, is located almost in the middle of the pointer. The temperature of the SMA wire was measured using an infrared-sensitive camera from *Micro-Epsilon* of type *640 VGA* and a microscope optic, resulting in a local resolution of $29\ \mu\text{m}$. The camera's depth of field only allowed for

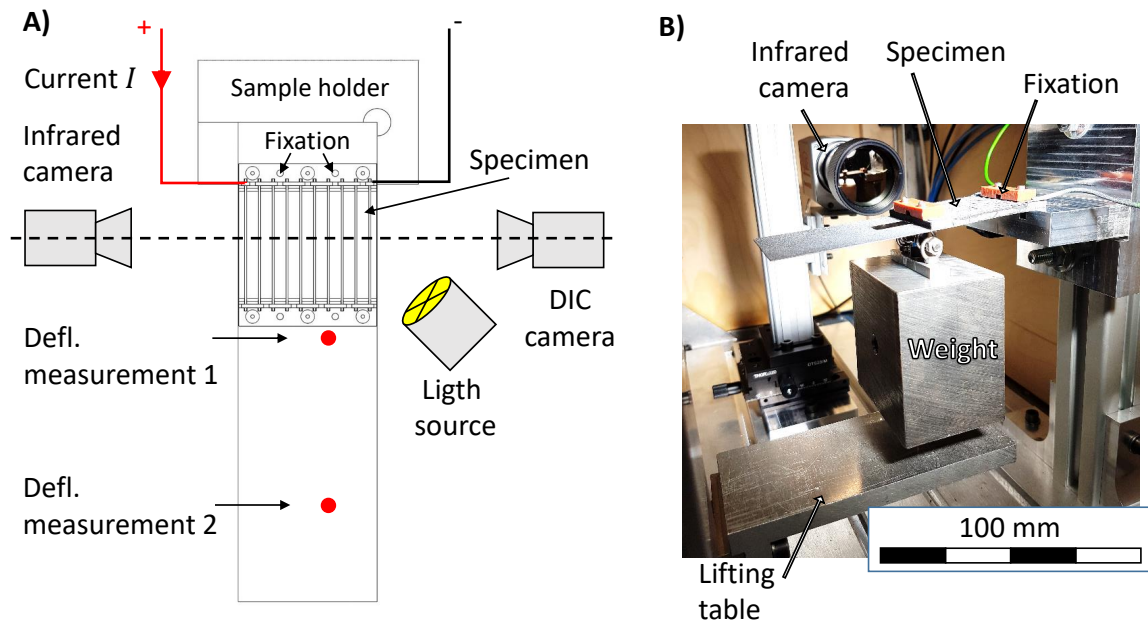


Figure 5.5: A: Test setup for experiments at RT given as scheme; B: Actuator positioning is shown in detail.

the temperature of the outermost SMA wire in the grid to be determined. Along the x-axis, about 21 mm of the middle section of the active area could be captured. Only the maximum temperature detected in the entire measuring range was evaluated. During heating, the hottest area is at the SMA wire. During cooling, this can change, and the hottest area is at the interlayer, as it has a greater capacity to store the temperature. The emission coefficient was not set, and the temperature was evaluated as measured. As mentioned in section 5.1, the samples were painted to guarantee a high and constant emission coefficient of about 0.955 in the investigated temperature range, which improved the accuracy of the temperature measurement. The thermal radiation is not emitted by the SMA wire itself but by the paint. As can be seen in figure 5.3, between the paint coat and SMA wire surface, there is a resin layer. Accordingly, the measured temperature corresponds to that. The monochrome camera from *Optronics* of type *CP 90-25P-M/C-72* was utilized to acquire high-resolution images of the speckled actuator surface. The camera lens consisted of components from *Schneider's UNIFOC* series, including a helical mount, a 75 mm distance element, and a macro lens. The camera sensor has dimensions of $23.03 \times 23.03 \text{ mm}^2$ and a resolution of 5120×5120 pixels, which were suitable for DIC analysis. In order to enable local measurement of displacement and strain of the SMA wire using this technique, the resin layer on the outermost SMA wire was removed. Adequate and constant illumination was provided by the photo light source *EFII 60 LED* from *Jinbei*. At the same time, the Fresnel lens *NG-10x* from *NanGuang* was employed to adjust the required focus of the light beam. However, it is essential to note that the surface temperature of the SMAHC specimen may increase up to $4 \text{ }^\circ\text{C}$ due to the

influence of the light source. The actuator was supplied with a controlled current flux using the programmable power supply *HMP4030* from *HAMEG* Instruments, allowing for precise current variations in steps of 0.001 A. The data acquisition (DAQ) system *T7 Pro* from *Labjack* was employed to measure the voltage drop across the SMA grid and temperature measurements using type K thermocouples with a diameter of 0.25 mm. Input signals at the *T7* had a resolution of at least 16 bits. Additionally, a *TIM 450* thermal camera from *Micro-Epsilon* with microscope optics was employed for a series of experiments to investigate thermal boundary conditions. This camera has a larger field of view but a poorer resolution, enabling the entire actuator to be captured. The resulting measurement field is illustrated in figure 5.6. The test setup was placed in

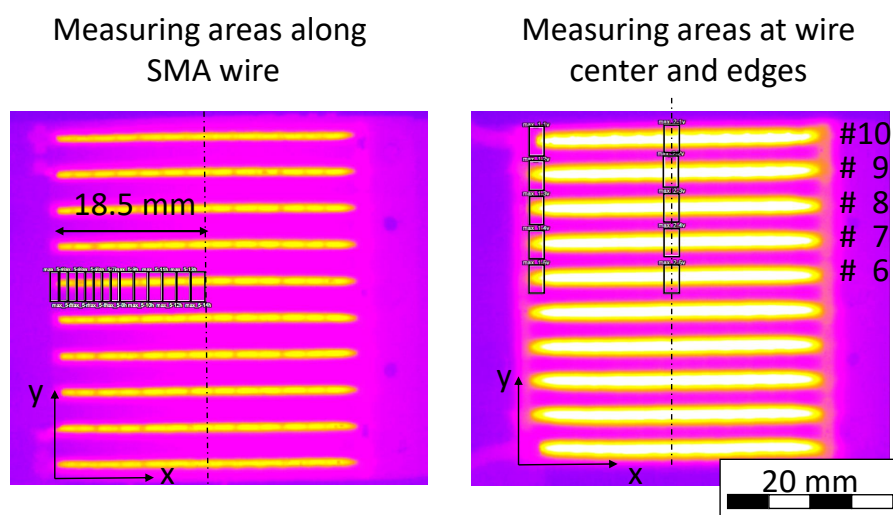


Figure 5.6: The temperature measurement areas and the sections for evaluating the boundary effect.

an oven, refrigerator, and freezer to adjust the ambient temperature. However, since these were not climate-controlled chambers, the humidity could not be regulated and was recorded instead. Figure 5.7 illustrates the test setup in the different test chambers and the corresponding average temperature and humidity. DIC measurements were not conducted in any of the chambers, and thermal imaging was only conducted in the refrigerator and oven.

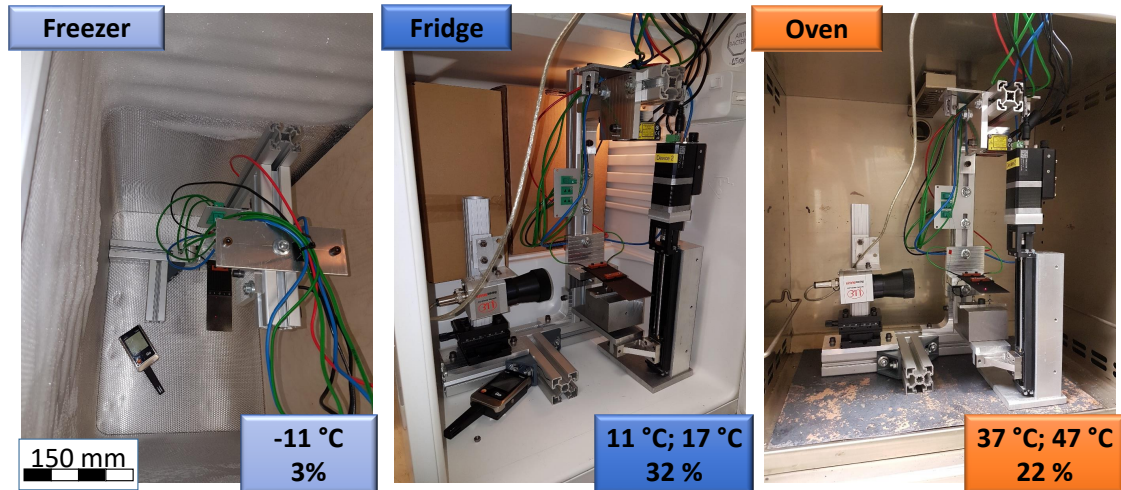


Figure 5.7: Test setup in different chambers to variate ambient conditions. Average test temperature and humidity are given for each environment.

5.2.2. Design of experiment

The goal of the experimental investigation was to study the effect of external load and ambient temperature on the shape adaptation behavior of the SMAHC. Thus, a 2-dimensional parameter space was created, spanning the temperature and external load ranges relevant to the actuator's intended applications, as shown in figure 5.8.

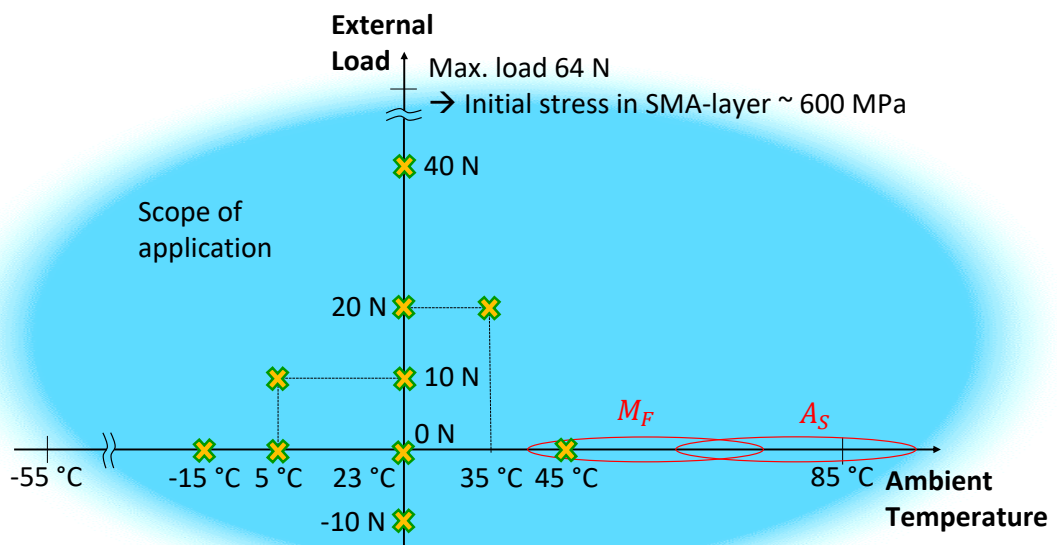


Figure 5.8: Design of experiment including crosses, marking the conditions of the experiments and actuator type with which the tests were performed.

The temperature range covered by the experiment spanned from $-15\text{ }^{\circ}\text{C}$ to $45\text{ }^{\circ}\text{C}$, focusing on temperatures less than or equal to the martensite finish temperature to utilize the full potential of the SMA. The range of external loads was determined by considering the functional fatigue and structural failure properties of the SMAHC, with the lower limit set at -10 N and the upper limit at 40 N to avoid exceeding the maximum permissible SMA wire tension of 400 MPa to ensure cyclic stability [126]. A Design of Experiment (DOE) was used to cover the parameter space with various test conditions. Crosses showing the conditions of the experiments and actuator type with which the tests were performed. All experiments were repeated with three individual specimens to ensure statistical validity.

5.2.3. Test process

A standardized protocol for testing was established for all experiments. This protocol, shown in figure 5.9, consisted of two phases: an activation phase, in which a controlled direct current flux of at least 0.5 A was applied to initiate the shape-memory effect, and a deactivation phase, in which the actuator cooled down.

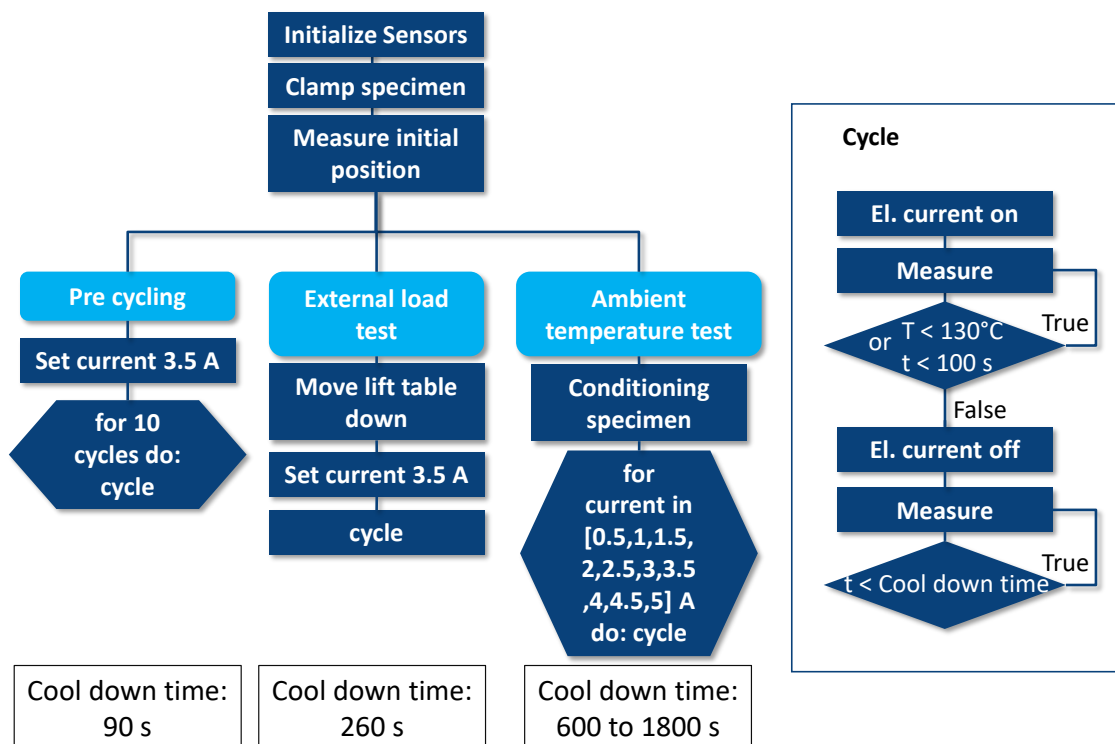


Figure 5.9: Standardized protocol for testing

During the activation phase, measurements were taken from all connected sensors. To prevent overheating of the SMA wires, the current flux was turned off if the infrared camera detected a temperature of $130\text{ }^{\circ}\text{C}$ or a time limit of 100 s was exceeded. This time limit

was set to ensure that the measurement time for each cycle was kept within a reasonable range, even if steady-state conditions were not fully met. After the current flux was turned off, data logging was continued until a specified cool-down time was reached. This time was chosen such that the temperature measured at the end of the cool-down phase was a maximum of 2 °C above the ambient temperature. A current of 0.2 A was supplied to measure the electrical resistance of the SMA wires during the cool-down phase. A current flux of this magnitude was found to have no significant effect on the temperature of the SMA wires, according to previous research [127].

Before each experiment, the sensors were initialized according to their specifications. The infrared camera was allowed a one-hour initialization period before data collection began. The SMAHC specimen was then securely mounted on the designated sample holder, and the initial position was recorded using two laser triangulation sensors. The tests were divided into pre-cycling, external load, and ambient temperature. A flow chart for the respective experiments can be seen in figure 5.9. Before any other experiment, every specimen underwent a series of pre-cycling tests to investigate possible run-in effects. This investigation was accomplished by performing ten standard cycles using a constant electrical current of 3.5 A and a cool-down time of 90 seconds. The external load tests were designed to examine the influence of different loading conditions on the shape adaptation behavior of the SMAHC. For this kind of experiment, a specific weight was applied to the actuator, and its response was monitored during loading and activation (Compare figure 5.10).

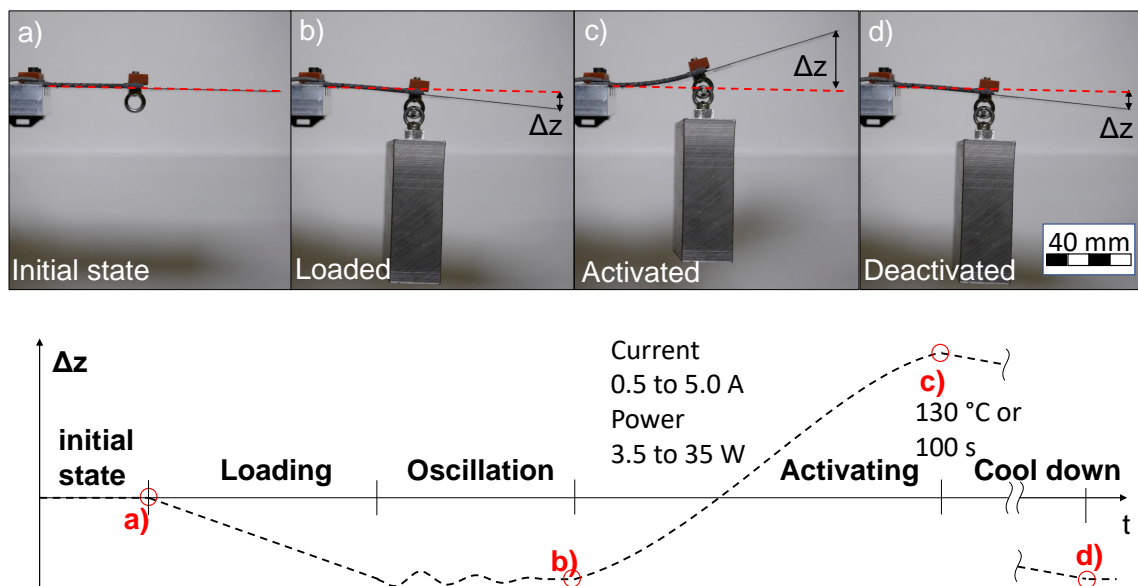


Figure 5.10: Illustration of load test cycle.

The loaded state of the actuator was reached by moving the lifting table down at a low speed, with slight oscillations being observed initially. Ten seconds after loading, the actuator stabilized, and a standard cycle was initiated with a current of 3.5 A. The standard cycle consisted of an activation phase, followed by a cool-down phase, during which the temperature of the actuator was monitored and recorded. Finally, the ambient temperature tests were conducted to investigate the effect of different ambient temperatures on the SMAHC's shape adaptation behavior. The specimens were first conditioned to the specific ambient temperature before performing a sequence of 10 standard cycles with varying electrical currents, starting from 0.5 A and ending at 5.0 A with a step size of 0.5 A. The cool-down time, in this case, was adjusted based on the ambient temperature.

5.3. Evaluation methodology

During the measurement the following data was recorded:

- **time in datetime**
- The maximum **Temperature in °C** measured at the outermost SMA wire of the SMAHC
- The distance P_f of the pointer related to the distance sensor at the deflection measurement position 2 **Position front in mm** (compare figure 5.11)
- The distance P_b of the pointer related to the distance sensor at the deflection measurement position 1 referred to as **Position back in mm** (compare figure 5.11)
- The **Voltage U in V** drop over the SMA wire grid
- The **Current I in A** through the SMA grid (compare figure 5.5).
- The temperature **T1** in °C measured with the thermocouple at central position (compare figure 5.4).
- The temperature **T2** in °C measured with the thermocouple below outermost SMA wire (compare figure 5.4).

From these data additional data was derived, according to the following schemes:

- The **Time t in s** since the respective cycle started.
- The **Resistance R in Ω** calculated as $R = U/I$

- The **Distance D0 in mm** between pointer and respective distance sensor at the beginning of the experiment. (compare figure 5.11)
- The **Deflection D in mm** of the pointer at respective distance sensor position along x-axis by subtracting the distance at the beginning of the experiment from the respective distance line by line according to $D = P - D_0$. (compare figure 5.11)
- The deflection of the substrate at the end of the active region referred to as **Active deflection in mm**, of the SMA-grid along the x-axis D_A was determined for unloaded actuator using equations 5.38, 5.39, 5.40. Where solving equation 5.38 allowed for evaluation of the bending radius BR for known active length a_l , deflection measurement position 1 or 2 in x-direction $spx_{1,2}$ and deflection $D_{1,2}$ at regarding position. Equation 5.40 represents the deflection at the end of the active area D_a . Position at the end of the active area along the x-axis changes during deflection and was calculated using equation 5.39.

$$D_{1,2} = \left(-\sqrt{BR_{sub}^2 - (BR_{sub} \cdot \sin(a_l/BR_{sub}))^2} + BR_{sub} \right) - (BR_{sub} \cdot \sin(a_l/BR_{sub})) \cdot \tan(a_l/BR_{sub}) + spx_{1,2} * \tan(a_l/BR_{sub}) \quad (5.38)$$

$$x_{max} = BR_{sub} \cdot \sin(a_l/BR_{sub}) \quad (5.39)$$

$$D_a = -\sqrt{BR_{sub}^2 - x_{max}^2} + BR_{sub} \quad (5.40)$$

The equation was derived in the appendix in section A.3.

- The electrical **Power P in W** supplied to the actuator was calculated according to the relationship $P = U \cdot I$.
- The **Energy E in J** supplied to the actuator was determined by line-by-line summation of the product of power P and timestep Δt corresponding to $\sum_{t=0}^t P \cdot \Delta t$.
- The **Mechanical work W in J** that was performed by the actuator was calculated as product of the displacement measured at deflection measurement position 1 and the applied external load according to $W = D_b \cdot F_{ext}$. In case of no load applied a load of 0.1 N was assumed.
- The **Efficiency η in %** was calculated as ratio between mechanical work performed W and supplied energy E according to $\eta = W/E$.

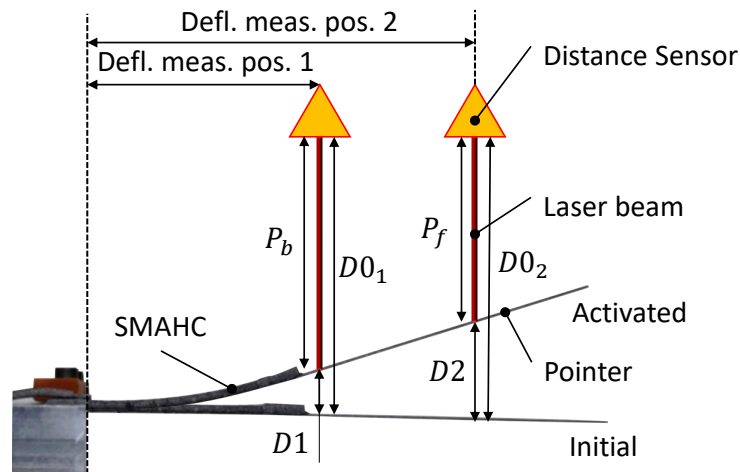


Figure 5.11: Distance measurement via laser triangulation sensors on the SMAHC's pointer.

The DIC analysis of the high-resolution monochrome images was conducted using the *GOM professional* software. Initially, the facet points were evenly distributed along the substrate or SMA wire. Subsequently, minor adjustments to the facet size and position were made to ensure the quality and traceability of the facet points. An example of the positions of the facet points used to determine the displacement of the substrate on an activated actuator is shown in figure 5.12.

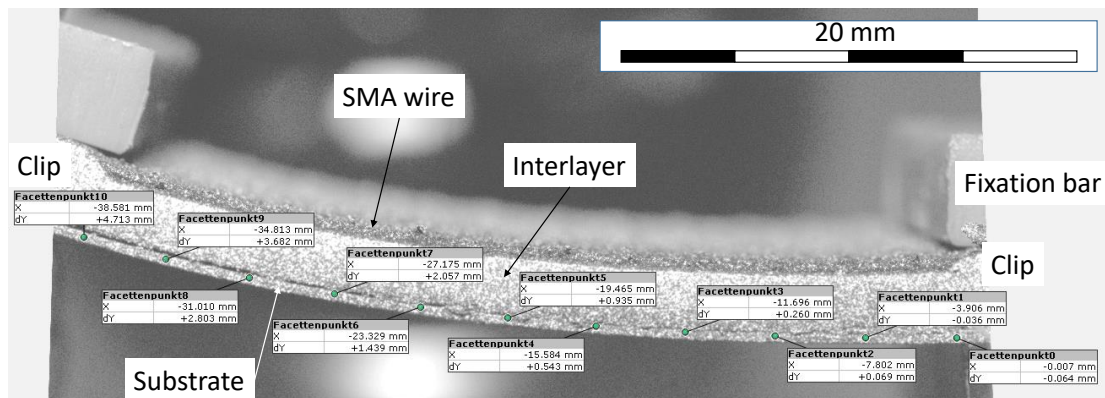


Figure 5.12: Example for facet point positions on activated SMAHC.

5.4. Results and discussion

Tests were carried out according to the design of experiment presented in section 5.2.2. A minimum of three independent measurements were used in each experiment. For statistical evaluation, Student's t-distribution was assumed. To ensure the validity of this assumption, chi-squared goodness-of-fit tests according to [128] were performed (compare figure A.2 and A.3). Additionally, each dataset underwent Nalimov outlier tests. The number of valid experiments, designated by 'n', is displayed in the graph or caption. The mean value is given as a solid line or dot, and the confidence interval of 95% is depicted as transparent surfaces or error bars. Only the mean value is displayed if there are fewer than two valid data sets.

Figure 5.13 depicts typical sensor measurements and the resulting data. During heating, the current flux was adjusted to a given amount. As resistance decreased during the activation phase, the voltage dropped, and the electrical power input had to decrease to sustain the current. Due to the low electrical current supply during cool down, the resistance measurement noise-to-signal ratio was high. Electrical capacity led to erroneous resistance measurements during power supply state change. For analysis, the resulting resistance peaks were stripped out. The power input corresponded to Joule or heat resistance input. The temperature of the SMA wires decreased after powering off. Due to the limited number of thermocouple measurements, evaluation of these showed large confidence intervals. At two positions along the pointer, actuator deflection was measured. Deflection measurement position 1 showed lesser deflections than deflection measuring position 2. Even 10 to 20 °C over the theoretical austenite finish temperature A_F^* , the deflection increased and did not attain equilibrium.

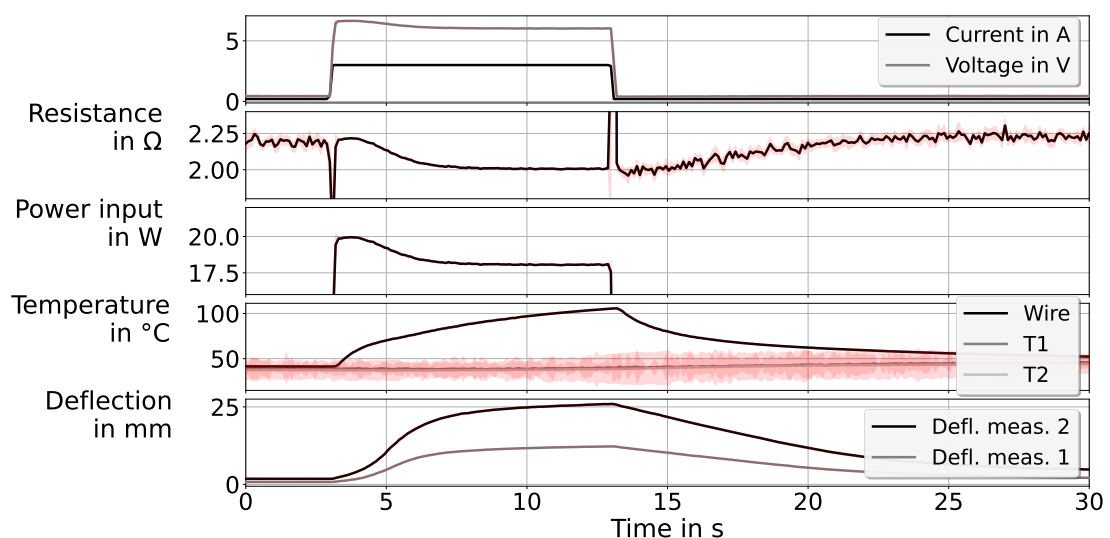


Figure 5.13: Examples of measurements taken by sensors and the data obtained from them.

5.4.1. Pre cycling

Each specimen was subjected to pre-cycle testing to assess the run-in behavior. In figure 5.14, the temperature-deflection hysteresis loops for each cycle are organized by actuator type. The cycle's deflection is reported relative to the initial position at the beginning of the experiment. Thus, the reference position is the initial position at the beginning of the first cycle. Values for deflection were derived from records of deflection measurement position 1.

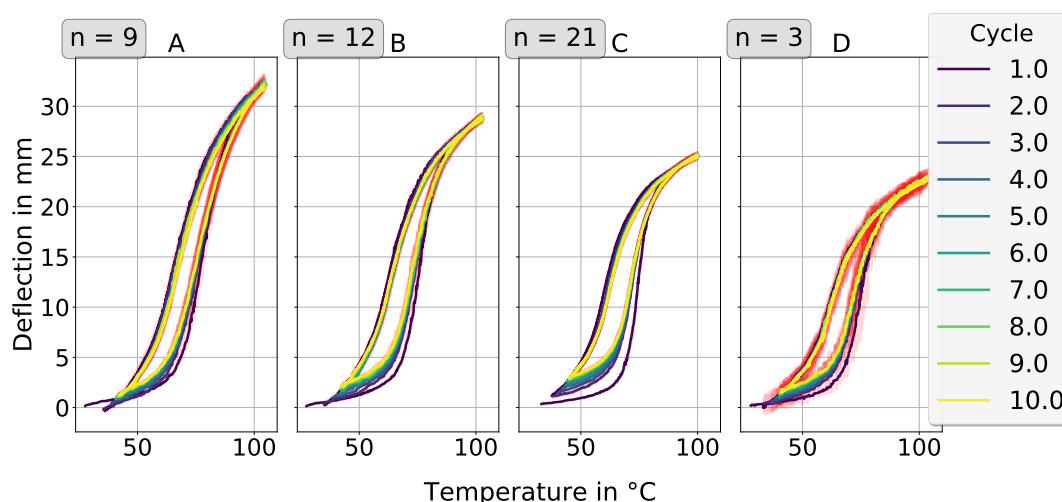


Figure 5.14: Temperature deflection hysteresis loops for pre-cycling, organized according to the kind of actuator.

The temperature deflection hysteresis loops provided numerous findings. Thick interlayers reduced maximum deflection as increased wire-substrate distance caused decreased curvature for the same SMA wire contraction. Thick substrates also reduced maximum deflection because of their enhanced related rigidity. The increased substrate rigidity raised the activation stress on SMA wires, thus reduced their contraction.

When the interlayer thickness decreased, or the substrate was more rigid, mechanical stresses in SMA wires raised, which caused the hysteresis width to grow. The observed behavior of the hysteresis corresponds to the behavior of single binary nickel-rich SMA crystals under the influence of external load [129].

Over several cycles, the deflection of the cold martensitic phase increased while the deflection of the hot austenitic phase remained constant. This behavior resembles that of SMA wires subjected to repeated temperature cycling [130].

The diagram 5.15 effectively shows the deviation of the mapped run-in effects. Each cycle contains data regarding the temperature, minimum and maximum position with

respect to the initial position, and the relative deflection. Each subtype of SMAHC is displayed separately.

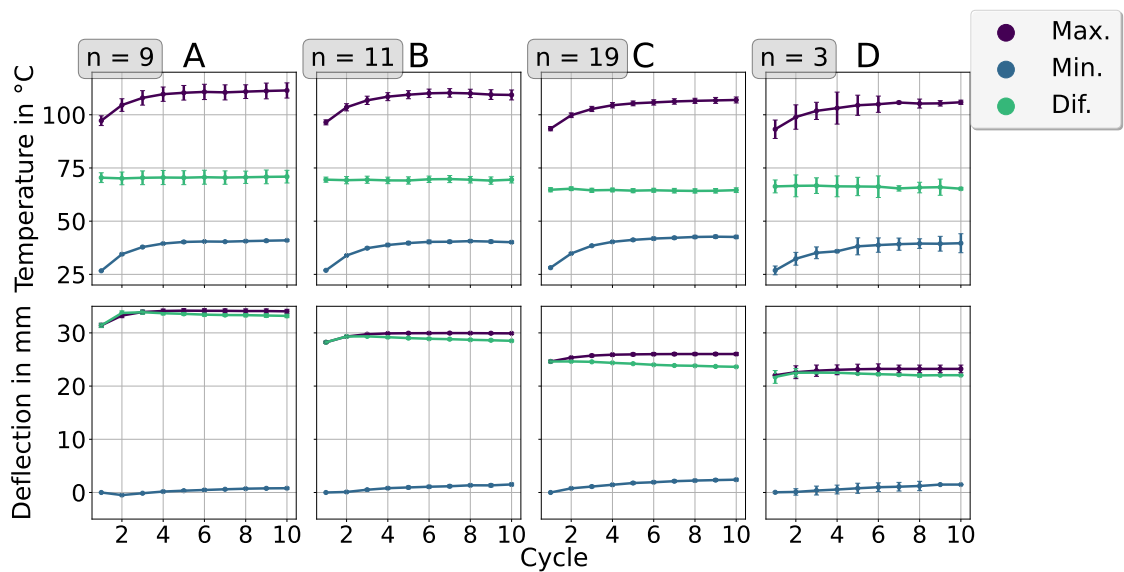


Figure 5.15: Run-in impact evaluation data display maximum and minimum position, relative deflection, and temperature readings for each cycle. Each subtype of SMAHC (defined by parameters given in table 5.2) is represented in a different graph. Plot lines are only a guide to the eye and do not necessarily show any physical relationship.

The cool-down period of 90 s did not allow the SMAHC to cool down to the respective ambient temperature. Temperature levels of all actuator types stabilized after 5 to 6 cycles and did not show significant changes anymore. While deflection in the austenitic state was almost constant for cycles between 5 and 10, the deflection in the martensitic state over cycles showed a gradient. This effect increased with a thicker interlayer and a thinner substrate, which can be explained by the lower related forces that pull back the SMA wires into the martensitic state at temperatures below M_s^* . Deflection changes between cycles 8 and 10 were below 1% independent of the type of actuator. The measured difference in deflections between two cycles was always less than the confidence interval, thus not significant. It was concluded that after the 10 cycles performed, no more relevant run-in effects occurred.

5.4.2. Activation at room temperature (RT)

All investigations in this section were conducted at RT. Figure 5.16 depicts the temperature trends for the various SMAHC subtypes over time.

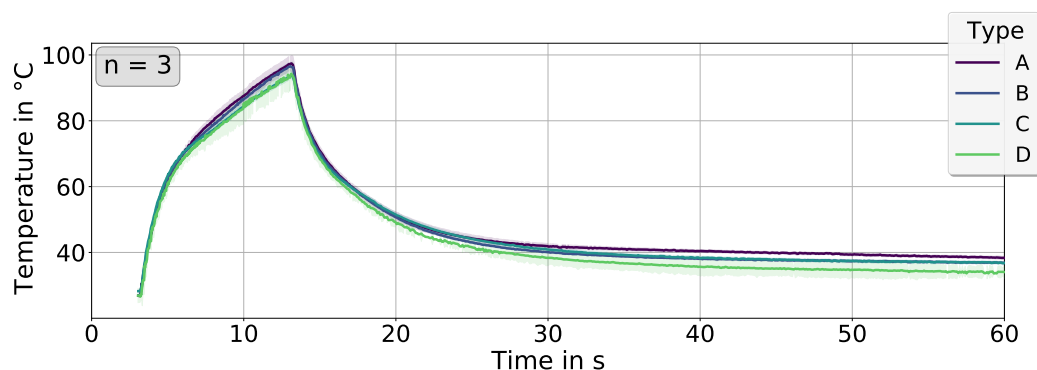


Figure 5.16: The rise and fall in temperature of SMA are shown against time for the various forms of SMAHC. The supplied current amounted to 3.5 A.

No significant changes in temperature gradients could be observed. For the applied current, this indicated that the heating and cooling of the SMA wires were unaffected by interlayer and substrate thickness, at least for the heating rate that resulted from the supplied current of 3.5 A.

At RT, various controlled electrical direct currents were used to initiate activation cycles. Cycles were completed with a 600-second cool-down period. The temperature hysteresis loop for different activation currents of actuator type C is depicted in figure 5.17.

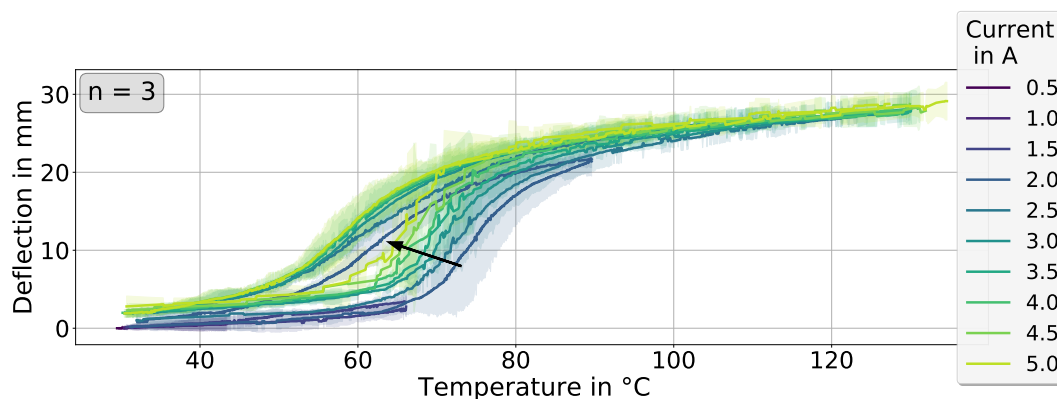


Figure 5.17: Temperature hysteresis loop at RT for various activation currents of actuator type C.

It was observed that for higher currents, constant deflection levels shifted towards lower temperatures. This effect was measured independent of the type of actuator, as depicted in the appendix A.7. Multiple causes account for this phenomenon.

Due to the measurement method, the temperature on the surface of the resin layer encasing the SMA wire was measured, not directly the wire's surface temperature. During heating, there was a temperature gradient between the surface of the SMA wire and the

coat. This gradient increased with rising heating rate.

The observed phenomenon might also be accounted for by the current-dependent temperature distribution along the x -axis of SMA wires. Due to the series connection, each SMA segment in the SMA grid possessed an identical electrical current flux. Heat losses in zones close to the anchoring generated a temperature gradient. Figure 5.18 shows the relevant temperature distribution for various currents. The temperature in the graph was normalized by comparing the measured temperature to the temperature margins of the actuator between RT and maximum temperature. Temperature data was recorded at the moment the power supply was turned off.

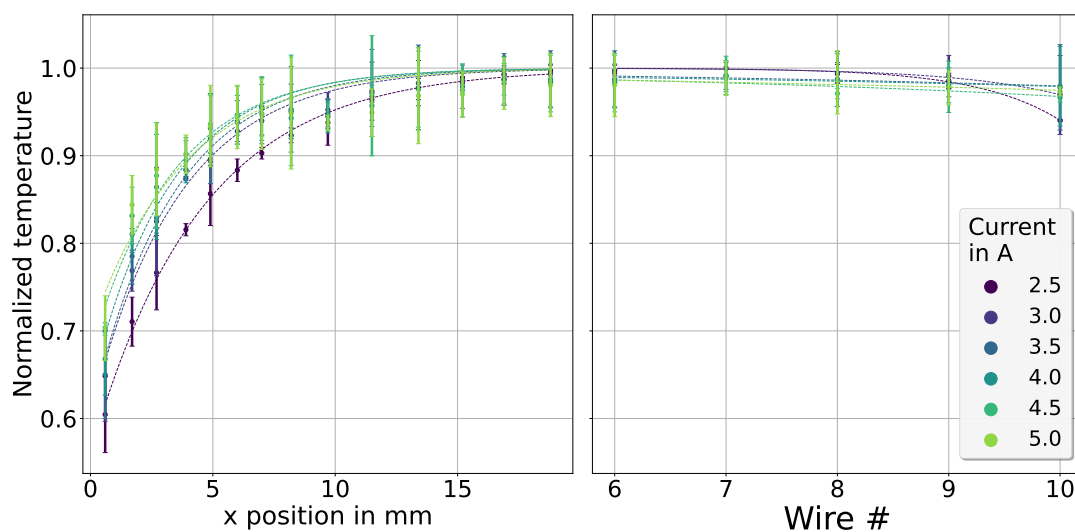


Figure 5.18: Normalized temperature distribution for various currents; left: along SMA wires x -axis from anchor to the center of the SMA wire, right: between SMA wire 6 to outermost SMA wire (compare measurement positions with figure 5.6)

The analysis of the temperature distributions showed that there was a tendency for lower currents to produce more significant temperature disparities. Approximately 10 % of the length of the SMA wire exhibited temperatures that were 10 % lower than the maximum temperature. The zone of the SMA wire close to the anchorage is thus delayed in phase transformation. According to this, the amount of alloy transformed, and thus the deflection at a given measured temperature, depends on the heating rate.

In a further experiment conducted at RT, the effect of the supplied current, and hence the electrical power on the activation time, was investigated. The activation time is defined as the period until a predetermined level of deflection is reached. In figure 5.19, each graph, ordered by actuator type, shows the ordinate as the time required to reach a specified deflection and the abscissa as the supplied current. The correlation between time and current can be approximated by a function that exhibits an asymptotic course along the

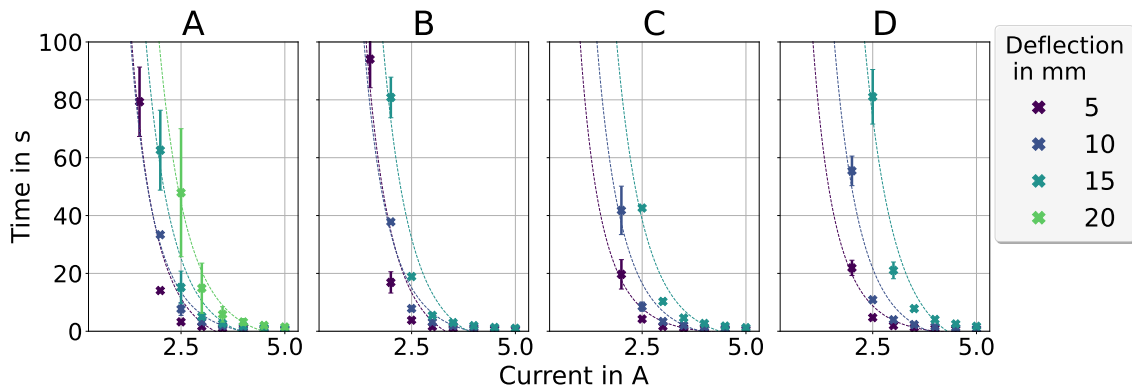


Figure 5.19: Correlation between time and supplied current to reach specific deflection levels sorted by actuator type.

current axis of the form $t = a + b \cdot e^{-x+c}$. The approximation is not due to a physical relationship. However, it was observed that for currents below 2.5 A, not all deflection levels could be achieved. For these low currents, the thermodynamic equilibrium between the electrical power input and power losses did not allow the SMA wires to heat up to temperatures above A_F^* .

In figure 5.20, the efficiency of actuator type C during activation is shown to be correlated with the deflection measured at position 2.

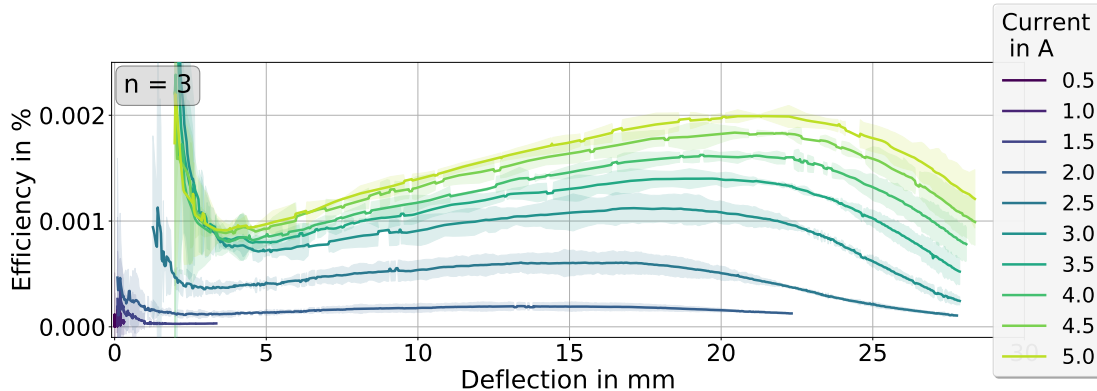


Figure 5.20: Efficiency on ordinate and deflection on abscissa for various supplied electrical currents to the actuator of type C.

The efficiency was calculated using the methodology outlined in Section 5.3. Since the experiment focused on comparing the efficiency under different current levels, no load was applied. Thus the efficiency values shown in this figure are low, as only the load of the pointer was lifted. All deflections are given concerning the initial position of the experiment's first cycle, carried out with a direct current of 0.5 A. As the deflection, after cooling, shifted to higher levels during the following cycles, it appeared like efficiency at the beginning of activation was infinite as no power was consumed, but the actuator

was already deflected. Therefore, the actuators' efficiency assessment was only done for deflection levels beyond 5 mm. In this case, the curves show a characteristic shape of increasing efficiency until reaching a peak and then decreasing. This shape mainly results from the SMA's behavior, as a transformation peak exists, where the ratio of mechanical energy output to energy input shows a maximum. The position of this peak shifts with the influence of the supplied current. It was observed that there was a strong correlation between efficiency and the current supply level. Specifically, it was found that efficiency could be doubled when using a supplied current of 5 A instead of 3 A. This high potential for efficiency increase in SMA wire actuators through fast activation has already been investigated in previous studies, such as by [70]. The increase in efficiency can be attributed to a decrease in heat losses. For given SMAHC, these losses depend primarily on the temperature difference between the SMA and the environment as well as the duration of this temperature difference. With increased supply current, the time required to reach the austenite finish temperature A_f decreased, resulting in a reduction in heat losses.

A shift of the efficiency peak to higher deflections with increasing supply currents was observed. The measurement curves show that the drop in efficiency after the efficiency peak was more distinct than the rise in efficiency before. Therefore, when designing actuators focusing on efficiency, the actuators' deflection at peak efficiency should not be exceeded. In figure 5.21, the efficiencies for the four types of actuators without the influence of an external load were compared.

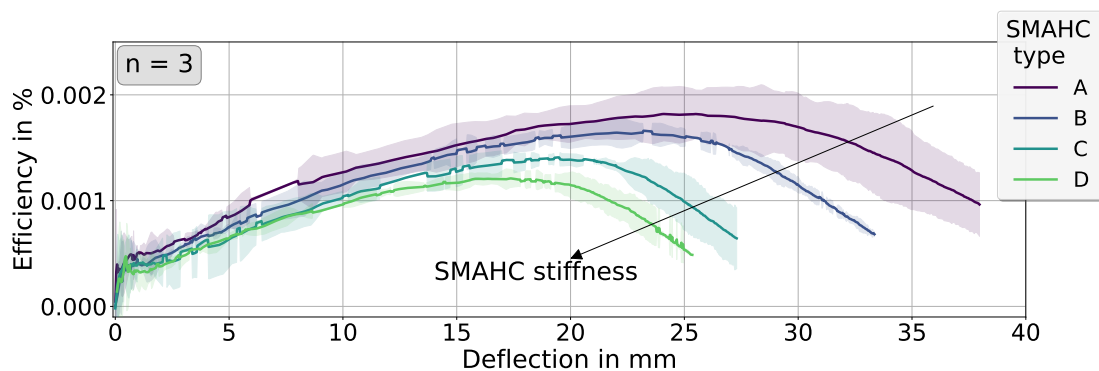


Figure 5.21: Comparison of correlation between deflection and efficiency during activation for different actuator types.

Smaller interlayer thickness increased efficiency since the deflection for the same SMA wire contraction was raised. For thicker substrates, the efficiency was reduced since the increased stiffness resulted in a decrease in deflection and an increase in stress, leading to an increase in the austenite finish temperature A_f .

5.4.3. Activation under influence of external loads

At RT, activation cycles were performed with and without external loads. The deflection is reported relative to the actuator's initial position without an external load applied. Arrows in the graph indicate deflection under loading conditions prior to activation. Initially, the temperature deflection hysteresis loops with and without external load for the four types of actuators were analyzed (compare figure 5.22).

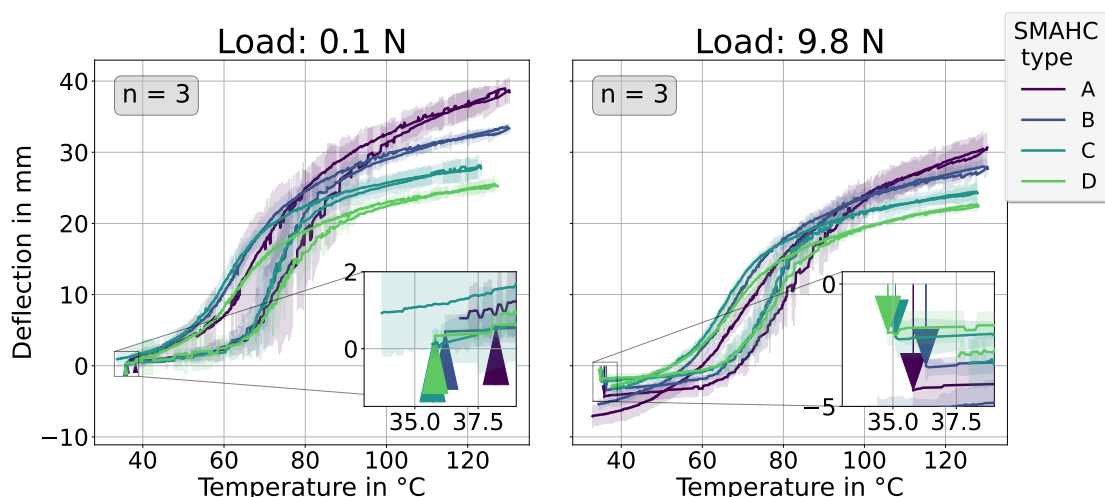


Figure 5.22: Hysteresis loop for temperature deflection curve without and with an external load applied.

In the absence of an external load, the actuator did not deflect at the beginning of the cycle. The experiment revealed considerable differences of the different SMAHC types in the deflection attained at 120 °C. Even though this temperature is above the stress-affected austenite finish temperature A_F^* , an increase in deflection could still be recorded for all types of actuators and both loads. The temperature distribution depicted in image 5.18 provides a possible explanation for this phenomenon. As can be seen, in the SMA wires regions close to anchorage, the transition occurred delayed due to higher heat losses. Only the maximum temperature along the SMA wire's x-axis was used to analyze the activation under load. It thus appears from the diagram that the austenite finish temperature A_F had been exceeded, and the deflection continued to rise. For loaded and unloaded SMAHCs, temperature-dependent hysteresis loops revealed significant changes in deflection. The magnitude of deflection under initial loading was defined by the SMAHC's stiffness and the applied external load. With lower actuator stiffness, the load had a more significant influence on the deflection in the activated state. As a result, due to the applied load, differences in deflection between actuator types in the activated state were reduced.

Relationships between the external load and the deflection in the different states are depicted in figure 5.23. The deflection for the respective SMAHC type is given for the three states loaded, activated at 120 °C, and deactivated (compare figure 5.10). Additionally, for all three states, the deflection is given for loaded and unloaded conditions.

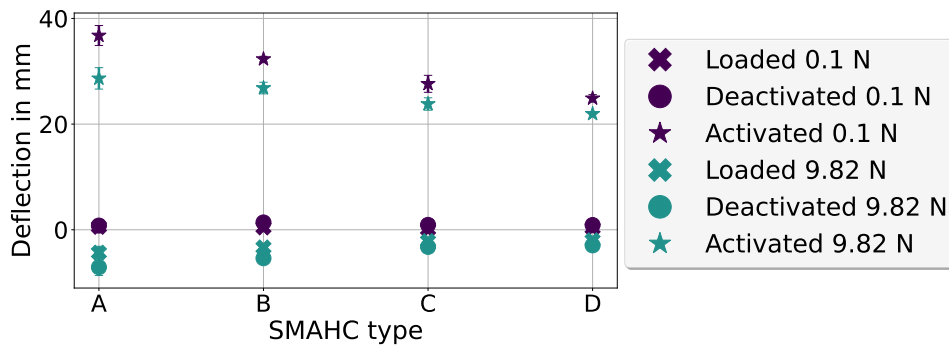


Figure 5.23: Deflection of the four different types of actuators under three states, each with two loading conditions. States are defined as: **Loaded**: initial application of external load; **Activated**: activation of SMAHC by heating SMA wires to at least 120°C; **Deactivated**: cooling back down to RT.

It was observed that with lower actuator stiffness, deflection in the activated state reduced with applied load. In the case of applied external load, all actuators demonstrated a substantial negative deflection after they were cooled back down to RT. This effect was also more pronounced with lower actuator stiffness. In a separate experiment, the effect of varying external loads on the performance was examined as an example for the actuator of type C. Figure 5.24 depicts the temperature-deflection hysteresis loops of five different external loads.

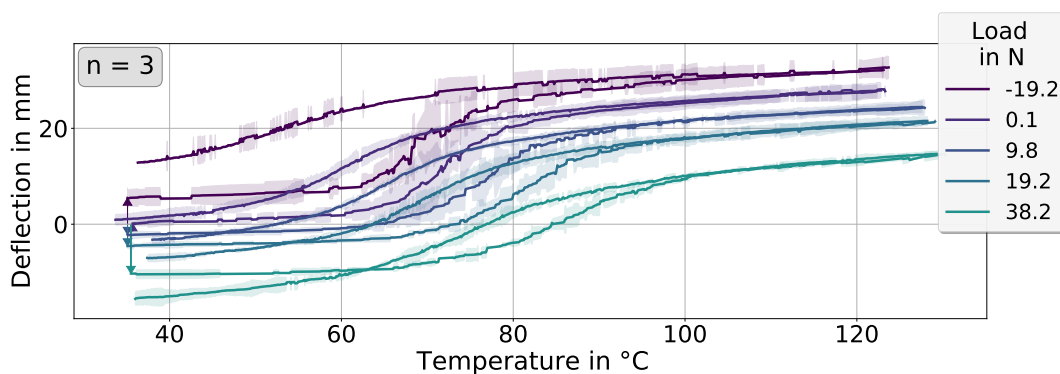


Figure 5.24: Temperature deflection hysteresis loops for the type C actuator under five different external loads. During activation, 3.5 A of current was supplied.

It was found that hysteresis widths were shrinking with increasing load. The same applied to deflection levels concerning the initial state, which also shrank with greater loads. The deflection of the loaded actuator before and after activation varied. As this phenomenon suggested that plastic deformation of the SMAHC occurred during activation, it is further referred to as pseudoplastic deformation. For negative loads, the deflection increased after deactivation, whereas for positive loads, the deflection decreased. For further investigation, an experiment was conducted with subsequent unloaded activation after loaded activation. The results, showing the deflection over the load in the respective state, are given in figure 5.25.

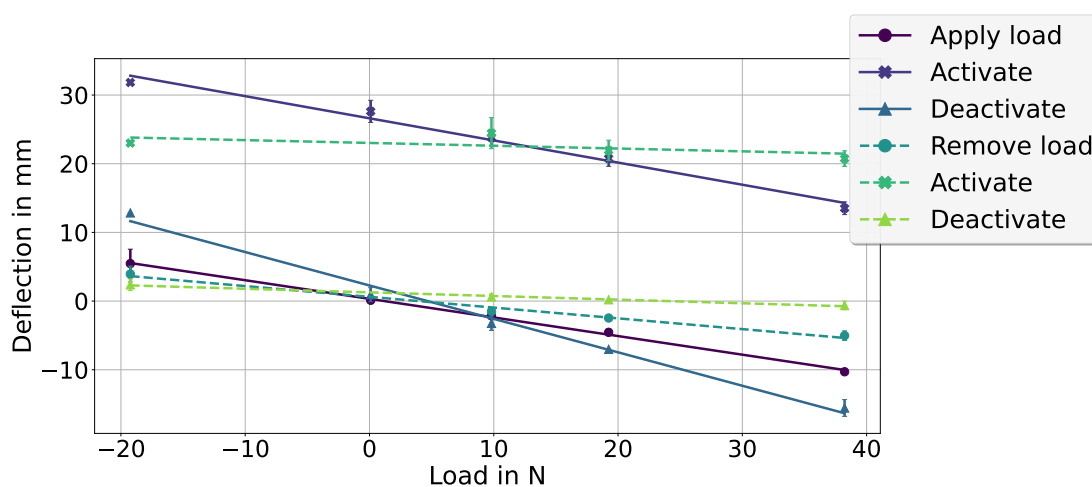


Figure 5.25: Deflection for six different actuator states (apply external **load**, **activate** SMAHC by heating SMA wires to at least 120°C, **deactivate** by cooling back down to RT, **remove** external load, **activate** and **deactivate** again without external load) under the influence of external loads, measured for SMAHC type C. Deflection measured at position 2.

A linear function was found to accurately approximate the correlation between load and deflection for the investigated states, although this does not allow for a statement about a physical connection. During the first step of the experiment, the load was applied. Due to the applied external loads, the actuators deflected in the positive direction for positive loads and in the negative direction for negative loads. When positive loads were applied, the SMA wires were loaded in tension. For negative loads, they were loaded in compression. The pieces of SMA wires used for the grid assembly had a high ratio between cross-section and length. Therefore buckling was expected, when subjected to compression loads. However, the results indicate that the SMA wires could absorb compressive forces, which suggests that buckling was either disabled or at least limited. The linear approximation of the deflection under initial loading conditions and in the loaded activated state showed almost the same slope. Thus, relative displacement along the z-axis at the

measuring point remained constant, regardless of the load.

Subsequent deactivation, still under the influence of external load, showed that the actuators' deflection was enhanced compared to the initial position with the load applied. After removing the load, the actuators did not return to their initial position. Plastic deformation was observed regardless of the load. The subsequent unloaded activation cycle revealed a pseudoplastic behavior of the SMAHC as the negative deflection after cool-down shrank. It can be concluded that SMAHC can partially "recover" its shape. This behavior can be related to the SMA wires. Due to the increased load, more units transformed to stress-induced detwinned martensite during cool-down.

Figure 5.26 depicts the evaluation of efficiency concerning deflection measured at position 2 for the four actuator types with an applied load of 9.8 N.

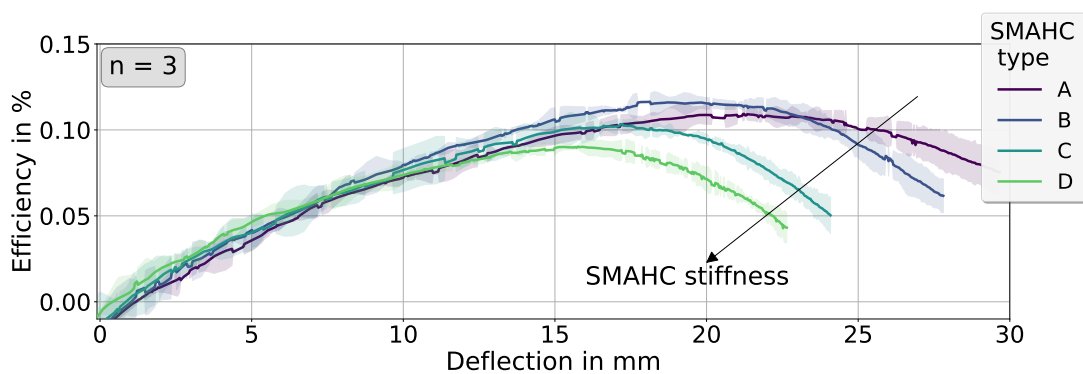


Figure 5.26: Comparison of correlation between deflection and efficiency during activation for different actuator types under the influence of external load of approximately 9.8 N.

The actuator of type B showed the highest efficiency when subjected to an external force of 9.8 N. Comparing these findings to those provided in figure 5.21, in which no external loads were applied and actuator type A exhibited the highest efficiency, the effect of interlayer thickness on efficiency becomes evident.

The found correlation comes from the mechanical tensions within the SMA wires. Thinner interlayers in SMA resulted in increased stresses for a constant external load. Due to the increased stresses, the transition temperatures rose, and the elastic strain of single phases increased. The combination of these factors made the actuator of type B for the given conditions superior to all other investigated types. Consequently, for each condition, there exists the most efficient configuration.

On the other hand, figure 5.27 shows that there is an external load for every type of actuator with which the highest possible efficiency can be achieved.

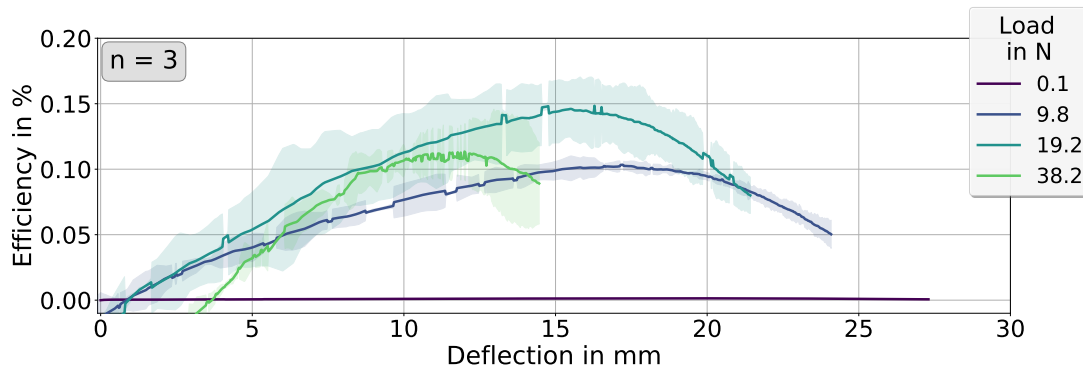


Figure 5.27: Actuators' efficiency during activation is given in dependency on their deflection and for various external loads. SMAHC used was of type C. Electrical current during activation was 3.5 A.

The results of the DIC analysis are discussed in the following. Figure 5.28 and 5.29 show the bend lines of the actuators measured on the substrate. The solid lines represent the bend lines of the various actuators in the initial state with the load applied, while the dashed lines represent the bend lines in the activated state at a temperature of 120°C. For evaluation 10, along the x-axis, equally spaced facet points were used. Between those positions, lines were interpolated linearly. In figure 5.28, the actuators are varied while the load level is constant at 9.8 N, while in figure 5.29, the load is varied for the actuator of type C.

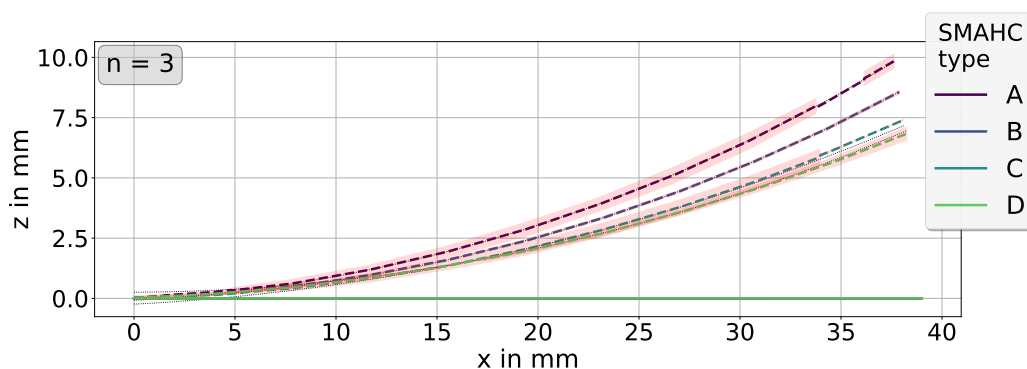


Figure 5.28: Bend line under the influence of external load of 9.8 N for various actuator types.

As the bending moment is constant along the neutral axis of the substrate, the bend lines for the unloaded actuator might be approximatively characterized by a circular arc (dotted lines). Significant variances between experimental and approximated bend lines were found in the regions close to the anchorage. A possible explanation for the deviation can be given by the temperature distribution as transformation in regions close to the

anchorage was delayed.

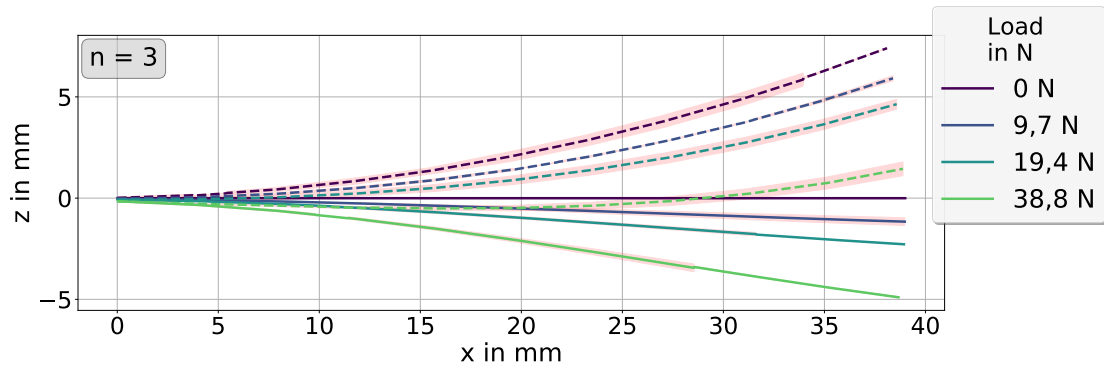


Figure 5.29: Bend line of actuator type C under influence of various loads.

Due to the external load, the bending moment was no longer constant along the x-axis. Therefore, the bend line could not be described by a circular arc.

The strain distribution in the SMA wire along its major axis was investigated by evaluation of the change in distance between two facet points. A facet point density study was conducted to ensure that the amount of facet points used for analysis has no significant effect on the measured strain distribution. The related graphs can be found in the appendix A.5. Figure 5.30 shows the strain distribution under load (compare figure 5.10 state b) and figure 5.31 under load in the activated state (compare figure 5.10 state c).

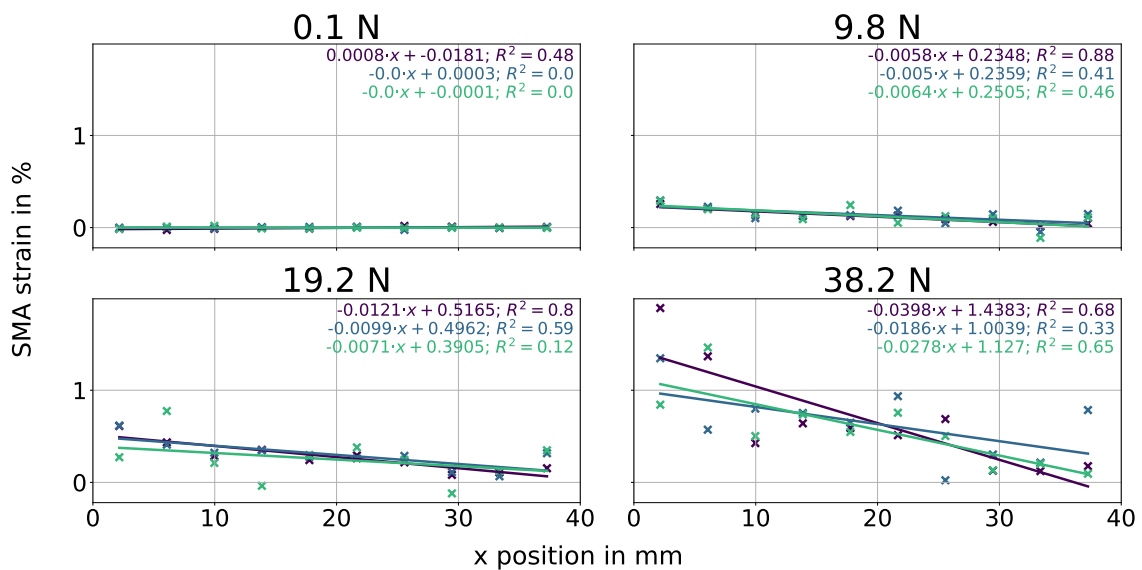


Figure 5.30: Strain distribution along the SMA wire's major axis under the influence of various loads in the initially loaded state. Each measurement was repeated three times. The strain distribution was linearly approximated for each experiment.

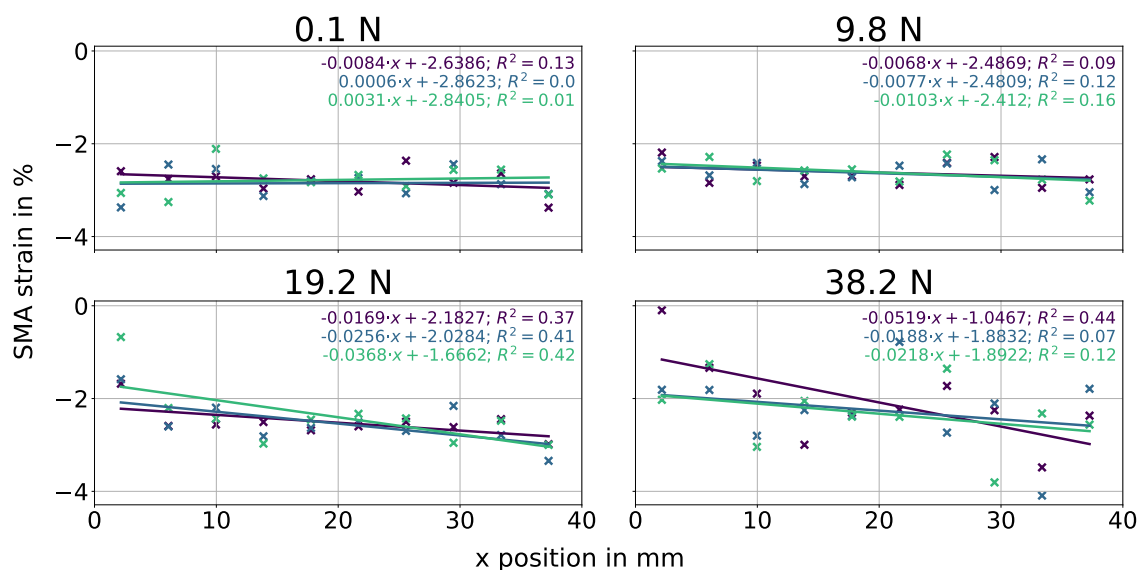


Figure 5.31: Strain distribution along the SMA wire's major axis under the influence of various loads in the activated state. Each measurement was repeated three times. The strain distribution was linearly approximated for each experiment.

In order to ensure the correct interpretation of the results, some additional information about the transformation process is given here. The transformation of individual crystals is a fast process, so from an engineering point of view, the entire crystal transforms simultaneously [131]. Additionally, the crystal undergoes an elastic transformation due to the external load. The measured strain values plotted here represent an average of all crystals in the evaluated range. In the absence of external load, the strain along the SMA wire was close to 0, and no strain distribution was observable. This load-free arrangement was used to approximate the systematic inaccuracy of the measuring method. At the constrained end of the actuator, the average strain level increased significantly as the load increased, whereas the strain level remained nearly constant at the free-end. A similar trend in strain distribution was also observed for the active state under external force. This strain distribution indicated, contrary to expectations, that shear stresses were transferred between the SMA wires and the interlayer.

Regarding the control of SMAHCs, their electrical resistance is an essential measurable parameter as it allows self-sensing. The best-case scenario for self-sensing capability is when the applied load does not affect the resistance-deflection correlation. This relationship was investigated. Results are given in figure 5.32, where the resistance is plotted against deflection for various loads. Several significant changes in the correlation between resistance and deflection could be observed for varying loading conditions. Increased resistance peaks for higher external loads can be attributed to the corresponding SMA wire's elongation and the simultaneous diameter reduction. It was found that the resistance at the same deflection level was lower for raised external loads. To explain this observation,

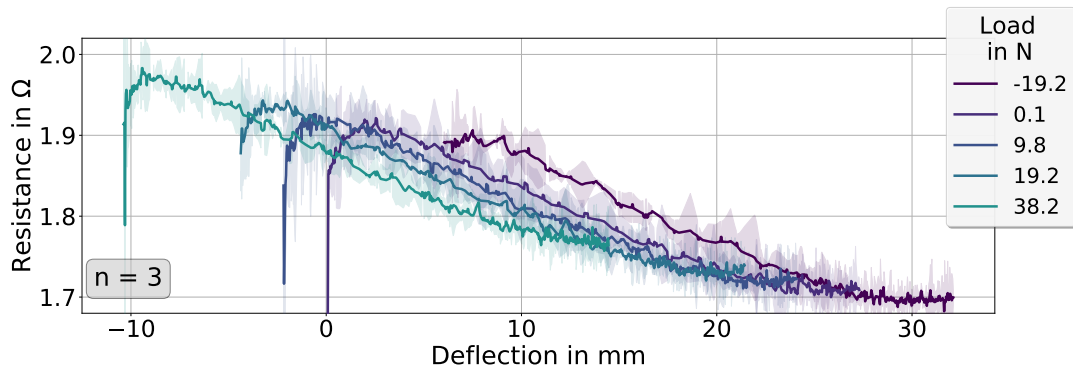


Figure 5.32: Change of electrical resistance during activation over SMAHC deflection for different external loads. SMAHC of type C was used for experiment. Supplied current during activation was 3.5 A.

the relationships between resistance, external load, and deflection must be clarified. A higher austenitic proportion of the SMA wires is required to keep the deflection level constant while raising the external load. At the same time, the proportion of elastic strain of all phase components in the alloy increases due to the added load. Increased elastic strain generally causes a rise in the resistance of an electrical conductor. If boundary conditions are disregarded, resistances can only decrease in the activated state under a higher load if the resistance in the austenitic phase is lower than that of the martensitic phase. Anchoring, as a boundary condition, also provides an explanatory possibility. Due to the particular type of anchoring, occurring tensile forces can reduce the contact resistance between the anchor bar and the SMA wires.

The measured resistance discrepancies were within a range of 12%.

5.4.4. Activation under influence of ambient temperatures

Experiments conducted without external loads but under varied ambient temperatures led to the following results.

In figure 5.33, the time to reach the type-specific maximum deflection of an actuator t_{max} is plotted against the supplied current for different ambient temperatures. The maximum deflections were defined for each actuator using the deflections measured at 120°C (compare figure 5.23). The lines between measurement points are intended as a guide for the eye. Nevertheless, a function of the type $t_{max} = a \cdot \exp^{-I/b}$, where I is the supplied current, and a and b are fit parameters, fits the data fairly good. The exponential correlation emphasizes the significant influence of ambient temperature on the actuator performance. For SMAHC type D, the experiment at a temperature of -10°C was not carried out.

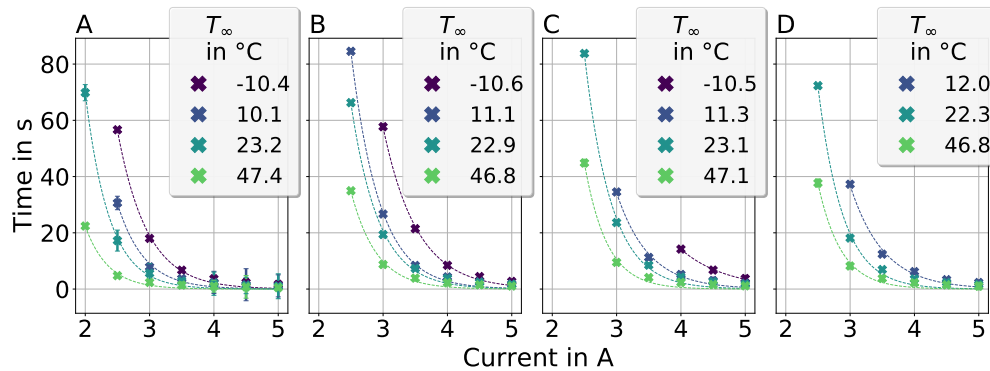


Figure 5.33: Time to reach defined type-specific maximum deflection in dependency of applied current and ambient temperature for the different types of SMAHC. $n = 3$ for all experiments.

It was found that activation time increased with lower current and temperature levels. The stated maximum deflection was not attained for electrical currents for which no measuring point is shown on the graph. Fewer measurement points can be found in the graph for thicker interlayer thickness. Thus, thicker interlayer thickness caused reduced system dynamics. As the amount of measuring points in the graphs for types C and D are identical, it was concluded that substrate thickness did not influence thermal system dynamics.

Figure 5.34 shows the efficiency of SMAHC type C for different ambient temperatures. The two graphs given illustrate different possibilities of efficiency definition.

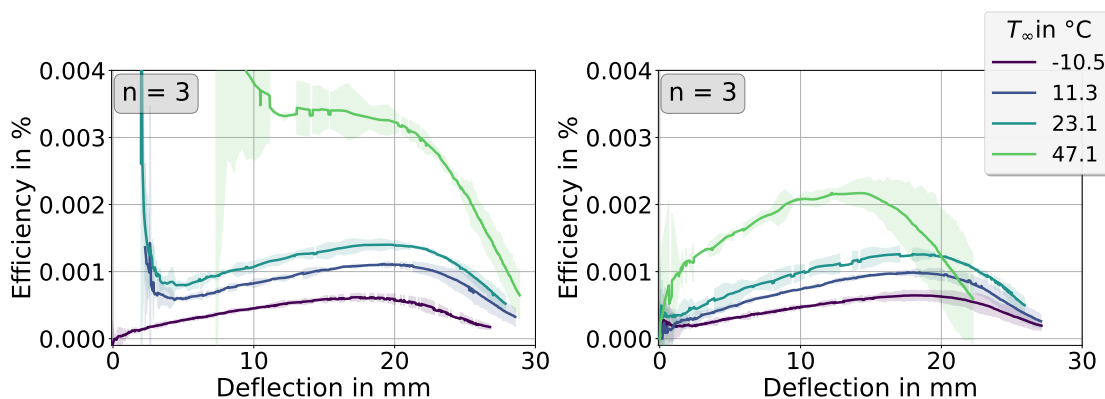


Figure 5.34: SMAHC type C efficiency during activation against deflection for various ambient temperatures. The electrical current during activation was 3.5 A. Left: Reference position for deflection is the initial position of an experiment at RT; Right: Reference position for deflection is the initial position of the respective cycle.

In the left figure, the deflection is referenced to the experiment's initial position at RT, and in the right figure to the cycle start position. The significant deviation between the

definitions could be traced to the fact that the actuator did not return to its initial position after activation at ambient temperatures beyond $-10\text{ }^{\circ}\text{C}$ due to the pseudoplastic effects (discussed on the basis of figure 5.25). Figure 5.35 shows the deflection against the current for the four actuator types and various ambient temperatures. An increase in the temperature or current raised the permanent deflection after activation. Raising the ambient temperature from -10 to $23\text{ }^{\circ}\text{C}$ led to almost tripling the actuator's efficiency. Higher ambient temperatures generally brought increased efficiency as the initial temperature was close to the transformation temperatures, and less energy was needed to initialize phase transformation. However, it was also observed that the SMAHCs' permanent deflection level decreased for currents above 2 A and temperatures from $11\text{ }^{\circ}\text{C}$. At $-10\text{ }^{\circ}\text{C}$, the actuator's position after activation was even below the initial position. Electrical resistance

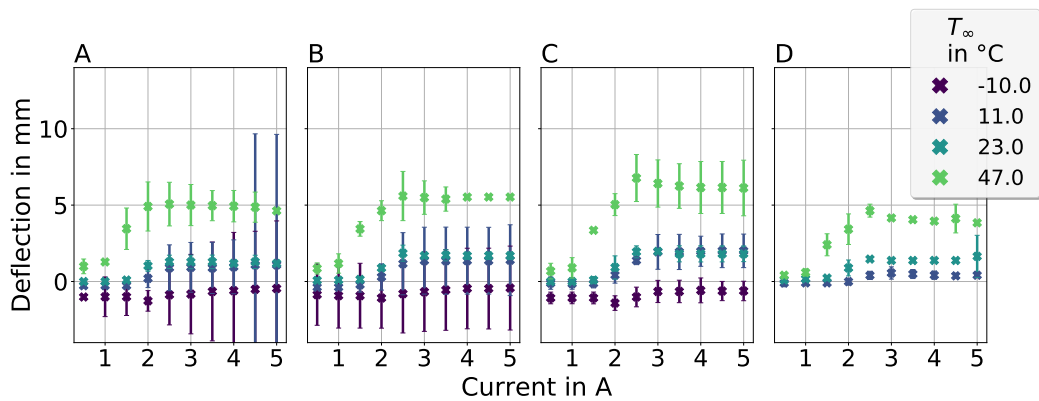


Figure 5.35: SMAHCs permanent deflection after cool-down with various electric currents and under the influence of different ambient temperatures.

under the influence of ambient temperatures was also investigated. Results are illustrated in figure 5.36. No significant changes were observed.

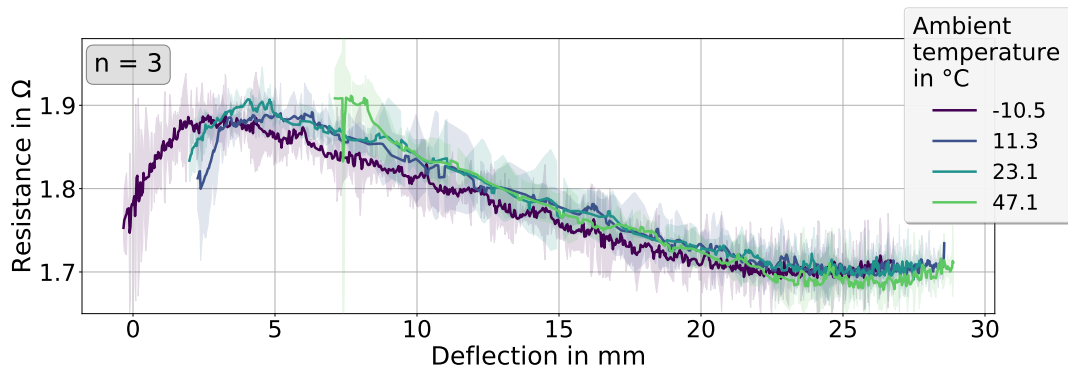


Figure 5.36: Change of electrical resistance during activation against deflection for different ambient temperatures. The supplied current was 3.5 A ; SMAHC type C was used for the experiment.

5.4.5. Conclusion

The following major impacts were discovered based on the examined range of external load, ambient temperature, and applied current flow:

- Cyclic change in deflection is only significant for less than the first three cycles. Since all actuators were pre-cycled, cycle-dependent functional features are disregarded.
- After the initial cycles, the SMAHC is permanently deflected in the inactive state.
- There is a significant temperature distribution along SMA wires central axis.
- The correlation between current intensity, activation time, and deflection magnitude is substantial.
- Deflection magnitude depends significantly on the thickness of the interlayer and the stiffness of the substrate.
- External loads lead to a significant decrease in the deflection related to the initial state of the actuator. The deflection related to the position of the loaded, non-activated actuator remains almost constant regardless of the load in the investigated load range.
- Under the influence of external load, the SMAHC undergoes pseudoplastic deformation after an activation cycle.
- Full linkage between the SMA and interlayer can be assumed as no buckling or detachment of the wires could be observed.
- There is a distribution of strain along the SMA wire in the case that an external load is applied.
- The ambient temperature significantly impacts the activation time of a constant current supply.
- Ambient temperature does not significantly influence the correlation between electrical resistance and deflection.

6. SMAHC model development

This chapter discusses the modeling technique for SMAHC, the underlying assumptions, and the implementation of the model equations. The model develops relationships between time, deflection, power consumption, and mechanical load-bearing capacity to characterize the unimorph deformation behavior of the SMAHC appropriately. The model includes the most significant parameters that impact the dynamic characteristic of SMAHCs, such as laminate stiffness, interlayer thickness, performance of the SMA and SMA volume content as well as geometric and thermal characteristics of all single components. The model provides the ability to predict transient shape change while considering design elements and boundary conditions, such as ambient temperature and external stresses. The SMAHC system and its various influences and parameter interactions are represented in the diagram 6.1.

The complexity in the SMAHC modeling results from the unique material behavior of the

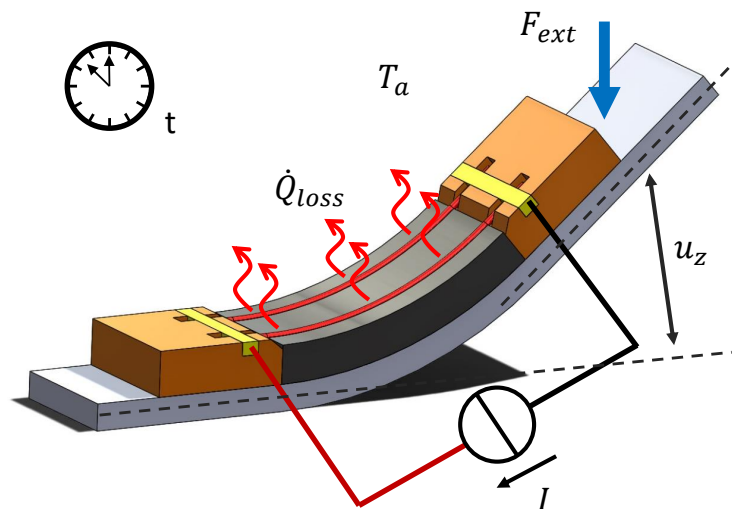


Figure 6.1: The SMAHC system and its various influences and parameter interactions.

SMA wires and the involvement of various physical disciplines. To describe all effects of interest, the model has to include the electrical, thermal, and mechanical domains. The modeling was accomplished in three steps. A model of the SMA wire was created, that allowed for a description of the relevant electro-thermomechanical effects. Since the focus is on transient modeling of SMAHC to determine their energy consumption and dynamic deformation behavior, observed cyclic and pseudoplastic effects, which play a minor role for these actuator properties, were not modeled. The SMAHC transient behavior was

modeled in the next step without considering external loads. In this case, the curvature of SMAHC was assumed constant along the s -axis. In the final step, the influence of external loads was considered.

6.1. Lumped SMA wire model

The lumped 1D SMA model describes a piece of homogeneous, finitely long SMA wire. It can describe the electro-thermomechanical behavior along one axis of the SMA. To reflect all of the material's properties, the model is required to have a constitutive equation, an evolution rule for the martensite phase fraction, and equations describing the material's thermal, mechanical, and electrical domain behavior. The assumptions underpinning the subsequent equations are considered in the following subsections.

6.1.1. Constitutive model and hardening law

Assumptions:

1. The transformation process is slow and, therefore, assumed to be quasi-static. Rate dependencies of material parameters were neglected.
2. The thermal expansion of the single phases is much smaller in magnitude than expansion due to transformation, and the thermoelastic tensor was therefore neglected $\Theta = 0$. This assumption is common regarding modeling SMA-driven actuators [132].
3. The transformation tensor Ω is the product of the martensite ratio-dependent Young's modulus $E(\xi)$ and transformation strain ϵ_{tr} (compare equation 2.7) [56].
4. The current transformation strain $\epsilon_{tr,curr}$ depends on the external load condition. The correlation is given by equation 2.9 [61].
5. The model is one dimensional. Influences and effects across the s -axis of the wires are ignored.

Governing equations:

The constitutive 1D SMA model chosen is based on equation 2.4 and modified according to the simplifications given by assumptions 2 and 5. The transformation strain ϵ_{tr} is stress-dependent according to equation 2.9. The relationship between elastic modulus E and martensite fraction ξ , referred to as hardening law, is given by equation 2.8. The initial strain ϵ_0 as well as the transformation strain ϵ_{tr} is given as the wires transformation strain under the influence of external load $\epsilon_{tr,curr}$. Substituting the equations and taking

the assumptions into account, the resulting constitutive equation is given by 6.41.

$$\sigma - \sigma_0 = E(\xi)(\epsilon - \epsilon_{tr,curr}) + \epsilon_{tr,curr} \cdot E(\xi)(\xi - \xi_0) \quad (6.41)$$

6.1.2. Martensite fraction and hysteresis model

Assumptions:

1. The model is only valid for alloys where $M_s < A_s$ which is the case for the investigated alloy and for most commercially available SMAs [52].
2. It is not distinguished between stress-induced and thermal-induced martensite fractions. Only one martensitic variant ξ is assumed.
3. Temperature dependencies of material parameters were neglected, and it was assumed that they only vary due to changes in phase fraction. This is a common assumption in many cases, as in the considered temperature area, temperature influence on properties is significantly lower than the influence due to the phase fraction. [65]
4. Clausius-Clayperon or stress-induced coefficients are unique concerning the four transformation temperatures. This deviates from usual assumptions. However, the measurement results in section 7.2 show that the coefficients of the start and finish temperatures of the individual phases differ significantly from each other.
5. A linear correlation between transformation temperature and mechanical stress of the SMA is assumed. [61]

Governing equations:

The martensite fraction remains constant if no phase transformation occurs. Hardening is described by the cosine model, as described by equations 2.5 for heating and cooling. The transformation range is limited by stress-dependent transformation temperatures and occurs between the start and finish temperatures. The transformation from martensite to austenite takes place if the supplied power exceeds the power losses, that is, $P_{el} > \dot{Q}_{loss}$ and $\dot{E} > 0$. Conversely, the reverse transformation occurs when $P_{el} \leq \dot{Q}_{loss}$ and $\dot{E} \leq 0$. Six cases determine if and what transformation occurs, as summarized by equations 6.43 and 6.44. The relationship between the transformation temperature and mechanical stress is given by the equations listed in 6.42. The zones of phase transformation are therefore limited by straight lines in the stress-temperature diagram (see figure 2.6).

$$\begin{aligned}
A_s^\sigma &= A_s + \frac{\sigma}{C_{As}} \\
A_f^\sigma &= A_f + \frac{\sigma}{C_{Af}} \\
M_s^\sigma &= M_s + \frac{\sigma}{C_{Ms}} \\
M_f^\sigma &= M_f + \frac{\sigma}{C_{Mf}}
\end{aligned} \tag{6.42}$$

$$P_{el} > \dot{Q}_{loss} : \quad \xi_{M \rightarrow A} = \begin{cases} 1, & T \leq A_s^\sigma \\ \frac{1}{2} \left[\cos \left(\frac{\pi}{A_f^\sigma - A_s^\sigma} (T - A_s^\sigma) \right) + 1 \right], & A_s^\sigma < T < A_f^\sigma \\ 0, & T \geq A_f^\sigma \end{cases} \tag{6.43}$$

$$P_{el} \leq \dot{Q}_{loss} : \quad \xi_{A \rightarrow M} = \begin{cases} 0, & T \geq M_s^\sigma \\ \frac{1}{2} \left[\cos \left(\frac{\pi}{M_s^\sigma - M_f^\sigma} (T - M_f^\sigma) \right) + 1 \right], & M_s^\sigma < T < M_f^\sigma \\ 1, & T \leq M_f^\sigma \end{cases} \tag{6.44}$$

6.1.3. Lumped capacitance model

Assumptions:

1. The wire is thin, so the internal thermal gradient in the yz-plane is negligible and lumped capacity approach is valid [65]. The biot number has to be much smaller than 1 to assure the validity of this assumption [133]. In [49], it is explained that this assumption is valid for embedded SMA if the volume fraction of the SMA in the composite is less than 25% and the ratio between the diameter and length of the SMA is small.
2. Effects of changes in the SMA's volume, length, and surface on the heat transfer to the surroundings are negligible. [65]
3. For the energy balance, mechanical energies play a subordinate role, as they are at least one magnitude smaller than other shares and are therefore neglected. [69]

Governing equations:

The thermodynamic model is based on energy conservation, as described in equation 2.14. This model includes components for internal energy (see equation 2.15) and transformation energy (see equation 2.16). The transformation enthalpy is a function of the derivative of the martensite fraction. When no transformation occurs, the derivative of the martensite

fraction is zero, and so is the transformation enthalpy. The SMA wire's internal energy change during transformation is given by equation 6.45. Using the cosine martensite fraction and hysteresis law and differentiating it with respect to temperature, equation 6.46 is derived for the cumulated change in internal energy and transformation enthalpy for transformation to austenite, and equation 6.47 is derived for the transformation to martensite.

$$\dot{U} + \dot{H}_{tr} = m \cdot c \cdot \dot{T} + m \cdot \Delta H_{tr} \cdot \dot{\xi} \quad (6.45)$$

$$\dot{U} + \dot{H}_{tr} = \rho \cdot V \left[c + \Delta H_{tr} \frac{\pi}{2(A_f^\sigma - A_s^\sigma)} \sin \left(\frac{\pi}{(A_f^\sigma - A_s^\sigma)} (T - A_s^\sigma) \right) \right] \frac{dT}{dt} \quad (6.46)$$

$$\dot{U} + \dot{H}_{tr} = \rho \cdot V \left[c + \Delta H_{tr} \frac{\pi}{2(M_s^\sigma - M_f^\sigma)} \sin \left(\frac{\pi}{(M_s^\sigma - M_f^\sigma)} (T - M_f^\sigma) \right) \right] \frac{dT}{dt} \quad (6.47)$$

6.1.4. Electrical domain

Assumptions:

1. The Joule heating model describes power dissipation due to electrical current flux.
2. Electrical resistivity only depends on martensite fraction ξ . Changes due to material temperature and stress are ignored. [65]
3. Only one martensitic phase is taken into account. [76]
4. Changes in resistance due to variations in wire length and cross-section are negligible compared to changes due to phase transition. [65]
This assumption depends on the resistivity measurement method. The measured electrical resistance is related to the length and diameter of the wire at RT after normalization. The measurement method is described in detail in chapter 7
5. The wire is assumed to be a 1D resistor.
6. Supplying direct current is assumed. The used SMA wires have a relatively low mass. Thus electrical effects due to the capacity and inductivity are negligible.
7. The resistance dependency of single phases on temperature and stress is neglected. [65]

Governing equations:

The electrical power dissipation, P_{el} , due to the electrical current flux, I , and electrical resistance, R , is given by equation 2.28. The resistivity of the SMA wire, which depends on the respective phase fraction, ξ , can be described using the mixture rule by Voigt

according to equation 2.33. The wire's resistance is a function of resistivity, ρ_{res} , and its length, L , and cross-section, A , as described in equation 2.30. The exact definition of resistivity and resistance applicable in this study is explained in section 7. Due to the chosen measurement method for the electrical resistance in the martensitic and austenitic states, further assumptions are necessary. As previously noted, the phase composition of twinned and untwinned martensite cannot be determined in the martensitic state. Thus, the electrical resistance is assumed to be identical for both phases, with an error of about 10% [134]. Based on these assumptions, the electrical resistance, R , is determined as a function of the martensite fraction, ξ , according to equation 6.48.

$$R = \frac{L_{RT}}{A_{RT}} [\rho_M \cdot \xi + \rho_A \cdot (1 - \xi)] \quad (6.48)$$

6.1.5. Heat losses

Assumptions:

1. The length of the SMA wire is assumed to be long compared to the diameter. Thus, conductive losses in the clamping at both ends are neglected. This assumption is not typical for external wires [65] but for embedded wires [49], which is what this work focuses on.
2. As discussed below, the influence of thermal radiation is not negligible in the temperature range the SMA was planned to be used. However, radiation is of minor importance and thus is not considered what is a common assumption [65].
3. Only free convection was taken into account.

In the following, the influence of thermal radiation is roughly estimated, and its significance for the modeling is discussed. The emissivity of the wire, ϵ , is influenced more by the surface condition than the phase state. It has been reported to range from 0.2 to 0.3 [135], 0.66 [67, 136], up to 0.86 [137]. In this study, the wire was painted to enable infrared imaging, and its emissivity was estimated to be approximately 0.955. The power loss caused by thermal radiation and convection to the surrounding environment can be calculated using equation 2.17. The graph in 6.2 shows the ratio of the radiative and convective energy losses (E_{rad}/E_{conv}) for different ambient temperatures (T_∞) as a function of the SMA wire temperature. The calculation assumes that an infinitely long, horizontally positioned wire of constant temperature freely floats in a constant-temperature gas. Free convection is assumed, and the heat transfer coefficient is given by equations 2.18 and 2.19. The influence of thermal radiation is proportional to the ambient temperature in the

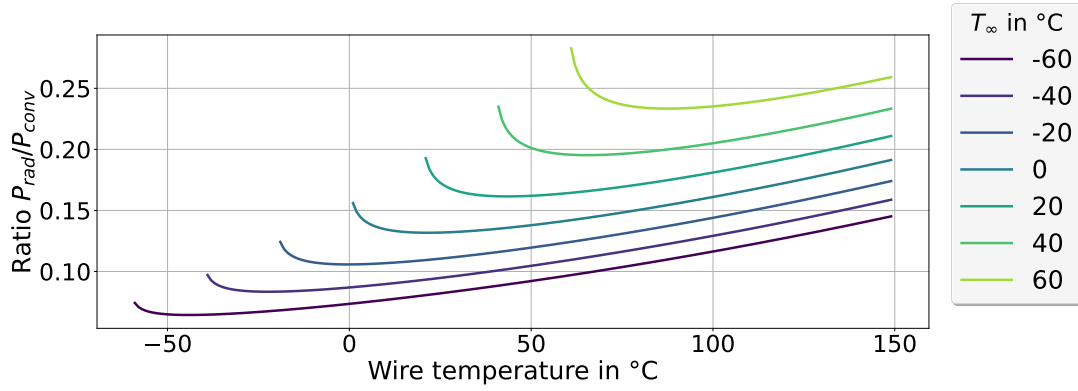


Figure 6.2: The ratio between energy losses due to radiation and convection E_{rad}/E_{conv} for different ambient temperatures T_{∞} plotted against SMA wire temperature.

region of concern. The contribution of thermal radiation in the relevant range is no less than a fourth of that of convection and is thus not negligible when the model is applied to a single wire that is not embedded. However, radiation is irrelevant for an implanted or coated wire. Thus, radiation in the following is ignored.

Governing equations:

Due to the assumptions made, the equation for the energy conservation 2.14 simplifies to 6.49. Additionally, the conductive heat loss \dot{Q}_{cond} equals zero for a single, not embedded wire.

$$P_{el} = \dot{U} + \dot{H}_{tr} + \dot{Q}_{conv} + \dot{Q}_{cond} \quad (6.49)$$

The free convective heat loss coefficient α for the single not embedded wire in relation to the Earth's gravitational field can be approximated using the equations 2.18, 2.19 and 2.23.

6.1.6. Mechanical domain

The SMA wire can be integrated with an external mechanical system in the mechanical domain. This work focuses on two types of external load applied to the SMA wire: a constant load and a load imposed by a spring. When a constant load, such as weight, is applied to the vertically positioned SMA wire, it can be represented by the initial stress σ_0 induced in the wire. The initial length is defined as the length of the wire in the austenitic state. If the SMA wire is subjected to a spring, the stress due to an external load σ is dependent on the strain ϵ , typically described by the elastic modulus of the spring $E_{spring} = \sigma_{SMA}/\epsilon$. However, the relevant parameter for springs is not the elastic modulus but the spring stiffness D . The elastic modulus and spring stiffness are related through equation 6.50, where L_0 is the initial length of the wire and A is the cross-sectional area.

It is assumed that the cross-section of the SMA wire remains constant under external loads.

$$E_{ext} = D \cdot \frac{L_0}{A} \quad (6.50)$$

Finally, the mechanical stress in the SMA wire is proportional to the strain of the SMA wire according to equation 6.51. The strain is always related to the length of the SMA in the load-free austenitic state, i.e., in its shortest form.

$$\sigma = \sigma_0 - E_{ext} \cdot (\epsilon_{tr,curr} - \epsilon) \quad (6.51)$$

6.1.7. Model algorithm

The system of ordinary differential equations (ODEs) represented by the 12 independent equations listed above is used to calculate the state variables of the SMA segment given the input variables. The initial value problem is solved using the forward Euler scheme. The algorithm can be divided into two steps: initialization and solving. The program flow chart in figure 6.3 illustrates the entire solution algorithm. All material parameters

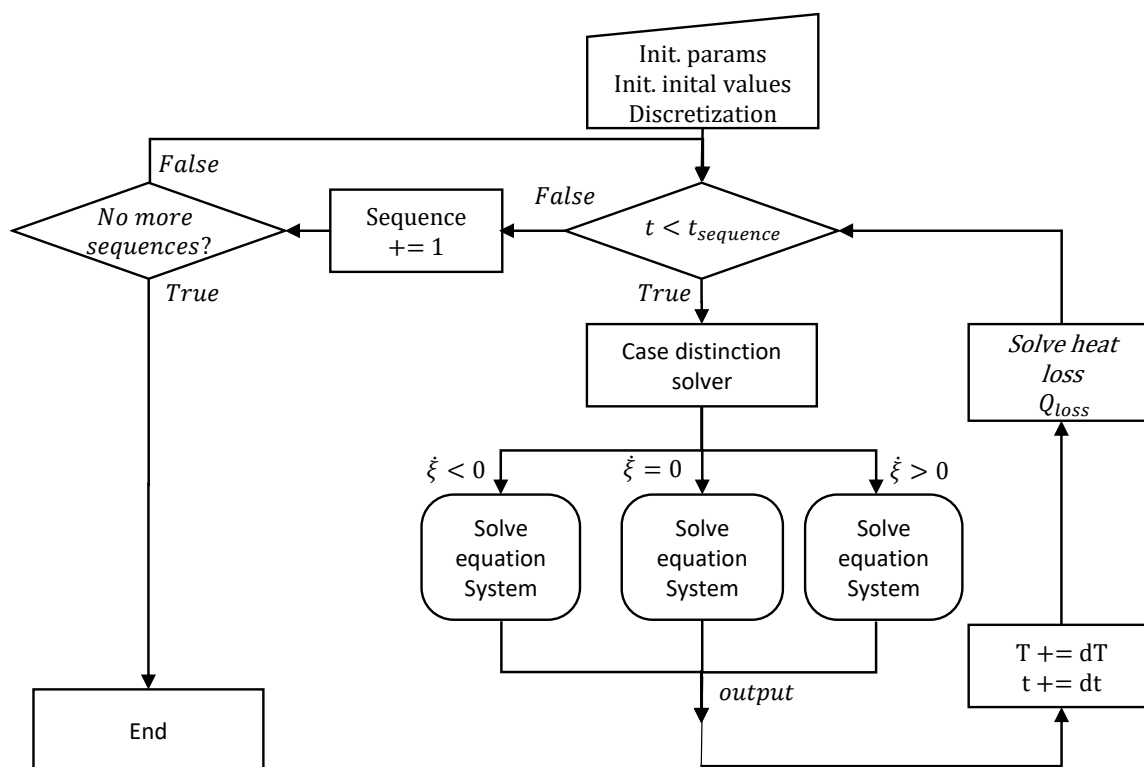


Figure 6.3: Illustration of the computation process for the lumped SMA model.

and environmental influences are input during the initialization step, along with the initial values and time step. During the solving process, for each time step of length dt , the state variables, including the martensite fraction ξ , current transformation strain ϵ_{tr} , strain ϵ ,

stress-dependent transformation temperatures A_s^σ , A_f^σ , M_s^σ , M_f^σ , SMA temperature T_{SMA} , electrical power input P_{el} , the difference of SMA energy potential $\Delta U + \Delta H_{tr}$, electrical resistance R , and elastic modulus E are computed using numerical methods. The forward Euler scheme was selected for its ease of implementation. However, its accuracy and stability heavily depend on the step size. Figure 6.4 schematically illustrates the equation system that must be solved for each time step. The inputs and outputs of the model

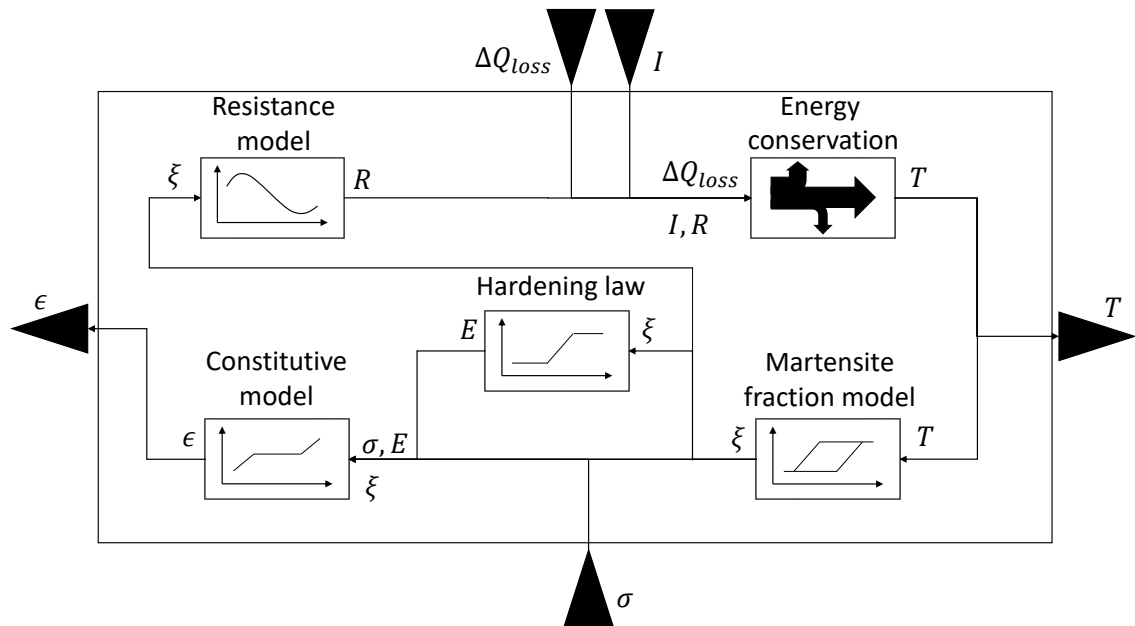


Figure 6.4: Schematic of the lumped SMA wire model. The block diagram depicts the inputs and outputs of the respective subsystems and the system. The inputs and outputs of the entire system can be viewed as interfaces that allow the lumped SMA model to be coupled with a mechanical domain model and a thermodynamic domain model.

are depicted at the boundaries of the block diagram. Arrows pointing into the block represent the inputs necessary to solve the system of equations, while arrows pointing away from the block indicate the generated outputs. The electrical current, I , must be provided as input, while the heat loss, ΔQ_{loss} , and the mechanical strain can either be specified by the user or derived using respective domain model extensions. The heat loss is typically a function of the SMA wire's temperature and stress, which can be constant or a function of the wire's strain. Before solving for the state variables, it is necessary to determine the current transformation state of the SMA segment. There are three possible states: transformation from the martensitic to the austenitic state, the transformation from the austenitic to the martensitic state, or no transformation. The decision tree used to make this determination is depicted in figure 6.5. In case, the temperature of the SMA segment is below the stress-dependent martensite finish temperature M_f^σ or beyond the stress-dependent austenite finish temperature A_f^σ , the martensite fraction ξ remains unchanged. If the internal energy of the SMA segment increases ($\Delta U > 0$) due to heating,

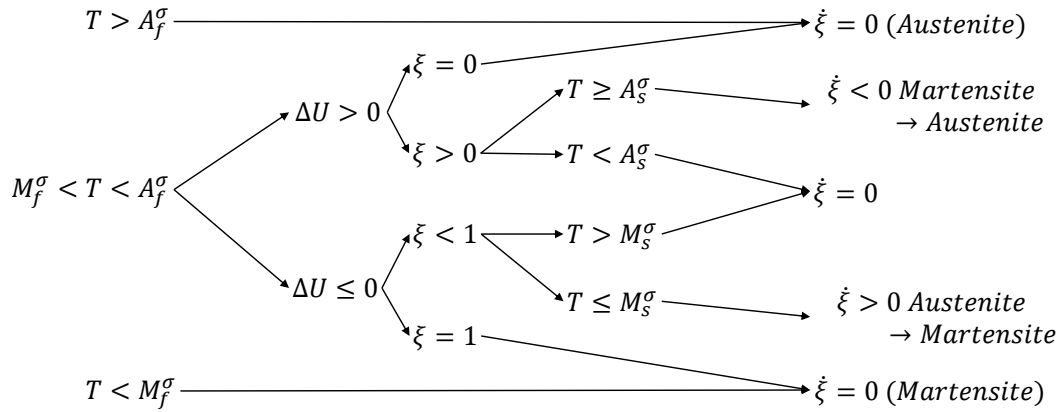


Figure 6.5: Illustration of the decision tree for finding the appropriate martensite fraction computation rule.

the current transformation state of the SMA must be considered. If the alloy is in a fully austenitic state ($\xi = 0$), the martensite fraction does not change. Similarly, the martensite fraction remains unchanged if the temperature is below the austenite start temperature A_s^σ . On the other hand, if the temperature exceeds the austenite start temperature A_s^σ , and the transformation is incomplete, the martensite fraction decreases. Similarly, in the case of cooling, there are two possibilities for changing the martensite fraction, and the appropriate calculation rule can be selected from the decision tree. The simulation is divided into successive sequences, each defined by the current and its duration. Once all sequences are processed, the simulation is completed and ready for evaluation.

6.2. SMAHC model without influence of external load

This section covers the techniques to develop a model capable of predicting the behavior of the SMAHC when no external loads are present. Two domains are added to the model to extend the SMA wire model built in section 6.1 to describe the complete SMAHC. The thermal domain allows for simulating the SMA wire's heat losses. The mechanic domain closes the SMA-wires stress-strain feedback loop and approximates the SMAHC's bending and deflection due to wire strain. Subsequently, the modeling of these two domains is thoroughly described.

6.2.1. Mechanical domain

Assumptions:

1. The SMA layer is considered a homogeneous layer with the properties of SMA and constant thickness within the entire active area. This is a common assumption

- [122, 94].
2. The SMA is an anisotropic material. Effects regarding the SME along the y-axis are neglected. (Compare e.g. [122])
 3. The stiffness of the interlayer in the s-direction is neglectable, so the contraction or stretching of the SMA is not hindered by this layer. This assumption is reasonable since the intermediate layer has low mechanical characteristics, especially compared to the substrate.
 4. The stiffness of the interlayer in the t-direction is infinite. Thus the distance between the SMA layer and substrate is assumed to be constant. Despite the low mechanical properties of the interlayer, this assumption is reasonable because the interlayer is thin, and deformations in the t-direction are, therefore, negligible.
 5. The actuator is infinitely extended in the y-direction, which results in infinite periodic conditions.
 6. The SMA layer is connected to the substrate along the x-axis by an infinite number of fixing points. According to the results from Section 5.4.3, this assumption is permissible.
 7. As the maximum ratio between the SMA layer and interlayer for the configurations studied is less than 0.05, the SMA layer thickness is assumed much smaller compared to the interlayer thickness.
 8. All components weigh zero, or gravitational forces are disregarded. This assumption is reasonable because the actuator's weight is small compared to the actuator potential. [17]
 9. The substrate is isotropic and homogeneous material.
 10. The elastic modulus of the substrate is constant in the area of interest.
 11. The deflections of the SMAHC in the xz-plane are in the range of the actuator's length (compare figure 5.1).
 12. Strains in the SMA layer are of up to 5%. Locally, higher strains do occur [136], but for the assumption of homogeneous strain along the s-axis of the SMA wire, this assumption is reasonable for loaded SMA in cyclic loaded service [126].
 13. Mechanical effects due to clips and fixation are neglected.
 14. The SMAHC is fixed with 0 DOF on the constrained end.
 15. All state variables for all wire segments are identical. In section 5.4.3 it was shown that proportional to the external load, strain distributions develop along the s-axis of the SMA wires. In the activated state, however, the ratios between maximum

and minimum strain lie in a range that allows the assumption of homogeneous distribution. This assumption should be tested for higher loads than those studied in this work.

16. The initial stress σ_0 addresses the mechanical load of the SMAs in their initial state and is, therefore, set to zero.

The mechanical system that resulted from the stated assumptions is depicted in figure 6.6 A). The system comprises the substrate and a homogenized SMA layer set to a specific distance from the substrate. Because the interlayer has no substantial impact on the systems, it is disregarded. As all y-direction effects were disregarded, the system is simplified to two dimensions (illustrated on the right side of figure 6.6 B). In this 2D depiction, the system consists of a substrate and an SMA layer. However, both layers are shown as a single piece for convenience. The SMAHC is fixed at the constrained end, and the free end can move in the xz-plane. During activation, each element with length ds experiences a curvature proportional to the angle's derivative Φ . Figure 6.7

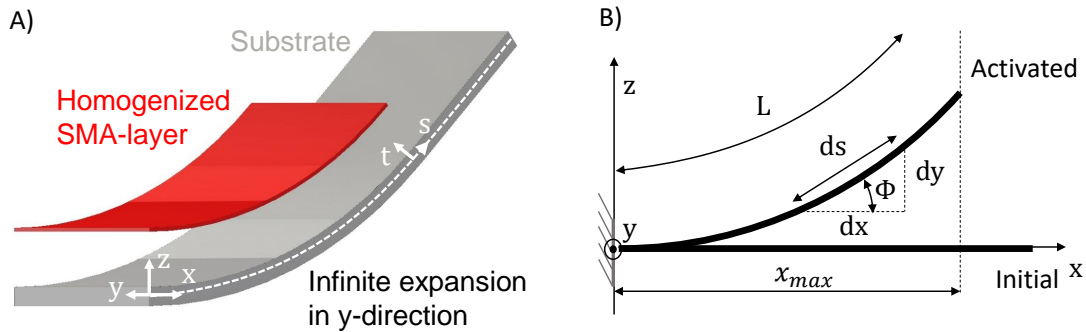


Figure 6.6: Visualization of the SMAHC system's mechanical domain. A) A 3D example of the modeling-relevant components. The homogenized SMA layer is at a specific distance from the substrate, and because the interlayer has no substantial impact on the systems, it is disregarded. B): The 3D system can be reduced to a 2D mechanical system based on the assumptions made.

illustrates the ratios of forces at an infinitesimal SMAHC element. Due to the strain in the SMA-layer σ_{SMA} , a bending moment M_{SMA} proportional to the constant lever arm t_{SMA} operates on the substrate, causing the element to be curved by the angle Φ . The lever arm is expressed as the distance between the neutral axis of the substrate and the center of the SMA wire. **Governing equations:**

The homogenized SMA layer thickness, t_{hsl} , is determined by equation 6.52[89].

$$t_h = \frac{n \cdot \pi \cdot d^2}{4 \cdot w} \quad (6.52)$$

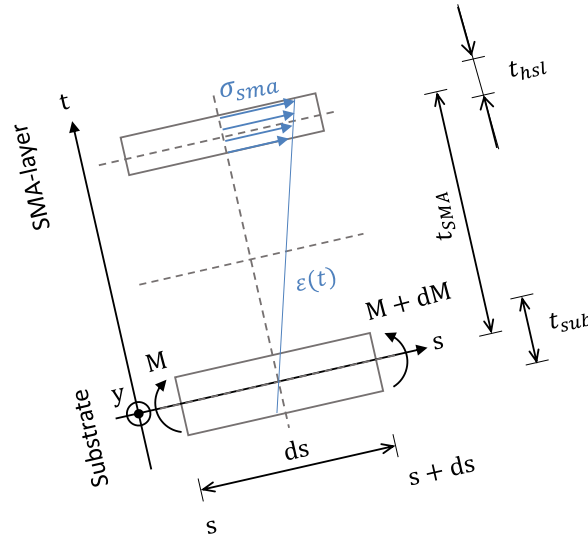


Figure 6.7: Force ratios at an infinitesimal SMAHC section. The SMA layer and the substrate are crucial for mechanical domain modeling.

As the deflections of the SMA model were within the range of the actuators' length, the basic assumptions of elementary beam theory, according to Euler-Bernoulli, were no longer valid. Hence, beam deflection along the x-axis and the shortening of the moment arm for the loaded actuator were ignored. The mathematical description of large deflections was instead described by the differential equation of elastic beam given by equation 2.35. The bending moment, M , acting on the substrate can be described as a function of the force from the SMA, F_{SMA} , and the moment arm, t_{SMA} , resulting in equation 6.53.

$$M = F_{SMA} \cdot t_{SMA} = \sigma_{SMA} \cdot t_{hsl} \cdot w_{cell} \cdot t_{SMA} \quad (6.53)$$

The area moment of inertia concerning the y-axis of the rectangular substrate I_y was given as a function of its width w_{cell} and its thickness t_{sub} . [138]

$$I = \frac{w_{cell} \cdot t_{sub}^3}{12} \quad (6.54)$$

In [139] a geometrical condition for the radius of curvature $BR_{sub} = \frac{ds}{d\phi}$ in dependence of the SMA-wires strain ϵ_{SMA} was introduced.

$$\frac{d\phi}{ds} = \frac{\epsilon_{SMA}}{t_{SMA}} \quad (6.55)$$

Merging equations 6.52, 2.35, 6.53, 6.54, 6.55 results in the correlation of SMA stress and strain due to the influence of substrate bending given by equation 6.56.

$$\sigma_{SMA} = (\epsilon_{SMA} - \epsilon_{SMA,0}) \cdot \frac{E_{sub} \cdot t_{sub}^3}{12 \cdot t_{hsl} \cdot t_{SMA}^2} \quad (6.56)$$

For the known strain of the SMA layer along the s-axis, the radius of curvature can be derived from equation 6.55. Since external loads are of no concern in this part and gravitational forces and temperature distributions along the central axis of the wire were disregarded, the radius of curvature along the s-axis is assumed to be constant. Thus, the deflected actuator may be characterized as a segment of a circular arc. Assuming the constant curvature radius, the Z coordinate for such a geometric element at location X, beginning at the origin of the coordinate system, may be calculated by equation 6.57.

$$z = -\sqrt{BR_{sub}^2 - x^2} + BR_{sub} \quad (6.57)$$

Due to the cantilever beam's large deflection, the free end's position along the x-axis changes throughout activation. The bending radius defines the location of the free end along the x-axis, which may be determined using the equation 6.58.

$$x_{max} = BR_{sub} \cdot \sin\left(\frac{L}{BR_{sub}}\right) \quad (6.58)$$

6.2.2. Thermal domain

Since the SMA wires are embedded in the SMAHC, the heat conduction to neighboring layers and the convection of these layers to the environment must be addressed.

Assumptions:

1. The geometric extension of the SMAHC in the y direction is infinite. There are infinite symmetric boundary conditions between any two wires. This assumption is appropriate as temperature differences between wires are below 10% (compare figure 5.18)
2. The geometric extension of the SMAHC in the x direction is infinite. Boundary effects at the wire ends due to fixation are neglected. In figure 5.18 it can be seen that there is a significant temperature distribution along the wire that effects about 25% of the wire. This assumption is used to reduce model complexity and is not physically justifiable.
3. The temperature across the cross-section of the SMA is homogeneously distributed. [49]
4. Only free convection is considered.
5. The shape of the SMAHC does not change during activation. Influences of geometric changes on heat transport are thus neglected.

6. The SMAHC is in a horizontal position.
7. Half of the cross-section of the wire is embedded in the interlayer, and half is exposed to the environment (compare figure 5.3).
8. Thermal influences due to the thin resin layer surrounding the wire are neglected. This assumption is appropriate because the thermal mass of the resin layer is small compared to the SMA wire and the interlayer. (compare figure 5.3).
9. Thermal influences due to sewing threads are neglected.
10. Heat losses due to thermal radiation are neglected.

According to the assumptions, there was no temperature gradient along the s -axis. Therefore, the model is simplified to two dimensions, and only temperature distributions in the yz -plane are considered. Due to periodic boundary conditions, it is sufficient to analyze only one cell's thermodynamic states. A cell is a volume with infinite extension in the x -direction and finite extension in the y -direction that is defined by periodic boundaries. According to the assumptions, the temperature distribution over the cross-section of the SMA wire is uniform. Figure 6.8 A depicts the 3D body of the SMAHC with the relevant modeling components for the thermal domain. Even though only two wires and a finite extension of the SMAHC are depicted, one must consider an indefinite extension in the xy -plane and an infinite number of parallel wires spaced equally apart. As the model is simplified to two dimensions, just the cross-section in the zy -plane (see figure 6.8 B) needs to be considered for simulating heat losses. As shown in 6.8 B, the heat losses are separated

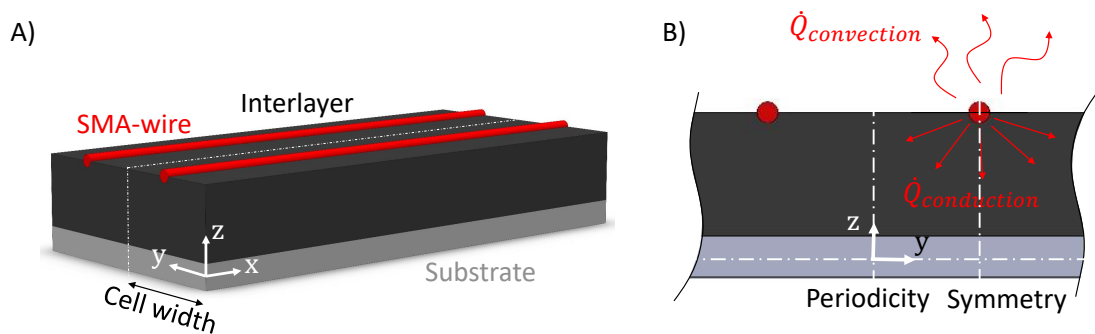


Figure 6.8: The thermal domain of the SMAHC system is visualized. The system is constructed with adjacent, periodically arranged cells. A) A 3D illustration of the modeling-relevant components. B) The thermal domain can be reduced to two dimensions due to the assumption of a uniform temperature distribution. It is only necessary to model the temperature distribution in the yz -plane.

into convective flux to the environment and conductive flux to the interlayer. It is assumed that half of the wire's surface is in contact with the separation layer, and the other half is in contact with the environment. Convective heat transfer to the surroundings \dot{Q}_{conv} of

the upper half of the wire is derived from a lumped model approach. It is assumed that the wire is exposed to the surroundings in order to determine the convective heat loss. The corresponding heat transfer coefficient is approximated by equations 2.18, 2.19, and 2.19. A 2D method with spatial discretization in the yz -plane was established to model the conductive heat loss \dot{Q}_{cond} . The interlayer and substrate are modeled as 2D objects,

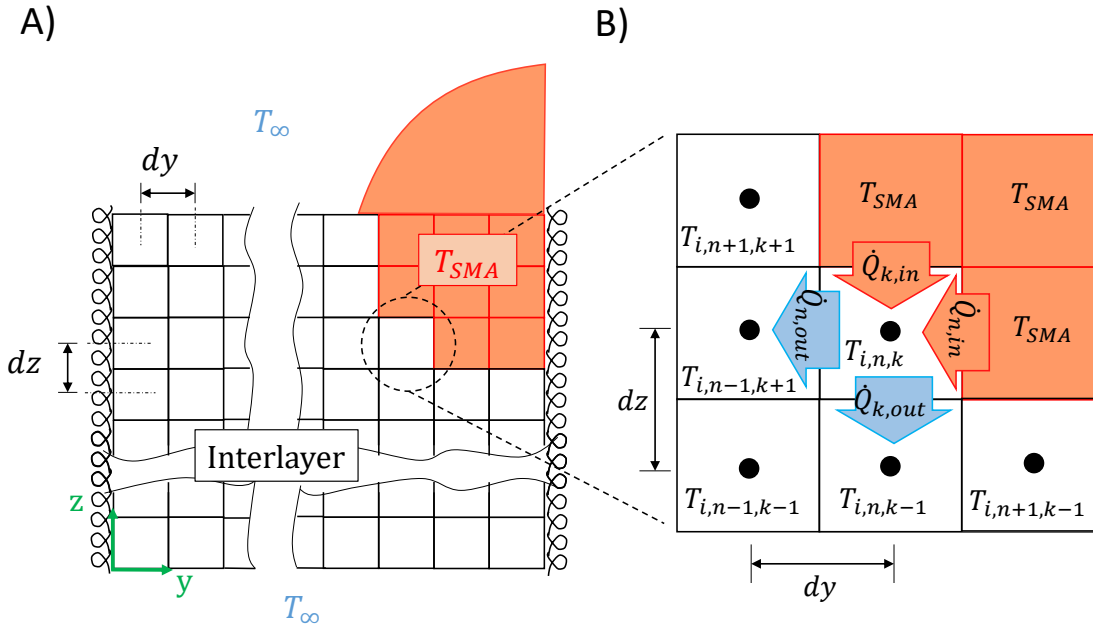


Figure 6.9: A) Illustration of the approach to 2D thermal system modeling. The interlayer and substrate were spatially discretized in the z and y directions. Utilizing symmetry and periodicity while disregarding substrate-related effects minimizes the area to be studied. B) Specify the 2D mesh, including SMA and interlayer elements. The heat transfer between nodes is illustrated for the node with the index i,n,k .

as shown in figure 6.9. The spatial differentiation in the y - and z -directions are equal, with $dy = dz$. The mesh consists of nodes with properties of the interlayer and SMA nodes, as illustrated in figure 6.9 A. At the beginning of each heat transfer simulation step, the temperature of all SMA wire nodes is set to the current temperature of the SMA T_{SMA} . The transient heat flow is computed by solving the heat conservation equation 2.14 for each node. The explicit finite difference method with forward difference in time and central difference in space propagation is used to solve this fundamental transient heat transfer problem. Nodal computations take place in the center of each element, indexed with n,k (see figure 6.9 B). The sequential solution of the system of equations results in a numerical error, which can be affected by variations in the time increment. The maximum permissible time increment is derived from the Courant-Friedrichs-Lewy (CFL) stability criteria [50] and is smaller by decades compared to the time increment that allows for a stable solution of the SMA material model. The time increment of the heat transfer problem is therefore decoupled from that of the SMA wire segment. While a time step

is solved for the SMA model, multiple time steps can be solved for the heat transport problem, with the temperature increase of the SMA being linearly approximated. The entire algorithm of the SMAHC model is illustrated in the flow chart in figure 6.11. Figure 6.9 B provides a detailed view of the 2D spatial differentiation scheme, which considers only direct neighbors along the y - and z -axis and ignores those along the diagonal. The temperature at the time step $t + 1$ is given by equation 6.59. The change in the internal energy of an element is equal to the sum of heat flows in the neighboring elements.

$$T_{n,k,t+1} = T_{n,k,t} + \frac{\lambda_{int}}{\rho_{int} \cdot c_{int}} \cdot (T_{n,k-1,t} + T_{n,k+1,t} + T_{n-1,k,t} + T_{n+1,k,t} - 4 \cdot T_{n,k,t}) \cdot \frac{dt}{dz^2} \quad (6.59)$$

The accuracy of the geometric representation of the wires depends on the mesh element size. A coarse mesh results in a geometric error. Convergence studies determined the optimal temporal and spatial discretization as a tradeoff between computation time and accuracy (compare figure A.13, A.14 and A.15). The symmetry condition and periodicity are utilized to reduce computational effort, and the temperature field is reduced accordingly. The heat transport at the periodic or symmetric edges is equal to zero. The heat transport at the lower and upper edges is given by heat transfer to the surroundings, with the Nusselt number calculated using equations A.75 and A.74 for a plate emitting heat on the upper and lower sides, respectively. The substrate does not play a significant role in the heating or cooling behavior under the conditions being investigated and is therefore neglected (see figures 5.16 and 5.33).

6.3. SMAHC model with influence of external load

The model is extended to simulate the SMAHC under the influence of external loads. While the assumptions and governing equations for the SMAs' behavior and the thermal domain model of the SMAHC remain the same, the assumptions and equations for the mechanical domain are expanded. According to the characterization experiments described in chapter 5, a static point load acting on the SMAHC is considered. As shown in figure 6.10, the load vector always points in the direction of the negative z -axis and induces a bending moment in the actuator. Accordingly, the moment equilibrium of an infinitesimal element of the actuator in the xz -plane is obtained by equation 6.60.

$$M(x) = F_z \cdot (L - \Delta d_x - x) + M_{SMA} \cdot H(s - L) \quad (6.60)$$

The first term describes the bending moment initiated by the external load, and the second is the one initiated by the SMA. The Heavyside function $H(s)$ indicates that the bending moment due to the SMA only occurs in the area of the active length L of the actuator. A coordinate transformation between the X and S coordinate is done by the

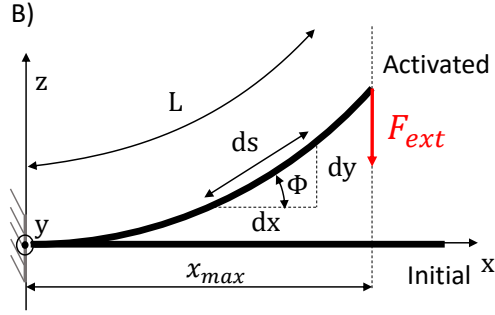


Figure 6.10: 2D representation of the mechanical domain, including the external force vector F_{ext} .

geometric relationship with the curvature at an infinitesimal element of the actuator given by equation 6.61.

$$x = \cos(\Phi) \cdot s \quad (6.61)$$

Equations 6.60 and 6.61 are substituted into the differential equation for the elastic beam 2.35. Deriving the resulting equation twice according to the coordinate S gives the derivative for the curvature Φ'' of the actuator by equation 6.62. Whereby $\delta(s)$ is the Dirac delta distribution.

$$\Phi'' = \frac{1}{E_{sub} \cdot I_{sub}} \cdot (-F_z \cdot \cos(\Phi) + M_{SMA} \cdot \delta(s - L)) \quad (6.62)$$

Equations 6.63 to 6.65 represent the boundary conditions.

$$\Phi(s = 0) = 0 \quad (6.63)$$

$$\Phi'(s = L) = M_{FGL} \quad (6.64)$$

$$\Phi'(s = 0) = m_0 \quad (6.65)$$

The curvature Φ' at the position $s = L$ can be estimated by solving the differential equation 6.62 numerically for the estimated curvature m_0 at the position $s = 0$. The calculated curvature $\Phi'(s = L)$ should match the boundary condition specified in 6.64. The difference between these two values is minimized to within a predefined deviation using the secant method. The solution to equation 6.62 is obtained using the Runge-Kutta method with the known value for m_0 . Finally, the rotation angle around the y-axis at any point along the SMAHC is determined, allowing for the calculation of deflections in the x- and z-directions using equations 6.66 and 6.67.

$$\Delta x(s) = \int (\cos(\Phi) - 1) ds \quad (6.66)$$

$$\Delta z(s) = \int \sin(\Phi) ds \quad (6.67)$$

6.4. Model algorithm

Figure 6.11 depicts the model algorithm's flowchart. The algorithm consists of the initialization and solving process. Initialization comprises the domains of the SMA model and the mechanical and thermal domain of the SMAHC system. The user must define all material and geometric parameters and the initial values and discretization parameters. In addition, the type of model used to approximate the heat loss due to conductivity can be selected. During the initialization of the thermal domain, the number of steps to be performed for a time step of the SMA model is distinguished based on the mesh-dependent stability criterion.

A list of sequences must be provided as input for processing. Each sequence is specified by the electrical current delivered and the exposure time, denoted by $t_{sequence}$. The solving process begins with the first sequence. As the model is not fully-coupled, the domains are solved sequentially. Sequential solving includes solving the SMA model, the thermodynamic domain, and the mechanical domain of the SMAHC system. The calculation rule for the change in martensite fraction and the change in enthalpy is determined using the decision tree depicted in figure 6.5 to solve the SMA model. With a known rule for the evolution of martensite fraction, the nonlinear equation system of the SMA model is solved. The resulting output is utilized in the thermal and mechanical domains.

Each call to the heat transfer algorithm takes the SMA Temperature T_{SMA} as input. Initially, the increase in temperature is linearized based on the specified number of steps. The following methods are repeated during each heat transfer time step. First, the time and linearized temperature of the SMA are incremented. Subsequently, the respective step's conductive energy loss E_{cond} is calculated, and the temperature field is updated. The energy losses of all time steps are cumulated. After executing the last iteration loop, the total heat loss E_{loss} is obtained by summing the cumulated conductive and convective heat losses. This heat loss is utilized as an input for the SMA model in the next step.

The mechanical domain equations system is solved using the martensite fraction, an output of the SMA model. Ultimately, this yields the SMAHC bend line for each time step. The solution procedure is executed with constant supplied current as long as the simulated time is less than the sequence time. If there are other sequences to process, they are processed sequentially until the final one, at which point the solution process concludes.

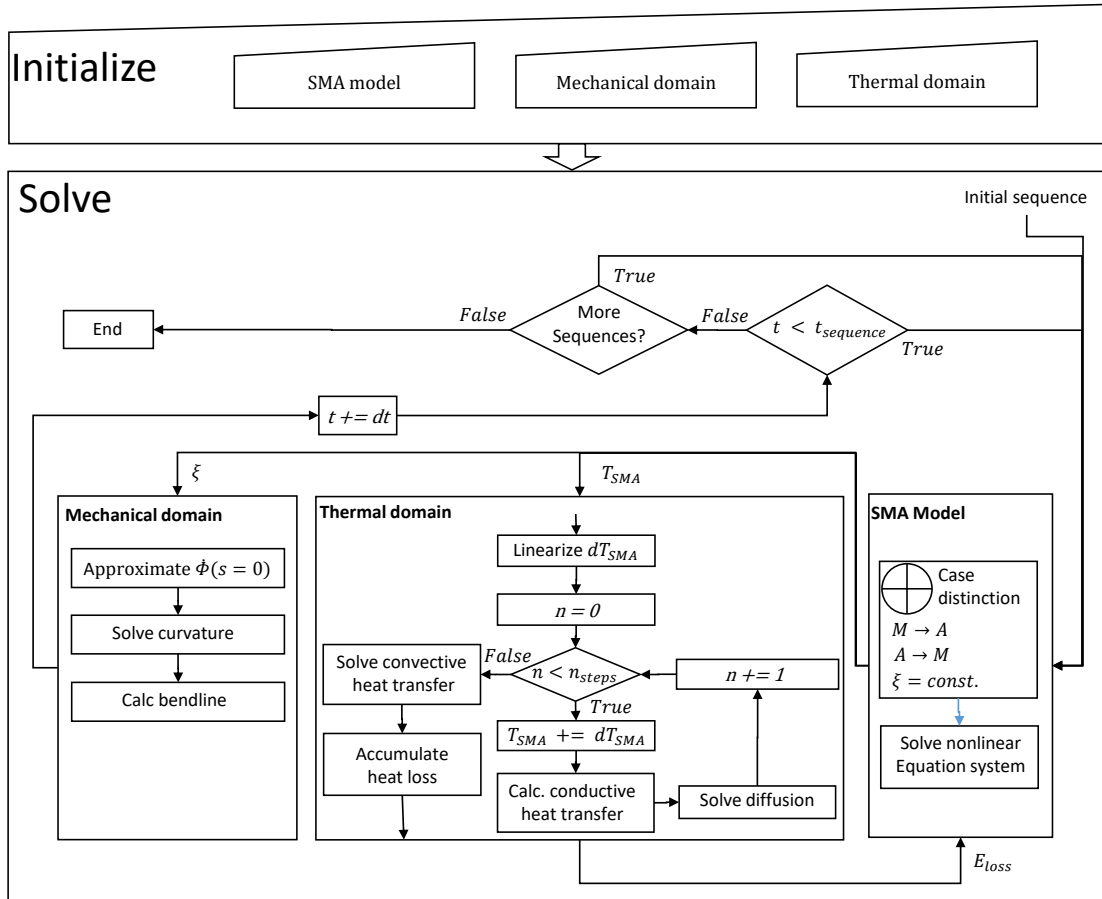


Figure 6.11: Model algorithm flow chart.

6.4.1. Implementation

The physical model is implemented using the Python programming language. The **main** program A.6.1 includes the initialization and subsequently runs a while loop, incrementing time until the specified time to simulate is reached. The initialization includes also the generation of a **Heat_transfer** object (compare class definition A.6.3), that represents the heat transfer model and the generation of a **Mechanical_domain** object (compare class definition A.6.4), that represents the mechanical domain model. During execution of the main program for every time step the **lumped SMA model** script A.6.2 is called to solve for the SMA's state variables. The lumped SMA model starts with a case distinction, that implements the decision tree, realized as nested conditional expressions. Depending on the conditions, a sub-function solves the equation system for an SMA wire section. The **scipy.optimize** library's **fsolve** function was used for this purpose, as it can handle any nonlinear equation system. The roots of the equation system are found for a given start estimation, with the output from the previous increment serving as the start estimation for the current increment. For the first increment, initial values for the stress of the SMA, its martensite fraction, and the temperature of the SMA and interlayer must be

estimated according to the actuator's initial state. For example for a SMAHC exposed to a specific ambient temperature below austenite start temperature, it is appropriate to set the temperature of the interlayer and SMA to the ambient temperature and the martensite fraction to one. The initial mechanical stress is zero if the SMA grid is mounted without preload. Table 6.1 comprises the user input besides SMAHC properties, and table A.9 in the appendix gives an overview over all parameters describing the SMAHC's material and geometric properties. In the subsequent step after solving for the SMA's state variables, the temperature is incremented, and the heat transfer objects **do_timestep** method is executed to compute energy loss due to conduction. The computation time is kept low by solving the diffusion equation using high-performance matrix operations from the **NumPy** package. The curvature at the clamping position of the SMAHC is calculated using the Newton-Raphson method. This method is implemented as **newton** function, and part of the **scipy.optimize** package. The Runge-Kutta method is used to solve for the curvature and slope. This method is implemented as **solve_ivp** function and part of the **scipy.integrate** package. The function enables solving initial value problems. For convenience, the entire code is broken down into the aforementioned four scripts that can be found in the appendix in section A.6:

- **Main**
- **Lumped SMA model**
- **Heat transfer model**
- **Mechanical domain model**

An overview over all essential variables used is provided by figure A.9 and A.10. Each simulation's result is initially stored in RAM as a NumPy array. The time resolved output variables generated are listed in table 6.2.

Table 6.1: Additional user input parameters beside SMAHC geometric and material parameters.

| Parameter | Description |
|------------------------|---|
| <i>load</i> | External static load, pointing in the negative z-direction |
| <i>alpha_elastomer</i> | Heat transfer coefficient between elastomer and ambient. The coefficient can be approximated according to [71]. Equations can be found in the appendix A.1. |
| <i>Tu</i> | Ambient and initial temperature of the SMA and the interlayer |
| <i>sequences</i> | Sequences composed of supplied current and exposure time |

Table 6.2: Time resolved output of the implemented SMAHC model.

| Parameter | Description |
|--|---|
| <i>mf</i> | An averaged martensite fraction for all elements in s-direction |
| <i>T</i> | The homogeneous SMA wire's temperature |
| <i>stress</i> | An SMA wire's stress in s-direction averaged over all elements |
| <i>strain</i> | An SMA wire's strain in s-direction averaged over all elements |
| <i>r</i> | The homogeneous SMA wire's resistivity |
| resistance | The homogeneous SMA wire's resistance |
| <i>real_A_s</i> , <i>real_A_f</i> , <i>real_M_s</i> , <i>real_M_f</i> | The stress-influenced transformation temperatures |
| <i>E</i> | The SMA wire's Young's Modulus |
| <i>eps_tr</i> | The current maximum, stress dependent transformation strain of the SMA wires |
| <i>u_d</i> | The interlayer's temperature field |
| <i>Ein</i> | The electrical energy supplied to an SMA wire |
| alpha | The temperature dependent convective heat transfer coefficient for the upper half of the wire |
| <i>E_conv</i> | The convective energy loss of an SMA wire |
| <i>E_cond</i> | The conductive energy loss of an SMA wire |
| <i>E_loss</i> | The sum of energy losses of an SMA wire |
| <i>U</i> | The change in internal energy of an SMA wire |
| <i>a</i> | The proportion of specific heat during the transformation of an SMA wire |
| <i>deflection</i> | The deflection at the end of active area in z-direction |
| <i>xmax</i> | The position in x-direction of the end of active area |

7. Identification of material parameters

Respective materials were characterized to quantify the material properties necessary for SMAHC modeling. The tables in section 7.2 provide characterization results of the SMA wires, the elastomer utilized for the interlayer, and the steel used for the substrate. Since the clip and crimp anchor are not accounted for in the model, these materials were not further examined. Before each table, the property determination procedures and methodologies are presented.

7.1. Methods

This section presents the techniques utilized to estimate the properties of materials necessary for modeling the SMAHC.

Before testing, each SMA wire was load-free, heated to 130 °C for 10 minutes, and then cooled to RT to guarantee proper characterization conditions. As a compromise, a temperature of 130 °C was selected to ensure that the temperature was above the austenite transformation point while avoiding overheating. This process is referred to as normalization. The SMA wires were subjected to the same normalization procedure during the production of the SMAHCs 5.1.

Transformation temperatures A_s, A_f, M_s, M_f :

Using Differential Scanning Calorimetry (DSC), all transformation temperatures in load-free states, including austenite start and finish and martensite start and finish temperatures, were measured. *Mettler Toledo GmbH's DSC 3+* instrument was utilized for the trials. As this is a fundamental measurement for SMA characterization, the *ASTM F2004* provides a standard [140], and the DSC manufacturer provides a guideline [141]. [142] provides expanded information on the experimental approach and data analysis procedure. The standard requires that the trials be repeated with at least five samples. The bottom of the sample pan needs to be covered as much as possible by the specimen to achieve efficient heat transfer and guarantee proper measurement. Several wire sections were used to obtain the required coverage. Figure 7.1 displays an example of a sample pan

containing wire pieces. The wires' sample weight was around 40 mg. The experiment



Figure 7.1: Sample pan for DSC measurement filled with SMA wire sections to achieve high pan coverage.

was also conducted with the elastomer used as interlayer and the steel used as substrate. The sample weight of steel was 55 mg, whereas the elastomer was 25 mg. A *Mettler Toledo Excellence Plus* balance with a resolution of 1/100 mg was utilized for weighing the sample weight. The DSC experimental approach consisted of seven sections.

1. Cool down from RT to -90 °C
2. Isotherm for 10 min
3. Heat to 150 °C
4. Isotherm for 5 min
5. Cool down to -90 °C
6. Isotherm for 10 min
7. Heat to RT

The heating and cooling rates were set to 10 K/s following [142]. The austenitic transformation temperatures were then derived by analyzing the endothermic transformation peak that emerged during heating in process section 3. For analysis, both sides of the peak were fitted with tangential lines, and transformation temperatures were then denoted by intersections of these lines with the baseline. The martensitic and R-phase transformation temperatures were derived from the exothermic transformation peak of process section 5 using the same methodology. An exemplary measurement is shown in figure 7.2.

Latent heat $\Delta H_{M \rightarrow A}$, $\Delta H_{A \rightarrow R}$, $\Delta H_{R \rightarrow M}$:

The latent heat was derived using the same procedures to estimate the transformation temperatures. The area enclosed by the corresponding peaks and baseline on the thermogram provided these values. Additionally, integration limits were specified along the temperature axis. The exothermic transition maxima of the austenite to R-phase transformation and the R-phase to martensite transformation coincided. The integration limit for

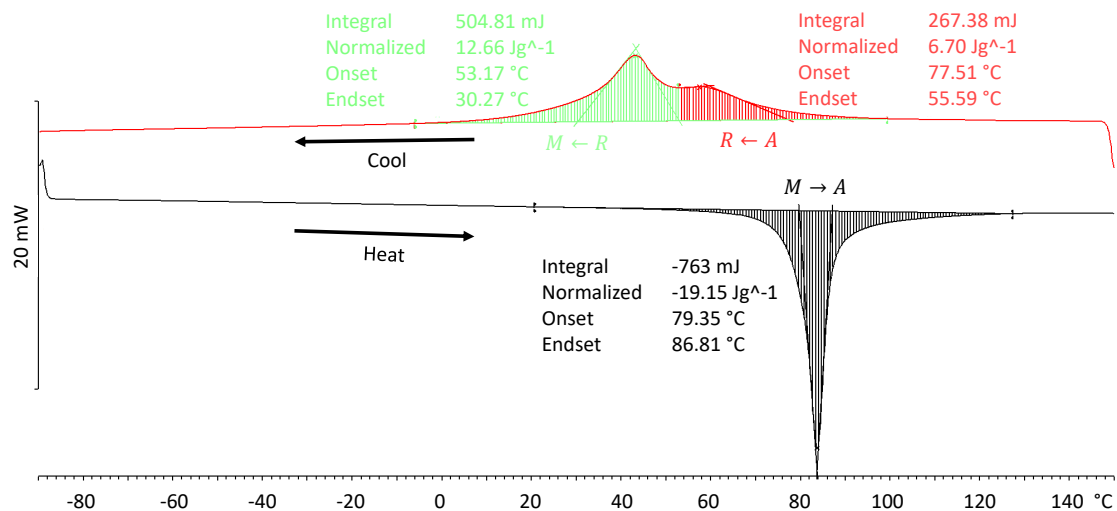


Figure 7.2: An exemplary DSC measurement with the first heating and second cooling curves as well as the evaluated latent heats and on- and endset temperatures.

each peak was established where the local minimum exists between the two transformation peaks.

Specific heat capacity c_M , c_A , c_{int} , c_{sub} :

The specific heat capacity was determined using the same experiment to estimate the transformation temperatures. The same measuring instrument and procedure were used for the steel and the elastomer. Laser cutting was utilized to prepare steel samples with a diameter of 4.80 mm. The elastomer samples, with a diameter of 4.5 mm, were prepared by punching from mats having a flat surface. Two comparison measures were conducted according to the standard *DIN EN ISO 11357* [143]. One was conducted with an empty sample pan and the other with a sapphire. Using the manufacturer-supplied software *Mettler STARe V16*, the heat capacity was computed using the sample curve, the empty sample pan reference curve, and the sapphire curve.

Diameter, thickness, length d , t_{sub} , p_{SMA} :

The wire's diameter was measured using an external micrometer, *Mitutoyo Digital Typ. No. MDC-25MXT*. The measurement was repeated on three different samples at three separate locations. The diameter measurement was confirmed by analysis of microscope images taken with *Leica's DM 6000M*-type reflected light microscope. The microscope photos were captured at 250x magnification. The thickness of the substrate and the distance between the wire's center and the substrate's surface was also measured using microscope images. An exemplary microscope image is given in figure 7.3. **Density** ρ_{SMA} , ρ_{int} , ρ_{sub} :

The density was measured according to Archimedes' principle with the help of the weigh

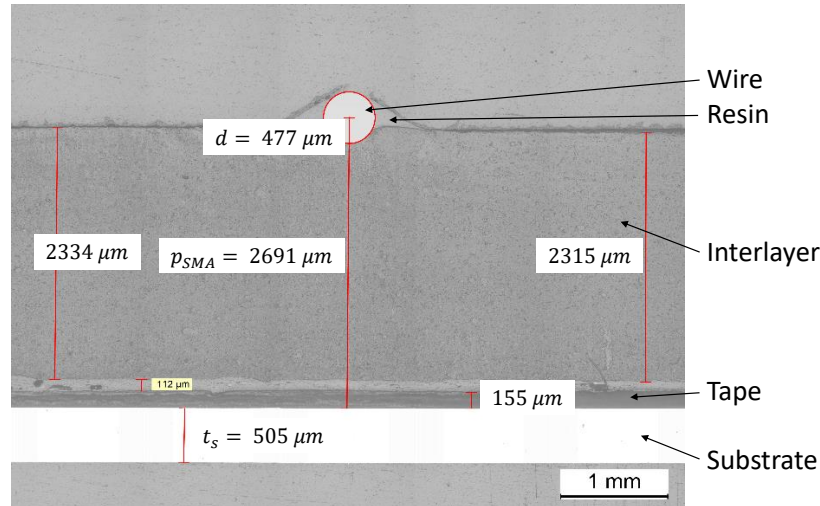


Figure 7.3: Exemplary microscope image showing measurement of distance between SMA wire and substrate p_{SMA} , substrate thickness t_s and SMA diameter d .

Ohaus DV214C, including *density measurement kit 00223015*. The methodological procedure followed the standard *DIN EN ISO 1183* [144]. The weight of the sample was measured in air and distilled water with a known density. According to Archimedes' principle, the buoyancy and, thus, the density of the sample can be determined.

Modulus of elasticity E_A , E_M , E_{Sub} :

The modulus of elasticity of the steel was measured using the universal testing machine *Zwick/Roell Retroline 1445*. The load cell used from AST of type KAP-S had a nominal measuring range of 10 kN with an accuracy class of 0.05. Test specimens in the form of dogbones were cut out of a plate by laser cutting. Measurement was carried out at RT following standard *DIN EN ISO 6892* [145]. The data acquisition started from a preload of 2 MPa, and the test was performed at a speed of 1 mm/min. The experiment was repeated with 6 valid samples. The modulus of elasticity of the SMA wire was measured in martensitic and austenitic states separately. In order to vary specimen temperature during the test, the *Zwick/Roell 1485* universal test machine was used for the monotonic loading experiments. The test device provides a temperature chamber that allows measurement under different ambient and, thus, specimen temperatures. Tensile tests were carried out according to the instructions given in [61]. The free length of the wire specimen was 120 mm. The preload was 1 N. Martensitic state parameters were conducted at an ambient temperature below martensite finish temperature M_f (-25 °C) and for the austenitic state beyond austenite finish temperature A_f (110 °C). Before the experiment, the temperature chamber was conditioned at respective temperatures for one hour. Prior to every test, the specimen was conditioned at the respective temperature for 10 minutes. Tests were carried out quasi-static with a strain rate of 1 %/min to avoid influences on wire temperature

due to latent heat. In each case, two tests were performed until specimen failure and two with unloading after previously specified strains were reached. The elastic modulus could be determined by applying tangents to the respective measurement curves.

Resistivity ρ_A, ρ_M :

The electrical resistance was measured using a four-wire measurement. The system source meter used to carry out the experiments was the *2601 A* from *Keithley*. Resistance was measured at RT and in a temperature chamber beyond austenite finish temperature A_f (100 °C). The measuring current was kept constant at 0.1 to avoid influencing the wire temperature due to Joule's heat. Resistance measurement was performed with at least three different wire lengths to determine parasitic resistances such as junction and lead resistances. The resistances were plotted over the respective wire length. The slope of the linear relationship correlated with the length-specific resistance and the ordinate intercept with the parasitic resistances. Wire length and crosssection were only measured at a temperature below M_f (RT). Therefore the variables were denoted as L_{RT} and A_{RT} . At this temperature, the wire's state in terms of phase composition was undefined. Both twinned and untwinned martensite were present. No distinction between the two martensitic phases was made, and measured resistance at RT was referred to as martensite resistance R_M . To not distinguish between martensitic phases and not consider changes in the diameter during the phase transformation are common assumptions for lumped models [65]. Finally martensite resistivity ρ_M is defined as $R_{RT} \cdot A_{RT}/L_{RT}$ and austenite resistivity ρ_A as $R_{100^\circ C} \cdot A_{RT}/L_{RT}$.

Stress free transformation strain $\epsilon_{tr,TWE}$:

The transformation strain caused by residual stresses in the trained wire was determined using two test rigs. With both test configurations, the same value was determined. The objective was to compare the degree to which different test procedures yield distinct outcomes. The first test device was the *TA Instruments Discovery DMA850*. The test was conducted with a restricted force of 0.6 N. While the force was controlled, the temperature in the test chamber was altered as follows:

1. Heat from RT to 150 °C
2. Cool down to - 40 °C
3. Heat to 150 °C
4. Cool down to RT

The temperature was controlled by employing a closed feedback loop. The rate of heating and cooling was fixed at 10 K/min. During experimentation, the temperature in the

gas-filled chamber was measured using a thermocouple that was put in close proximity to the specimen but did not contact it. Due to the relatively high rate of temperature change, there was a lag between the measured ambient temperature and the temperature of the specimen. For this reason, the measured temperature must not be utilized to infer the SMA temperature. However, the tested temperature range was much above the transition temperatures, so it was assumed that the transformation was completed in each instance. The reference length of the wire, which is needed for strain evaluation, was adjusted to a temperature above the austenite finish temperature A_f (150 °C). The transformation strain was then assessed during the third process sequence. For evaluation, the strain values at 23 °C and 130 °C were used, in contrast to the standard *ASTM E3098-17* [146] for assessing thermal free recovery. The standard prescribes the use of the strain values at the austenite start A_s and finish temperatures A_f . The deviation from the standard was necessary because conversion temperatures, as described above, could not be determined with sufficient accuracy. The temperatures used allowed the assumption of complete phase transformation. In general, the transformation strains measured this way were above those that would be determined according to the standard. It is essential to mention that DMA test equipment with liquid fluids and mixers achieves significantly improved heat transfer and increased temperature distinction accuracy.

The same test was conducted using an *IVW*-developed testbench approach, referred to as constant load testbench (CLT) in the following. The CLT is depicted in the appendix A.8. An SMA wire was secured between two clamps on the test apparatus. The top clamp had a fixed bearing, but the lower clamp was movable and had a single degree of freedom along the wire's axis. The weight of the bottom clamp and bearing was roughly 300 grams. Joule heat was applied to the 180 mm length of wire. The temperature was monitored along a 30-mm length of the wire during an experiment using thermal imaging. *Micro-Epsilon's VGA 640* infrared imager was combined with microscope optics for this purpose. Each wire was painted with a known emission coefficient to facilitate accurate temperature monitoring. The use of paint is detailed in section 5.1. *Panasonic's* laser triangulation sensor *HG-C1200-P* enabled 200 μm precise wire length measurements. There were three phases in the testing procedure. First, the actuator was heated to a temperature greater than austenite finish temperature A_f . The specimen secondly was cooled to RT from this initial condition and finally reheated to the starting temperature. Temperature and wire length were monitored throughout the last two steps. $\Delta I = 0.01A$ was the incremental change in current flux that caused the temperature to increase and decrease. For each step, the current was first adjusted to the new level. After a delay of 8 s, thermodynamic equilibrium was attained, and measurement readings were recorded. The evaluation of the transformation strain was carried out in the same way as outlined for the DMA. This approach had the advantage over measuring in a temperature chamber in that wire temperature was measured directly, and the wire itself was heated. Consequently, employing

the testbench approach of IVW, improved the temperature measurement's precision and accelerated the experiment. However, in the absence of a temperature chamber, lower temperature was restricted to RT, and the minimum mechanical load of 15 MPa was five times more than what was specified for the DMA.

Maximum transformation strain $\epsilon_{tr,max}$:

The current transformation strain at various constant stress levels was monitored. To determine the maximum transformation strain, as explained in section 2.2.2, the value pairs of stress and strain were fitted with equation 2.9. On the CLT (compare figure A.8), the requisite activation experiments on the SMA wire under the effect of varied external forces were performed. The test protocol was identical to that described for Stress-free transformation strain, except that weights were connected to the bottom clamp. Weights were connected after the wire was heated to a temperature above A_f . The reference length of the wire was in the high-temperature state. The experiment was conducted with 300, 4300, and 8300 g, corresponding to approximately 15, 215, and 415 MPa.

Stress influenced coefficients C_{As} , C_{Af} , C_{Ms} , C_{Mf} :

Clausius-Clapeyron or stress-influenced coefficients describe the influence of stress on the transformation temperatures of SMAs. For details, see figure 2.6 and review section 2.2.2. The coefficients were derived using the experimental data to characterize the maximum transformation strain. The tangent method was first used to evaluate the transformation temperatures for each load level (compare figure A.12 in the appendix). In figure 7.5, the respective transformation temperatures were plotted against the applied load, and the slope of the respective linear fit then provided the corresponding coefficient for each transformation temperature.

Heat conductivity λ :

Before testing, the specimens were conditioned for 2 hours according to *ISO 291*. An experiment to characterize the heat conductivity was carried out following *DIN EN ISO 11357-8* [147] using the *DSC 831e from Mettler Toledo*. Test specimens with a diameter of 5.5 mm and height of 3 mm were punched out of an elastomer mat with a smooth surface. Gallium with certified purity was used as the melting substance. The experiment was carried out with specimen and reference at a heating rate \dot{T} of 0.5 K/min until 10 K beyond the melting temperature of the gallium was reached. The heat flux \dot{Q} was recorded during the experiment. Subsequently, the gradients of the melting peaks of the reference $\dot{Q}_r/\Delta T_r$ and the specimen $\dot{Q}_s/\Delta T_s$ were evaluated using *Mettler Toledo's* software. The thermal conductivity could then be calculated according to $\lambda = h/(A \cdot (\Delta T_s/\dot{Q}_s - \Delta T_r/\dot{Q}_r))$. The test was repeated 5 times.

7.2. Results

The tables 7.1 and 7.2 list the results of the characterizations assigned to the respective materials. figure 7.4 shows the exponential regression to determine the maximum transformation strain ϵ_{max} and the fit parameter $k_{\epsilon, tr}$. The current maximum transformation strain ϵ_{tr} is plotted against the constant load. Load-dependent transformation strain values from DMA for unloaded condition value and CLT measurements for loaded condition were used. In figure 7.5, the evaluation of the stress-influenced coefficients is illustrated.

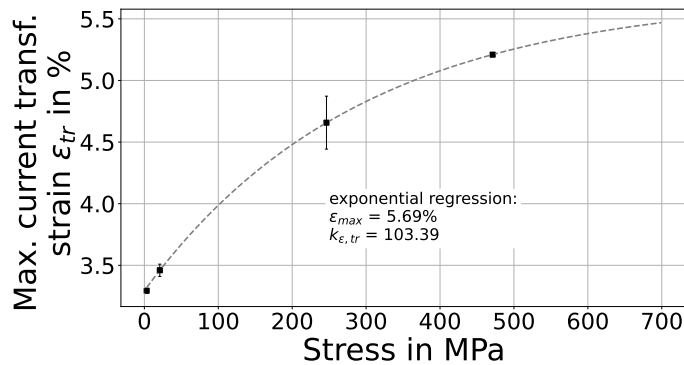


Figure 7.4: Determination of maximum transformation strain $\epsilon_{Tr,max}$ and fit coefficient $k_{\epsilon, tr}$ by exponential fit.

Measured values recorded with the DSC are shown in blue, and those recorded with the CLT are in shades of gray. If the DSC-measured values are included in the evaluation, low coefficients of determination are obtained for the linear fits. While the latent heat is evaluated for the determination of the transformation temperatures using DSC, the length change is evaluated for the determination by using the CLT. However, since the change in length of the SMA wire is of significant importance, the data recorded with the CLT were utilized for evaluation.

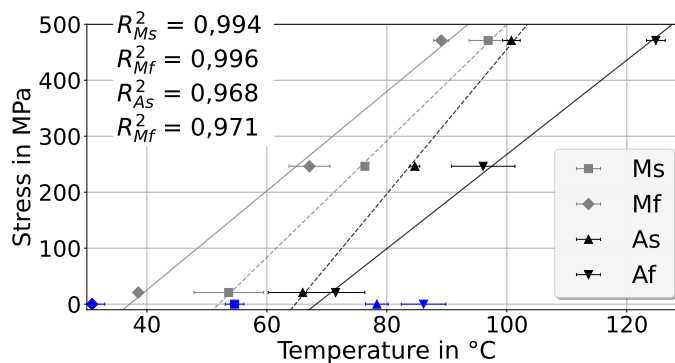


Figure 7.5: Determination of stress-influenced coefficients C_{Mf} , C_{Ms} , C_{As} , C_{Af} using linear fits. Blue: DSC measurements; Shades of gray: CLT measurements

Table 7.1: Results of the SMA characterization according to the methods described in the previous section.

| Parameter | Symbol | Unit | Mean | Confidence interval | Standard deviation | Individual measurements |
|-----------------------------------|------------------------------|-------------------|--------|---------------------|--------------------|-------------------------|
| Austenite start temperature DSC | A_s | °C | 78.34 | 0.71 | 0.77 | 7 |
| Austenite finish temperature DSC | A_f | °C | 86.12 | 1.41 | 1.522 | 7 |
| Martensite start temperature DSC | M_s | °C | 54.62 | 0.58 | 0.64 | 7 |
| Martensite finish temperature DSC | M_f | °C | 30.87 | 0.80 | 0.86 | 7 |
| Austenite start temperature CLT | A_s | °C | 64.70 | - | - | 1 |
| Austenite finish temperature CLT | A_f | °C | 68.17 | - | - | 1 |
| Martensite start temperature CLT | M_s | °C | 51.90 | - | - | 1 |
| Martensite finish temperature CLT | M_f | °C | 36.87 | - | - | 1 |
| Density | ρ | kg/m ³ | 6561 | 169 | 250 | 11 |
| Diameter | d | mm | 0.472 | 0.001 | 0.001 | 18 |
| Specific heat capacity @ 0 °C | c_M | J/kgK | 444.29 | 25.52 | 44.19 | 14 |
| Specific heat capacity @ 120 °C | c_A | J/KgK | 488.57 | 33.09 | 57.30 | 14 |
| Latent heat | $\Delta H_{M \rightarrow A}$ | J/kg | -18580 | 444 | 480 | 7 |
| Latent heat | $\Delta H_{A \rightarrow R}$ | J/kg | 6819 | 900 | 975 | 7 |
| Latent heat | $\Delta H_{R \rightarrow M}$ | J/kg | 12869 | 822 | 888 | 7 |
| Youngs modulus | E_A | GPa | 30.25 | 2.25 | 0.25 | 2 |
| Youngs modulus | E_M | GPa | 19.17 | 0.59 | 0.24 | 3 |
| Resistivity | $\rho_{el,A}$ | $\Omega mm^2/m$ | 0.802 | 0.001 | 0.000 | 3 |
| Resistivity | $\rho_{el,M}$ | $\Omega mm^2/m$ | 0.820 | 0.011 | 0.009 | 5 |
| Free transformation strain | $\epsilon_{Tr,TWE}$ | % | 3.29 | 0.02 | 0.02 | 5 |
| Maximum Transformation strain | $\epsilon_{Tr,max}$ | % | 5.69 | - | - | 1 |
| Stress influenced coefficients | C_{As} | MPa/°C | 12.92 | - | - | 1 |
| Stress influenced coefficients | C_{Af} | MPa/°C | 8.42 | - | - | 1 |
| Stress influenced coefficients | C_{Ms} | MPa/°C | 10.40 | - | - | 1 |
| Stress influenced coefficients | C_{Mf} | MPa/°C | 8.87 | - | - | 1 |
| Fit parameter | $k_{\epsilon,tr}$ | - | 103.39 | - | - | 1 |

Table 7.2: Results of the steel and elastomer characterization according to the methods described in previous section

| Parameter | Symbol | Unit | Mean | Confidence interval | Standard deviation | Individual measurements |
|--------------------------------|-----------------|-------------------|---------|---------------------|--------------------|-------------------------|
| Steel | | | | | | |
| Density | ρ_{sub} | kg/m ³ | 7876 | 53 | 74 | 10 |
| Specific heat capacity @ 23°C* | c_{sub} | J/KgK | 484.00 | 24.33 | 19.60 | 5 |
| Youngs modulus | E_{sub} | GPa | 215.67 | 3.19 | 3.03 | 6 |
| Heat conductivity @ 23 °C* | λ_{sub} | J/KgK | 14.88 | 0.18 | 0.15 | 5 |
| Inerlayer | | | | | | |
| Density | ρ_{int} | kg/m ³ | 1038 | 2 | 1 | 3 |
| Specific heat capacity @ 20°C | c_{int} | J/kgK | 1619.00 | 25.08 | 35.06 | 10 |
| Heat conductivity | λ_{int} | W/mK | 0.180 | 0.005 | 0.004 | 5 |

* The values were not determined experimentally but were taken from the data sheets of several manufacturers. [148, 149, 150, 151, 152]

8. Model validation

This chapter validates the SMA and the SMAHC model. First, the SMA model was validated by comparing simulation results, using the material parameters found in chapter 7 as input, with experimental data. For this purpose, an experiment with SMA wires was conducted under spring load conditions. Subsequently, the SMAHC model synthesized in chapter 6 was validated by comparing simulation results with SMAHC characterization data from chapter 5. Before each validation, a convergence study was performed to establish the model's optimal temporal or spatial step size. The findings of the convergence studies are provided in the appendix in section A.8.

8.1. SMA wire model validation

The behavior of the SMA, acting against a spring with a linear characteristic, was investigated. The results were used for validation purposes. For this reason, the wire was fastened horizontally at its two ends. One end was fixed with zero degrees of freedom, while the other was attached to a leaf spring. The test setup is depicted in figure 8.1.

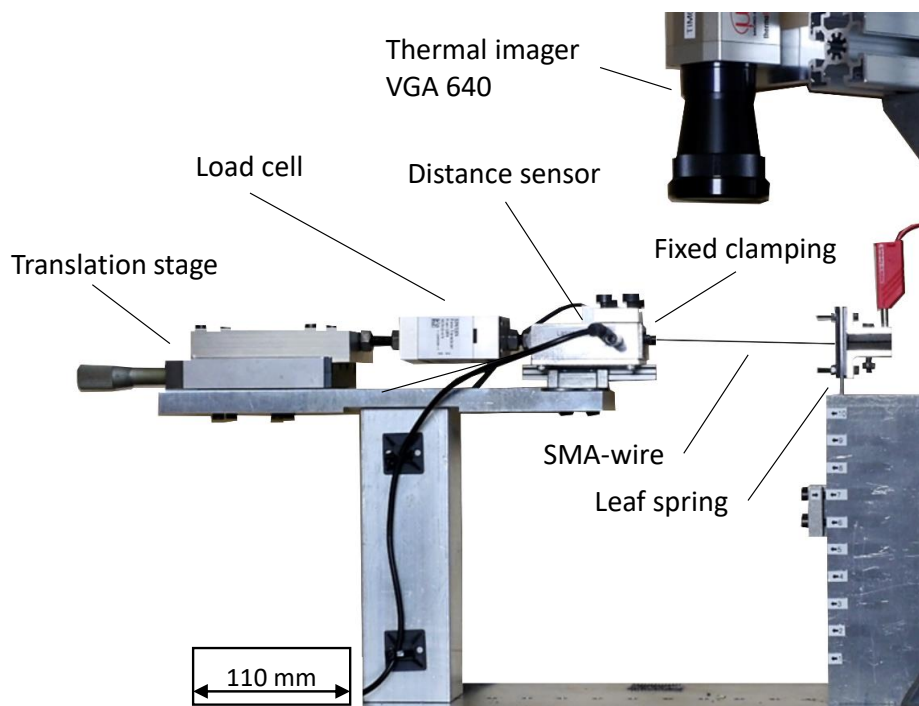


Figure 8.1: Leaf spring test setup and components.

A wire was fixed at the beginning of the experiment, and a 3 N preload was manually added using a translation stage. Force was measured by a load cell on the side with the fixed clamping. The SMA was heated, and phase transition was initiated by delivering a continuous direct current of 2.0 A. The spring was deflected due to wire contraction, which corresponded to an increase in load. After measuring a temperature of 130 °C at the SMA wires surface, the supply current was cut off, and the wire was cooled by free convection. Throughout the procedure, the spring deflection and load were measured. In order to calculate the stress-strain ratio resulting from the spring's stiffness D , the stiffness was converted to the associated modulus E_S using the equation 8.68, where L_0 is the length of the wire in a stress-free austenitic condition and A is the cross-section of the wire.

$$E_S = D \frac{L_0}{A} \quad (8.68)$$

The charts in figure 8.2 show the comparison between experimental data and simulation results. On the left may be seen the thermomechanical coupling, and on the right, the electro-thermomechanical coupling. The stiffness of the spring was 15.5 N/mm, and the preload was 30 MPa. The wire was heated with a current of 2.0 A for 9.5 seconds.

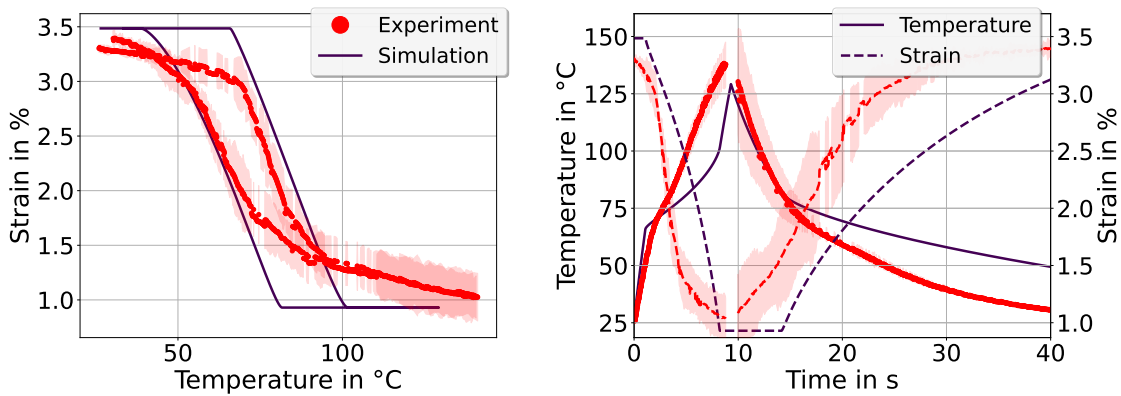


Figure 8.2: Validation of SMA wire model for SMA wire operating against a spring with linear characteristics; Left: Thermomechanical validation; Right: Electro-thermomechanical validation.

The experimental and simulated temperature-strain hysteresis curves agree well when compared. The variances between the maximum and minimum strains that occur are respectable.

The simulated transient deflection curve shows abrupt changes at the end of the martensite to austenite transformation and at the beginning of the re-transformation. This abrupt transformation initiation contrasts the experiment, which demonstrates a constant curve with smooth transitions. An explanation can be given by the cosine approach used for hardening law. This approach allows the simulation of continuous transitions of the martensite fraction-temperature hysteresis curve but leads to abrupt initiation of transient

martensite fraction curve. This abrupt initiation in turn, effects the course of simulated parameters that depend on the martensite fraction. This parameters may all reflect the abrupt transformation initiation. This correlation is clarified in the next section.

Thermal effects due to clamping of the free wire were neglected. In reality, these effects also lead to smoother transitions since the areas of the wire close to the clampings are heated and cooled with a delay depending on the electric current.

While the simulation adequately approximates the heating process, the elongation of the wire during cooling is delayed, and the respective curve gradient is too low. This discrepancy may be an indication of an underestimated cooling rate. The cooling rate in the experiment is increased due to heat dissipation through the fixation.

In general, an overestimation of the influence of the transformation enthalpy can be observed. This overestimation plays a minor role in modeling the SMAHC since the influence of the transformation enthalpy on the time course of the temperature curve decreases with increasing heat transfer into the environment or surrounding layers [49].

8.2. SMAHC model

This section validates the SMAHC model with and without the influence of a static external load. First, the thermomechanical and electro-thermomechanical validation was performed without the influence of an external static load but considering various ambient temperatures. Subsequently, the SMAHC model was validated, taking external loads into account. Figure 8.3 provides an overview of the different state variable evolutions during a SMAHC type C heating-cooling cycle. The SMAHC was heated with a current of 4 A until its temperature reached 130 °C and cooled down under the influence of free convection. Wherever possible, experimentally derived data were compared. The simulation was conducted utilizing the respective parameters used for experimentation.

In the graph in the upper left, the various energy components of the process are examined. The red curve represents the experimentally determined accumulation of electrical energy input, whereas the purple curve represents the simulated accumulation. The accumulated energy input increases during heating, whereas during cooling, no further energy is added, and the level remains constant. The accumulated energy loss is the total of convective and conductive loss fractions. The simulated conductivity fraction is decades more than the convective fraction. For given circumstances, this is feasible. The internal energy shows a maximum at the end of the heating phase. The wire's stored energy is then discharged to the surroundings during the cooling phase.

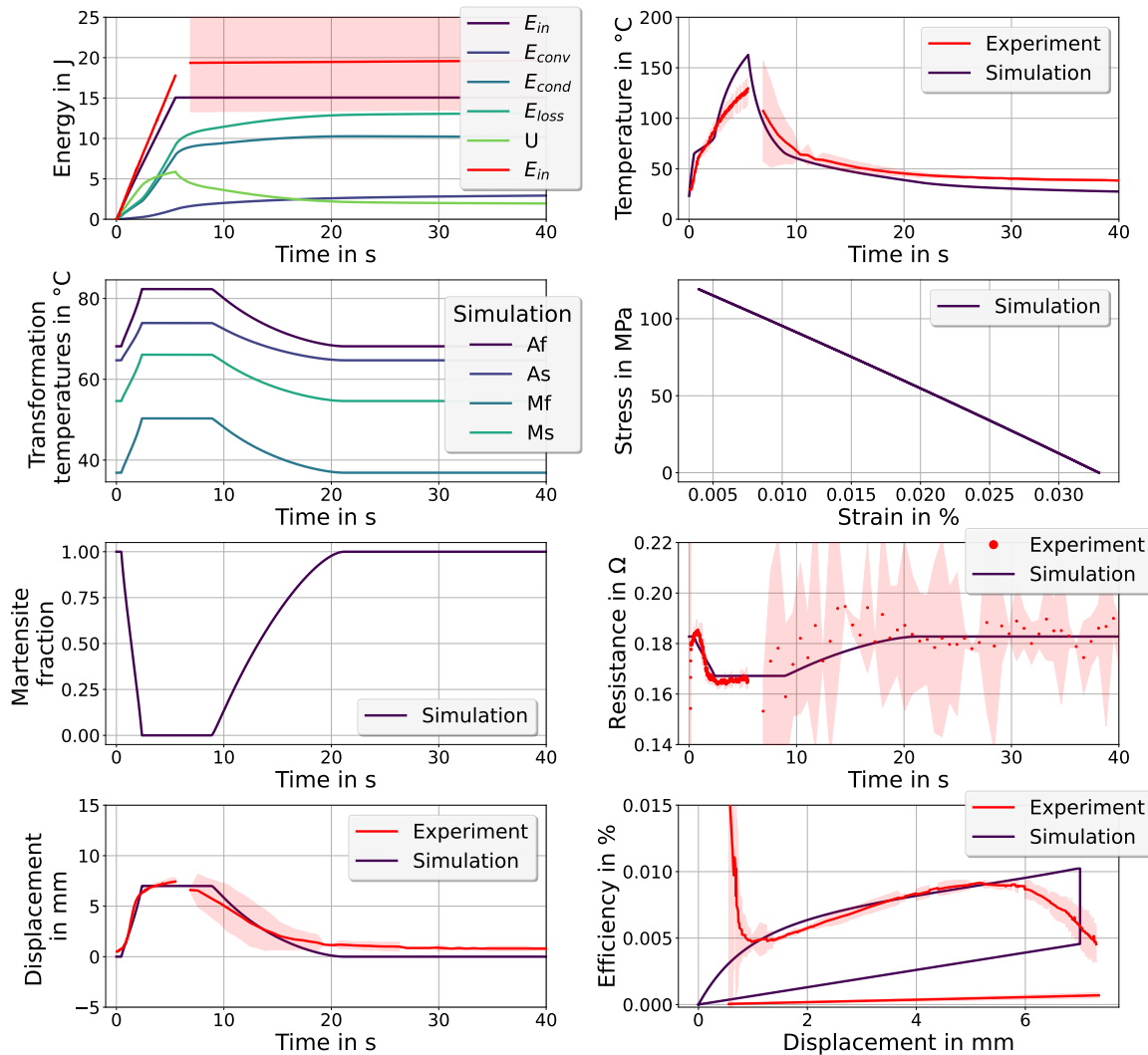


Figure 8.3: Example of the transient SMAHC model's output. At RT, without the influence of an external load, the activation (4 A for 5.5 s) and deactivation (free convection 60 s) cycle of an actuator of type C was simulated and compared with experiments. The simulation findings are shown by solid purple lines, whereas the experimental data are represented by red dots and the confidence interval is displayed for each experiment. Where necessary, a legend provides additional information.

The observed and simulated temperature curves are compared. The simulated impact of enthalpy is overestimated, as is the temperature at the end of the heating phase. However, the temperature was not recorded directly on the wire's surface but rather on the surface of the surrounding resin layer. Consequently, the actual wire temperature must be expected to be higher than the recorded value. The surrounding resin layer also functions as a thermal capacitor, which explains why the impact of enthalpy is reflected only faintly in the measurement.

During the activation phase, the increased stress in the wires caused the transformation temperatures to rise, and vice versa for the cooling process. The behavior simulated is feasible but cannot be compared to actual data. The same holds for the martensite proportion and the stress-strain relationship.

Discrepancies were found when comparing the predicted electrical resistance to experimental data for a single wire. Differences in the qualitative curve progression may be explained by the fact that, for the used modeling approach, the effect of temperature on the single-phase resistance was neglected. Particularly at the beginning of activation, the experiment demonstrated an increase in resistance due to the alloy's temperature increase. The simulation showed constant resistance until phase transformation was initialized and the resistance reduced. The same applies to the cooling process. The minor deviations between simulated and experimental data indicate that the assumptions made fulfill their purpose.

The simulated and experimentally determined deflection at the end of the active length of the SMAHC is compared. The qualitative progression of the simulated deflection curve shows a significant deviation from the experimental data. While the experimental determination is smooth, the simulated curve shows abrupt transitions between areas of transformation and constant deflection. Simulated deflection stays constant when the martensite fraction assumes one of the two extrema. As discussed in the previous section, this discontinuity of the simulation is due to the modeling approach used to describe the hardening or hysteresis.

The experimental deflection-efficiency curve shows a parabolic course and a maximum within deflection limits. As the simulated time-deflection curve's steepest gradient occurs at the end of the austenite transformation, the maximum efficiency was also simulated to occur at the end. The maximum efficiency, therefore, was simulated to occur when the maximum deflection is reached. Due to the qualitative discrepancies between simulated and experimental data, the model does not allow for predicting the optimal deflection in terms of efficiency.

8.2.1. Without external load applied

The correct mechanical output for a given thermal input is a prerequisite for the proper functionality of the electro-thermomechanical model. The thermomechanical coupling of the model was validated by comparing experimental and simulated deflection-temperature curves (compare figure 8.4). The deflection was evaluated at the end of the active area of the SMAHCs s-axis.

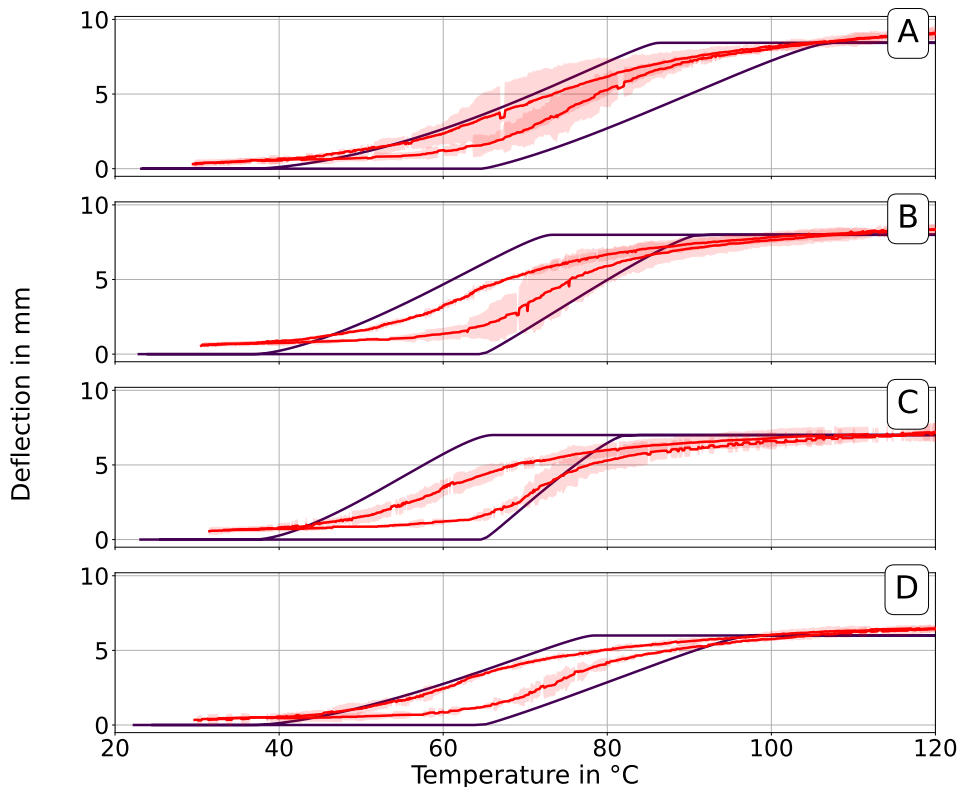


Figure 8.4: Thermomechanical validation of the SMAHC model for the four types of SMAHC without taking external loads into account. Experiments were carried out with supplied electrical current of 3.0 A.

The model is reasonable, even though the simulated results of the deflection are partly outside the 95% confidence interval of the experimentally determined results. The maximum displacement achieved at 120 °C for each actuator type demonstrates good agreement between experiment and simulation. In any case, the experimentally determined deflection hysteresis falls within the approximated hysteresis, which indicates an overestimation of the hysteresis width. The observed overestimation can be explained by the piecewise linear approximation of material properties, leading to distinct phase transformation zones. The distinct zones contrast the real-world smooth transition zones caused by the alloy's stochastic grain size and orientation distribution. Furthermore, the charts show the corre-

lation between interlayer thickness, hysteresis width, and transformation temperature for both, experimental and simulated data. The findings can be attributed to the fact that a thinner interlayer thickness causes higher stress in the SMA layer for the same level of deflection during activation. Higher stress, in turn, causes the hysteresis width to shrink and the transformation temperatures to increase. The simulated data overestimates these effects compared to the experimental data. The overestimation of the hysteresis width shows an anti-proportional relationship with the SMA's mechanical stress. Particularly for lower mechanical stresses, the beginning of reconversion is assumed to occur at too low temperatures.

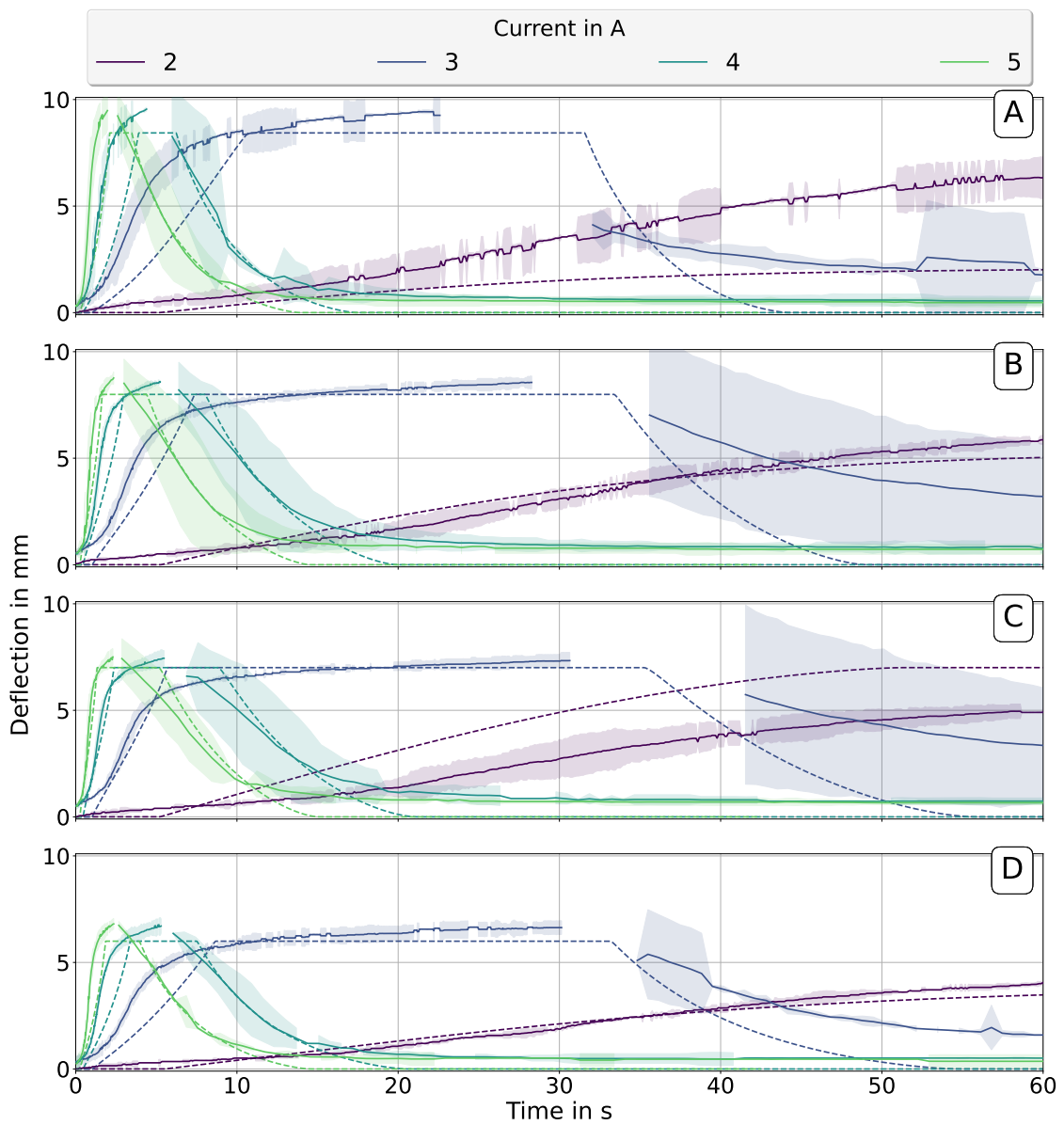


Figure 8.5: Electro-thermomechanical validation of the SMAHC model at RT, featuring a comparison between experiment (solid line) and simulation (dashed line) for four types of SMAHC, each activated with four different supplied currents (2 to 5 A).

The coupling of the electro-thermomechanical model was validated in the subsequent step. For this purpose, experimental and simulated data of dynamic deflection were compared. The results are depicted in figure 8.5 for activation and deactivation of various actuator types and current levels at RT. In addition, figure 8.6 depicts results for SMAHC of type C at various ambient temperatures and current levels.

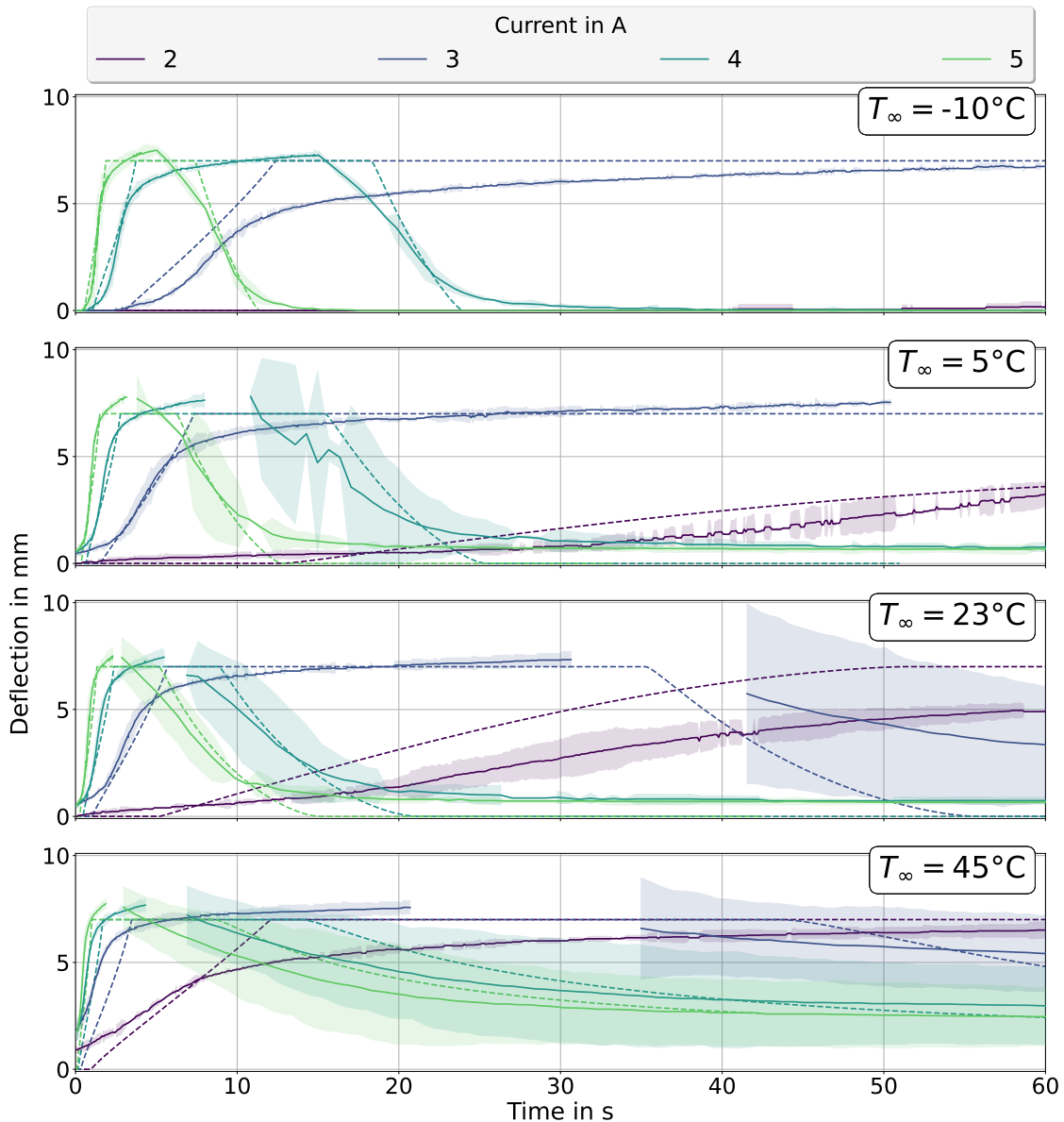


Figure 8.6: Validation of the electro-thermomechanical SMAHC model for SMAHC of type C at varied ambient temperatures. The experiment (solid line) and simulation (dashed line) for each ambient temperature level were compared using four kinds of electrical currents (2 to 5 A).

The simulations correspond well with the investigated experimental transient heating behavior, particularly for SMAHC of type B and C at currents exceeding 2 A. The simulated dynamic heating shows a significant delay for actuators of types A and D. These two

types exhibit comparatively higher mechanical stresses in the SMA layer in the activated state. It was found that deviation between experiment and simulation correlates with this mechanical stress. During the thermomechanical validation, a similar tendency to overestimate the martensite-to-austenite transition temperatures and hysteresis width for types A and D was identified.

Regardless of the SMAHC type, the transient cooling behavior for relatively high currents and short exposure durations exhibits excellent agreement between experiment and modeling. For lower currents, however, the cooling behavior is modeled too quickly. An underestimated potential for heat storage and an overestimation of convective heat losses provide possible explanations. Underestimation of the heat storage may be due, for instance, to the wire's resin coating being neglected.

At an ambient temperature of 23 °C, the experimental and simulation-determined heating and cooling behavior agreed most closely. With decreasing ambient temperature, the curves deviated. During activation, the simulated deflection was delayed, and the gradient of the cooling process was overestimated. The deviations were found regardless of the supplied current.

The activation time was significantly underestimated for an ambient temperature of 45 degrees Celsius, whereas the deactivation time was significantly overestimated, particularly for higher supply currents.

8.2.2. With influence of external load

The thermomechanical coupling was validated first. The experimental and simulative data are compared in figure 8.7 for the actuator of type C and various loading conditions. The electro-thermomechanical model was subsequently validated for the same actuator and loading conditions. Corresponding data of simulation and experiment can be found in figure 8.8.

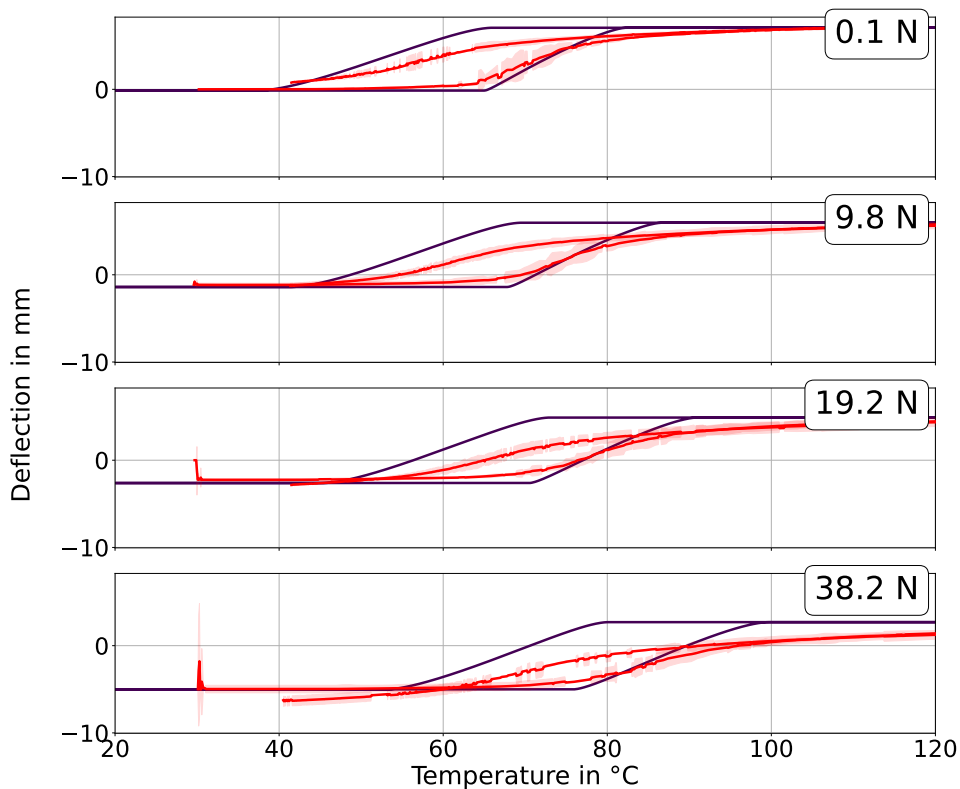


Figure 8.7: Thermomechanical validation of the SMAHC model for the actuator of type C and four different external loading conditions. Experiments were carried out with supplied electrical current of 3.5 A.

There was a good agreement between the experimental and simulated maximum and minimum deflection, except for an applied external load of 38.2 N. Except for this loading condition, the deflection temperature hysteresis is within the simulated one. While a good agreement between experiment and simulation is found for the heating process, higher deviations are found for the retransformation. The pseudoplastic deformation, mainly observed at the highest load level, is not represented by the model.

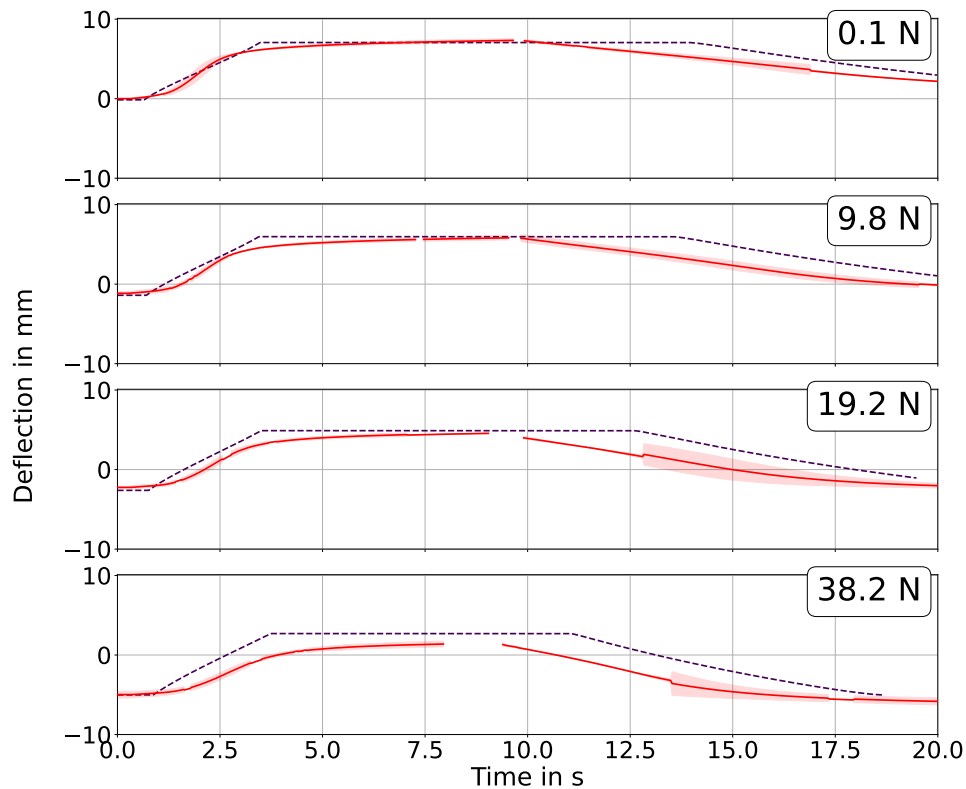


Figure 8.8: Electro-thermomechanical validation of the SMAHC model for the actuator of type C at various loading conditions. Comparison between experiment (solid line) and simulation (dashed line) was carried out with supplied current of 3.5 A.

The phase transformation and related deflection were estimated to occur prematurely with increased loading conditions. In contrast, the simulation estimated that the retransformation begins delayed, regardless of the applied external load. In terms of quality, the thermomechanical and electro-thermomechanical behaviors of the SMAHC are depicted accurately. Quantitatively, the model exhibits substantial discrepancies, but depending on the application, it can be sufficiently accurate for modeling the transient behavior of the SMAHC.

9. Summary & Conclusion

The objective of this thesis was to establish a transient electro-thermomechanical model capable of characterizing the shape-morphing capabilities of SMAHCs. Inputs to the model include geometric and material design factors, electrical current supply conditions and ambient conditions, while outputs include the SMAHC's deflection, load-carrying capacities, bandwidth, and energy consumption. The model extends existing models to include aspects of external influences so that, for example, the efficiency and dynamics of the SMAHC can be predicted as a function of external mechanical loads and different ambient temperatures. A further focus of the work is on the comprehensive experimental validation of the model as well as the free accessibility, which was realized by implementation using Python.

Four primary questions had to be answered for the model to be realized. First, it was experimentally investigated how essential design characteristics, such as external load, ambient temperature, and supplied electrical current, affect the actuators' deflection, actuation dynamics, and energy consumption. The range of external loads examined was from -0.2 to 0.8 N/mm of actuator width, the range of ambient temperatures was from -10 to 47 °C, and the range of supplied currents was from 0.5 to 5 A. The outcomes of the experiments answered questions regarding the impact of design parameters and boundary conditions on the output and their interrelationships. Based on the findings, a model was synthesized from the bottom up using well-established equations, methodologies, and solution procedures, taking into account numerous simplifications and assumptions. For modeling purposes, the shape-adaptive SMAHC system was separated into four domains. The material domain describes the SMA's behavior, the thermal, the mechanical, and the electrical domain of the entire system. The modeling approach resulted in the requirement of finding the correct input parameters. In subsequent step, all required parameters were measured, and measuring techniques were established. The final step validated the model by comparing experimental and simulated data. The thermomechanical validation was conducted by comparing temperature-deflection hysteresis curves, and the electro-thermomechanical validation was conducted by comparing time-deflection curves. The findings demonstrate that the activation behavior of a SMAHC at RT and with minimal mechanical stress induced in the SMA wires can be predicted with considerable but tolerable errors despite the numerous assumptions and simplifications applied. If the boundary conditions deviate from this, the experimental and simulated results diverge more. For certain combinations of boundary conditions, they can become so large that the model's

application becomes unreasonable.

This work advances the research on shape-adaptive SMAHC by structured actuation tests, which were used for the validation of an electro-thermomechanical model. The model is superior to existing models because it can forecast the transient shape change by considering design-relevant characteristics and boundary conditions. Existing methods permitted accurate thermomechanical behavior prediction or simplified electro-thermomechanical behavior prediction without addressing ambient temperatures and external mechanical loading conditions.

In the future, these findings can be used to design shape-adaptive SMAHC under various ambient temperatures. For instance, requirements on the perimeter can be deduced for worst-case scenarios (low ambient temperature, high load,...). On this basis, it is possible to estimate if a system is practical or can be operated profitably.

The model's validity is generally restricted to the range of experimental tested boundary conditions and design parameters. In future research, it is advised to explore experimentally the behavior of SMAHCS under the influence of ambient temperatures in the range of -60°C , as correct operation at this temperature is required, for instance, in the aviation industry. There is currently no model component implemented for internal hysteresis loops, and it is impossible to simulate the pseudoplastic behavior of the SMAHC following activation by external loads. In future work, these model components might be added; their implementation would enable the simulation of control feedback loops. A fundamental area for improvement of the study is that only a small number of cycles were experimentally studied. Cyclic effects such as SME degradation were not accounted for in the model. Specifically, the influence of external stresses on cycle stability cannot be assessed using the model. For numerous applications, the high cycle fatigue behavior is of critical importance. The extension of the model for cyclic actuator behavior would need to be accompanied by substantial experimental effort. The model's thermodynamic applicability is restricted to situations of free convection. Model improvement is the implementation of equations for determining the influence of forced convection and validating their application through experimentation. More extensive modifications, such as accepting fiber-reinforced composites as a substrate or simulating fully embedded SMA wires, are challenging. Usage of proprietary software for more complex geometries and conditions is advised.

Bibliography

- [1] M. Miodownik, "Why the story of materials is really the story of civilisation," *The Observer*, Sep. 2014.
- [2] T. L. Turner, "A New Thermoelastic Model for Analysis of Shape Memory Alloy Hybrid Composites," *Journal of Intelligent Material Systems and Structures*, vol. 11, no. 5, pp. 382–394, May 2000.
- [3] Z. Chaudhry and C. A. Rogers, "Bending and Shape Control of Beams Using SMA Actuators," *Journal of Intelligent Material Systems and Structures*, vol. 2, no. 4, pp. 581–602, Oct. 1991.
- [4] C. Rogers, "Response of composite beams to an internal actuator force," in *32nd Structures, Structural Dynamics, and Materials Conference*. Baltimore, MD, U.S.A.: American Institute of Aeronautics and Astronautics, Apr. 1991.
- [5] M. Gurka, S. Nissle, M. Hübler, and M. Kaiser, "Active Vortex Generator Deployed on Demand by Active Hybrid Composites From Shape Memory Alloys and Fiber Reinforced Polymers," in *ASME 2017 Conference on Smart Materials, Adaptive Structures and Intelligent Systems*. American Society of Mechanical Engineers Digital Collection, Nov. 2017.
- [6] T. L. Turner, R. H. Cabell, R. J. Cano, and G. A. Fleming, "Design, fabrication, and testing of a SMA hybrid composite jet engine chevron," in *Smart Structures and Materials 2006: Smart Structures and Integrated Systems*, vol. 6173. International Society for Optics and Photonics, Apr. 2006, pp. 392–406.
- [7] CompActive, "Anwendungen," [online], <https://compactive.de/videos/>, (Date last accessed 09-Dec-2022).
- [8] CompActive, "Aktorik im Automobilbau – MiniVent," [online], <https://compactive.de/minivent/>, (Date last accessed 07-Mar-2023), May 2021.
- [9] J. Mohd Jani, M. Leary, A. Subic, and M. A. Gibson, "A review of shape memory

- alloy research, applications and opportunities," *Materials & Design (1980-2015)*, vol. 56, pp. 1078–1113, Apr. 2014.
- [10] M. Riva, P. Bettini, L. Di Landro, G. Sala, and A. Airoidi, "Carbon Fiber-Reinforced Smart Laminates with Embedded SMA Actuators—Part II: Numerical Models and Empirical Correlations," *Journal of Materials Engineering and Performance*, vol. 18, no. 5, pp. 672–678, Aug. 2009.
- [11] P. Bettini, M. Riva, G. Sala, L. Landro, A. Airoidi, and J. Cucco, "Carbon Fiber Reinforced Smart Laminates with Embedded SMA Actuators—Part I: Embedding Techniques and Interface Analysis," *Journal of Materials Engineering and Performance*, vol. 18, pp. 664–671, Aug. 2009.
- [12] P. Šittner and R. Stalmans, "Developing hybrid polymer composites with embedded shape-memory alloy wires," *JOM*, vol. 52, no. 10, pp. 15–20, Oct. 2000.
- [13] J. Mohd Jani, M. Leary, A. Subic, and M. Gibson, "A review of shape memory alloy research, applications and opportunities," *Materials and Design*, vol. 56, pp. 1078–1113, April-2014.
- [14] D. C. Lagoudas, *Shape Memory Alloys*. Boston, MA: Springer US, 2008, vol. 1.
- [15] K. Otsuka and C. M. Wayman, *Shape Memory Materials*. Cambridge university press, 1999.
- [16] M. Mertmann and G. Vergani, "Design and application of shape memory actuators," *The European Physical Journal Special Topics*, vol. 158, no. 1, pp. 221–230, May 2008.
- [17] J. E. Huber, N. A. Fleck, and M. F. Ashby, "The selection of mechanical actuators based on performance indices," *Proceedings of the Royal Society of London. Series A: Mathematical, Physical and Engineering Sciences*, vol. 453, no. 1965, pp. 2185–2205, Oct. 1997.
- [18] W. Huang, "On the selection of shape memory alloys for actuators," *Materials & Design*, vol. 23, no. 1, pp. 11–19, Feb. 2002.
- [19] D. Reynaerts and H. V. Brussel, "Design aspects of shape memory actuators," *Mechatronics*, vol. 8, no. 6, pp. 635–656, Aug. 1998.

- [20] N. Himmel, "Bauweisen und Smart Structures," in *Handbuch Verbundwerkstoffe: Werkstoffe, Verarbeitung, Anwendung*. Carl Hanser Verlag GmbH Co KG, Jul-2014.
- [21] M. Neitzel, P. Mitschang, and U. Breuer, *Handbuch Verbundwerkstoffe: Werkstoffe, Verarbeitung, Anwendung*. Carl Hanser Verlag GmbH Co KG, Jul. 2014.
- [22] C. Zweben, "Tensile strength of hybrid composites," *Journal of Materials Science*, vol. 12, pp. 1325–1337, 1977.
- [23] U. P. Breuer, *Commercial Aircraft Composite Technology*. New York, NY: Springer Berlin Heidelberg, 2016.
- [24] C. A. Rogers and H. H. Robertshaw, "Development of a novel smart material," in *Proceedings of the 1988 Winter Annual Meeting of the American Society of Mechanical Engineers*, 1988, pp. 1–5.
- [25] J. Bhaskar, A. Kumar Sharma, B. Bhattacharya, and S. Adhikari, "A review on shape memory alloy reinforced polymer composite materials and structures," *Smart Materials and Structures*, vol. 29, no. 7, p. 073001, Jul. 2020.
- [26] J. A. Balta, J. Simpson, V. Michaud, J. A. E. Månson, and J. Schrooten, "Embedded shape memory alloys confer aerodynamic profile adaptivity," *Smart Materials Bulletin*, vol. 2001, no. 12, pp. 8–12, Dec. 2001.
- [27] M.-W. Han, H. Rodrigue, H.-I. Kim, S.-H. Song, and S.-H. Ahn, "Shape memory alloy/glass fiber woven composite for soft morphing winglets of unmanned aerial vehicles," *Composite Structures*, vol. 140, pp. 202–212, Apr. 2016.
- [28] C. A. Rogers, "Active vibration and structural acoustic control of shape memory alloy hybrid composites: Experimental results," *The Journal of the Acoustical Society of America*, vol. 88, no. 6, pp. 2803–2811, Dec. 1990.
- [29] R. Wu, M.-W. Han, G.-Y. Lee, and S.-H. Ahn, "Woven type smart soft composite beam with in-plane shape retention," *Smart Materials and Structures*, vol. 22, no. 12, p. 125007, Nov. 2013.
- [30] S. Lacasse, P. Terriault, C. Simoneau, and V. Brailovski, "Design, manufacturing, and testing of an adaptive composite panel with embedded shape memory alloy

- actuators," *Journal of Intelligent Material Systems and Structures*, vol. 26, no. 15, pp. 2055–2072, Oct. 2015.
- [31] S. Nissle, M. Kaiser, M. Hübler, M. Gurka, and U. Breuer, "Adaptive vortex generators based on active hybrid composites: From idea to flight test," *CEAS Aeronautical Journal*, vol. 9, no. 4, pp. 661–670, Dec. 2018.
- [32] G. Jodin, J. SCHELLER, E. DUHAYON, J.-F. ROUCHON, M. Triantafyllou, and M. BRAZA, "An Experimental Platform for Surface Embedded SMAs in Morphing Applications," *Solid State Phenomena*, vol. 260, pp. 69–76, Jul. 2017.
- [33] A. A. Villanueva, K. B. Joshi, J. B. Blottman, and S. Priya, "A bio-inspired shape memory alloy composite (BISMAC) actuator," *Smart Materials and Structures*, vol. 19, no. 2, p. 025013, Jan. 2010.
- [34] A. K. Elwaleed, N. A. Mohamed, M. J. M. Nor, and M. M. Mustafa, "A new concept of a linear smart actuator," *Sensors and Actuators A: Physical*, vol. 135, no. 1, pp. 244–249, Mar. 2007.
- [35] M. Cho and S. Kim, "Structural morphing using two-way shape memory effect of SMA," *International Journal of Solids and Structures*, vol. 42, no. 5, pp. 1759–1776, Mar. 2005.
- [36] Y. Nakano, M. Fujie, and Y. Hosada, "Hitachi robot hand," *Robotics age*, vol. 6, no. 7, pp. 18–20, 1984.
- [37] C. Rogers, C. Liang, and J. Jia, "Behavior of shape memory alloy reinforced composite plates. I - Model formulations and control concepts," in *30th Structures, Structural Dynamics and Materials Conference*. Mobile, AL, U.S.A.: American Institute of Aeronautics and Astronautics, Apr. 1989.
- [38] A. Baz, K. Imam, and J. McCoy, "Active vibration control of flexible beams using shape memory actuators," *Journal of Sound Vibration*, vol. 140, pp. 437–456, Aug. 1990.
- [39] F. Daghia, D. J. Inman, F. Ubertini, and E. Viola, "Shape Memory Alloy Hybrid Composite Plates for Shape and Stiffness Control," *Journal of Intelligent Material Systems and Structures*, vol. 19, no. 5, pp. 609–619, May 2008.

- [40] S.-M. Yang, J.-H. Roh, J.-H. Han, and I. Lee, "Experimental Studies on Active Shape Control of Composite Structures using SMA Actuators," *Journal of Intelligent Material Systems and Structures*, vol. 17, no. 8-9, pp. 767–777, Sep. 2006.
- [41] J. Mabe, F. Calkins, and G. Butler, "Boeing's Variable Geometry Chevron, Morphing Aerostructure for Jet Noise Reduction," in *47th AIAA/ASME/ASCE/AHS/ASC Structures, Structural Dynamics, and Materials Conference*. Newport, Rhode Island: American Institute of Aeronautics and Astronautics, May 2006.
- [42] J.-E. Bidaux, J.-A. E. Manson, and R. Gotthardt, "Active modification of the vibration frequencies of a polymer beam using shape memory alloy fibres," in *3rd International Conference on Intelligent Materials and 3rd European Conference on Smart Structures and Materials*, vol. 2779. SPIE, 1996, pp. 517–522.
- [43] K.-t. Lau, "Vibration characteristics of SMA composite beams with different boundary conditions," *Materials & Design*, vol. 23, no. 8, pp. 741–749, Dec. 2002.
- [44] S. Orlando, F. Marulo, M. Guida, and F. Timbrato, "Bird strike assessment for a composite wing flap," *International Journal of Crashworthiness*, vol. 23, no. 2, pp. 219–235, Mar. 2018.
- [45] D. S. Burton, X. Gao, and L. C. Brinson, "Finite element simulation of a self-healing shape memory alloy composite," *Mechanics of Materials*, vol. 38, no. 5, pp. 525–537, May 2006.
- [46] F. Pinto, F. Ciampa, M. Meo, and U. Polimeno, "Multifunctional SMArt composite material for in situ NDT/SHM and de-icing," *Smart Materials and Structures*, vol. 21, no. 10, p. 105010, Aug. 2012.
- [47] V. Kecman, Ed., *State-Space Models of Lumped and Distributed Systems*, ser. Lecture Notes in Control and Information Sciences. Berlin/Heidelberg: Springer-Verlag, 1988, vol. 112.
- [48] J. Mohd Jani, M. Leary, and A. Subic, "Designing shape memory alloy linear actuators: A review," *Journal of Intelligent Material Systems and Structures*, vol. 28, no. 13, pp. 1699–1718, Aug. 2017.
- [49] L. Hawkins, B. Vick, and C. Rogers, "An investigation of the transient thermal

- response of a shape memory alloy composite beam," in *31st Structures, Structural Dynamics and Materials Conference*, 1990, p. 941.
- [50] C.-D. Munz and T. Westermann, *Numerische Behandlung gewöhnlicher und partieller Differenzialgleichungen: Ein anwendungsorientiertes Lehrbuch für Ingenieure*. Berlin, Heidelberg: Springer Berlin Heidelberg, 2019.
- [51] H.-D. Alber, *Materials with Memory: Initial-Boundary Value Problems for Constitutive Equations with Internal Variables*. Springer, Nov. 2006.
- [52] C. Liang and C. A. Rogers, "One-Dimensional Thermomechanical Constitutive Relations for Shape Memory Materials," *Journal of Intelligent Material Systems and Structures*, vol. 1, p. 28, Apr-1990.
- [53] K. Tanaka and S. Nagaki, "A thermomechanical description of materials with internal variables in the process of phase transitions," *Ingenieur-Archiv*, vol. 51, no. 5, pp. 287–299, Sep. 1982.
- [54] K. Tanaka, "THERMOMECHANICAL SKETCH OF SHAPE MEMORY EFFECT: ONE-DIMENSIONAL TENSILE BEHAVIOR." *Res Mechanica: International Journal of Structural Mechanics and Materials Science*, vol. 18, no. 3, pp. 251–263, 1986.
- [55] D. C. Lagoudas, Z. Bo, and M. A. Qidwai, "A UNIFIED THERMODYNAMIC CONSTITUTIVE MODEL FOR SMA AND FINITE ELEMENT ANALYSIS OF ACTIVE METAL MATRIX COMPOSITES," *Mechanics of Composite Materials and Structures*, vol. 3, no. 2, pp. 153–179, Jun. 1996.
- [56] L. Brinson, "One-Dimensional Constitutive Behavior of Shape Memory Alloys: Thermomechanical Derivation with Non-Constant Material Functions and Redefined Martensite Internal Variable," *Journal of Intelligent Material Systems and Structures*, vol. 4, no. 2, pp. 229–242, Apr. 1993.
- [57] W. Voigt, "Ueber die Beziehung zwischen den beiden Elasticitätsconstanten isotroper Körper," *Annalen der Physik*, vol. 274, no. 12, pp. 573–587, 1889.
- [58] F. Auricchio and J. Lubliner, "A uniaxial model for shape-memory alloys," *International Journal of Solids and Structures*, vol. 34, no. 27, pp. 3601–3618, 1997.
- [59] F. Auricchio and E. Sacco, "A one-dimensional model for superelastic shape-memory

- alloys with different elastic properties between austenite and martensite," *International Journal of Non-Linear Mechanics*, vol. 32, no. 6, pp. 1101–1114, Nov. 1997.
- [60] Z. Bo and D. C. Lagoudas, "Thermomechanical modeling of polycrystalline SMAs under cyclic loading, Part I: Theoretical derivations," *International Journal of Engineering Science*, vol. 37, no. 9, pp. 1089–1140, Jul. 1999.
- [61] D. Hartl and D. Lagoudas, "Thermomechanical Characterization of Shape Memory Alloy Materials," in *Shape Memory Alloys*. Boston, MA: Springer US, 2008, vol. 1, pp. 53–119.
- [62] S. De la Flor, C. Urbina, and F. Ferrando, "Constitutive model of shape memory alloys: Theoretical formulation and experimental validation," *Materials Science and Engineering: A*, vol. 427, no. 1, pp. 112–122, Jul. 2006.
- [63] X. D. Zhang, C. A. Rogers, and C. Liang, "Modelling of the Two-Way Shape Memory Effect," *Journal of Intelligent Material Systems and Structures*, vol. 8, no. 4, pp. 353–362, Apr. 1997.
- [64] C. Zanotti, P. Giuliani, A. Tuissi, S. Arnaboldi, and R. Casati, "Response of NiTi SMA wire electrically heated," in *European Symposium on Martensitic Transformations*, EDP Sciences, 2009.
- [65] J. M. Jani, S. Huang, M. Leary, and A. Subic, "Numerical modeling of shape memory alloy linear actuator," *Computational Mechanics*, vol. 56, no. 3, pp. 443–461, Sep. 2015.
- [66] H. Meier and L. Oelschlaeger, "Numerical thermomechanical modelling of shape memory alloy wires," *Materials Science and Engineering: A*, vol. 378, pp. 484–489, Jul. 2004.
- [67] B.-C. Chang, J. A. Shaw, and M. A. Iadicola, "Thermodynamics of Shape Memory Alloy Wire: Modeling, Experiments, and Application," *Continuum Mechanics and Thermodynamics*, vol. 18, no. 1-2, pp. 83–118, Jul. 2006.
- [68] P. L. Potapov and E. P. Da Silva, "Time Response of Shape Memory Alloy Actuators," *Journal of Intelligent Material Systems and Structures*, vol. 11, no. 2, pp. 125–134, Feb. 2000.

- [69] R. Neugebauer, A. Bucht, K. Pagel, and J. Jung, "Numerical simulation of the activation behavior of thermal shape memory alloys," in *Industrial and Commercial Applications of Smart Structures Technologies 2010*, vol. 7645. International Society for Optics and Photonics, Mar. 2010, p. 76450J.
- [70] P. Motzki, T. Gorges, M. Kappel, M. Schmidt, G. Rizzello, and S. Seelecke, "High-speed and high-efficiency shape memory alloy actuation," *Smart Materials and Structures*, vol. 27, no. 7, p. 075047, Jun. 2018.
- [71] V. D. Ingenieure and VDI-Gesellschaft Verfahrenstechnik und Chemieingenieurwesen, Eds., *VDI-Wärmeatlas: mit 320 Tabellen*, 11th ed., ser. Springer Reference. Berlin: Springer Vieweg, 2013.
- [72] S. W. Churchill and H. H. S. Chu, "Correlating equations for laminar and turbulent free convection from a horizontal cylinder," *International Journal of Heat and Mass Transfer*, vol. 18, no. 9, pp. 1049–1053, Sep. 1975.
- [73] J. T. Cieśliński, S. Smolen, and D. Sawicka, "Free Convection Heat Transfer from Horizontal Cylinders," *Energies*, vol. 14, no. 3, p. 559, Jan. 2021.
- [74] A. Eisakhani, W. Ma, J. Gao, J. R. Culham, and R. Gorbet, "NATURAL CONVECTION HEAT TRANSFER MODELLING OF SHAPE MEMORY ALLOY WIRE," in *Smart Materials, Structures & NDT in Aerospace*, Montreal, Quebec, Canada, Nov-2011, p. 10.
- [75] J. M. Jani, S. Huang, M. Leary, and A. Subic, "Analysis of Convective Heat Transfer Coefficient on Shape Memory Alloy Actuator under Various Ambient Temperatures with Finite Difference Method," *Applied Mechanics and Materials*, vol. 736, pp. 127–133, Mar. 2015.
- [76] H. Song, E. Kubica, and R. Gorbet, "RESISTANCE MODELLING OF SMA WIRE ACTUATORS," in *Smart Materials, Structures & NDT in Aerospace*, Montreal, Quebec, Canada, 2011, p. 10.
- [77] S. G. Shu, D. C. Lagoudas, D. Hughes, and J. T. Wen, "Modeling of a flexible beam actuated by shape memory alloy wires," *SMART MATERIALS & STRUCTURES*, vol. 6, pp. 255–277, Feb-1997.
- [78] George Sidebotham, *Heat Transfer Modeling*. New York, NY, USA: Springer, 2015.

- [79] G. Kirchhoff, "Ueber die Auflösung der Gleichungen, auf welche man bei der Untersuchung der linearen Vertheilung galvanischer Ströme geführt wird," *Annalen der Physik*, vol. 148, no. 12, pp. 497–508, 1847.
- [80] V. Novák, P. Šittner, G. N. Dayananda, F. M. Braz-Fernandes, and K. K. Mahesh, "Electric resistance variation of NiTi shape memory alloy wires in thermomechanical tests: Experiments and simulation," *Materials Science and Engineering: A*, vol. 481–482, pp. 127–133, May 2008.
- [81] K. E. Bisshopp and D. C. Drucker, "Large deflection of cantilever beams," *Quarterly of Applied Mathematics*, vol. 3, no. 3, pp. 272–275, Oct. 1945.
- [82] R. van de Schoot, J. de Bruin, R. Schram, P. Zahedi, J. de Boer, F. Weijdema, B. Kramer, M. Huijts, M. Hoogerwerf, G. Ferdinands, A. Harkema, J. Willemsen, Y. Ma, Q. Fang, S. Hindriks, L. Tummers, and D. L. Oberski, "An open source machine learning framework for efficient and transparent systematic reviews," *Nature Machine Intelligence*, vol. 3, no. 2, pp. 125–133, Feb. 2021.
- [83] F. Auricchio and E. Sacco, "A temperature-dependent beam for shape-memory alloys: Constitutive modelling, finite-element implementation and numerical simulations," *Computer Methods in Applied Mechanics and Engineering*, vol. 174, no. 1, pp. 171–190, May 1999.
- [84] F. Auricchio and L. Petrini, "A three-dimensional model describing stress-temperature induced solid phase transformations: Thermomechanical coupling and hybrid composite applications," *International Journal for Numerical Methods in Engineering*, vol. 61, no. 5, pp. 716–737, 2004.
- [85] N. Papenfuss and S. Seelecke, "Simulation and control of SMA actuators," in *1999 Symposium on Smart Structures and Materials*, V. V. Varadan, Ed., Newport Beach, CA, Jun. 1999, p. 586.
- [86] B. Davis, T. L. Turner, and S. Seelecke, "Measurement and Prediction of the Thermomechanical Response of Shape Memory Alloy Hybrid Composite Beams," *Journal of Intelligent Material Systems and Structures*, vol. 19, no. 2, pp. 129–143, Feb. 2008.
- [87] T. L. Turner, R. H. Cabell, R. J. Cano, and R. J. Silcox, "Development of a Pre-

- liminary Model-Scale Adaptive Jet Engine Chevron," *AIAA Journal*, vol. 46, no. 10, pp. 2545–2557, Oct. 2008.
- [88] T. L. Turner and H. D. Patel, "Analysis of SMA Hybrid Composite Structures in MSC.Nastran and ABAQUS," *Journal of Intelligent Material Systems and Structures*, vol. 18, no. 5, pp. 435–447, May 2007.
- [89] Y.-K. Choi and M. Salvia, "Manufacture and experimental and theoretical evaluation of adaptative glass/epoxy composites with embedded shape memory alloy wires," in *SPIE's 8th Annual International Symposium on Smart Structures and Materials*, C. S. Lynch, Ed., Newport Beach, CA, USA, Jul. 2001, p. 366.
- [90] S. S. Sun, G. Sun, F. Han, and J. S. Wu, "Thermoviscoelastic analysis for a polymeric composite plate with embedded shape memory alloy wires," *Composite Structures*, vol. 58, no. 2, pp. 295–302, Nov. 2002.
- [91] P. Scaron, V. Michaud, and J. Schrooten, "Modelling and Material Design of SMA Polymer Composites," *MATERIALS TRANSACTIONS*, vol. 43, no. 5, pp. 984–993, 2002.
- [92] Q. Li, S. Seelecke, M. Kohl, and B. Krevet, "Thermo-mechanical finite element analysis of a shape memory alloy cantilever beam," in *Smart Structures and Materials*, D. K. Lindner, Ed., San Diego, CA, Mar. 2006, p. 61661Z.
- [93] B. S. Balapgol, K. M. Bajoria, and S. A. Kulkarni, "A two-dimensional finite element analysis of a shape memory alloy laminated composite plate," *Smart Materials and Structures*, vol. 15, no. 4, pp. 1009–1020, Aug. 2006.
- [94] X. Gao, D. Burton, T. Turner, and L. Brinson, "Finite element analysis of adaptive-stiffening and shape-control SMA hybrid composites," *Journal of Engineering Materials and Technology*, vol. 128, no. 3, pp. 285–293, 2006.
- [95] H. Sepiani, F. Ebrahimi, and H. Karimipour, "A mathematical model for smart functionally graded beam integrated with shape memory alloy actuators," *Journal of Mechanical Science and Technology*, vol. 23, no. 12, pp. 3179–3190, Dec. 2009.
- [96] S. Yang, S. S. Seelecke, and Q. Li, "Finite element analysis of SMA beam bending using COMSOL," in *SPIE Smart Structures and Materials + Nondestructive Eval-*

- uation and Health Monitoring, Z. Ounaies and J. Li, Eds., San Diego, California, USA, Mar. 2009, p. 72890S.
- [97] K. Tohgo and Y. Shimamura, "Reciprocating Bending Deformation and Mechanical Response of Shape-control Plate Using NiTi Shape Memory Alloy Wire," *Journal of Intelligent Material Systems and Structures*, vol. 21, no. 9, pp. 941–951, Jun. 2010.
- [98] M. Zakerzadeh, H. Salehi, and H. Sayyaadi, "Modeling of a Nonlinear Euler-Bernoulli Flexible Beam Actuated by Two Active Shape Memory Alloy Actuators," *Journal of Intelligent Material Systems and Structures*, vol. 22, no. 11, pp. 1249–1268, Jul. 2011.
- [99] B.-S. Jung, J.-P. Kong, N. Li, Y.-M. Kim, M.-S. Kim, S.-H. Ahn, and M. Cho, "Numerical simulation and verification of a curved morphing composite structure with embedded shape memory alloy wire actuators," *Journal of Intelligent Material Systems and Structures*, vol. 24, no. 1, pp. 89–98, Jan. 2013.
- [100] M. Hübler, M. Gurka, S. Schmeer, and U. P. Breuer, "Performance range of SMA actuator wires and SMA–FRP structure in terms of manufacturing, modeling and actuation," *Smart Materials and Structures*, vol. 22, no. 9, p. 094002, Aug. 2013.
- [101] M. K. Abbas, M. A. Elshafei, and H. M. Negm, "Modeling and analysis of laminated shape memory alloy composite plates," *Journal of Thermoplastic Composite Materials*, vol. 29, no. 1, pp. 103–142, Jan. 2016.
- [102] M. Gurka, M. Huebler, M. Kaiser, and S. Nissle, "Active Hybrid Composite Actuators-A Comparison of Different Design Approaches," in *ACTUATOR 2018; 16th International Conference on New Actuators*. VDE, 2018, pp. 1–4.
- [103] C. Cherif, R. Hickmann, A. Nocke, R. Fleischhauer, M. Kaliske, and S. Wießner, "Simulation-based development of adaptive fiber-elastomer composites with embedded shape memory alloys," *Journal of Industrial Textiles*, vol. 48, no. 1, pp. 322–332, Jul. 2018.
- [104] R. Behnke, H. Dal, and M. Kaliske, "An extended tube model for thermo-viscoelasticity of rubberlike materials: Parameter identification and examples," *PAMM*, vol. 11, no. 1, pp. 353–354, 2011.
- [105] S. Kapuria and H. N. Das, "Improving hydrodynamic efficiency of composite marine

- propellers in off-design conditions using shape memory alloy composite actuators," *Ocean Engineering*, vol. 168, pp. 185–203, Nov. 2018.
- [106] HN. Das and S. Kapuria, "Adaptive pitch control of full-scale ship composite propeller using shape memory alloy to enhance propulsive efficiency in off-design conditions," *Journal of Intelligent Material Systems and Structures*, vol. 30, no. 10, pp. 1493–1507, Jun. 2019.
- [107] N. Keshtkar and K. Röbenack, "Mathematical Modeling of Fiber-Elastomer Composites with Embedded Shape Memory Alloys," in *2020 24th International Conference on System Theory, Control and Computing (ICSTCC)*, Oct. 2020, pp. 477–482.
- [108] H. Jin, E. Dong, M. Xu, and J. Yang, "A Smart and Hybrid Composite Finger with Biomimetic Tapping Motion for Soft Prosthetic Hand," *Journal of Bionic Engineering*, vol. 17, no. 3, pp. 484–500, May 2020.
- [109] R. Srivastava and B. Bhattacharya, "Thermoelastic and vibration response analysis of shape memory alloy reinforced active bimorph composites," *Smart Materials and Structures*, vol. 30, no. 1, p. 015033, Jan. 2021.
- [110] N. V. Viet and W. Zaki, "Modeling bending behavior of shape memory alloy wire-reinforced composites: Semi-analytical model and finite element analysis," *Chinese Journal of Aeronautics*, vol. 34, no. 8, pp. 176–191, Aug. 2021.
- [111] M. Kaiser, M. Gurka, and M. Kunzler, "Airfoil trailing edge morphing based on modified SMAHC concept: Design, implementation, and experimental studies," in *Active and Passive Smart Structures and Integrated Systems XVI*, J.-H. Han, S. Shahab, and J. Yang, Eds. Long Beach, United States: SPIE, Apr. 2022, p. 70.
- [112] L. Zhang, W. Liao, and B. Liu, "Multiscale Simulation Based on the Generalized Method of Cells for Shape Memory Alloy Hybrid Composites," *Journal of Materials Engineering and Performance*, vol. 31, no. 7, pp. 5747–5757, Jul. 2022.
- [113] F. Lohse, K. Kopelmann, H. Grellmann, M. Ashir, T. Gereke, E. Häntzsche, C. Sennewald, and C. Cherif, "Experimental and Numerical Analysis of the Deformation Behavior of Adaptive Fiber-Rubber Composites with Integrated Shape Memory Alloys," *Materials*, vol. 15, no. 2, p. 582, Jan. 2022.
- [114] B. Liu, Q. Wang, S. Hu, W. Zhang, and C. Du, "On thermomechanical behaviors of

- the functional graded shape memory alloy composite for jet engine chevron," *Journal of Intelligent Material Systems and Structures*, vol. 29, no. 14, pp. 2986–3005, Aug. 2018.
- [115] F. Daghia, D. J. Inman, F. Ubertini, and E. Viola, "Active shape change of an SMA hybrid composite plate," *Smart Structures and Systems*, vol. 6, no. 2, pp. 91–100, Mar. 2010.
- [116] A. J. Theodore and P. L. Bishay, "Experimental analysis of fiber-reinforced laminated composite plates with embedded SMA wire actuators," *Composite Structures*, vol. 292, p. 115678, Jul. 2022.
- [117] R. W. Wheeler, O. Benafan, F. T. Calkins, X. Gao, Z. Ghanbari, G. Hommer, D. Lagoudas, D. Martin, D. E. Nicholson, A. Petersen, F. R. Phillips, A. P. Stebner, and T. L. Turner, "Engineering design tools for shape memory alloy actuators: CASMART collaborative best practices and case studies," *Journal of Intelligent Material Systems and Structures*, vol. 30, no. 18-19, pp. 2808–2830, Nov. 2019.
- [118] A. Czechowicz, "An insight into VDI2248 guideline for shape memory alloy actuators," in *ASM International - International Conference on Shape Memory and Superelastic Technologies, SMST 2019*, 2019, pp. 22–23.
- [119] CompActive, "Curve plugged 3950E10," [online], <https://compactive.de/Konfigurationen/L%2039/plugged/Curve%20plugged%203950E10.pdf>, (Date Last Accessed 27-Feb-2023).
- [120] Compactive, "Curve plugged 3950E20," [online], <https://compactive.de/Konfigurationen/L%2039/plugged/Curve%20plugged%203950E20.pdf>, (Date Last Accessed 27-Feb-2023).
- [121] CompActive, "Curve plugged 3950E24," [online], <https://compactive.de/Konfigurationen/L%2039/plugged/Curve%20plugged%203950E24.pdf>, (Date Last Accessed 27-Feb-2023).
- [122] M. Hübler, S. Nissle, M. Gurka, and U. Breuer, "Fiber-reinforced polymers with integrated shape memory alloy actuation: An innovative actuation method for aerodynamic applications," *CEAS Aeronautical Journal*, vol. 7, no. 4, pp. 567–576, 2016.

- [123] P. Motzki, "Efficient SMA Actuation—Design and Control Concepts," in *Proceedings of the First International Electronic Conference on Actuator Technology: Materials, Devices and Applications*, vol. 64. Multidisciplinary Digital Publishing Institute, Nov-2020, p. 20.
- [124] P. Motzki, J. Kunze, A. York, and S. Seelecke, "Energy-efficient SMA Vacuum Gripper System," in *Proceedings of the ACTUATOR*, Berlin, Deutschland, Jun-2016.
- [125] B. Reedlunn, S. Daly, L. Hector, P. Zavattieri, and J. Shaw, "Tips and tricks for characterizing shape memory wire part 5: Full-field strain measurement by digital image correlation," *Experimental Techniques*, vol. 37, no. 3, pp. 62–78, May 2013.
- [126] L. Fumagalli, F. Butera, and A. Coda, "SmartFlex® NiTi Wires for Shape Memory Actuators," *Journal of Materials Engineering and Performance*, vol. 18, no. 5-6, pp. 691–695, Aug. 2009.
- [127] M. Kaiser, N. Neblung, and M. Gurka, "Implementation and Investigation of a Compact, Powerful System for Diagnosis and Control of Shape Memory Alloys in Technical Applications," in *ASME 2019 Conference on Smart Materials, Adaptive Structures and Intelligent Systems*. American Society of Mechanical Engineers Digital Collection, Dec. 2019.
- [128] N. Balakrishnan, V. Voinov, and M. S. Nikulin, *Chi-Squared Goodness of Fit Tests with Applications*. Academic Press, Jan. 2013.
- [129] H. Sehitoglu, R. Hamilton, H. J. Maier, and Y. Chumlyakov, "Hysteresis in NiTi alloys," *Journal de Physique IV (Proceedings)*, vol. 115, pp. 3–10, Jun. 2004.
- [130] G. S. Mammano, "Effect of Stress, Heating Rate, and Degree of Transformation on the Functional Fatigue of Ni-Ti Shape Memory Wires," *Journal of Materials Engineering and Performance*, vol. 24, p. 11, May-2015.
- [131] K. Bhattacharya, S. Conti, G. Zanzotto, and J. Zimmer, "Crystal symmetry and the reversibility of martensitic transformations," *Nature*, vol. 428, no. 6978, pp. 55–59, Mar. 2004.
- [132] L. C. Brinson and M. S. Huang, "Simplifications and Comparisons of Shape Memory

- Alloy Constitutive Models," *Journal of Intelligent Material Systems and Structures*, vol. 7, no. 1, pp. 108–114, Jan. 1996.
- [133] Y. Tadesse, N. Thayer, and S. Priya, "Tailoring the Response Time of Shape Memory Alloy Wires through Active Cooling and Pre-stress," *Journal of Intelligent Material Systems and Structures*, vol. 21, no. 1, pp. 19–40, Jan. 2010.
- [134] X. Wu, Y. Fan, and J. Wu, "A study on the variations of the electrical resistance for NiTi shape memory alloy wires during the thermo-mechanical loading," *Materials & Design*, vol. 21, no. 6, pp. 511–515, Dec. 2000.
- [135] T. C. da Silva, M. V. Costa Sá, E. P. da Silva, and F. C. da Silva, "Emissivity Measurements on Shape Memory Alloys," in *Proceedings of the 2016 International Conference on Quantitative InfraRed Thermography*. QIRT Council, 2016.
- [136] C. Churchill, J. Shaw, and M. Iadicola, "TIPS AND TRICKS FOR CHARACTERIZING SHAPE MEMORY ALLOY WIRE: PART 4 - THERMO-MECHANICAL COUPLING," *Experimental Techniques*, vol. 34, no. 2, pp. 63–80, Mar. 2010.
- [137] J. A. Shaw and S. Kyriakides, "On the nucleation and propagation of phase transformation fronts in a NiTi alloy," *Acta Materialia*, vol. 45, no. 2, pp. 683–700, Feb. 1997.
- [138] D. Gross, W. Hauger, J. Schröder, and W. A. Wall, *Technische Mechanik 2, ser. Springer-Lehrbuch*. Berlin, Heidelberg: Springer Berlin Heidelberg, 2014.
- [139] P. Lu, F. S. Cui, and M. J. Tan, "A theoretical model for the bending of a laminated beam with SMA fiber embedded layer," *Composite Structures*, vol. 90, no. 4, pp. 458–464, Oct. 2009.
- [140] ASTM F2004-17 "Test Method for Transformation Temperature of Nickel-Titanium Alloys by Thermal Analysis": ASTM International, Oct-2017.
- [141] N. Fedelich, "Charakterisierung von Formgedächtnislegierungen, Teil 1: Charakterisierung mittels DSC," *Thermal Analysis UserCom 40 - Mettler Toledo*, no. 40, pp. 10–15, Feb-2014.
- [142] J. Shaw, C. Churchill, and M. Iadicola, "TIPS AND TRICKS FOR CHARACTERIZING SHAPE MEMORY ALLOY WIRE: PART 1-DIFFERENTIAL SCANNING

- CALORIMETRY AND BASIC PHENOMENA," *Experimental Techniques*, vol. 32, no. 5, pp. 55–62, Sep. 2008.
- [143] DIN 51007:2019-04 "Thermische Analyse (TA) – Differenz-Thermoanalyse (DTA) und Dynamische Differenzkalorimetrie (DSC) – Allgemeine Grundlagen": Beuth-Verlag, Apr-2019.
- [144] DIN EN ISO 1183-1:2019-09 "Kunststoffe - Verfahren zur Bestimmung der Dichte von nicht verschäumten Kunststoffen - Teil 1: Eintauchverfahren, Verfahren mit Flüssigkeitspyknometer und Titrationsverfahren": Beuth-Verlag, Sep-2019.
- [145] DIN EN ISO 6892-1:2020-06 "Metallische Werkstoffe - Zugversuch - Teil 1: Prüfverfahren bei Raumtemperatur": Beuth-Verlag, Jun-2020.
- [146] ASTM-E3098 "Standard test method for mechanical uniaxial pre-strain and thermal free recovery of shape memory alloys.": ASTM International, 2017.
- [147] DIN EN ISO 11357-8:2020-01 "Kunststoffe - Dynamische Differenz-Thermoanalyse (DSC) - Teil 8: Bestimmung der Wärmeleitfähigkeit": Beuth-Verlag, May-2021.
- [148] Notzgroup, "Datasheet Steel 1.4310," [online], https://www.notzgroup.com/media/wysiwyg/PDF/JAS/werkstoffe/1.4310_DE.pdf, (Date Last Accessed 27-Feb-2023).
- [149] HSM-Stahl, "Datasheet Steel 1.4310," [online], https://www.hsm-stahl.de/fileadmin/user_upload/datenblatt/HSM_Datenblatt_1.4310.pdf, (Date Last Accessed 27-Feb-2023).
- [150] Matthey, "Datasheet Steel 1.4310," [online], https://www.matthey.ch/fileadmin/user_upload/downloads/fichetechnique/DE/1.4310_C.pdf, (Date Last Accessed 27-Feb-2023).
- [151] DEW-Stahl, "Datasheet Steel 1.4310," [online], https://www.dew-stahl.com/fileadmin/files/dew-stahl.com/documents/Publikationen/Werkstoffdatenblaetter/RSH/1.4310_de.pdf, (Date Last Accessed 27-Feb-2023).

- [152] UHE, "Datasheet Steel 1.4310," [online], <https://www.uhe.de/fileadmin/m/materialien/1.4310.pdf>, (Date Last Accessed 27-Feb-2023).

A. Appendix

A.1. Fundamentals

The Nusselt number for a horizontal infinitely extended plate emitting heat on the upper surface is given by equation A.69 for laminar flow and by equation A.70 for turbulent flow. The transition to turbulent flow is defined by A.71. For heat emitted on the lower side of the plate the Nusselt number can be calculated for laminar flow, limits given by equation A.73, using expression A.72. In any case the characteristic length of a rectangular plate with edge length a and b is defined as $L = \frac{a \cdot b}{2 \cdot (a+b)}$.

$$Nu = 0.766 \left\{ Ra \left[1 + \left(\frac{0.322}{Pr} \right)^{11/20} \right]^{-20/11} \right\}^{1/5} \quad (\text{A.69})$$

$$Nu = 0.15 \left\{ Ra \left[1 + \left(\frac{0.322}{Pr} \right)^{11/20} \right]^{-20/11} \right\}^{1/3} \quad (\text{A.70})$$

$$Ra \left[1 + \left(\frac{0.322}{Pr} \right)^{11/20} \right]^{-20/11} \leq 7 \cdot 10^4 \quad (\text{A.71})$$

$$Nu = 0.6 \left\{ Ra \left[1 + \left(\frac{0.492}{Pr} \right)^{9/16} \right]^{-16/9} \right\}^{1/5} \quad (\text{A.72})$$

$$10^3 < Ra \left[1 + \left(\frac{0.492}{Pr} \right)^{9/16} \right]^{-16/9} < 10^{10} \quad (\text{A.73})$$

For surfaces emitting heat on the lower side and inclined by angle ϕ with respect to the vertical, within the limits of the Rayleigh number given by $10^{-1} < Ra < 10^{12}$, the nusselt number can be approximated using equation A.74. For a plate emitting heat on

the upper side the correlation between inclination and Nusselt number is given by equation A.75.[71]

$$Nu = \left\{ 0.825 + 0.387 \left[Ra \cdot \cos(\phi) \cdot \left[1 + \left(\frac{0.492}{Pr} \right)^{9/16} \right]^{-16/9} \right] \right\}^2 \quad (A.74)$$

$$Nu = 0.56 \cdot \left(10^{(8.9-0.00178 \cdot \phi-1.82)} \cdot \cos(\phi) \right)^{1/4} + 0.13 \left(Ra^{1/3} - 10^{\left(\frac{8.9-0.00178 \cdot \phi-1.82}{3} \right)} \right) \quad (A.75)$$

A.2. State of the art

TITLE-ABS-KEY (('Shape memory alloy 'OR niti* OR sma) AND ('SMAHC 'OR 'hybrid composite ') AND (model* OR design) AND ('deflect* 'OR 'bend* 'OR 'morph* 'OR 'shape adapt* '))

A.3. Active deflection approximation

The geometric system to be investigated (compare figure A.1) consists of a section of known length curved with a constant radius and a section of constant slope connected to it. From the differential equation of the bending line 2.35, equation A.76 is obtained for a constant bending moment M and constant stiffness EI along the bending beam, where BR is the radius of curvature. [81]

$$\frac{d\Phi}{ds} = \frac{1}{BR_{sub}} \quad (A.76)$$

Integration of the curvature changes over the entire length of the curved section a_l , provides the angle at the end of the curved section $\Phi(a_l)$, according to equation A.77.

$$\Phi(a_l) = \frac{1}{BR_{sub}} \int_0^{a_l} ds = \frac{a_l}{BR_{sub}} \quad (A.77)$$

With the geometrical condition A.78 the maximum extension of the curved section in x-direction x_{max} can be derived using equation A.76 and A.79.

$$ds = \frac{dx}{\cos(\Phi)} \quad (A.78)$$

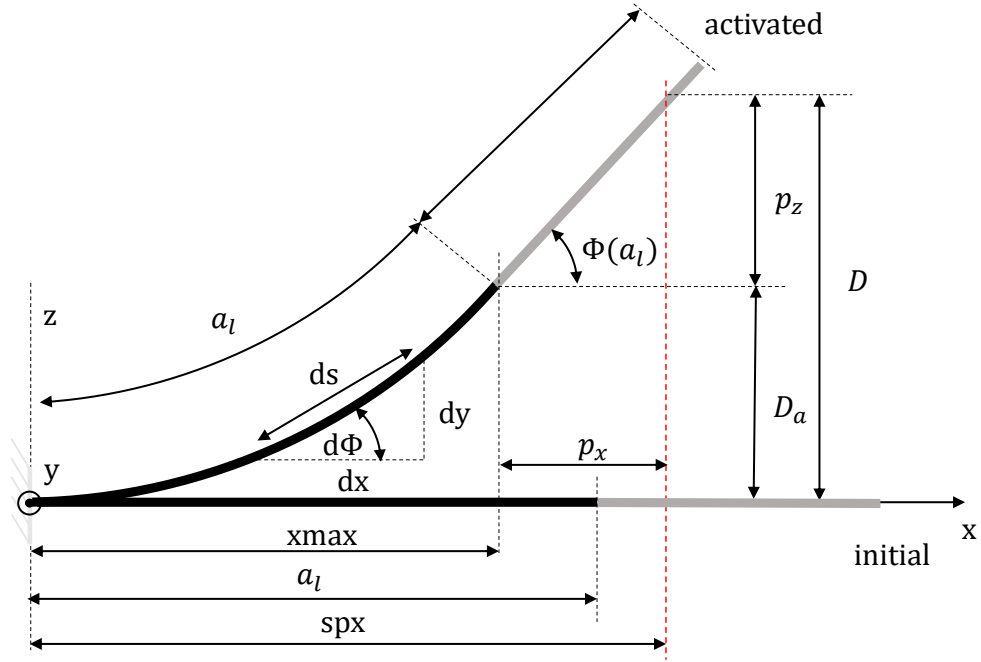


Figure A.1: Geometric system for active deflection approximation from known deflection at certain measurement deflection position. System is composed of a section with constant curvature and a straight section.

$$x_{max} = BR_{sub} \int_0^{\frac{a_l}{BR_{sub}}} \cos(\Phi) d\Phi = BR_{sub} \cdot \sin\left(\frac{a_l}{BR_{sub}}\right) \quad (\text{A.79})$$

The deflection at the deflection measurement position D is composed of the proportion of the curved section D_a , which corresponds to the deflection at the end of the active area, and the proportion of the straight section p_z which is given by equation A.81, according to equation A.80. With the help of the circle equation, the deflection at the end of the active area D_a can be expressed by equation A.82.

$$D = D_a + p_z \quad (\text{A.80})$$

$$p_z = p_x \cdot \tan\left(\frac{a_l}{BR_{sub}}\right) \quad (\text{A.81})$$

$$D_a = -\sqrt{BR_{sub}^2 - x_{max}^2} + BR_{sub} \quad \text{where } x \in \mathbb{R} | 0 \leq x \leq x_{max} \quad (\text{A.82})$$

In turn, p_x is given by equation A.83.

$$p_x = s_{px} - x_{max} \quad (\text{A.83})$$

Substituting equations A.81, A.82, A.83, A.79 into A.80 yields equation 5.38.

A.4. SMAHC characterization

Temperature in °C

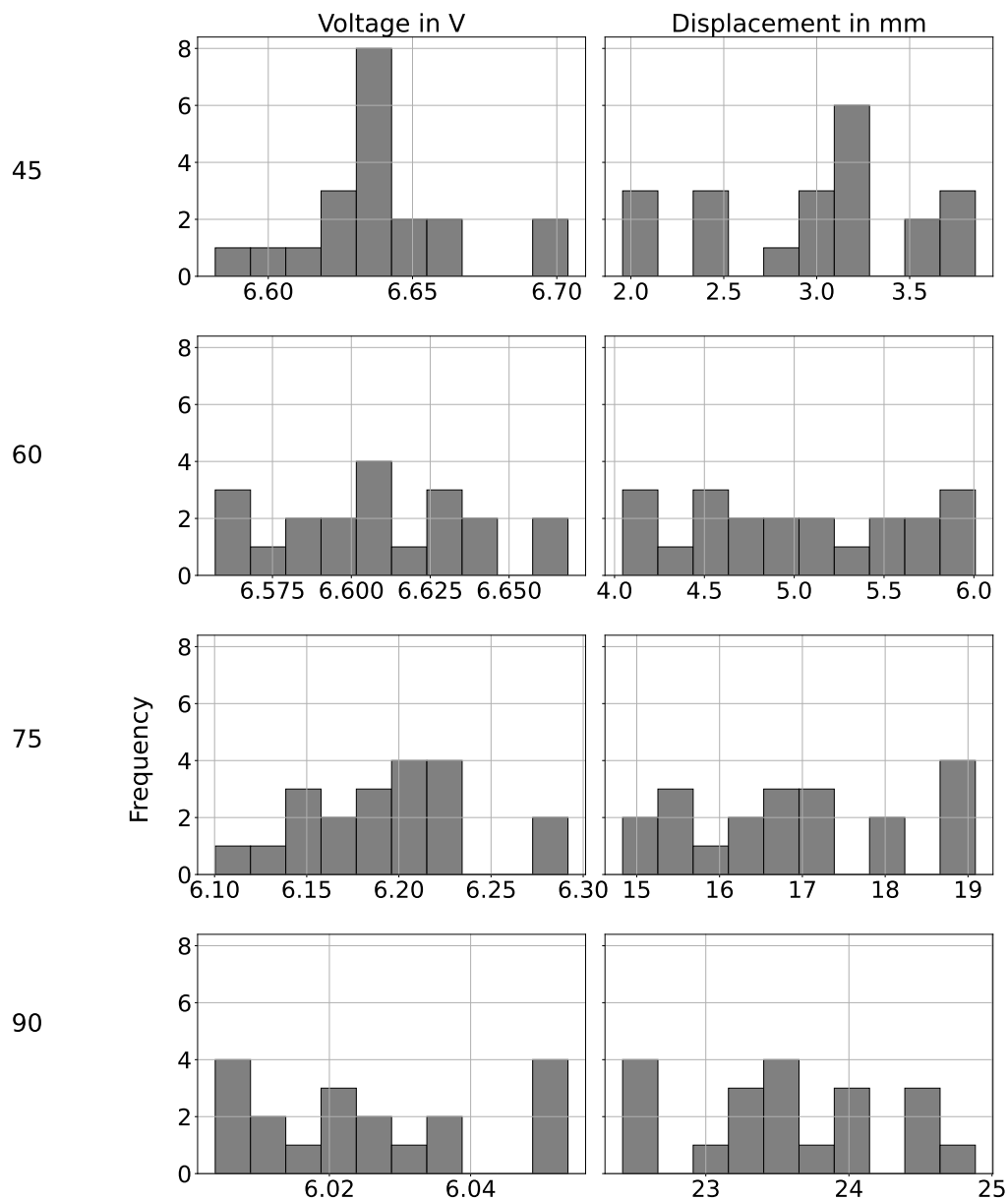


Figure A.2: Distribution of measured data for the last cycle of precycle experiments. Experiment was carried out with 21 SMAHC's of type C. Histograms show data recorded at different measured temperature levels during activation, or quantities derived from them. Chi-squared goodness-of-fit tests according to [128] indicated that a Student's t-distribution can be assumed in every case.

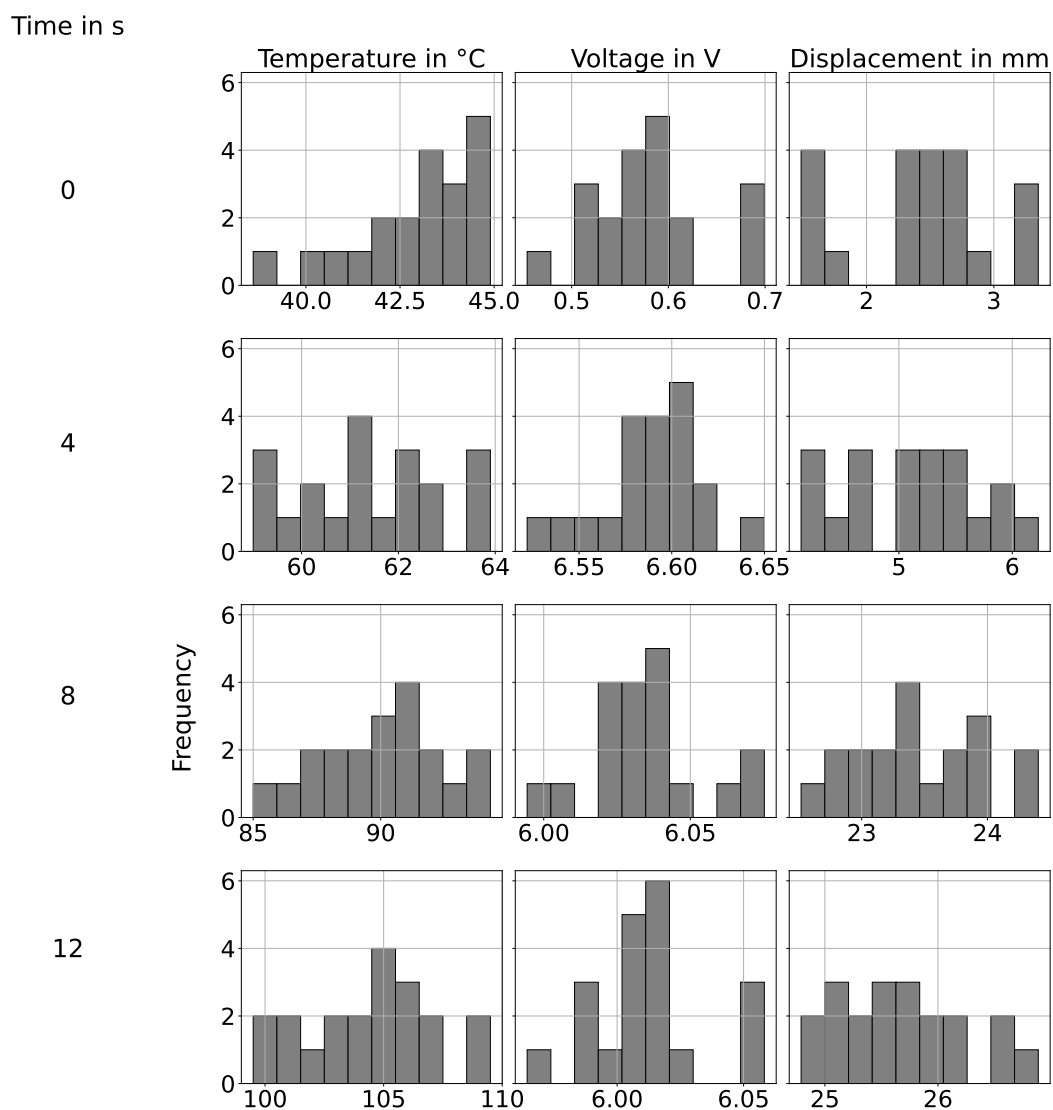


Figure A.3: Distribution of measured data for the last cycle of precycle experiments. Experiment was carried out with 21 SMAHC's of type C. Histograms show data recorded at different run times of the experiment, or quantities derived from them. Chi-squared goodness-of-fit tests according to [128] indicated that a Student's t-distribution can be assumed in every case.

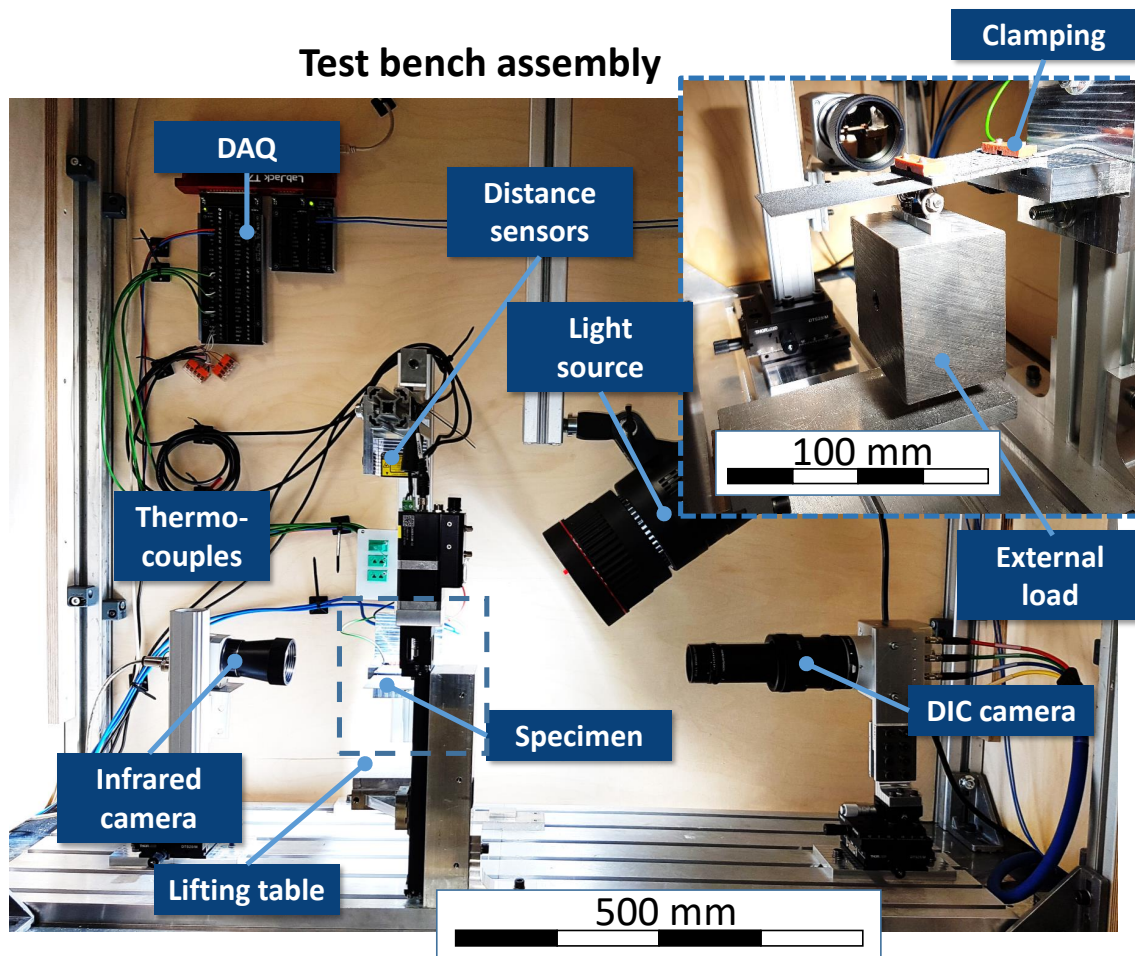


Figure A.4: Picture of the test setup for experiments at RT. Actuator positioning is shown in detail.

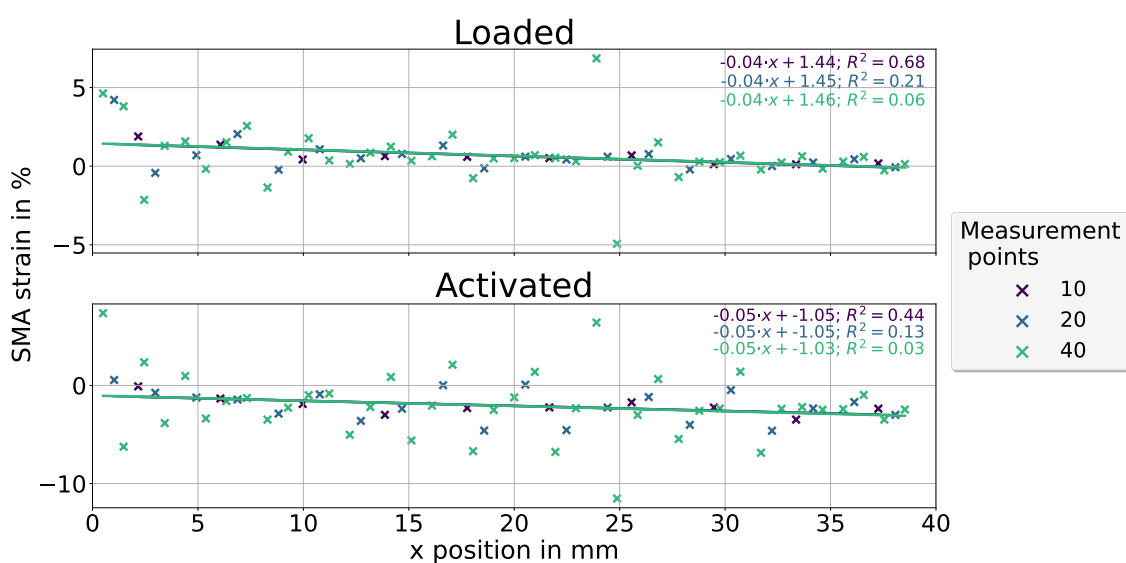


Figure A.5: Investigation of influence of facet point density along SMA wire on linear curve fit.

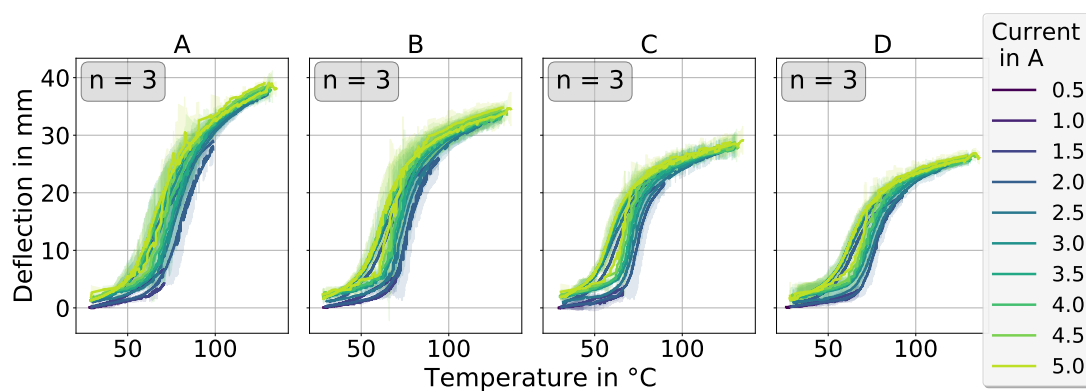


Figure A.6: Temperature hysteresis loops for different activation currents at RT sorted by actuator type.

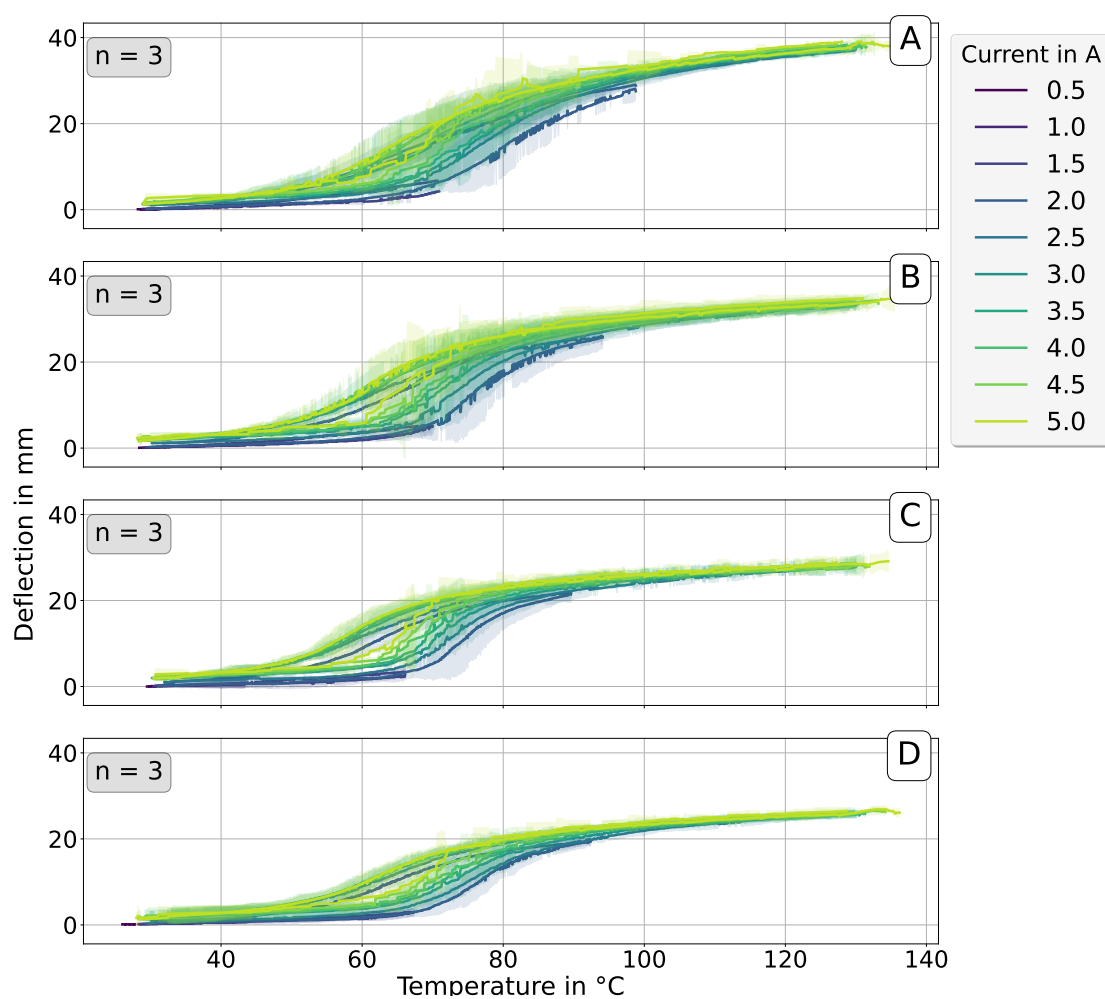


Figure A.7: Temperature hysteresis loop at RT for various activation currents and actuator types.

A.5. Test setups

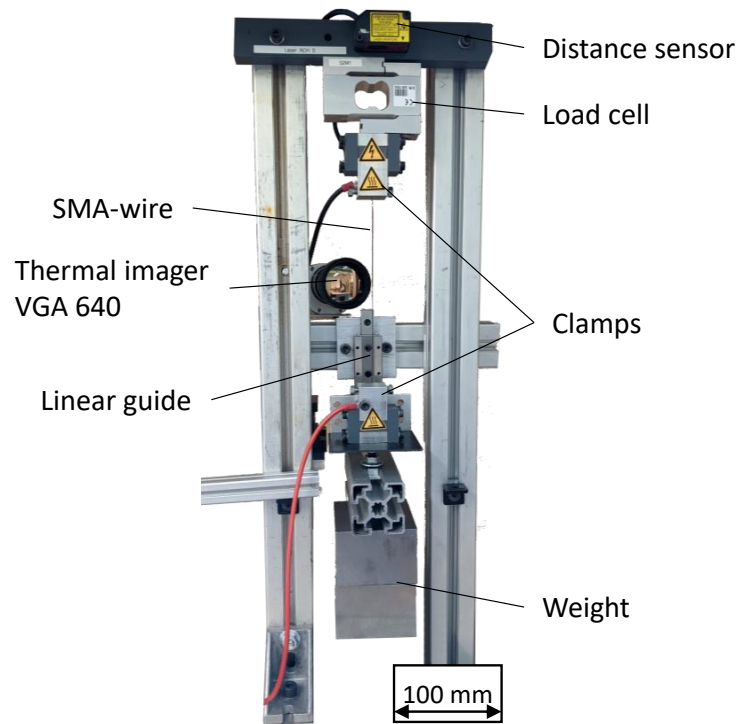


Figure A.8: Constant load test setup and components.

A.6. Python scripts

| <i>SMAHC</i> | SMAHC |
|---------------------|---|
| <i>width</i> | Width of the SMAHC |
| <i>length</i> | Active length of the SMAHC |
| <i>dist_sub_sma</i> | Distance between centerline of the substrate and centerline of the SMA |
| <i>hslt</i> | Homogeneous SMA-layer thickness, according to equation \ref{eq_homogenius_layer} |
| <i>stiffness</i> | Stiffness of the SMAHC against the SMA contraction according to equation \ref{eq_substrate_bending} |
| <i>w</i> | SMA wire |
| <i>g</i> | Grid |
| <i>s</i> | Substrate |
| <i>d</i> | Interlayer |

| <i>w</i> | SMA wire |
|-----------------------------|---|
| <i>rho</i> | Density |
| <i>diameter</i> | Diameter |
| <i>radius</i> | Radius |
| <i>Crossection_area</i> | Crossection area |
| <i>Circumference</i> | Circumference |
| <i>CMs</i> | Stress induced coefficient of Martensite start temperature |
| <i>CMf</i> | Stress induced coefficient of Martensite finish temperature |
| <i>CAs</i> | Stress induced coefficient of Austenite start temperature |
| <i>CAf</i> | Stress induced coefficient of Austenite finish temperature |
| <i>As</i> | Austenite start temperature |
| <i>Af</i> | Austenite finish temperature |
| <i>Ms</i> | Martensite start temperature |
| <i>Mf</i> | Martensite finish temperature |
| <i>max_strain_zero_load</i> | Transformation strain for zero load level $\epsilon(\sigma = 0)$ |
| <i>EA</i> | Young's modulus in austenitic state |
| <i>EM</i> | Young's modulus in martensitic state |
| <i>dH_M_to_A</i> | Transformation enthalpie for martensite to austenite transformation |
| <i>dH_R_to_M</i> | Transformation enthalpie for R-phase to martensite transformation |
| <i>cA</i> | Specific heat capacity in austenitic state |
| <i>cM</i> | Specific heat capacity in martensitic state |
| <i>rM</i> | Resistivity in martensitic state |
| <i>rA</i> | Resistivity in austenitic state |
| <i>k</i> | Exponential fit coefficient for transformation strain distinction |
| <i>max_trans_strain</i> | Maximum transformation strain ϵ_{max} |
| <i>length</i> | Length |
| <i>volume</i> | Volume |
| <i>mass</i> | Mass |
| <i>surface</i> | Surface |
| <i>resM</i> | Resistance in martensitic state |
| <i>resA</i> | Resistance in austenitic state |

| <i>g</i> | Grid |
|-------------|---|
| <i>n</i> | Amount of wires |
| <i>dist</i> | Distance between parallel wire centerlines |
| <i>resM</i> | The grids resistance in martensitic state for series connection |
| <i>resA</i> | The grids resistance in austenitic state for series connection |

| <i>d</i> | Interlayer |
|---------------|------------------------|
| <i>length</i> | Length |
| <i>heigth</i> | Thickness |
| <i>width</i> | Width |
| <i>lam</i> | Thermal conductivity |
| <i>c</i> | Specific heat capacity |
| <i>rho</i> | Density |

| <i>s</i> | Substrate |
|---------------|------------------------|
| <i>length</i> | Length |
| <i>heigth</i> | Thickness |
| <i>width</i> | Width |
| <i>I</i> | Area moment of inertia |
| <i>E</i> | Young's modulus |
| <i>lam</i> | Thermal conductivity |
| <i>c</i> | Specific heat capacity |
| <i>rho</i> | Density |

Figure A.9: Tables containing the attributes and their description for the SMAHC and components.

| <i>Variable</i> | <i>Data type</i> | <i>Description</i> |
|--|----------------------------|--|
| <i>load</i> | <i>float</i> | Static external load at end of active area |
| <i>alpha_elastomer</i> | <i>float</i> | Heat transfer coefficient between elastomer and surroundings |
| <i>Tu, T0, dT, T</i> | <i>float</i> | Ambient-, initial-, incremental-, Temperature |
| <i>sequences</i> | <i>list</i> | List of sequences including time and supplied current for sequence |
| <i>dt</i> | <i>float</i> | Temporal increment |
| <i>dx</i> | <i>float</i> | Spatial increment |
| <i>mf0, mf_1, mf</i> | <i>float</i> | Initial-, constant-, martensite fraction |
| <i>stress0, stress</i> | <i>float</i> | Initial and SMA wire stress |
| <i>strain0, strain</i> | <i>float</i> | Initial and SMA wire strain |
| <i>real_As, real_Af, real_Ms, real_Mf</i> | <i>float</i> | Stress influenced transformation temperatures |
| <i>resistance</i> | <i>float</i> | SMA wire resistance |
| <i>R</i> | <i>float</i> | Bending radius |
| <i>eps_tr</i> | <i>float</i> | Current maximum transformation strain |
| <i>xmax</i> | <i>float</i> | Maximum expansion of the SMAHC in x-direction |
| <i>S</i> | <i>SMAHC</i> | SMAHC object |
| <i>u0_d, u_d</i> | <i>np-array</i> | Interlayer temperature field |
| <i>U</i> | <i>float</i> | Incremental change in internal energy |
| <i>Ein</i> | <i>float</i> | Incremental electrical energy supplied to the system |
| <i>E_cond, E_conv, E_loss</i> | <i>float</i> | Incremental conductive-, convective-, accumulated Energy loss |
| <i>E_cond_sum, E_conv_sum, E_loss_sum, Ein_sum, Usum</i> | <i>float</i> | Incremental cumulative energy amounts |
| <i>data_array</i> | <i>np-array</i> | Array for data storage |
| <i>t, t_tot</i> | <i>float</i> | Current simulated time, total time to simulate |
| <i>current</i> | <i>float</i> | Supplied current |
| <i>E</i> | <i>float</i> | The SMA's Young's modulus |
| <i>L0</i> | <i>float</i> | The SMA's initial length |
| <i>deflection</i> | <i>float</i> | Deflection of the SMAHC at end of active length |
| <i>dt_max</i> | <i>float</i> | Maximum time increment for heat transfer simulation according to Courant-Friedrichs-Lewy stability criteria |
| <i>nsteps</i> | <i>float</i> | Number of increments of the heat transfer simulation for one increment of the overall transient SMAHC simulation |
| <i>nx_d</i> | <i>int</i> | Number of elements of interlayer representation in x-direction |
| <i>ny_d</i> | <i>int</i> | Number of elements of interlayer representation in y-direction |
| <i>a</i> | <i>float</i> | Specific heat capacity during transformation |
| <i>td</i> | <i>float</i> | Thermal diffusivity inside the interlayer |
| <i>tds</i> | <i>float</i> | Thermal diffusivity between surface of the interlayer and ambient |
| <i>md</i> | <i>Mechanical_domain</i> | Mechanical domain model object |
| <i>ht</i> | <i>Heat_transfer</i> | Heat transfer model object |
| <i>hc</i> | <i>horizontal_cylinder</i> | Horizontal cylinder object that allows for determination of the heat transfer between the upper half of the wire and the ambient |
| <i>A_sma</i> | <i>float</i> | Cumulative crosssection of all wires in the grid |
| <i>phi, phidot</i> | <i>list</i> | List of the angles of curvature and list of all derivatives for all elements that represent the mechanical system of the SMAHC |
| <i>elements</i> | <i>List</i> | List of all elements that represent the mechanical system of the SMAHC |
| <i>phi0, phi_d_0</i> | <i>float</i> | Angle of curvature and derivative at fixed end of the SMAHC $\Phi(L = 0)$ and $\Phi'(L = 0)$ |
| <i>M_sma</i> | <i>float</i> | Bending moment exerted by the SMA |

Figure A.10: Table declaring and describing the essential variables used for script implementation.

A.6.1. Main

```

1   -*- coding: utf-8 -*-
2   """
3   Created on Fri Jul 8 17:21:57 2022
4   @author: Max kaiser
5   @mail: max.kaiser@ivw.uni-kl.de
6   @facility: Leibniz Institut für Verbundwerkstoffe GmbH
7   @license: MIT License
8   @copyright: Copyright (c) 2023 Leibniz Institut für Verbundwerkstoffe GmbH
9   @Version: 0.0.
10  """
11  # =====
12  # Load modules
13  # =====
14 import json
15 import numpy as np
16 import os
17  #In-house modules
18 from utils.material import SMAHC
19 from SMAHC_model.SMA_model.lumped_sma_model import sma_model as sm
20 from SMAHC_model.Heat_transfer_model.twoD_elastomer import Heat_transfer
21 from SMAHC_model.Heat_transfer_model.heat_transfer_coefficient import horizontal_cylinder
22 from SMAHC_model.Mechanic_domain_model.twoD_mechanic_model import Mechanical_domain
23 from project_root import get_project_root
24
25  # =====
26  # Initialize
27  # =====
28  #Path of the local repository
29 root = get_project_root()
30  #Read input data from INPUT.txt and load parameters
31 with open(root+os.sep+"INPUT.txt") as input_data_file:
32     ipt_dct = json.load(input_data_file)
33     load = ipt_dct['Load']
34     alpha_elastomer = ipt_dct['Alpha_elastomer']
35     Tu = ipt_dct['Ambient_temperature']
36     sequences = ipt_dct['Sequences']
37     dt = ipt_dct['Time_increment']
38     dx = ipt_dct['Spatial_increment']
39     mf0 = ipt_dct['mf0']
40     stress0 = ipt_dct['stress0']
41     S = SMAHC(ipt_dct['Actuator_type'])
42  #Initialize state variables
43     L0 = S.w.length
44     E_cond, E_conv, E_loss, U, Ein = 0,0,0,0,0
45     E_cond_sum, E_conv_sum, E_loss_sum, Ein_sum, Usum = 0,0,0,0,0
46     a,dT, t, deflection = 0,0,0,0,0
47     T = Tu
48     T0 = Tu
49     stress = stress0
50     E = S.w.EM
51     mf = mf0
52     mf_1 = mf0
53     r = S.w.rM
54     resistance = S.w.resM
55     real_As = S.w.As + stress0/S.w.CAs
56     real_Af = S.w.Af + stress0/S.w.CAf
57     real_Mf = S.w.Mf + stress0/S.w.CMf
58     real_Ms = S.w.Ms + stress0/S.w.CMs

```

```

59 eps_tr = S.w.max_strain_zero_load + \
60     (S.w.max_trans_strain - S.w.max_strain_zero_load)*(1-np.exp(-S.w.k*(stress0)/S.w.EA))
61 strain0 = eps_tr
62 strain = strain0
63 R = np.inf
64 xmax = S.length
65 #Initialize mechanical domain model
66 md = Mechanical_domain(S, 2000, load, mf0)
67 #Initialize conductive heat transfer model
68 ht = Heat_transfer(S, dx, Tu, alpha_elastomer, dt)
69 u0_d = ht.u0_d
70 u_d = ht.u_d
71 #Initialize convective heat transfer coefficient
72 hc = horizontal_cylinder(S.w.diameter, Tu, 'dry_air')
73 #Create array for result data storage
74 column_names = ['t', 'dt', 'stress0', 'mf0', 'strain0', 'L0', 'E_loss', 'current', \
75                'stress', 'T', 'E', 'mf', 'strain', 'r', 'resistance', 'real_As', \
76                'real_Af', 'real_Mf', 'real_Ms', 'a', 'U', 'dT', 'Ein', 'E_cond', \
77                'E_conv', 'E_loss', 'E_cond_sum', 'E_conv_sum', 'E_loss_sum', 'Ein_sum', \
78                'Usum', 'deflection', 'xmax', 'eps_tr', 'alpha']
79 t_tot = sum(sequence[1] for sequence in sequences)
80 data_array = np.ones((int((t_tot-t)/dt), len(column_names)))
81 #Initialize counters
82 data_array_idx = 0
83
84 # =====
85 # Simulate
86 # =====
87 #Work through all sequences
88 for sequence in sequences:
89     sequence_end = t + sequence[1]
90     current = sequence[0]
91     #Simulate the sequence for the respective time period t
92     while t < sequence_end:
93         #Increment the time
94         t += dt
95         #Solve mechanical domain model
96         stress0, deflection, xmax = md.solve(mf)
97         #Solve SMA model
98         E, mf, strain, r, resistance, real_As, real_Af, real_Mf, real_Ms, a, U, dT, Ein, \
99         stress, eps_tr = sm(S.w, dt, stress0, mf0, strain0, L0, E_loss, \
100                            current, stress, T, E, mf, strain, r, resistance, \
101                            real_As, real_Af, real_Mf, real_Ms, a, U, dT, Ein, \
102                            -S.stiffness, mf_1, eps_tr)
103         #Increment temperature
104         T += dT
105         #Solve conductive heat transfer model
106         u0_d, u_d, E_cond = ht.do_timestep(u0_d, u_d, T0, T)
107         T0 = T
108         #Calculate temperature dependent heat transfer coefficient of the upper
109         #half of the wire
110         alpha = hc.alpha(T)
111         #Calculate the convective energy loss of the upper half of the wire
112         E_conv = L0 * np.pi * S.w.diameter * (T-Tu) * dt * hc.alpha(T)
113         #Sum up the heat losses
114         E_loss = E_cond + E_conv
115         #Cumulating the energy components
116         Ein_sum += Ein
117         Usum += U

```

```

118     E_cond_sum += E_cond
119     E_conv_sum += E_conv
120     E_loss_sum += E_loss
121     #Write data to array
122     data_array[data_array_idx] = [t, dt, stress0, mf0, strain0, L0, E_loss, current, \
123                                 stress, T,E, mf, strain, r, resistance, real_As, \
124                                 real_Af, real_Mf, real_Ms, a, U, dT, Ein, E_cond, \
125                                 E_conv, E_loss, E_cond_sum, E_conv_sum, E_loss_sum, \
126                                 Ein_sum, Usum, deflection, xmax, eps_tr, alpha]

```

A.6.2. Lumped SMA model

```

1  # -*- coding: utf-8 -*-
2  """
3  Created on Tue Dec 14 16:40:32 2021
4  @author: Max kaiser
5  @mail: max.kaiser@ivw.uni-kl.de
6  @facility: Leibniz Institut für Verbundwerkstoffe GmbH
7  @license: MIT License
8  @copyright: Copyright (c) 2023 Leibniz Institut für Verbundwerkstoffe GmbH
9  @Version: 0.0.
10  """
11  # =====
12  # Load modules
13  # =====
14  from scipy.optimize import fsolve
15  import numpy as np
16  # =====
17  # System of Equations to be solved for transformation from martensite to austenite
18  # =====
19  def heat_MtoA(vars, *args):
20      dt, stress0, mf0, strain0, L0, Eloss, current, T, w, lam_coeff, mf_1, mfm1 = args
21      E, mf, strain, r, resistance, real_As, real_Af, real_Mf, real_Ms, a, U, dT, Ein, \
22          stress, eps_tr = vars
23      #Constitutive Model
24      eq14 = w.EM * mf + w.EA * (1 - mf) - E
25      eq11 = E * (strain - eps_tr) - E * eps_tr * (mf - mf0) - (stress)
26      #Resistance Model
27      eq3 = w.rM * mf + w.rA * (1 - mf) - r
28      eq4 = r * L0 / (np.pi * ((w.diameter/2)**2)) - resistance
29      #Phase fraction Model
30      eq5 = w.As - real_As + (stress) / w.CAs
31      eq6 = w.Af - real_Af + (stress) / w.CAf
32      eq7 = w.Mf - real_Mf + (stress) / w.CMf
33      eq8 = w.Ms - real_Ms + (stress) / w.CMs
34      #Heat capacitance model
35      eq9 = w.dH_M_to_A * (np.pi / (2 * (w.Af - w.As + stress * (1/w.CAf - 1/w.CAs)))) * \
36          np.sin(np.pi * (T - w.As - stress/w.CAs) / (w.Af - w.As + stress * (1/w.CAf - 1/w.CAs))) - a
37      eq10 = L0 * np.pi * (w.diameter/2)**2 * w.rho * (((w.cA + w.cM)/2) + a) * dT - U
38      eq1 = mf_1 * 0.5 * (np.cos(np.pi * (T - w.As - stress/w.CAs) / \
39          (w.Af - w.As + stress * (1/w.CAf - 1/w.CAs))) + 1) - mf
40      #Joule heat Model
41      eq12 = resistance * current * current * dt - Ein
42      eq13 = U + Eloss - Ein
43      eq2 = lam_coeff * (eps_tr - strain) + (stress - stress0)
44      eq15 = w.max_strain_zero_load + (w.max_trans_strain - w.max_strain_zero_load) * \
45          (1 - np.exp(-w.k * (stress) / w.EA)) - eps_tr
46      return [eq1, eq2, eq3, eq4, eq5, eq6, eq7, eq8, eq9, eq10, eq11, eq12, eq13, eq14, eq15]

```

```

47 # =====
48 # System of Equations to be solved for transformation from austenite to martensite
49 # =====
50 def cool_AtoM(vars, *args):
51     dt, stress0, mf0, strain0, L0, Eloss, current, T, w, lam_coeff, mf1, mfm1 = args
52     E, mf, strain, r, resistance, real_As, real_Af, real_Mf, real_Ms, a, U, dT, Ein, \
53         stress, eps_tr = vars
54     #Constitutive Model
55     eq1 = w.EM * mf + w.EA * (1 - mf) - E
56     eq2 = E * (strain - eps_tr) - E * eps_tr * (mf - mf0) - (stress)
57     #Resistance Model
58     eq3 = w.rM * mf + w.rA * (1 - mf) - r
59     eq4 = r * L0 / (np.pi * ((w.diameter/2)**2)) - resistance
60     #Phase fraction Model
61     eq5 = w.As - real_As + (stress) / w.CAs
62     eq6 = w.Af - real_Af + (stress) / w.CAf
63     eq7 = w.Mf - real_Mf + (stress) / w.CMf
64     eq8 = w.Ms - real_Ms + (stress) / w.CMs
65     #Heat capacitance model
66     eq9 = w.dH_R_to_M * (np.pi / (2 * (real_Ms - real_Mf))) * \
67         np.sin(np.pi * (T - real_Mf) / (real_Ms - real_Mf)) - a
68     eq10 = L0 * np.pi * (w.diameter/2)**2 * w.rho * (((w.cA+w.cM)/2) + a) * dT - U
69     eq11 = 0.5 * (np.cos(np.pi / (real_Ms - real_Mf)) * (T - real_Mf)) + 1) - mf
70     #Joule heat Model
71     eq12 = resistance * current * current * dt - Ein
72     eq13 = U + Eloss - Ein
73     eq14 = lam_coeff * (eps_tr - strain) + (stress - stress0)
74     eq15 = w.max_strain_zero_load + (w.max_trans_strain - w.max_strain_zero_load) * \
75         (1 - np.exp(-w.k * (stress) / w.EA)) - eps_tr
76     return [eq1, eq2, eq3, eq4, eq5, eq6, eq7, eq8, eq9, eq10, eq11, eq12, eq13, eq14, eq15]
77 # =====
78 # System of Equations to be solved when martensite fraction is constant
79 # or no transformation occurs
80 # =====
81 def const_mf(vars, *args):
82     dt, stress0, mf0, strain0, L0, Eloss, current, T, w, lam_coeff, mf1, mfm1 = args
83     E, mf, strain, r, resistance, real_As, real_Af, real_Mf, real_Ms, a, U, dT, Ein, \
84         stress, eps_tr = vars
85     #Constitutive Model
86     eq1 = w.EM * mfm1 + w.EA * (1 - mfm1) - E
87     eq2 = E * (strain - eps_tr) - E * eps_tr * (mfm1 - mf0) - (stress)
88     #Resistance Model
89     eq3 = w.rM * mfm1 + w.rA * (1 - mfm1) - r
90     eq4 = r * L0 / (np.pi * ((w.diameter/2)**2)) - resistance
91     #Phase fraction Model
92     eq5 = w.As - real_As + (stress) / w.CAs
93     eq6 = w.Af - real_Af + (stress) / w.CAf
94     eq7 = w.Mf - real_Mf + (stress) / w.CMf
95     eq8 = w.Ms - real_Ms + (stress) / w.CMs
96     #Heat capacitance model
97     eq9 = 0 - a
98     eq10 = L0 * np.pi * (w.diameter/2)**2 * w.rho * (((w.cA+w.cM)/2)) * dT - U
99     eq11 = mf - mfm1
100    #Joule heat Model
101    eq12 = resistance * current * current * dt - Ein
102    eq13 = U + Eloss - Ein
103    eq14 = lam_coeff * (eps_tr - strain) + (stress - stress0)
104    eq15 = w.max_strain_zero_load + (w.max_trans_strain - w.max_strain_zero_load) * \
105        (1 - np.exp(-w.k * (stress) / w.EA)) - eps_tr

```

```

106     return [eq1, eq2, eq3, eq4, eq5, eq6, eq7, eq8, eq9, eq10, eq11, eq12, eq13, eq14, eq15]
107 # =====
108 # Decision tree for distinguishing of transformation state
109 # =====
110 def sma_model(w, dt, stress0, mf0, strain0, L0, Eloss, current, stress, T, E, mf, strain, r,\
111             resistance, real_As, real_Af, real_Mf, real_Ms, a, U, dT, Ein,\
112             lam_coeff, mf_1, eps_tr):
113     mfm1 = mf
114     all_args = (dt, stress0, mf0, strain0, L0, Eloss, current, T, w, lam_coeff, mf_1, mfm1)
115     ipt = (E, mf, strain, r, resistance, real_As, real_Af, real_Mf, real_Ms, a, U, dT,\
116           Ein, stress, eps_tr)
117     opt = (E, mf, strain, r, resistance, real_As, real_Af, real_Mf, real_Ms, a, U, dT,\
118           Ein, stress, eps_tr)
119     if T > real_Af:
120         mfm1 = 0
121         all_args = (dt, stress0, mf0, strain0, L0, Eloss, current, T, w, lam_coeff, mf_1,\
122                   mfm1)
123         opt = fsolve(const_mf, ipt, args = all_args, xtol = 1e-10)
124     elif T < real_Mf:
125         mfm1 = 1
126         all_args = (dt, stress0, mf0, strain0, L0, Eloss, current, T, w, lam_coeff, mf_1,\
127                   mfm1)
128         opt = fsolve(const_mf, ipt, args = all_args, xtol = 1e-10)
129     else:
130         if U > 0:
131             if mf <= 0:
132                 mfm1 = 0
133                 all_args = (dt, stress0, mf0, strain0, L0, Eloss, current, T, w, lam_coeff,\
134                             mf_1, mfm1)
135                 opt = fsolve(const_mf, ipt, args = all_args, xtol = 1e-10)
136             else:
137                 if T <= real_As:
138                     opt = fsolve(const_mf, ipt, args = all_args, xtol = 1e-10)
139                 else:
140                     opt = fsolve(heat_MtoA, (E, mf*0.99, strain, r, resistance, real_As,\
141                                           real_Af, real_Mf, real_Ms, a, U, dT, Ein, \
142                                           stress, eps_tr), \
143                               args = all_args, xtol = 1e-10)
144         else:
145             if mf >= 1:
146                 mfm1 = 1
147                 all_args = (dt, stress0, mf0, strain0, L0, Eloss, current, T, w, lam_coeff,\
148                             mf_1, mfm1)
149                 opt = fsolve(const_mf, ipt, args = all_args, xtol = 1e-10)
150             else:
151                 if T >= real_Ms:
152                     opt = fsolve(const_mf, ipt, args = all_args, xtol = 1e-10)
153                 else:
154                     opt = fsolve(cool_AtoM, (E, mf*1.01, strain, r, resistance, real_As,\
155                                           real_Af, real_Mf, real_Ms, a, U, dT, Ein,\
156                                           stress, eps_tr),\
157                               args = all_args, xtol = 1e-10)
158     return opt

```

A.6.3. Heat transfer model

```

1 # -*- coding: utf-8 -*-
2 """

```

```

3 Created on Mon Nov 29 16:11:17 2021
4 @author: Max kaiser
5 @mail: max.kaiser@ivw.uni-kl.de
6 @facility: Leibniz Institut für Verbundwerkstoffe GmbH
7 @license: MIT License
8 @copyright: Copyright (c) 2023 Leibniz Institut für Verbundwerkstoffe GmbH
9 @Version: 0.0.
10 """
11 # =====
12 # Load modules
13 # =====
14 import numpy as np
15 # =====
16 # Heat transfer class
17 # =====
18 class Heat_transfer:
19     #Initialize Heat transfer problem
20     def __init__(self, SMAHC, dx, Tu, a_air, dt): # a_air 35
21         self.name = '2D_elastomer_only'
22         self.S = SMAHC
23         self.dx = dx*1000 # dx in mm
24         self.dx2 = self.dx**2 # dx^2 in mm^2
25         self.dt = dt
26         self.l = self.S.length
27         self.Tu = Tu
28         # Calculate thermal diffusivity td in mm^2/s for the interlayer
29         self.td = 1000*1000*self.S.d.lam/(self.S.d.rho*self.S.d.c)
30         # Calculate heat transfer coefficient to the surroundings tds in mm/s for interlayer
31         self.tds = 1000* a_air/(self.S.d.rho*self.S.d.c*self.dx)
32         # Calculate number of elements of mesh in x-direction nx_d and in y direction ny_d
33         self.nx_d, self.ny_d = int(1000*self.S.d.height/self.dx)+\
34             1, int((1000*self.S.g.dist/2)/self.dx)+2
35         # Calucalte maximum permissible discrete time step according to \
36         #Courant-Friedrichs-Lewy stability criteria
37         self.dt_max = 0.5*(self.dx2/(2*self.td))
38         if self.dt_max > self.dt:
39             self.dt_max = self.dt
40         # Initialize array
41         self.u0_d = Tu * np.ones((self.nx_d, self.ny_d))
42         self.u_d = self.u0_d.copy()
43         # Create mask for boundary conditions
44         self.u_d_boundary = np.zeros((self.nx_d, self.ny_d), dtype=bool)
45         # Calculate constant for heat flux determination of one time step
46         self.E_cond_const = 2 * self.S.d.lam * self.l * self.dt_max
47         # Create mask for sma wire
48         self.u_heat = self.u_d_boundary.copy()
49         #Deterimen all cells that belong to SMA-wire
50         for i in range(self.nx_d):
51             for j in range(self.ny_d):
52                 p = np.sqrt((i*self.dx-0)**2 + (j*self.dx-((self.S.g.dist*1000)/2))**2)
53                 if p < (self.S.w.radius*1000) +self.dx/2:
54                     self.u_heat[i,j] = True
55         #Determine all cells that belong to SMA-wire surface
56         self.surface_lst = []
57         for i in range(self.nx_d):
58             for j in range(self.ny_d):
59                 if self.u_heat[i,j] == True and self.u_heat[i+1,j] == True:
60                     self.surface_lst.append([i,j])
61                 break

```

```

62         elif self.u_heat[i,j] == True and self.u_heat[i+1,j] == False:
63             self.surface_lst.append([i,j])
64         else:
65             pass
66         #Boundary symmetrie right
67         self.u_d_right = self.u_d_boundary.copy()
68         self.u_d_right[:,self.ny_d-1] = np.ones(self.nx_d)
69         #Boundary symmetrie left
70         self.u_d_left = self.u_d_boundary.copy()
71         self.u_d_left[:,0] = np.ones(self.nx_d)
72         #Boundary symmetrie down
73         self.u_tdown = self.u_d_boundary.copy()
74         self.u_tdown[self.nx_d-1,:] = np.ones(self.ny_d)
75         #Heat transfer boundary condition to the surroundings
76         self.u_d_up = self.u_d_boundary.copy()
77         self.u_d_up[0,:] = np.zeros(self.ny_d)
78         self.u_d_up[0,:np.where(self.u_heat[0,:]==True)[0][0]] == True
79         #Calculate the number of time steps to do for one time step of the main script
80         self.nsteps = int(self.dt/self.dt_max)
81         if self.nsteps == 0:
82             self.nsteps = 1
83         # Do timestep method to do one time step regarding the main script
84         def do_timestep(self, u0_d, u_d, Tsm0, Tsm):
85             #Initialize time step
86             E_cond = 0
87             dT = (Tsm-Tsm0)/self.nsteps
88             #Run time steps according to number of time steps necessary
89             for step in range(1,self.nsteps+1):
90                 #Linearize temperature change
91                 u0_d[self.u_heat] = Tsm0 + dT * step
92                 #Calculate heat flux between SMA-wire surface and interlayer for one time
93                 #step in the thermal domain
94                 T_dif = 0
95                 for se in self.surface_lst[1:-2]:
96                     T_dif += u0_d[se[0],se[1]-1] + u0_d[se[0]+1,se[1]]
97                 T_dif = (2 * len(self.surface_lst[1:-2]) * Tsm) - T_dif
98                 E_cond += self.E_cond_const * T_dif
99                 # Update temperature field using forward-difference in time,
100                # central-difference in space scheme
101                u_d[1:-1, 1:-1] = u0_d[1:-1, 1:-1] + (self.dt_max/self.dx2) * self.td * \
102                    (u0_d[2:, 1:-1] + u0_d[:-2, 1:-1] + u0_d[1:-1, 2:] + \
103                     u0_d[1:-1, :-2] - 4*u0_d[1:-1, 1:-1])
104                #Update temperature field at boundaries
105                u_d[self.nx_d-1, 1:-1] = u0_d[self.nx_d-1, 1:-1] + self.td * \
106                    (self.dt_max/self.dx2) * (u0_d[self.nx_d-1, 1:-1] + \
107                     u0_d[self.nx_d-1, 2:] + u0_d[self.nx_d-1, :-2] - 3*u0_d[self.nx_d-1, 1:-1]) \
108                    - self.tds*self.dt_max*(u0_d[self.nx_d-1, 1:-1]-self.Tu)
109                u_d[self.u_d_right] = u_d[:,self.ny_d-2]
110                u_d[self.u_d_left] = u_d[:,1]
111                u_d[0, 1:-1] = u0_d[0, 1:-1] + self.td * (self.dt_max/self.dx2) * \
112                    (u0_d[1, 1:-1] + u0_d[0, 2:] + u0_d[0, :-2] - 3*u0_d[0, 1:-1]) - \
113                    self.tds*self.dt_max*(u0_d[0, 1:-1]-self.Tu)
114                #Copy temperature field
115                u0_d = u_d.copy()
116            return u0_d, u_d, E_cond

```

A.6.4. Mechanical domain

```

1   -*- coding: utf-8 -*-
2  """
3  Created on Mon Feb 6 16:45:56 2023
4  @author: Max kaiser
5  @mail: max.kaiser@ivw.uni-kl.de
6  @facility: Leibniz Institut für Verbundwerkstoffe GmbH
7  @license: MIT License
8  @copyright: Copyright (c) 2023 Leibniz Institut für Verbundwerkstoffe GmbH
9  @Version: 0.0.
10 """
11 # =====
12 # Load modules
13 # =====
14 import numpy as np
15 from scipy.integrate import solve_ivp
16 from scipy.optimize import newton
17 # =====
18 # Mechanical domain class
19 # =====
20 class Mechanical_domain:
21     #Initialize
22     def __init__(self, SMAHC, nodes, load, mf0):
23         self.S = SMAHC
24         self.n = nodes
25         self.dx = self.S.length / self.n
26         self.load = load
27         self.A_sma = self.S.g.n * self.S.w.crosssection_area
28         self.elements = np.linspace(0, self.S.length, self.n)
29         self.phidot = np.zeros(self.n)
30         self.phi0 = 0
31         self.mf0 = mf0
32     #Method to return derivatives phi' and phi of bendline as system of first order DEQ
33     def f(self, s, k):
34         k0, k1 = k
35         phi_d = k1
36         phi_dd = 1 / (self.S.s.E * self.S.s.l) * (-self.load * np.cos(k0)) + \
37             1 / (self.S.s.E * self.S.s.l)
38         return phi_d, phi_dd
39     def findphi_d_0(self, phi_d_0, mf):
40         #The system of DEQ (f) is numerically integrated using the initial values phi(L=0)
41         #and phi'(L=0) and evaluated for all elements with help of the solve_ivp
42         #(solve initial value problem) function.
43         sol = solve_ivp(self.f, (0, self.S.length), (self.phi0, phi_d_0), \
44             t_eval = self.elements)
45         #sol.y returns the values for phi and phi' for all elements
46         phi, phidot = sol.y
47         #Find E-modulus for sma wire E_sma for given martensite fraction mf
48         E_sma = (self.S.w.EA * (1 - mf) + self.S.w.EM * mf)
49         #Bending moment as function of the SMAHC's curvature
50         M_sma = (sum((-phidot * self.S.dist_sub_sma) / self.n) \
51             - self.S.w.max_strain_zero_load * (mf - self.mf0)) \
52             * E_sma * self.A_sma * self.S.dist_sub_sma
53         #Returns the function from which the root is to be found.
54         return phidot[-1] - 1 / (self.S.s.E * self.S.s.l) * M_sma
55     def find_phi_phidot(self, mf):
56         # Find value for phi'(L=0) depending on the martensite fraction using the
57         # Newton-Raphson-method
58         phi_d_0 = newton(self.findphi_d_0, 0, maxiter = 200, tol = 1e-7, args = (mf,))
59         # Solve the initial value problem again with known phi'(L=0)

```



```
60     sol = solve_ivp(self.f, (0, self.S.length), (self.phi0, phi_d_0),\  
61                   t_eval=self.elements)  
62     phi, phidot = sol.y  
63     #Returns phi and phi'  
64     return phi, phidot  
65 #Method for evaluating the stress, deflection and xmax  
66 def solve(self, mf):  
67     #Find the curvature for all elements  
68     phi, phidot = self.find_phi_phidot(mf)  
69     #Create empty lists for deflection (s_z) and regarding x coordinate (s_x)  
70     s_x = np.zeros(self.n)  
71     s_z = np.zeros(self.n)  
72     #Calculate position of element in x and z direction  
73     for i in range(1, self.n):  
74         s_x[i] = self.dx * np.cos(phi[i]) + s_x[i-1]  
75         s_z[i] = self.dx * np.sin(phi[i]) + s_z[i-1]  
76     #Calculate average stress in SMA  
77     stress0 = -self.load * (s_x[-1]/2)/(self.S.dist_sub_sma*self.A_sma)  
78     #Find deflection at the end of active length  
79     deflection = s_z[-1]  
80     #Find xmax  
81     xmax = s_x[-1]  
82     return stress0, deflection, xmax
```

A.7. Identification of material parameters

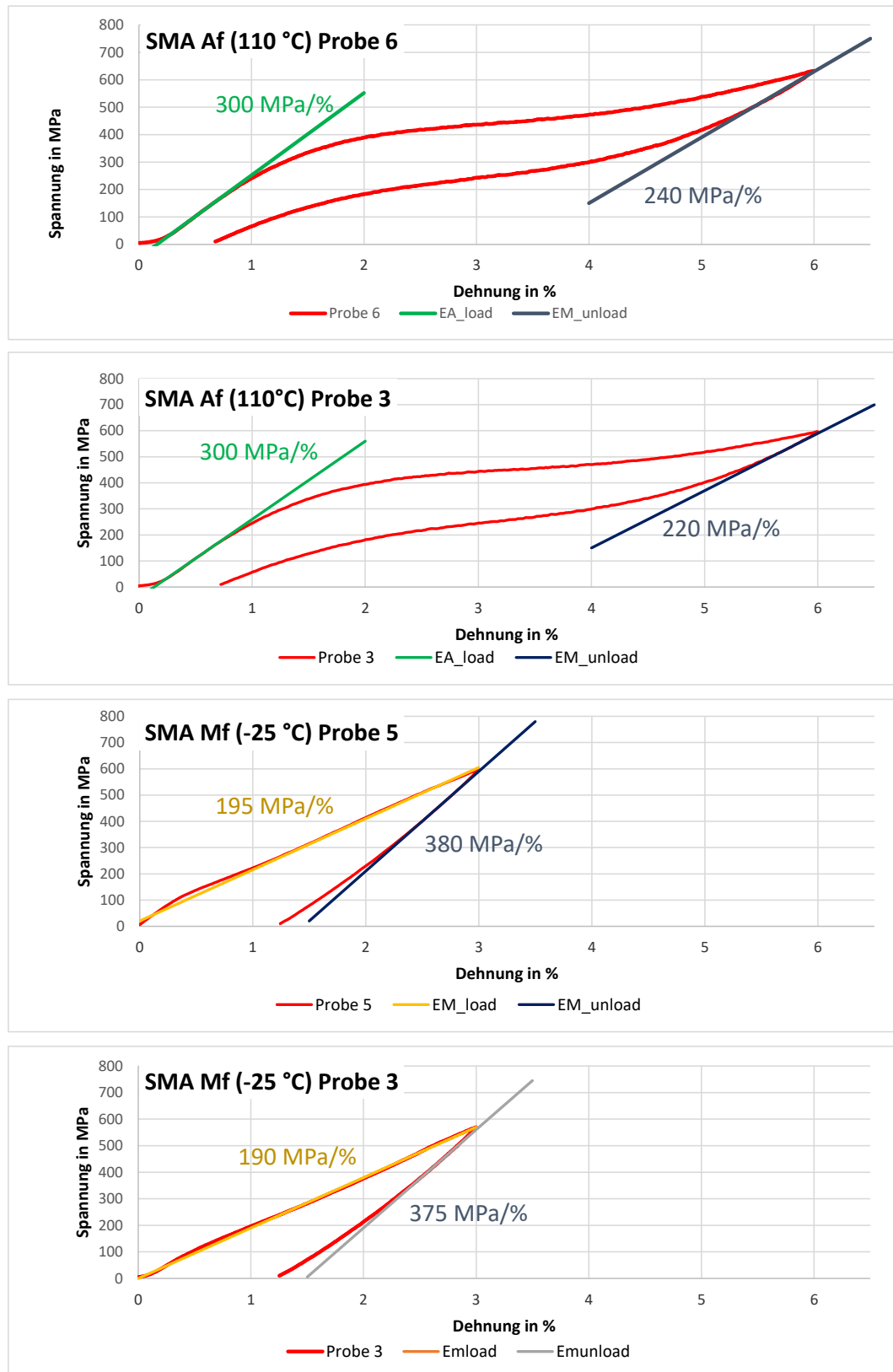


Figure A.11: Measurement-evaluation of tensile tests on SMA wires at different temperatures.

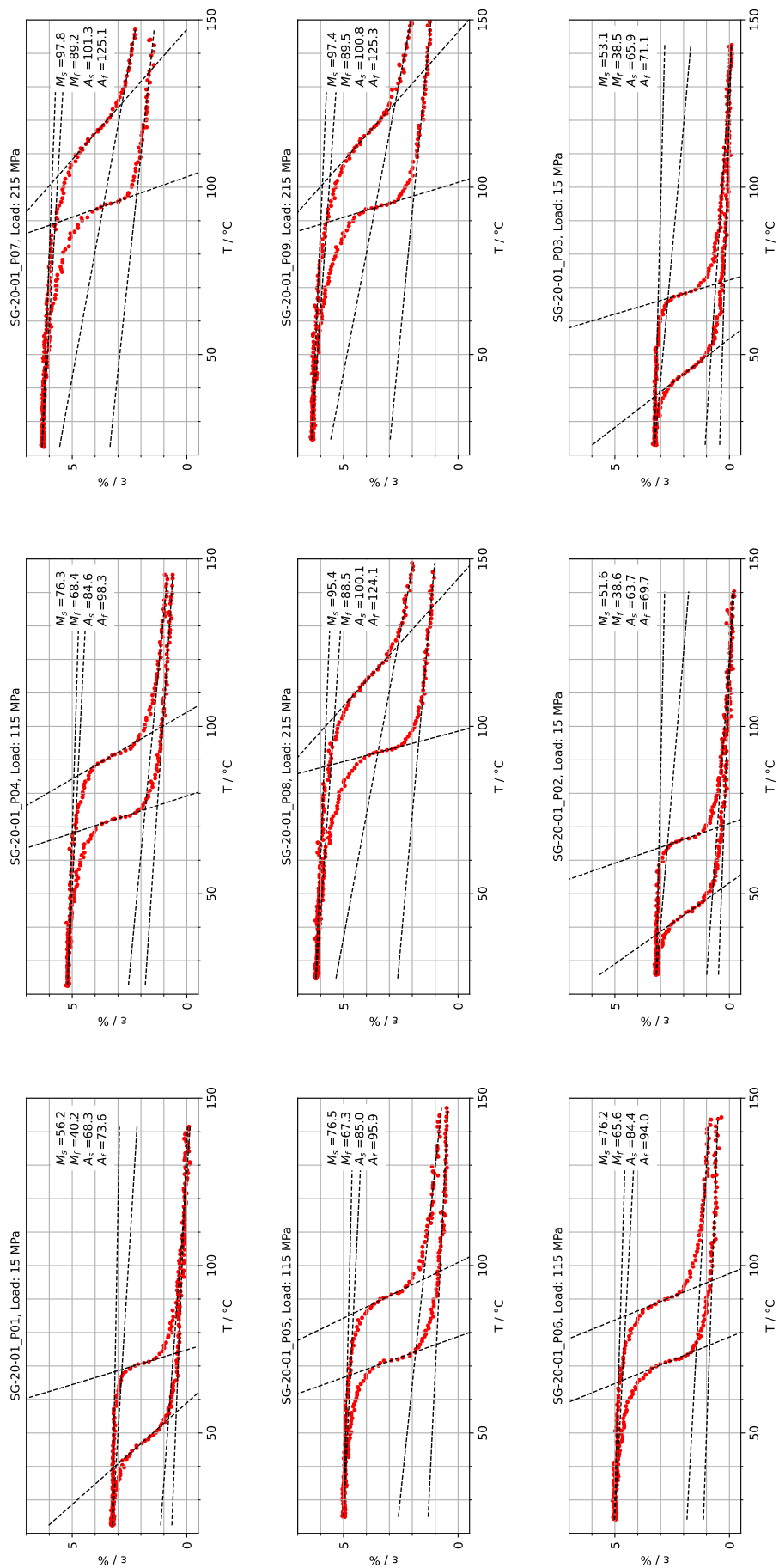


Figure A.12: Constant load experiments on SMA wire under influence of various loads.

A.8. Convergence studies

There were convergence studies conducted to identify the proper temporal and spatial discretization. The appropriate temporal increment for the lumped SMA model was distinguished according to figure A.13. The critical temperature difference remained considerably below one percent for all investigated time increments. An increment of $10e-02$ offers the optimal balance between calculation time and precision. Using the results depicted in figure A.14, the spatial discretization of the intermediate layer was calculated. A spatial discretization of $1e-05$ m was found to be necessary for accurate results. Finally a convergence study was conducted to identify a proper temporal discretization for the SMAHC model with the results depicted in figure A.15.

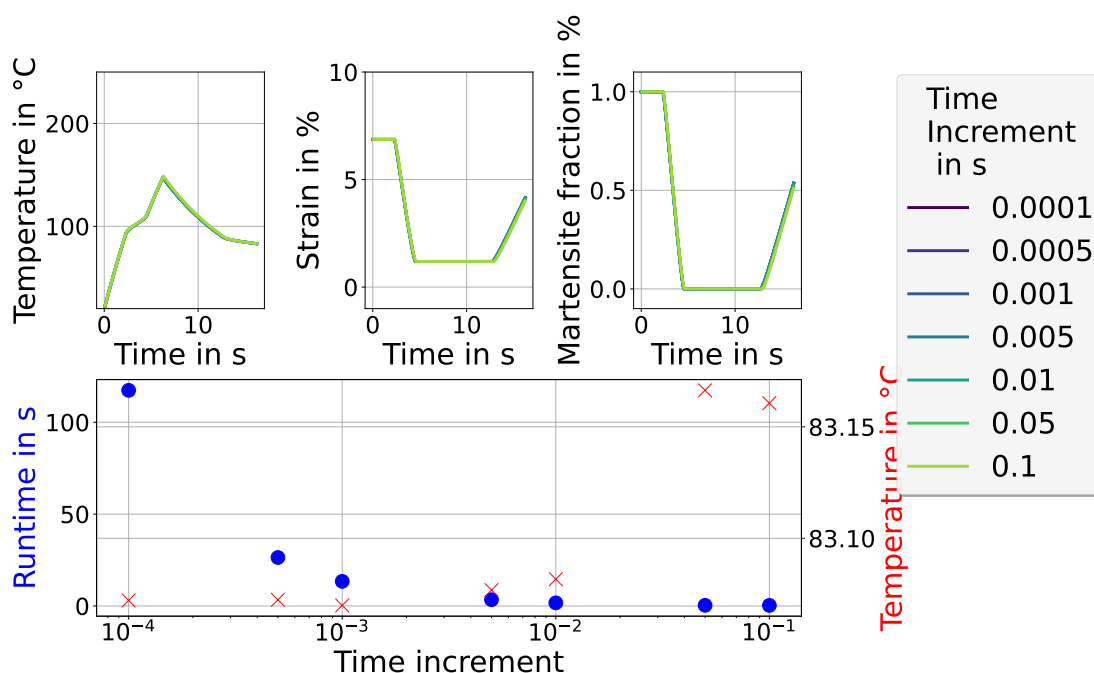


Figure A.13: Convergence study to determine the temporal resolution for the SMA model as tradeoff between runtime and accuracy.

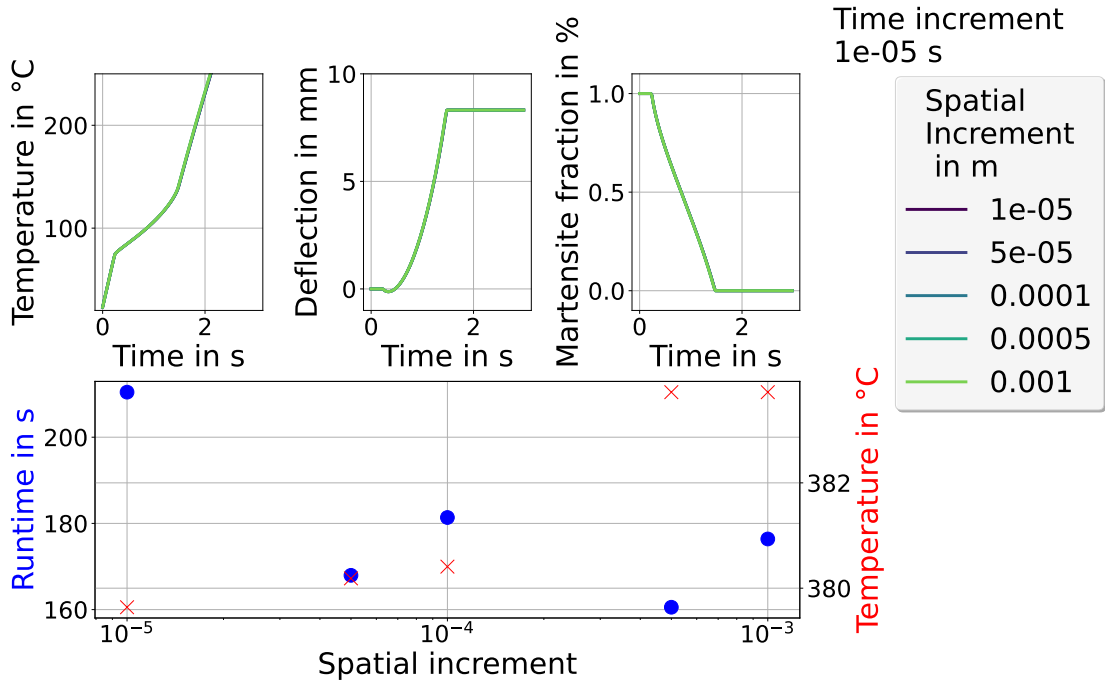


Figure A.14: Convergence study to determine the spatial resolution of the interlayer in the yz-plane as tradeoff between runtime and accuracy. Essential parameters are: Current: 5 A; SMAHC type A. The temporal step size is constant and set to 1e-05 s.

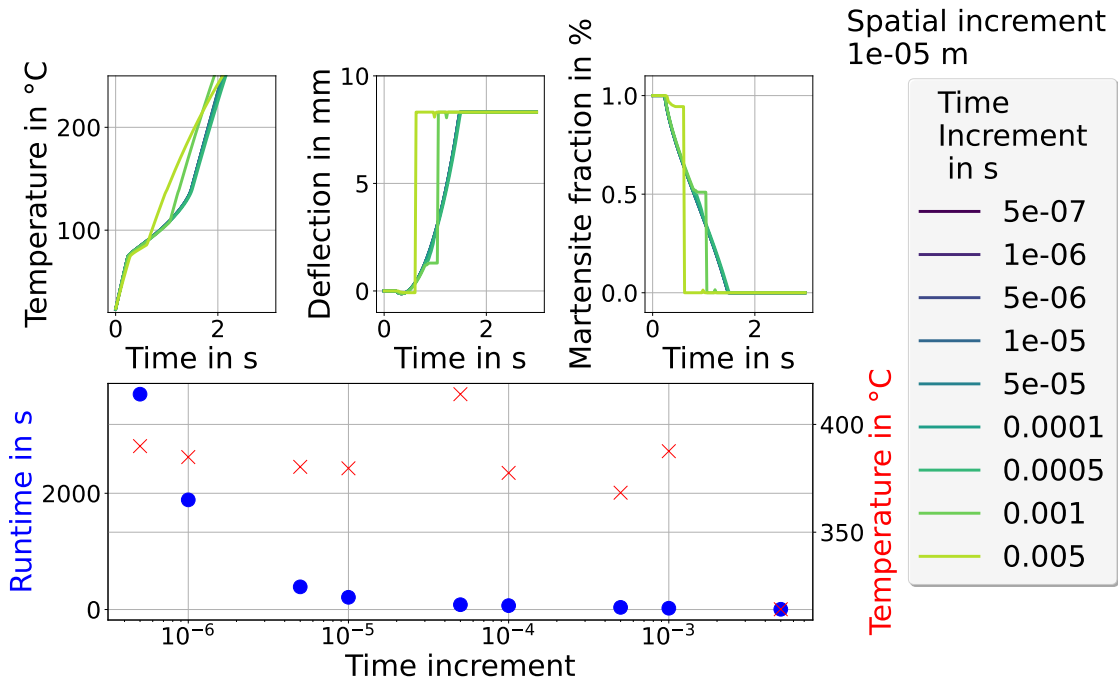


Figure A.15: Convergence study to determine the temporal resolution for the SMAHC model as tradeoff between runtime and accuracy. Essential parameters are: Current: 5 A; SMAHC type A. The spatial step size is constant and set to 1e-05 m.

A.9. Betreute Arbeiten

1. Rami Al-Khamissi: *Erweiterung des thermodynamischen Modells für aktive Shape Memory Alloy Hybrid Composites zur Formkontrolle*, IVW Bericht 22-040, Leibniz Institut für Verbundwerkstoffe GmbH, Kaiserslautern, Studienarbeit 2022
2. Simon Fischer: *Erweiterung eines Modells für aktive Shape Memory Alloy Hybrid Composites zur Formkontrolle*, IVW Bericht 22-024, Leibniz Institut für Verbundwerkstoffe GmbH, Kaiserslautern, Masterarbeit 2022
3. Benedikt Fols: *Experimentelle Untersuchungen an Möglichkeiten zur Kraftübertragung zwischen Formgedächtnislegierungen und Faserkunststoffverbunden im modularen Aufbau*, IVW Bericht 20-013, Institut für Verbundwerkstoffe GmbH, Kaiserslautern, Diplomarbeit 2020
4. Nils Neblung: *Untersuchung des Aktuierungsverhaltens in blockierten Hybridverbunden im Verbund mit Formgedächtnislegierungen*, IVW Bericht 19-049, Institut für Verbundwerkstoffe GmbH, Kaiserslautern, Diplomarbeit 2019
5. Yannick Ranker: *Konzept und Aufbau einer 1D morphenden Oberfläche für hohe Dehnungen*, IVW Bericht 19-048, Institut für Verbundwerkstoffe GmbH, Kaiserslautern, Studienarbeit 2019
6. Manuel Kunzler: *Auslegung und Aufbau einer FGL basierten adaptiven Wölbklappe nach dem Gegenspieler Prinzip*, IVW Bericht 19-047, Institut für Verbundwerkstoffe GmbH, Kaiserslautern, Diplomarbeit 2019
7. Nils Neblung: *Aufbau einer robusten Self-Sensing basierten Regelung von Formgedächtnislegierungen für den Einsatz in mobilen Anwendungen*, IVW Bericht 19-020, Institut für Verbundwerkstoffe GmbH, Kaiserslautern, Studienarbeit 2019
8. Gökhan Kolukisa: *Konzipierung und Aufbau eines Prototypen einer morphenden, spaltfreien Wölbklappe mit neuartigen Aktor-Konzepten*, IVW Bericht 19-009, Institut für Verbundwerkstoffe GmbH, Kaiserslautern, Masterarbeit 2019

A.10. Curriculum vitae

Max Kaiser

Lebenslauf

Persönliche Daten

Geburtsort: Neustadt an der Weinstraße

Beruflicher Werdegang

- 12.2017 - 04.2023 Wissenschaftlicher Mitarbeiter und Doktorand, Leibniz-Institut für Verbundwerkstoffe GmbH, Kaiserslautern, Abteilung: Werkstoffwissenschaften, Kompetenzfeld: Tailored and Smart Composites
- 12.2015 - 05.2016 Wissenschaftliche Hilfskraft am Lehrstuhl für Mechanische Verfahrenstechnik der TU Kaiserslautern.

Studium

- 10.2011 - 11.2017 Diplomstudium Maschinenbau an der Technischen Universität Kaiserslautern
Abschluss: Diplom-Ingenieur
- Diplomarbeit mit dem Thema „Konzipierung und Implementierung eines Regelungssystems für neuartige Aktoren auf Hybridverbundbasis“
 - Studienarbeit mit dem Thema „Bestimmung der Durchflusskennwerte von Carbonkeramiken“
 - Projektarbeit mit dem Thema „Untersuchung an Seitenkanalverdichtern hinsichtlich der Einsetzbarkeit für hohe Druckdifferenzen“

Schulbildung

- 08.2008 - 06.2011 Technisches Gymnasium Neustadt an der Weinstraße
Abschluss: Allgemeine Fachhochschulreife

Praktika

- 06.2016 - 11.2016 Praktikum bei der KSB SE & Co. KG Frankenthal
- 10.2013 - 11.2013 Praktikum bei der BASF SE Ludwigshafen

